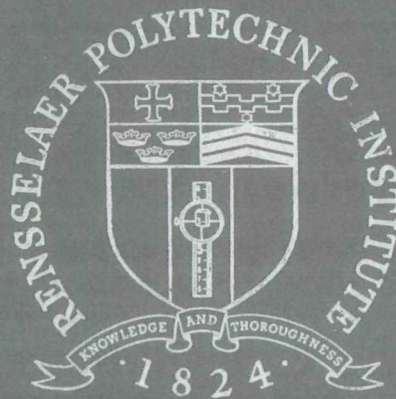


INSTRUMENTS FOR PLANETARY PROBES

N 7 3 2 2 3 9 2

John B. Hudson

to the National Aeronautics and Space
on NASA Grant # NGR 33-018-066



Rensselaer Polytechnic Institute

Troy, New York 12181

PROBLEMS AFFECTING THE FIDELITY OF PRESSURE MEASURING
INSTRUMENTS FOR PLANETARY PROBES

N 73 22 392

John B. Hudson

Final Report to the National Aeronautics and Space Administration
on NASA Grant # NGR 33-018-066

Materials Division
Rensselaer Polytechnic Institute
Troy, NY 12181

November 1972

ABSTRACT

This report summarizes progress made under the subject grant during the period September 1, 1966 to August 31, 1972. The principal aims of the research carried out were to determine the nature and magnitude of surface-related effects that can cause errors in pressure measuring instruments, with special reference to instruments intended for use as planetary probes, and to suggest ways and means of mitigating or avoiding these effects in practical instruments.

The bulk of the research carried out involved studies of the interaction of gases with clean surfaces of the metals likely to be used as gauge construction materials, with special emphasis being placed on the adsorption, chemical reaction and electron-induced desorption processes of these gases. The results indicated that all metals tested were subject to surface processes which would degrade gauge fidelity. It was also found, however, that the formation of inert adsorbed layers on these metal surfaces, such as carbon on platinum, greatly reduced or eliminated these effects. This process, combined with a system design which avoids contact between reactive gases and hot filaments, appears to offer the most promising solution to the gauge fidelity problem.

INTRODUCTION

The following report summarizes research carried out under NASA Grant No. NGL 33-018-066 during the period between September 1966 and August 1972. The original aim of the project was to investigate those processes which can occur in gauges for the measurement of pressure in ultrahigh vacuum systems which will cause erroneous pressure readings. Later on in the project, the aims were focused more specifically on the problems peculiar to pressure measuring instruments to be used in planetary probes.

It was realized early in the project that the observed pressure measurement errors could be divided into two general classes. There are first those associated with the normal operating process of the gauge, such as the so-called "X-ray effect" in ionization gauges, errors due to pressure differences between the active volume of the gauge and the main chamber of the vacuum system, and errors due to a non-uniform flux of molecules within the system, such as one finds particularly in cryopumped systems. Errors of this sort, and the design principles required to minimize and avoid them have been studied extensively in the past (see, for example, the review in the book by Redhead, Hobson and Kornelsen (1)). It was thus decided not to include considerations of this sort in the present study.

The second type of measurement error is associated with processes occurring in the gauge which are not connected

with the basic operating principle of the gauge, and which, for the most part, involve interactions between surfaces in the gauge and gases in the system. These include the "pumping" of gases by ionization and burying within the walls of the gauge, formation of ions by the interaction of electrons with gases adsorbed on gauge elements (primarily grids), decomposition of reactive gases on heated surfaces within the gauge (especially filaments) and the formation of new gas-phase species by surface chemical reactions. It is this aspect of the gauge fidelity problem which has been the subject of the present study. Those aspects of this problem that we have studied, and the conclusions that we have drawn are summarized below.

RESEARCH CARRIED OUT

During the course of this study, several experimental investigations relevant to the problems being studied were carried out. We will summarize the methods and results of all of these studies before drawing general conclusions in a later section.

Gauge Calibration System

As a preliminary to definitive studies of surface effects in gauges, a vacuum system was constructed to permit calibration of ionization gauges against a primary standard over a wide range of pressures. The system constructed was based on the "reference transfer" system of wide-range

calibration (2). It consisted of two pyrex chambers, connected to one another by a small orifice having a calibrated conductance. One of these chambers was connected through a larger calibrated conductance to a pumping system which consisted of a liquid-nitrogen-trapped mercury diffusion pump. The other was connected to a sensitive, liquid-nitrogen-trapped McLeod gauge (CVC model GM-110), which served as the reference for all calibrations, and to a gas inlet valve. Both chambers were provided with several ports for the mounting of test gauges and in addition a "reference transfer" gauge, a GE model 22GT102 ionization gauge, was mounted between the two chambers with ultrahigh vacuum valves which permitted it to be connected to one or the other chamber at any time. Gauges could be calibrated directly against the McLeod gauge in the upstream chamber in the pressure range down to 10^{-5} torr, and indirectly, using the "reference transfer" gauge down to 10^{-10} torr in the downstream chamber.

This system was used to calibrate a number of ion gauges for use in subsequent studies, and to assess the gross effects of ambient gas composition on gauge performance. Significant electron-induced desorption (EID) effects were found for the operation of gauges with molybdenum grid structures operating in oxygen atmospheres, as has also been observed by others (3). Attempts to modify this effect by operating the grid at elevated temperatures were unsuccessful, as no improvement in the EID problem was observed at temperatures below which the heat input to the grid caused excessive outgassing from other surfaces in the gauge.

Adsorption and Electron-Induced Desorption of Gases

These studies constitute one of the two major experimental lines of attack carried out under the grant. A number of gas-surface combinations were studied, in varying detail, to determine both the kinetics of their adsorption and desorption processes, and also their behavior when subjected to low energy electron bombardment. The aim of this study was to assess the magnitude of the EID effects to be expected from the surfaces of a number of materials which might be used as grids in ion gauges and, hopefully, to find materials for which this problem was minimal.

These studies were carried out in an all-metal, ion pumped ultrahigh vacuum system, provided with the necessary instrumentation for measuring thermal flash adsorption and desorption kinetics and the kinetics of EID processes on the sample surface. This system is described in detail in the thesis "The Interaction of Hydrogen and Carbon Monoxide on Platinum (111)", by V. H. Baldwin, Jr., which is included as Appendix A to this report.

Initial studies made in this system were for the adsorption and EID of H_2 , H_2O , CO and O_2 on polycrystal tungsten. These measurements were made primarily as a test of system operating parameters, and yielded results similar to those observed by others for the same and similar gas-surface combinations (4,5,6). For example, H_s^+ surface peaks were observed for both H_2 and H_2O adsorption

on polycrystal tungsten, and O_s^+ surface peaks for the adsorption of CO and O_2 on the same surface. In the case of oxygen adsorption, the O_s^+ signal was observed to be proportional to the bombarding electron current, and to increase in the expected manner with increasing electron energy. For the case of CO adsorption, results indicated initial adsorption into a state of low EID cross section, followed by later adsorption into a state of high EID cross section, similar to the results obtained by Lichtman, McQuistan and Kirst (4) for the case of O_2 on molybdenum. It was also observed that the exposure to the electron beam had a significant cleaning effect on the surface, resulting in the removal of surface carbon. The observed appearance potential for CO on tungsten was 23 volts, similar to that observed by Menzel and Gomer (5).

After completion of these preliminary studies, a very detailed study was carried out of the adsorption and interaction of H_2 and CO on platinum. This study is discussed in detail in the aforementioned Appendix A, and has been reported in the open literature (7,8).

Adsorption and Surface Reaction Studies by LEED, AES, and EID

The other major experimental program carried out under this grant was a study of the initial interaction of O_2 with both clean and contaminated single crystal nickel surfaces. These studies were begun when it became apparent that the techniques used in the study of adsorption on platinum discussed above were inadequate to provide a complete understanding of

the surface processes involved. It was not possible, for example, to determine unequivocally the state of cleanliness of the sample surface, or the extent to which the adsorbed species formed an ordered structure on the surface. To circumvent these problems, another experimental system was constructed which included the capability of making low energy electron diffraction (LEED) and Auger electron spectroscopy (AES) measurements, in addition to the flash desorption and EID capabilities present in the previous system. This system is described in the theses, "Kinetics of the Reaction of Oxygen with Clean and with Sulfur Pre-Contaminated Nickel Single Crystal Surfaces", by Paul H. Holloway, which is included as Appendix B to this report.

This appended thesis covers in detail the measurements made in this study, including a discussion of the various reaction mechanisms operating and the range of temperature and O_2 pressure over which each is important.

The AES technique was also used in a second study of CO adsorption on Pt(111), whose aim was to clear up the aforementioned ambiguities in the initial study. The results of this study are summarized in the paper, "Adsorption and Decomposition of CO on Pt(111)", by J. M. Martinez and J. B. Hudson, which is included in this report as Appendix C.

This study yielded two major results. First, that the results previously obtained for CO adsorption on clean Pt(111) were valid, and that the surface cleaning technique had indeed

produced a clean surface. Second, and perhaps more important as far as the gauge fidelity problem is concerned, formation of a layer of carbon contamination on the platinum surface by electron bombardment produced a surface which was inert to CO adsorption and showed no surface ion peaks in EID studies, suggesting a possible solution to the EID problem.

PUBLICATIONS AND OTHER COMMUNICATION

The experimental studies discussed above have lead to 8 papers which have either been published or are in the process of publication:

"Coadsorption of Hydrogen and Carbon Monoxide on (111) Platinum", V. H. Baldwin, Jr. and J. B. Hudson, J. Vac. Sci. Tech., 8, 49 (1971).

"An Inexpensive Electron Gun with an Inert, Replaceable Filament", P. H. Holloway and J. B. Hudson, Rev. Sci. Inst., 43, 828 (1972).

"A Versatile Substrate Design for LEED and AES Studies in UHV", P. H. Holloway and J. B. Hudson, Rev. Sci. Inst., 43, 1045 (1972).

"The Kinetics of the Reaction Between Oxygen and Sulfur on an Ni(111) Surface", P. H. Holloway and J. B. Hudson, Surf. Sci., 73, 56 (1972).

"The Adsorption and Interaction of H₂, CO and CH₂O on Pt(111)", V. H. Baldwin, Jr. and J. B. Hudson, submitted to Surface Science.

"Kinetics of the Reaction of Oxygen with Clean Single Crystal Surfaces I: Ni(100) Surface", P. H. Holloway and J. B. Hudson, submitted to Surface Science.

"Kinetics of the Reaction of Oxygen with Clean Single Crystal Surfaces II: Ni(111) Surface", P. H. Holloway and J. B. Hudson, submitted to Surface Science.

"The Adsorption and Decomposition of CO on Pt(111)", J. M. Martinez and J. B. Hudson, J. Vac. Sci. Tech. (in press).

Results of the experimental studies have also served as the basis for the following oral presentations:

"Environmental Effects on Pressure Gauges", Langley Research Center of NASA, August 1969.

"Surface Physics and Catalysis", ESSO Research and Engineering Company, Linden, NJ, March, 1970.

"Coadsorption of Hydrogen and Carbon Monoxide on (111) Platinum", 17th National Symposium of the American Vacuum Society, Washington, DC, October 1970.

"Surface Reaction Studies by Electron - Surface Interaction Techniques", Research Laboratories, General Motors Co., September 1971.

"The Study of Surface Molecules by Electron-Adsorbate Interaction Techniques", Clarkson College of Technology, November 1971.

"Kinetics of the Reaction of Oxygen with a Clean (111) Nickel Single Crystal Surface", 19th National Symposium of the American Vacuum Society, Chicago, Ill., October 1972.

RELATION OF RESULTS TO OBJECTIVES OF THE GRANT

The most important conclusions that can be drawn from the EID studies of adsorption on metals are first that EID signals can be observed for a large number of gas metal combinations and second that significant ambiguities can be introduced into a mass spectrometric analysis by reactions at surfaces even when surfaces are maintained at fairly low temperatures. This latter point is illustrated by the studies of hydrogen, carbon monoxide, and formaldehyde adsorption on platinum. Similar EID behavior is observed from this surface, with large H_s^+ and moderate O_s^+ peaks, irrespective of the proportions of these gases introduced into the system, and the thermal desorption measurements show that formaldehyde is decomposed with a high efficiency on heated platinum. These results are significant insofar as attempts to reduce EID effects are concerned. One possible way of decreasing the EID signal from a surface is to operate the surface at a temperature high enough that the equilibrium adlayer population, and consequently the EID ion signal, are low. For the case of platinum, this result can be obtained at a temperature of about 400°C. However, the decomposition of formaldehyde at the platinum surface is efficient at this temperature. Thus the attempt to avoid problems due to EID introduces possibly more serious problems of sample decomposition.

On the other hand, the results of the studies of oxidation of nickel, and of the adsorption and decomposition

of CO on platinum do offer some suggestions for the control of surface problems in gauges. In both cases it was observed that after the initial, and in both cases rapid, adsorption processes had taken place, the metal surfaces were relatively inert to further adsorption. This was especially pronounced in the case of CO on platinum, after the CO had been decomposed to carbon by the electron beam. The resulting surface was completely inert to further CO adsorption. In the case of O₂ adsorption on nickel, the resulting adlayer showed a very low cross-section for EID, O_s⁺ ions being detected only with very great difficulty. For the case of CO adsorption on platinum, copious quantities of O_s⁺ and CO_s⁺ were observed when a fresh CO deposit was electron bombarded, but as the deposit was converted to carbon by continuous bombardment, these EID signals dropped to zero.

POSSIBLE PRACTICAL SOLUTIONS TO GAUGE FIDELITY PROBLEMS

The results detailed above indicate that several types of surface reactions can occur rapidly and extensively on even such relatively noble surfaces as single crystal platinum. Thus it is obvious that other approaches will be required if surface related loss of fidelity is to be avoided. These approaches can be divided into two classes: a search for surfaces that are truly inert to both chemisorption of gases and to the release of atoms or ions by processes such as EID, and the design of sampling systems in which the gas

sample does not collide with surfaces in the system in the course of the measuring process.

The study of surface inertness can be further subdivided into studies of clean surfaces, and studies of surfaces which, although not clean, have been treated in such a way that they are inert. The first category involves determination of the adsorption and EID behavior of such possible surface coatings as gold or pyrolytic graphite. The results of the study of CO adsorption and decomposition on platinum indicate that graphite may be a rewarding choice. The second category involves the controlled formation of contaminant layers, such as oxides, carbides or nitrides, on a number of metal surfaces, followed by adsorption and EID measurements on the resulting surfaces. Again, the results for CO decomposition on carbon, and in addition oxide formation on nickel provide encouragement for such studies. The important point here is to produce a surface which, while inert, is still a good enough electrical conductor that surface charging of ion and electron focussing elements does not become a problem.

The other approach, that of designing sampling systems in which contact between the sample and surfaces in the system is avoided, can be accomplished by the application of aerodynamic molecular beam techniques. These techniques involve introducing a gas sample, initially near atmospheric pressure, through a small nozzle into a region of high vacuum. This forms a supersonic free jet expansion. It is possible to sample the

core of this expansion without disturbing the flow pattern. The material thus sampled can then pass by line-of-sight through the ionization region of a mass spectrometer, and then on to a beam-stop chamber where the remaining gas is pumped away. It is also possible to modulate the molecular beam formed by the sampling probe before it reaches the mass spectrometer ion source and thus, by using lock-in and phase-sensitive detection techniques at the mass spectrometer output, to separate the signal arising from the sampled material from the signal arising from background gases in the ionization region and from electrical noise generated by the instrument. Instruments of this sort have been developed in the author's laboratory to carry out these measurement functions in a large laboratory system. Application of these principles to a flight instrument would involve redesign and miniaturization of all components, and extensive simplification of the entire instrument. However, the principles involved would be the same.

SUMMARY

The results cited above indicate that considerable progress has been made both toward an understanding of the surface-related effects which can cause infidelities in pressure measuring instruments, and toward application of this understanding to the development of instruments having a high fidelity. While no such instrument has been developed

and tested in the course of the present study, we do have in hand a number of criteria for the design of such a device. On the basis of our results to date, it appears that surface reaction and EID effects, at least for a number of the common residual gases, can be reduced to very low values by controlled carbon contamination of surfaces within the ion source.

If chemical reaction at heated filaments remains a problem, this can be mitigated or eliminated by use of a gas inlet configuration which avoids contact of gases with the filament, or by the alternative of using as an electron source some form of cold cathode, such as a field emitter or Penning discharge. Again in this case, carbon coating could be used to produce inert surfaces.

References

1. P. A. Redhead, J. P. Hobson, and E. V. Kornelsen, "The Physical Basis of Ultrahigh Vacuum", Chapman and Hall, London (1968), Chapters 7-9.
2. C. F. Morrison - Extended Abstracts - 13th National Vacuum Symposium of the AVS, 1966 - pp. 45-6.
3. P. A. Redhead, J. Vac. Sci. Technol., 3, 173 (1966).
4. D. Lichtman, R. B. McQuistan and T. R. Kirst, Surf. Sci., 5, 120 (1966).
5. D. Menzel and R. Gomer, J. Chem. Phys., 41, 3329 (1964).
6. D. R. Sandstrom, J. H. Leck, and E. E. Donaldson, J. Appl. Phys., 38, 2851 (1967).
7. V. H. Baldwin and J. B. Hudson, J. Vac. Sci. Tech., 8, 49 (1971).
8. V. H. Baldwin and J. B. Hudson, submitted to Surface Science.

APPENDIX A

The Interaction of Hydrogen and Carbon Monoxide
on Platinum (111)

by

Vania H. Baldwin, Jr.

THE INTERACTION OF HYDROGEN AND
CARBON MONOXIDE ON PLATINUM (111)

BY

VANIAH HARMER BALDWIN, JR.

A Thesis Submitted to the Faculty of the School of
Engineering (Materials Division) in Partial Fulfill-
ment of the Requirements for the Degree of
DOCTOR OF PHILOSOPHY

Major Subject: Materials Science

Approved by
Examining Committee:

Chairman

Member

Member

Member

Member

Rensselaer Polytechnic Institute
Troy, New York

January 1972

TABLE OF CONTENTS

	Page
LIST OF FIGURES	vi
ACKNOWLEDGEMENTS	x
ABSTRACT	xi
I. INTRODUCTION	1
II. HISTORICAL REVIEW	3
A. Methods for the Study of Adsorption	3
1. Adsorption Technique of Measuring Surface Coverage	3
2. Thermodesorption Technique of Measuring Surface Coverage	6
3. Electron Induced Desorption History and Technique	10
B. Previous Results for Hydrogen and Carbon Monoxide Adsorbed on Transition Metals	12
C. Original Plan of Investigation	18
III. THEORY	19
A. Electron - Adsorbate Interaction Theory	19
IV. EXPERIMENTAL	25
A. Apparatus	25
1. The Vacuum System	25
2. The Gas Dosing System	26
3. Component Configuration	26
4. Instruments and Accessories	29
(a) The Mass Spectrometer	29
(b) The Electron Gun	32
(c) The Substrate Temperature Programmer	34
B. Materials Used	36
1. Substrate Preparation and Characterization	36
2. Preparation of Gases	38
C. Techniques of Measurements and Experimental Manipulations	39

	Page
1. Purging of Gas Line	39
2. Pump Speed Determinations	39
3. Thermodesorption Determination	40
4. Adsorption Measurements	41
5. Electron Induced Desorption Determinations	42
(a) Adsorption	42
(b) Thermodesorption	43
(c) Isothermal Desorption	43
V. RESULTS	45
A. Adsorption Experiments	45
1. Carbon Monoxide Adsorption from Pure Carbon Monoxide	45
2. Carbon Monoxide Adsorption from Mixtures of Hydrogen and Carbon Monoxide	50
B. Thermodesorption Experiments	50
1. Adsorption of Hydrogen from Pure Hydrogen	50
2. Effect of Carbon Monoxide and Methane on the Initial Rate of Adsorption of Hydrogen	59
3. Adsorption of Hydrogen from Mixtures of Hydrogen and Carbon Monoxide	59
4. Thermodesorption of Carbon Monoxide in Pure Carbon Monoxide and in Hydrogen - Carbon Monoxide Mixture	70
C. The Electron Induced Desorption Spectrum	72
D. Electron Induced Desorbed Ion Study of Surface Coverage	74
1. Results with Pure Hydrogen Dosing	74
2. Effect of Carbon Monoxide on the H_S^+ Ion Current	76
3. Effect of Dosing with a Mixture of Hydrogen and Carbon Monoxide	81
4. Effect of Electron Beam Current	90
E. Electron Induced Desorbed Ion Behavior During Thermodesorption	92
F. Electron Induced Desorbed Ion Observation of Isothermal Desorption	94
G. The Electron Induced Desorbed O_S^+ Ion	98
H. Experiments with Formaldehyde	101
I. Graphical Comparison of Data	104
VI. DISCUSSION	111

	Page
A. Chemisorption of Pure Carbon Monoxide	111
B. Chemisorption of Pure Hydrogen	113
C. Interaction of Adsorbed Hydrogen and Carbon Monoxide	117
VII. CONCLUSIONS	128
A. Summary of Results	128
B. Significance of the Work	129
VIII. LITERATURE CITED	131

LIST OF FIGURES

		Page
Figure 1	Typical Pressure <u>versus</u> Time Curve During Adsorption of Carbon Monoxide	4
Figure 2	Schematic Potential Curves for Interaction between a Surface M and an Atom A, and between M and the Ion A^+	20
Figure 3	Potential Curves for Interaction between a Surface M and an Adsorbed Atom A	22
Figure 4	Schematic of Gas Dosing System and Forechamber	27
Figure 5	Schematic of Electron Induced Desorption Apparatus	28
Figure 6	Schematic of the Electron Gun, Substrate-Cage, and Ion Lens Assembly	31
Figure 7	Electron Gun Emission Controller Circuit	33
Figure 8	Substrate Temperature Controller and Programmer Circuit	35
Figure 9	Carbon Monoxide Coverage on Platinum (111) as a Function of Torr Seconds Exposure	47
Figure 10	Rate of Adsorption of Carbon Monoxide <u>versus</u> the Molecular Flux to the Surface at Various Fractional Coverages	48
Figure 11	The Sticking Probability of Carbon Monoxide on Platinum (111) as a Function of Coverage	49
Figure 12	Fractional Coverage of Carbon Monoxide as a Function of CO Exposure in Pure CO and Mixtures of CO and H_2	51
Figure 13	Thermodesorption Spectrum of Hydrogen from Platinum (111)	52
Figure 14	Fractional Coverage of Hydrogen as a Function of Time in Various Pressures of Hydrogen	54
Figure 15	Fractional Coverage of Hydrogen <u>versus</u> Hydrogen Exposure at Various Pressures	56

	Page
Figure 16	Rate of Adsorption of Hydrogen as a Function of the Square Root of Impingement Rate 57
Figure 17	Fractional Coverage of Hydrogen <u>versus</u> Hydrogen Dose, $t(P_{H_2})^{1/2}$ 58
Figure 18	Effect of Carbon Monoxide on the Initial Stage of Hydrogen Adsorption in 2.2×10^{-8} Torr Hydrogen 60
Figure 19	Effect of Methane on the Initial Stage of Hydrogen Adsorption from 2×10^{-8} Torr Hydrogen 61
Figure 20	Thermodesorption of Hydrogen from a Mixture of 2.8×10^{-9} Torr CO and 3×10^{-8} Torr H_2 63
Figure 21	Hydrogen Coverage <u>versus</u> Hydrogen Dose in Pure Hydrogen and Hydrogen-Carbon Monoxide Mixtures 65
Figure 22	Hydrogen Thermodesorption Spectra as a Function of Dose Time in a Mixture of 1×10^{-7} Torr H_2 and 3.2×10^{-8} Torr CO 69
Figure 23	Thermodesorption Spectra of Carbon Monoxide in Pure CO and in a CO + H_2 Mixture 71
Figure 24	Residual Gas and EID Spectra 73
Figure 25	EID H_S^+ Ion Current <u>versus</u> Hydrogen Dose in Various Mixtures of $H_2 + CO$ 75
Figure 26	EID H_S^+ Adsorptions 77
Figure 27	EID H_S^+ Ion Current During Various Gas Exposure Experiments 78
Figure 28	EID H_S^+ Ion Current <u>versus</u> Carbon Monoxide Dose at a Constant Hydrogen Dose of $t(P_{H_2})^{1/2} = 5 \times 10^{-2}$ Torr ^{1/2} Seconds in Pure Hydrogen and Residual Gas 82
Figure 29	EID H_S^+ Ion Current <u>versus</u> Time in a Mixture of 7.6×10^{-8} Torr H_2 and 4.8×10^{-9} Torr CO 83
Figure 30	Time to Maximum EID H_S^+ Ion Current in $H_2 + CO$ Mixtures as a Function of Carbon Monoxide Pressure 85

	Page
Figure 31	EID H_S^+ Adsorptions Normalized with Respect to Carbon Monoxide Dose 86
Figure 32	EID H_S^+ Ion Current as a Function of Hydrogen Dose, $t(P_{H_2})^{1/2}$ at a Constant Carbon Monoxide Dose of $tP_{CO} = 8 \times 10^{-7}$ Torr Seconds 88
Figure 33	Normalized EID Species Concentration as a Function of Carbon Monoxide Dose 89
Figure 34	Effect of Electron Bombardment Current on the H_S^+ Ion Current Behavior 93
Figure 35	Test for Order of Isothermal H_S^+ Decay 96
Figure 36	Plot of Log Stay Time <u>versus</u> Reciprocal Temperature 97
Figure 37	Adsorption and Desorption Kinetics of the H_S^+ and O_S^+ Ion Currents 100
Figure 38	Hydrogen, Carbon Monoxide, Formaldehyde and H_S^+ Adsorption versus Time 103
Figure 39	Composit Graph of Carbon Monoxide, β , γ , and Total Hydrogen Fractional Coverages and the EID H_S^+ Ion Current <u>versus</u> Time in a Mixture of 3.3×10^{-8} Torr Hydrogen and 4.9×10^{-9} Torr Carbon Monoxide 105
Figure 40	Composit Graph of Carbon Monoxide, β , γ , and Total Hydrogen Fractional Coverages and the EID H_S^+ Ion Current <u>versus</u> Time in a Mixture of 7.7×10^{-8} Torr Hydrogen and 4.9×10^{-9} Torr Carbon Monoxide 106
Figure 41	Composit Graph of Carbon Monoxide, β , γ , and Total Hydrogen Fractional Coverages and the EID H_S^+ Ion Current <u>versus</u> Time in a Mixture of 9.5×10^{-8} Torr Hydrogen and 7.5×10^{-9} Torr Carbon Monoxide 107
Figure 42	Thermodesorption Spectra of Hydrogen and Carbon Monoxide from a Mixture of 3×10^{-8} Torr Hydrogen and 7.8×10^{-9} Torr Carbon Monoxide 108
Figure 43	Hydrogen, Carbon Monoxide, and H_S^+ Thermo-desorption Spectra in a Mixture of 1×10^{-7} Torr H_2 and 3.2×10^{-8} Torr CO 109

Figure 44

Thermodesorption Spectra for Hydrogen, Carbon Monoxide, and the H_S^+ Ion Current in a Mixture of 3×10^{-8} Torr H_2 and 7.8×10^{-9} Torr CO

110

A C K N O W L E D G E M E N T S

The author wishes to express his sincere thanks to his advisor, Professor J. B. Hudson, for his guidance, patience, discussions and encouragement throughout the course of this study.

The help of the following individuals is gratefully acknowledged: G. Lavis for suggestions concerning mechanical design; A. Buttino for glass blowing; Mrs. M. Davis for the typing; A. Kinawi and D. Jenkins for their assistance.

Special thanks go to my wife, Susan, for her constant help throughout the course of this work.

This work was supported by the NASA under Grant NGL 33-018-017, monitored by the Instrument Research Division, Langley Research Center of NASA.

A B S T R A C T

The interaction of hydrogen and carbon monoxide with the platinum (111) surface at 300°K was studied by adsorption, thermodesorption and electron induced desorption techniques in an ultra-high vacuum system. A new technique, "EID observed isothermal desorption" was developed and used. The adsorption of carbon monoxide was found to obey first order kinetics with an initial sticking probability of 0.76 and resulted in one CO per two Pt sites. Hydrogen was adsorbed with an initial sticking probability of 7.5×10^{-3} and obeyed half order kinetics, interpreted as resulting from physisorption with rapid surface diffusion followed by slow dissociative chemisorption. The coverage of hydrogen was limited to 0.20, assuming one atom per site. The coadsorption of H₂ and CO resulted in attenuated adsorption and coverage of each gas, but not mutually. Carbon monoxide, or a reaction product (HCO)*, reduced the rate of hydrogen adsorption, while a second reaction product H(CO)_n appeared responsible for the attenuation of CO adsorption. Complementary data from several techniques enabled the selection of probable surface reactions occurring during thermodesorption. The EID H_S⁺ ion originated from a surface complex (HCO)*, formed by $H + CO \longrightarrow (HCO)^*$ and subsequently consumed by $(HCO)^* + nCO \longrightarrow H(CO)_n$. The EID O_S⁺ ion had the same origin as the H_S⁺ ion. Isothermal decomposition of (HCO)* followed first order kinetics with an activation energy of 30 kcal/mole.

PART I
I N T R O D U C T I O N

In the past decade many advances in the experimental study of chemisorption have been made. The production of ultra high vacuum was a prerequisite to fundamental chemisorption studies because chemisorption occurred almost as rapidly as impingement on the surface. With the advent of ultra high vacuum techniques, it was possible to produce atomically clean surfaces and to reduce the adsorption rate to a value that could be observed with available equipment. This accomplishment enabled the development of new techniques for studying chemisorption.

This work was concerned primarily with electron induced desorption (EID) using EID to clarify results from other techniques and developing a new technique utilizing the EID phenomenon. The gases chosen were hydrogen and carbon monoxide, the predominant residual gases in stainless steel ion pumped vacuum systems. The substrate chosen was platinum, an ionization gauge material whose EID characteristics had not been determined. A single plane of a platinum crystal was used, preventing complication of results by polycrystallinity.

The problems requiring investigation included:

- a) What are the kinetics of adsorption and desorption of hydrogen on platinum (111)?
- b) Do hydrogen and carbon monoxide mutually enhance the adsorption of one another on platinum (111) as they do on some other catalysts?

- c) What, if any, is the surface reaction product formed when hydrogen and carbon monoxide coadsorb on platinum (111)?
- d) Can EID be used to determine the surface coverage of hydrogen and of carbon monoxide during adsorption?

The problem was approached by determining the chemisorption characteristics of hydrogen and carbon monoxide on platinum (111) by the older techniques of adsorption and thermal desorption, followed by utilizing the EID technique in conjunction with the aforementioned techniques to study the interaction of the mixed gases. In addition, a new technique was developed, EID observed isothermal desorption, which contributed to the analysis of other data.

PART II

H I S T O R I C A L R E V I E W

A. Methods for the Study of Adsorption

1. Adsorption Technique of Measuring Surface Coverage

The "flash filament technique" and the modification of it referred to as the "adsorption technique" in this paper, were first made public by J. P. Molnar and C. D. Hartman at the M.I.T. Physical Electronics Conference on the 1st of April, 1950. In 1953 the techniques were explained in a paper published by J. A. Becker and C. D. Hartman.¹ Redhead has expanded the theory since then.²

When a constant leak of gas is allowed to enter a vacuum system that is being pumped at a constant rate, an equilibrium pressure, P_{eq} is attained. The situation is described by

$$L + R_w = KP_{eq} (S + S_w) \quad (1)$$

where L = input leak rate (molecules sec^{-1})

R_w = re-emission rate from system walls

$K = 3.22 \times 10^{19}$ molecules liter $^{-1}$ at $P = 1$ Torr and $T = 300^\circ\text{K}$

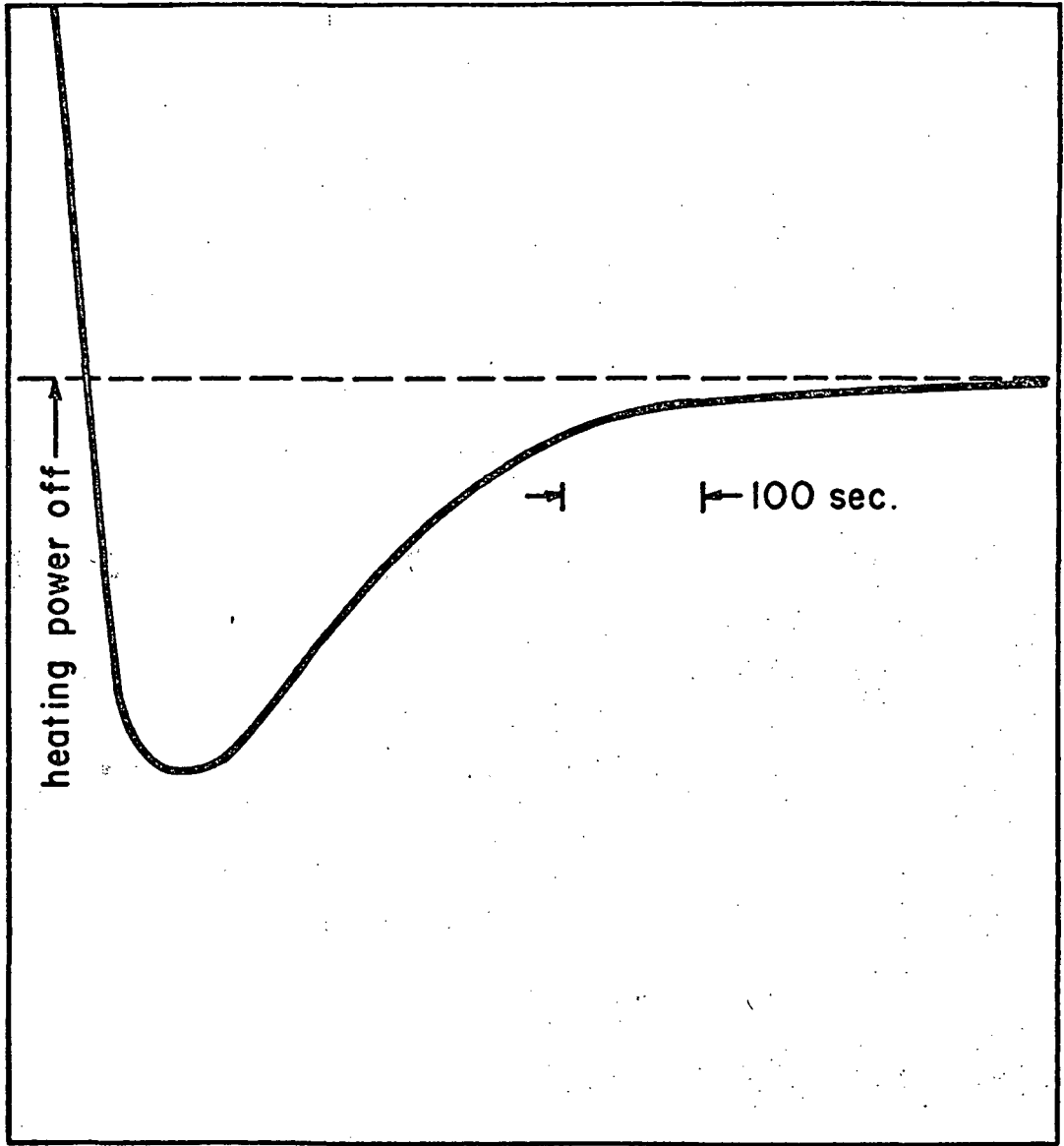
S = pump speed (liters sec^{-1})

S_w = equivalent pumping speed of the system walls

If a clean substrate surface is introduced into the system at equilibrium, it will adsorb gas, acting as an additional pump and lowering the pressure. The pressure will rise again as the substrate becomes covered with adsorbed gas. Figure 1 shows a typical adsorption determination. The amount of pressure drop is determined by the pumping speed, area of the substrate and the sticking probability. If the substrate area is equal to the area of the pumping orifice and

FIGURE 1
Typical Pressure versus Time Curve
during Adsorption of Carbon Monoxide.

PRESSURE (ARBITRARY) →



TIME →

the sticking probability is unity, then the pressure will drop to half the equilibrium value. This was approximately the case in this determination. Introducing a second term into equation (1) to account for molecules adsorbed by the substrate and a third term for the PV change:

$$L + R_w = KP (S + S_w) + \nu A s P + KV dP/dt \quad (2)$$

where ν = specific arrival rate of molecules at the substrate

$$(\nu = 3.70 \times 10^{20} \text{ molecules cm}^{-2} \text{ sec}^{-1} \text{ for CO at } 300^\circ\text{K and 1 Torr})$$

A = area of substrate (cm^2)

s = sticking probability on the substrate

From equations (1) and (2),

$$s = (KV/\nu AP) [(P_{eq} - P)/\tau] - dP/dt \quad (3)$$

or

$$s \approx (KV/\nu A \tau) [(P_{eq}/P) - 1] \quad (3a)$$

when $dP/dt \ll (P_{eq} - P)/\tau$, which is the case except at the beginning of the process. The pumping constant $\tau = V/S$, where V is the volume of the system.

If the leak rate is doubled, the pressures P and P_{eq} will be doubled, and the time for the adsorption process will be halved. The sticking probability is a quantity which characterizes the interaction between individual molecules and the surface and is independent of pressure. It is defined as the rate of chemisorption divided by the arrival rate on the surface;

$$s = (d\sigma/dt)/\nu P$$

where τ is the surface coverage in molecules/ cm^2 .

If the rate of evaporation of molecules from the surface \dot{D} , is considered, the rate of chemisorption is found as

$$d\sigma/dt = v_s P - \dot{D}$$

Assuming \dot{D} is negligible,

$$d\sigma = v_s P dt$$

$$\begin{aligned} \sigma(t) &= v_s \int_{t_s}^{t_f} P dt \\ &= (KV/A\tau) \left[\int_{t_s}^{t_f} (P_{eq} - P) dt + \tau(P_{eq} - P) \right] \\ \sigma(t) &\approx (KV/A\tau) \left[\int_{t_s}^{t_f} (P_{eq} - P) dt \right] \end{aligned} \quad (4)$$

where integration is from the starting time t_s to the finish time t_f in seconds.

The sticking coefficient and the total coverage may therefore be determined from pressure measurements during adsorption by the substrate.²

2. Thermodesorption Technique of Measuring Surface Coverage

Thermodesorption refers to the desorption of gas from a solid surface by a constantly increasing temperature. This technique was introduced by Hartman¹ and has since been expanded.^{3,4,5} The same experimental system is used as with the adsorption technique, the difference being in the temperature programming of the substrate.

The substrate is heated until all gas has been desorbed, then cooled for the time required to obtain the desired dose. Next the substrate is heated at a rate that is a known function of time. The pressure will at first rise due to desorption of adsorbed gas, then

fall owing to the continuous pumping. A typical thermodesorption determination has been traced to scale and is shown in Figure 13. In the present work, the system constants were such that the pressure rose about 5×10^{-7} Torr, irrespective of the dosing pressure. The area under this curve will yield the original surface coverage, (molecules cm^{-2}) prior to heating in the same manner as with adsorption:

$$\sigma_0 = (SK/A) \int_{t_s}^{t_f} (P - P_{eq}) dt \quad (5)$$

An examination of desorption kinetics provides additional information, although ideal experimental conditions for their application are seldom obtained. Consider a system which is being pumped at a constant speed, and into which gas is being leaked at a constant rate. At equilibrium, when the substrate is not adsorbing, $P = P_{eq}$ and

$$L = KSP_{eq} \quad (6)$$

If now the substrate is heated and it is assumed that gas is desorbed from the substrate but not adsorbed by any part of the system, then

$$A\dot{D}(t) + L = KS + KV(dP/dt). \quad (7)$$

Combining equations (6) and (7)

$$[d(P - P_{eq})/dt] + [(P - P_{eq})/\tau] = a\dot{D}(t) \quad (8)$$

where $a = A/KV$.

The rate of desorption from unit surface area is ⁴

$$\dot{D}(t) = (-d\sigma/dt) = v_n \sigma^n \exp(-E_d/RT) \quad (9)$$

where n is the order of the desorption reaction,

σ is the instantaneous surface coverage (molecules cm^{-2}),

v_n is the rate constant,

and

E_d is the activation energy of desorption (cal mole⁻¹).

Solving equation (9) to find the temperature (T_p) at which the desorption rate is a maximum under conditions of linear heating,

i.e., $T = T_0 + t$,

$$E_d/RT_p^2 = (v_1/\beta) \exp(E_d/RT_p) : \text{for } n = 1 \quad (10a)$$

and

$$E_d/RT_p^2 = (2\sigma_p v_2/\beta) \exp(E_d/RT_p) : \text{for } n = 2 \quad (10b)$$

where σ_p is the coverage at $T = T_p$ and v_1 is usually assumed to be 10^{13} sec⁻¹.

This shows that T_p , the temperature at the peak of the desorption curve, is independent of coverage for a first order reaction with constant E_d and dependent on coverage for a second order reaction, if the temperature rise is slow compared to the ratio of pumping speed to system volume.

For the case where the adsorbate exists in only one adsorbed state, Redhead³ has shown that

$$\sigma_p \approx \sigma_0/e \quad \text{for } n = 1 \quad (11a)$$

and

$$\sigma_p \approx \sigma_0/2 \quad \text{for } n = 2 \quad (11b)$$

Using these approximations and combining equation (9) with equation (10), one obtains

$$E = (e \dot{D}_p/\sigma_0\beta) RT_p^2 : \text{for } n = 1 \quad (12a)$$

$$= (4 \dot{D}_p/\sigma_0\beta) RT_p^2 : \text{for } n = 2 \quad (12b)$$

and

$$v_1 = (e \dot{D}_p/\sigma_0) \exp(e \dot{D}_p T_p/\sigma_0\beta) \quad (13a)$$

$$v_2 = (4 \dot{D}_p/\sigma_0) \exp(4 \dot{D}_p T_p/\sigma_0\beta) \quad (13b)$$

where \dot{D}_p is the rate of desorption at the peak of the desorption curve. \dot{D}_p may be found from equation (8). Since at the peak of the curve $d(P - P_{eq})/dt = 0$, then

$$\begin{aligned}\dot{D}_p &= (P - P_{eq})/\tau_a \\ &= (SK/A) (P - P_{eq})\end{aligned}\quad (14)$$

There are several facets of thermodesorption that require caution. The derivations given above apply to a single desorption peak and to the gas coming off the surface. It is tempting to assume that the species desorbing from the surface is the same species that was on the surface before flashing. This is not universally true.

Further, multiple thermodesorption peaks are commonly observed. This is attributed to multiple binding states on the surface.³ It is common practice to label these 1, 2, 3, ... and proceed with discussion about each state. A quantitative separation of the curves and determination of coverage of each state is not always valid and must be accepted as a crude estimate because thermally activated transition from one state to another during the flash is not unknown.² Thus, upon thermodesorption one might observe:

- a) Desorption of the adsorbed species from the binding state it existed in prior to desorption.
- b) Desorption of the adsorbed species from a binding state it transferred to at an earlier stage of thermodesorption.
- c) A combination of a) and b).
- d) Desorption of decomposition products of the adsorbed species.
- e) In the case of mixtures of gases, desorption of species from binding states that were the result of thermally activated interactions at an earlier stage of the thermodesorption flash.

3. Electron Induced Desorption History and Technique

When a beam of electrons impinges on a metal surface covered with an adsorbate, neutral and positively charged particles of adsorbate may be desorbed from the surface. This phenomenon has been variously called electron stimulated desorption, electron impact desorption and electron induced desorption. Its history is interesting partly because it has been known for so long yet only recently investigated in detail. As an analytical tool it predates this work only a few years.

Electron induced desorption of ions from the surface of an ion source in a mass spectrometer was first noted by Dempster in 1918.⁶ In 1942 Ishikawa⁷ noted and discussed the electron induced desorption of neutral particles, but his observations were limited to pressure changes. Plumlee and Smith⁸, in 1950, determined the efficiency of O_S^+ evolution from a molybdenum surface to be about 10^{-8} ion/electron at 300°K and found the desorbed ions had an energy of 10eV. (Lichtman's terminology⁹ of subscript s to denote EID particles will be used in this paper.) Ten years later Young¹⁰ studied the release of O_S^+ from oxidized Cu, Ni, Mo, Ta, and Ti surfaces. A very careful study was performed by Moore¹¹ in 1961. He determined the effect of 20 to 300 volt electrons on carbon monoxide adsorbed on molybdenum and tungsten surfaces. The carbon monoxide was dissociated, leaving carbon on the surface and producing O_S^+ ions which were detected with a mass spectrometer. Further work concerned with the effect on vacuum systems of gas release from surfaces under electron bombardment, and the effects on mass spectrometer ion sources was carried out by Degras¹², Petermann¹³, Marmet and Morrison¹⁴, and Davis¹⁵ in 1962-

1963 without a detailed examination of the process.

Redhead found serious errors in pressure measurement due to the formation of positive ions by electron bombardment of chemisorbed oxygen in Bayard-Alpert ionization gauges in 1963¹⁶ and made a careful study of the phenomenon in 1964¹⁷. Working at room temperature and above, he found two states of adsorption of oxygen on molybdenum. The energy distribution of the desorbed O_S^+ ions peaked at 6eV and the efficiency of production was 10^{-5} ion/electron. He was also able to determine that 50 neutrals were produced for every ion produced. The electron energy required to produce desorption agreed with calculated values and he proposed a theory for the mechanism of electron induced desorption.

Menzel and Gomer¹⁸ also made a careful study of electron induced desorption in 1964 using the field emission microscope. They presented a comprehensive theoretical interpretation of the phenomenon, which was essentially the same as Redhead's proposal. Their theory will be presented in section III of this paper under "Electron-Adsorbate Interaction Theory."

The technique of observing EID ions is simple in concept. The substrate is bombarded with electrons, commonly of 100eV energy. The electrons may come from an electron gun or simply a filament mounted close to the substrate. A grid near the substrate is biased negatively to attract and draw out EID ions. The ions may then be totally collected, providing quantitative yield data, or focused into a mass spectrometer for ion identification and relative yield data. If adsorbed particles can be desorbed by electron bombardment, then the surface coverage can be followed by observing the EID current during

adsorption or desorption.

B. Previous Results for Hydrogen and Carbon Monoxide
Adsorbed on Transition Metals

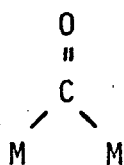
Electron induced desorption studies or the use of the electron probe surface mass spectrometer, as Lichtman calls it,⁹ on platinum have been pursued only by Huber and Rettinghaus. Indeed since the introduction of modern ultra high vacuum techniques, very little fundamental research has been performed on platinum. This would at first seem surprising until certain experimental factors are considered. Tungsten has been a favorite material to study when new instruments and techniques are developed because it is generally accepted that an atomically clean tungsten surface can be produced by heating to 2200^oK. Low melting metals can be difficult to impossible to clean in such manner.

Low-energy electron diffraction study of CO adsorption on (100) Pt by C. W. Tucker¹⁹ indicated that the CO molecule is adsorbed with its linear axis normal to the surface. (The temperature of adsorption was not given.) Two surface structures of CO were found, according to density of coverage, the low coverage structure exhibiting strong attractive interaction between some molecules. The high coverage structure could be converted to the low coverage structure by heating to 80^oC and all structure disappeared at 200^oC, indicating either mobility or desorption.

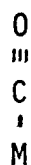
Morgan and Somorjai²⁰ found in addition, a work function decrease of 0.45eV when carbon monoxide was adsorbed on (100) Pt, indicating an electron donating adsorbate:

Lewis and Gomer²¹ have studied carbon monoxide adsorption on platinum by field emission microscopy. They found a physisorbed adsorbate below 55°K. Between 50°K and 250°K various rearrangements occurred and around 375°K - 400°K either rearrangement without affecting dipole moment or desorption without affecting work function occurred. Above 400°K desorption from electronegative states occurred. The surface diffusion of chemisorbed CO at 300°K was of two types, boundary free diffusion at low coverages and boundary diffusion at high coverage. This was explained by proposing an energy spectrum of adsorption sites. Diffusion was most rapid on the (111) plane indicating the least number of tight binding sites. Lewis and Gomer conclude that the behavior of carbon monoxide on platinum is complex and puzzling. It appears to them that the entire spectrum of CO adsorption involves only virgin or alpha like states.

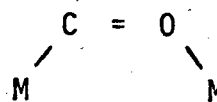
Sugita, Ebisawa and Kawasaki²² also found evidence of only one binding state on platinum when they exposed an evaporated film to carbon monoxide and followed the electrical resistance with gas uptake. They found 1.0 - 1.2 conduction electrons involved with each surface bond, suggesting alpha type bonding. The structures of the various types are:



Virgin



Alpha



Beta

Eischens, Pliskin and Francis²³ found two absorption peaks in the I-R when silica supported Pt was dosed with CO. One peak was very weak and was attributed to virgin CO by analogy with metal carbonyls

and the frequency shift involved. The strongest absorption was attributed to alpha type adsorption.

Whether the virgin or alpha structure predominates varies according to the physical form the platinum is examined in, i.e., silica supported, alumina supported, evaporated film, etc.²⁴ Some work on films has shown both types of adsorption.²⁵

Hydrogen adsorption on platinum has been studied by Mignolet²⁶ and Lewis and Gomer²⁷ using FEM techniques. They found two forms of adsorbed hydrogen, an electronegative layer that was chemisorbed atomic hydrogen and an electropositive layer of molecular hydrogen bound by charge transfer forces or Van der Waals forces. The electropositive layer desorbed from 200° to 250°K leaving the electronegative layer which was observed to desorb around 275° - 300°K. The hydrogen adsorbed on the (110) plane required somewhat higher temperatures to desorb, 300° - 325°K. At high coverages the lowest energy of desorption of the covalently bound hydrogen was about the same as the highest energy of desorption of the molecular electropositive layer, thus the distinction between adsorbed atomic and molecular hydrogen is blurred. Diffusion of the molecular layer set in above 20°K while diffusion of the covalently bound atomic hydrogen commenced at 100°K with an activation energy of 4.5 kcal. At 300°K to 500°K incoming hydrogen was not rapidly accommodated but diffused a considerable distance prior to dissociative chemisorption.

Flash filament studies of hydrogen on polycrystalline platinum wire using an ionization gauge detector were carried out by Wiesendanger²⁸. These revealed a single desorption peak around 190°C,

reaching a maximum coverage of 0.29 in 30 minutes in 6×10^{-8} Torr hydrogen. Longer doses exhibited a decline in the hydrogen peak and a rise of a 350°C peak attributed to carbon monoxide. A shoulder on the desorption curve at high dose times indicated that the desorption energy of hydrogen increased in the presence of carbon monoxide. The sticking probability for hydrogen was determined to be 10^{-3} .

Morgan and Somorjai²⁰ did not find any adsorption of hydrogen on (100) platinum until the pressure was raised above 2×10^{-5} Torr and the temperature raised to $500^{\circ}\text{C} - 1000^{\circ}\text{C}$. They then found a change in LEED pattern indicating a transformation from a (5 X 1) surface structure to a (2 X 2) structure. The high temperature required was attributed to the necessity of preventing carbon monoxide from the ambient from adsorbing. The (2 X 2) structure formed by hydrogen adsorption was stable and required a few minutes at 1200°C in vacuo to remove. They also found that if trace amounts of carbon were present on the surface, it was impossible to generate the (2 X 2) diffraction pattern. Mention was made that the co-adsorption of H_2 and CO produced a surface structure different from those formed by the chemisorption of CO or H_2 alone.

Huber and Rettinghaus²⁹ are the only other workers to investigate hydrogen and carbon monoxide adsorption on platinum by means of electron induced desorption. Their work was mostly at 2×10^{-10} Torr residual hydrogen pressure, and a rather high electron current density of 10^{-4} Amp/cm² on polycrystalline platinum. Residual gas analysis was not given, and surface coverage determinations were not attempted but rather they assumed a sticking probability of unity for hydrogen (as opposed to $10^{-3} - 10^{-2}$ found in this and other works).

and assumed that carbon monoxide had no influence on hydrogen adsorption which is also contrary to this and other work. Examination of the H_S^+ ion current showed it to be independent of hydrogen pressure. This was interpreted as the result of hydrogen adsorbing into "State I" followed by transition to "State II" on special sites that occupy about 10^{-3} of the surface. Since their electron beam current was high, extensive desorption due to electron bombardment occurred. This resulted in a "lower equilibrium" value of H_S^+ and an "Upper equilibrium" value, obtained by pulsed electron beam technique. The changes of these values were studied as a function of bombardment times and gas exposures. The results were explained on the assumption that surface diffusion of hydrogen is slow but increases after extended electron bombardment. Of particular interest is the fact that they found EID CO_S^+ . Other transition metals reported in the literature exhibited only O_S^+ from CO coverage. This is attributed to the high binding energy of CO on transition metals, making dissociation of the molecule easier than desorption, as an ion. Predictably, the CO_S^+ current disappeared upon heating to a rather low temperature of $250^\circ C$. The O_S^+ ion was not observed in their work. The nature of the experiments performed by Huber and Rettinghaus, dictated by the limitations of their system, do not lend themselves to direct comparison with the experiments performed in this work.

The interaction of hydrogen with molybdenum has been studied by Pasternak and Wiesendanger³⁰ using thermodesorption and ion gauge techniques. They found that the saturation coverage of hydrogen was independent of pressure but strongly dependent on substrate temperature. The maximum coverage at $225^\circ K$ was 1.4×10^{15} atoms/cm² and

about half this value at room temperature (300°K). The thermodesorption spectrum showed a single desorption peak for 300°K dosing. When the substrate was dosed at 225°K a very well defined second desorption peak appeared, equal to the original higher energy desorption peak. This was interpreted as the formation of two layers of gas, each of which contained close to two hydrogen atoms per molybdenum atom. The sticking probability for the first layer was 0.35. The adsorbed hydrogen was readily replaced by nitrogen at room temperature.

Lichtman⁹ was able to follow the surface coverage of hydrogen on molybdenum by observation of the H_S^+ ion current, and the coverage of carbon monoxide by the O_S^+ ion current.

The EID H_S^+ ion current resulting from hydrogen dosing of nickel (100) was studied by Lichtman, Simon and Kirst.³¹ The H_S^+ ion current described a rise, peak and decline as hydrogen coverage increased.

This was interpreted as adsorption into a weakly bound molecular state followed by transfer to a strongly bound atomic state. Williams and Gasser³² found a monotonic increase in H_S^+ ion current when polycrystalline nickel was exposed to hydrogen. The H_S^+ ion current remained constant when saturation coverage was attained. If, however, small amounts of carbon monoxide were introduced, the H_S^+ ion current increased. This was interpreted as an increase in the desorption cross section of hydrogen caused by coadsorption of carbon monoxide. No mechanism for this effect was proposed. (Their work was reported after the experimental work for this paper was completed.)

C. Original Plan of Investigation

The EID literature indicated that the EID ion current was proportional to surface coverage and that H_S^+ ions came from adsorbed hydrogen and O_S^+ ions came from adsorbed oxygen or carbon monoxide. From that information it was assumed that it would only be necessary to calibrate the H_S^+ ion current by running a thermodesorption coverage determination after equilibrium H_S^+ ion current was obtained with hydrogen dosing, then utilize the H_S^+ ion current to determine coverage versus time. Repeating this at several pressures would provide all the information needed to determine the kinetics of adsorption of hydrogen. Since this technique would produce a continuous plot of coverage versus time it would be more desirable than making point by point determinations, as required by the thermodesorption technique.

After determining the adsorption characteristics of hydrogen and carbon monoxide, the adsorption properties of gas mixtures could be determined in like manner. It was hoped that any reaction products could be observed either by their EID signal or by thermodesorption. Since a mass spectrometer was being used as a detector, the composition of any reaction products could be determined.

PART III
T H E O R Y

A. Electron - Adsorbate Interaction Theory

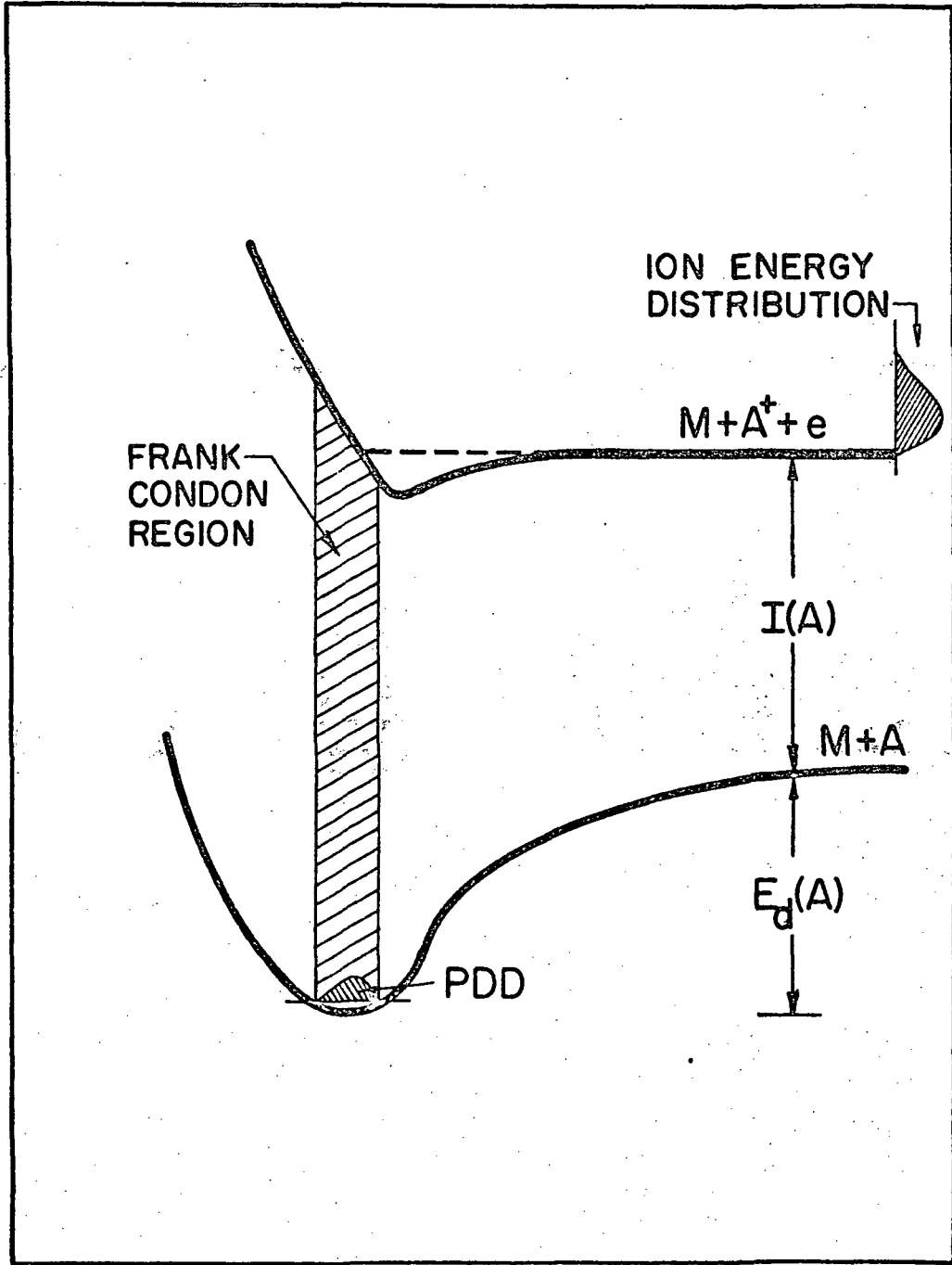
If a metal, M, covered with adsorbed gas atoms, A, is bombarded with electrons, the adsorbate may be desorbed from the surface in the form of positive ions, ground - state neutral atoms or excited neutral species. Conversion of the adsorbate from one binding state to another has also been observed. In the case of adsorbed molecules, fragments of the molecules may appear. If low energy electrons ($< 500\text{eV}$) are employed, this phenomenon cannot be explained by momentum transfer, with the possible exception of physically adsorbed gases.¹⁸

A mechanism for the production of neutral and ionic desorbed species has been proposed independently by Redhead¹⁷ and Menzel and Gomer¹⁸. They propose electronic excitation from a ground state to an ionic repulsive state. This is shown in Figure 2 where the lower curve is the potential energy of interaction between a metal adsorbent M and an adsorbate atom A and the upper curve is that of the metal and the ionic form of A.³³ The binding energy of the atom A is represented by the distance $E_d(A)$ while $I(A)$ represents the ionization potential of the free atom. The range of internuclear separation in the ground state is shown by the widths of the shaded band. Since the internuclear separation and velocity will not significantly change during an electronic transition, according to the Frank-Condon principle, electronic transitions from the ground state to the ionic state will be within the shaded area. Initially the bombarding electron causes a transition from the neutral to the ionic potential

FIGURE 2

Schematic Potential Curves for Interaction between a Surface M and an Atom A, and between M and the Ion A^+ . The PDD is the Square of the Wave Function for the Ground State M-A Oscillator.

POTENTIAL ENERGY



DISTANCE FROM SURFACE z

energy curve. The adsorbed ion may then undergo (1) de-excitation to the original neutral adsorbed state through Auger neutralization, or tunneling of an electron from the substrate to the adsorbed ion, (2) desorption as an ion with kinetic energy greater than zero, (3) desorption as a neutral when sufficient kinetic energy for desorption is acquired by the ion prior to Auger neutralization, or (4) de-excitation to a neutral adsorbed state different from the original. Several other possibilities have been suggested by Madey and Yates³³ as shown in Figure 3. Here the potential energy curve for the antibonding $(M + A)^a$ state is included. Transition to the antibonding state would produce a desorbed neutral. It is also possible for the $(M + A^+ + e^-)$ ionic state to be positioned so that the Frank-Condon region intercepts only the attractive portion of the curve. In this case excitation from the ground state to the $(M + A^+ + e^-)$ ionic state would not result in the desorption of ions. If excitation from the ground state to the repulsive part of the metastable state $(M + A^*)$ occurs, however, either a metastable species may desorb or an adiabatic crossing to the ionic curve $(M + A^+ + e^-)$ may occur, resulting in desorbed ions.

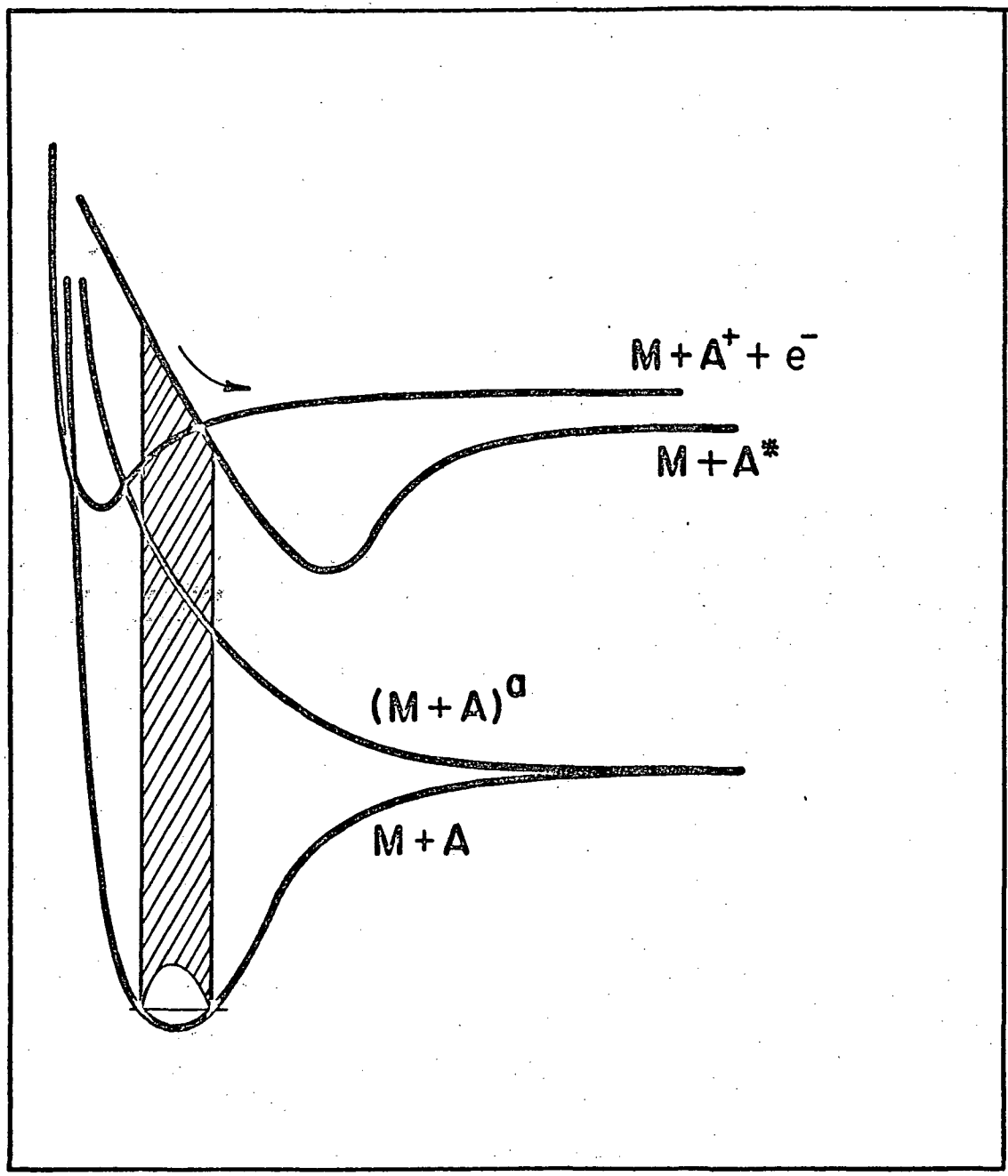
These are only the simplest of many possibilities, as suggested by the fact that the curves in Figure 3 are only the lowest members and the ground state.

Several theories for predicting the minimum energy an electron must have to produce an EID species have been offered and found to fit experimental results quite well. Redhead¹⁷ has proposed that in case of a diatomic molecule, A_2 that is dissociatively adsorbed, the threshold energy of bombarding electrons to produce an A^+ ion of zero

FIGURE 3

Potential Curves for Interaction between a Surface M and an Adsorbed Atom A. Possible Excited State including an Ionic State ($M + A^+ + e^-$), a Metastable-Atomic State ($M + A^*$), and the Antibonding State ($M + A$)^a are Also Shown.

POTENTIAL ENERGY \uparrow



DISTANCE FROM SURFACE, $z \rightarrow$

kinetic energy at distance $d = \infty$ is

$$V_{T(0)} = I(A) + E_d(A).$$

Experimental results for CO/W³⁴ and O₂/Mo¹⁷ verified this prediction. In practice, only those ions are detected that have a kinetic energy, E_k greater than zero. If the effective mass of the surface is much greater than that of the ion liberated, then conservation of momentum requires that the liberated ion possess virtually all the kinetic energy. Thus the threshold energy becomes $V_T = V_{T(0)} + E_k =$ energy of bombarding electron. This has been experimentally verified.¹⁷

The majority of excited adsorbed ions undergo de-excitation resulting in 10 to 100 times as many neutrals as ions ejected from the surface. Menzel and Gomer¹⁸ have presented a quantum-mechanical model proposing that the Auger neutralization or tunneling of an electron from the substrate to the adsorbed ion is responsible for this phenomenon. This neutralization is exponentially dependent on substrate-adsorbate distance causing the yield of EID ions to be dependent on this factor.

The ion current produced by EID is directly proportional to the electron bombardment current.¹¹ This linear relation is valid, of course, only when bombarding current is so low that the rate of removal of adsorbate is less than the rate of replacement, or insignificant in the time interval of measurement. Thus, for ionic desorption

$$i^+ = I_e Q^+ \sigma$$

where i^+ is the ion current, I_e the electron bombardment current, σ the population of adsorbed species (atoms or molecules/cm²) affected and Q^+ is the cross section for ionic desorption (cm²).

Typical total cross section values for ionic desorption are 10^{-18} to 10^{-23} cm^2 , where typical total cross sections for ionic and neutral species taken together are commonly 2 to 3 orders of magnitude larger.

The cross section has been observed in some cases to increase with temperature.⁴ This is attributed to the fact that at higher temperatures the increase in thermal vibration increases the average substrate-adsorbate distance, thus decreasing the Auger neutralization probability and increasing the ion yield.

PART IV
E X P E R I M E N T A L

A. Apparatus

The electron probe surface mass spectrometer, as Lichtman calls it,³¹ is not an instrument that can be purchased. At present, there is no agreed "best design" and most instruments reported in the literature are "one of a kind" models. The two desiderata in the design of the instrument used in this laboratory were 1) that a monopole mass spectrometer be used for a detector and 2) that a well defined beam of electrons be used. Since the system used was "one of a kind," the essential details will be described.

1. The Vacuum System

The vacuum chamber was constructed from 304 stainless steel pipes, welded together by the Tungsten Inert Gas method. Sexless ultra high vacuum flanges, made of 303 stainless steel and sealed with copper gaskets were used throughout. A flange mounted pyrex window enabled observation of the internal components. The volume of the experimental chamber was 1.9 liters.

Pumping of the system was accomplished with a combination 25 l/s triode ion pump and 550 l/s titanium sublimation pump (GE 22TP217). Determination of surface coverage by the thermodesorption method required accurate knowledge of pumping speed. Constancy of pumping speed was assured by an orifice 1.03 cm in diameter between the experimental chamber and the pumps. The calculated conductance of the orifice was 9.96 l/s for CO and 37.2 l/s for H₂. This was a value small compared to the measured speed of the pumps. The system base

pressure was 4×10^{-10} Torr.

The only gauge on the main chamber was a Bayard Alpert type ionization gauge (GE Model 22GT102) which communicated with the chamber through a short tube of greater diameter than the gauge grid, thus minimizing the pumping effect on the indicated pressure.

2. Gas Dosing System

The dosing gases were obtained from high pressure cylinders. Pressure regulators were attached directly to the cylinders and the low pressure output led to a gas manifold consisting of a length of stainless steel tubing. All connections were hard or soft silver soldered. The gas manifold had a thermistor type pressure gauge brazed to it and communicated to a Hoke valve and a Varian leak valve. The Hoke valve was used to evacuate the line and pressure regulator with a mechanical pump. The leak valve was mounted on a small chamber consisting of a 90° cross (X) connector with four flanges. One flange was blanked off, another terminated with a Bayard Alpert gauge identical to the type on the main experimental chamber, and the fourth flange connected this "forechamber" to the main experimental chamber through an orifice. The orifice was made by replacing the copper gasket between the flanges with a copper disk in which a tapered edge orifice of 1.61 mm diameter had been machined. This had a calculated conductance of 0.91 l/s for H_2 and 0.24 l/s for CO. The schematic of the dosing system and forechamber is shown in Figure 4.

3. Component Configuration

Figure 5 is a top view schematic of the experimental chamber with

FIGURE 4

Schematic of Gas Dosing System and
Forechamber.

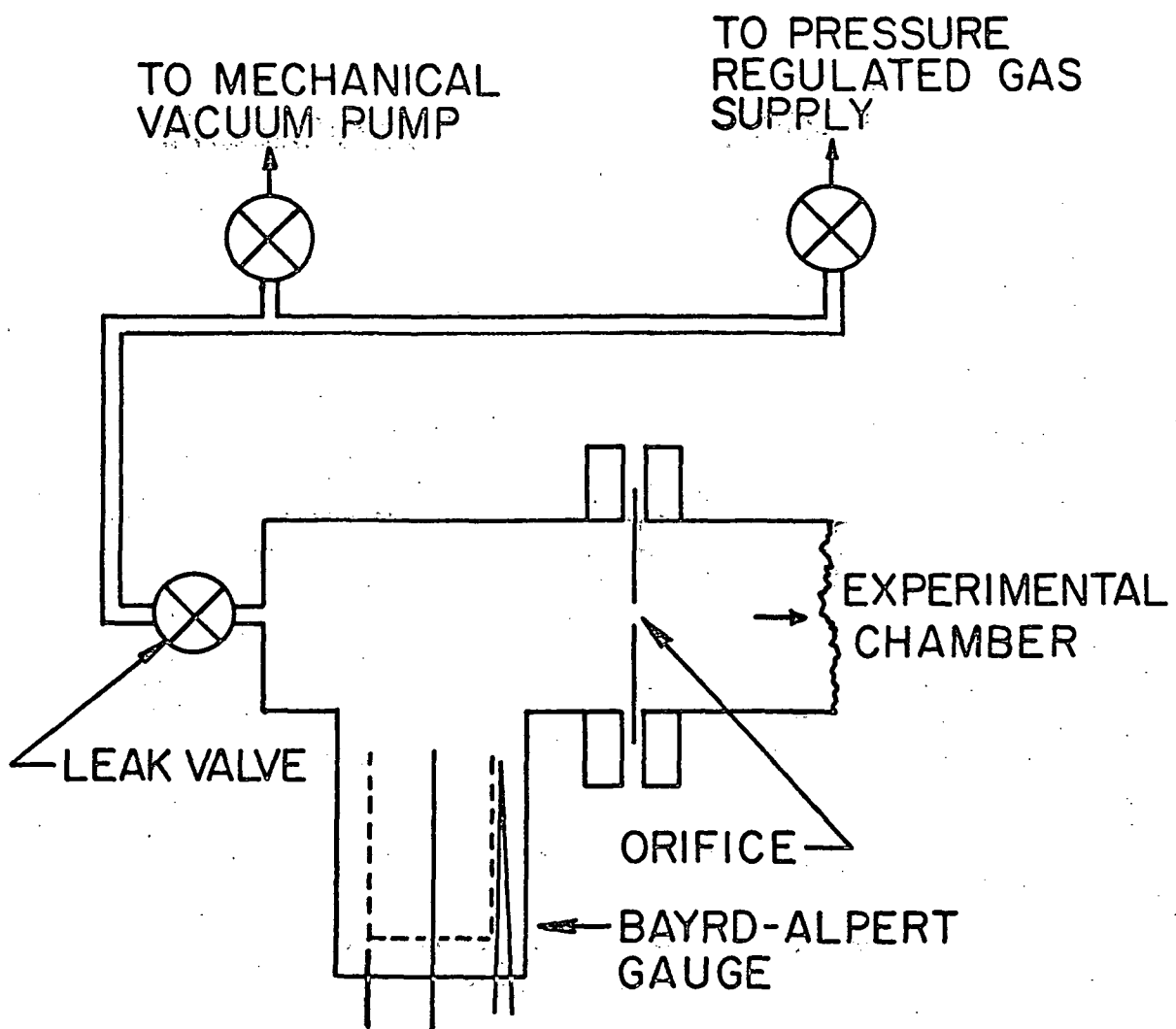
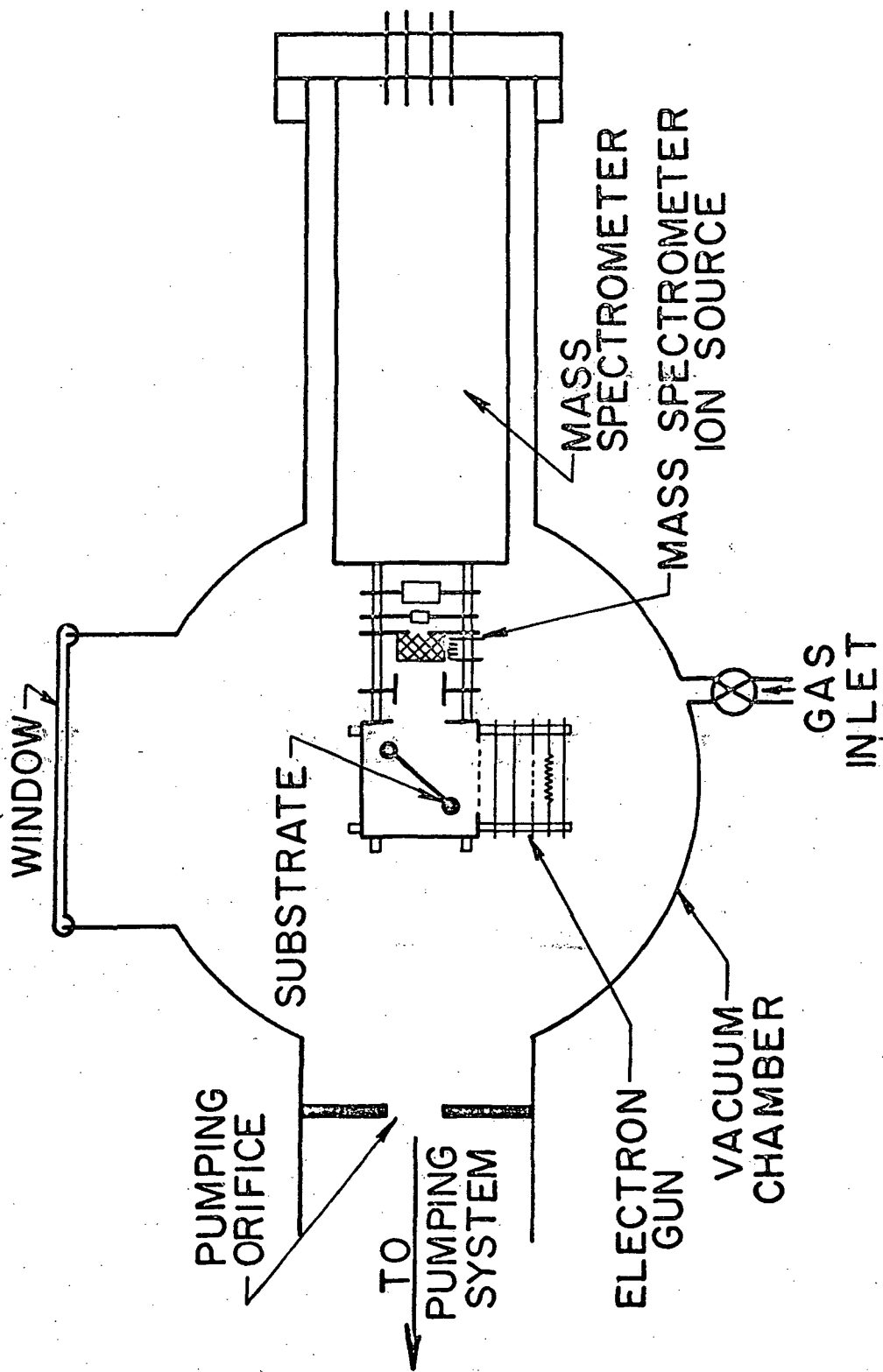


FIGURE 5
Schematic of Electron Induced Desorption Apparatus.



ELECTRON IMPACT DESORPTION APPARATUS

its major components. The mass spectrometer was supported from its flange. The electron gun, substrate support assembly and EID ion lens were made from 2.54 cm squares of 304 stainless steel with holes punched in the corners. These were assembled on 1.25 mm alumina rods with alumina spacer tubes and secured with spring loading against tungsten spring nuts that made a tight sliding fit on the rods. These components were part of an E.A.I. (Electron, Atom, Ion) Kit which was developed by C. K. Crawford and C. E. Woodward at the Massachusetts Institute of Technology.³⁵

The central assembly was a 2.54 cm cube referred to as the "cage." The substrate was a platinum ribbon 3 mm wide, 0.05 mm thick and 1.8 cm long, welded to 1.5 mm tantalum wire supports and mounted in the center of the cage with its plane lying in the (110) plane of the cube, as shown in Figure 5.

The electron gun assembly was mounted on one side of the cube and the ion lens assembly was mounted on an adjacent side. The sides opposite these were covered with nickel screens. The ions released from the substrate were drawn toward a 1.25 cm diameter hole in the side of the cage by the "EID Draw Out" screen, spaced 1 mm from the cage. After passing through this screen they encountered a cylindrical "EID Focus" lens mounted on the mass spectrometer ion source assembly, just above the ion source cage.

4. Instruments and Accessories

a) The Mass Spectrometer. The detector of EID ions was a prototype monopole mass spectrometer (General Electric) which could detect about 10^{-13} Torr of static partial pressure. The mass spectro-

meter consisted of three basic sections:

1) An ion source which ionized gas phase molecules by electron impact within a screen cage, accelerated the ions, and focused them on the analyzer entrance. (The ion source was not used when detecting EID ions.)

2) An analyzer which allowed only ions of a given e/m ratio to pass through.

3) A detector consisting of a 10-stage electron multiplier with the associated voltage dropping resistors attached so that only three vacuum feed throughs were necessary. The gain of the detector was estimated at 10^5 with 300 volts/stage bias.

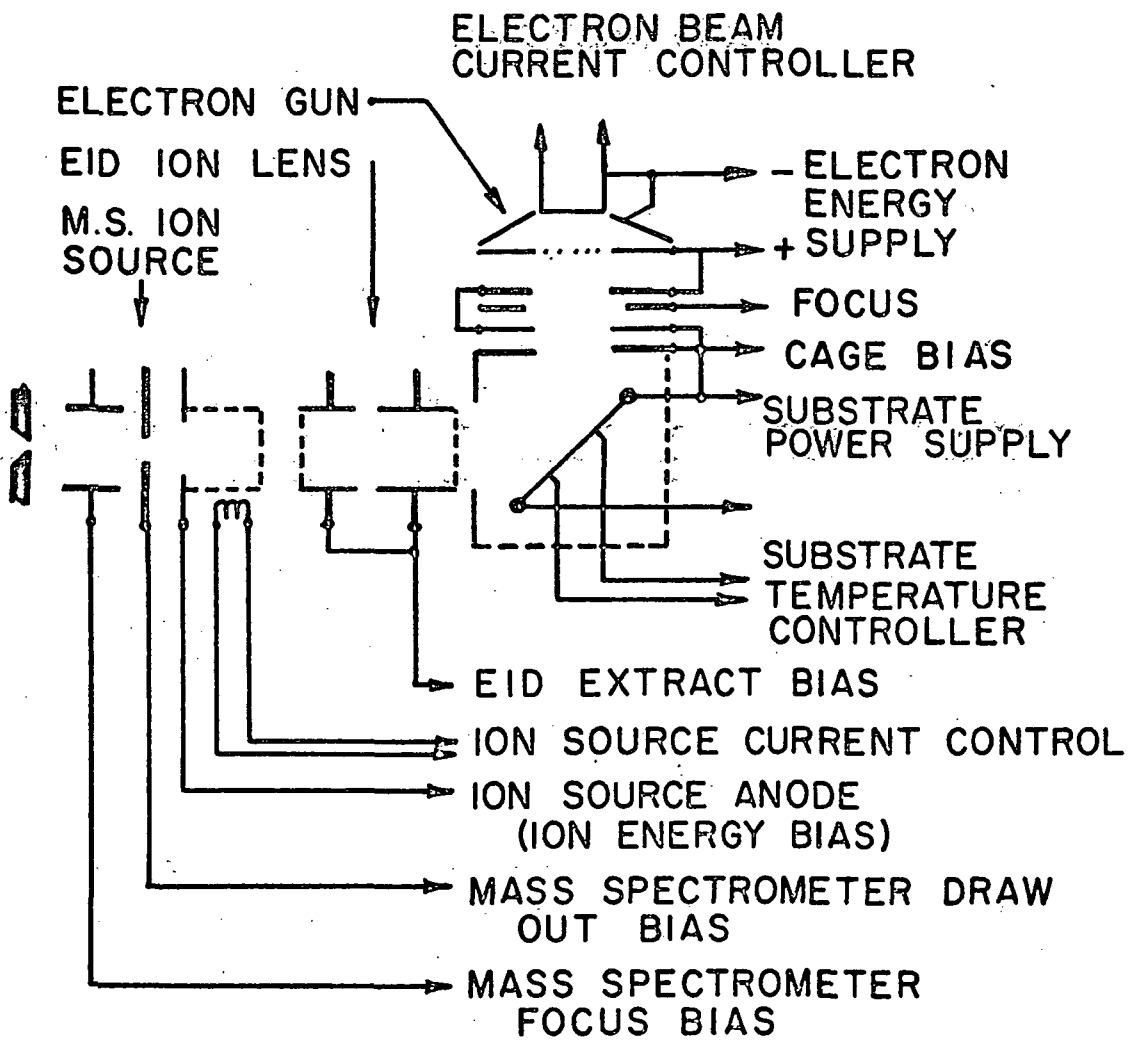
The multiplier output was converted from current to voltage by a Keithley Type 610R Electrometer. This provided a 0 - 10 volt signal which was recorded by a Moseley X - Y recorder.

The mass spectrometer was also used to measure partial pressures. For this purpose the ion source was operated with 3×10^{-3} amp emission current at 50 volts electron energy and 9eV ion energy.

Detection of EID ions required that the mass spectrometer ion source be biased differently with no electron emission. This was accomplished with two sets of bias controls and a switch to select between them.

In the "EID mode" of operation the substrate and cage were +25.6 volts with respect to ground and the EID Extract and Focus electrodes at -225 volts. The mass spectrometer draw out lens was at -300 volts, ion source anode at ground and focus lens at +67 volts. The electron gun operated from a floating supply of 102 volts from cathode to anode and cage. Figure 6 is a schematic of the electrode system.

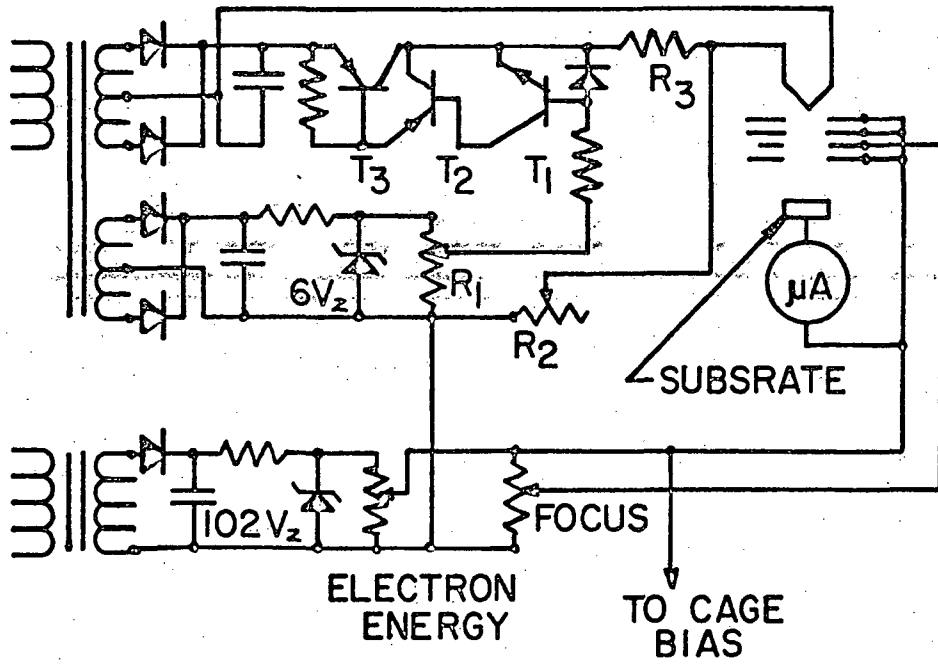
FIGURE 6
Schematic of the Electron Gun,
Substrate-Cage, and Ion Lens
Assembly.



b) The Electron Gun. Several electron guns were constructed and tested for beam homogeneity with a fluorescent screen. The most suitable design proved to be a relatively short gun consisting of a Pierce type electron gun³⁶ followed by an einzel lens.³⁷ The cathode was a directly heated 1 mm wide rhenium ribbon. The gun gave an electron beam 1 mm X 10 mm in cross section. An einzel lens was used for focusing without affecting the beam energy. The beam current was regulated by a feed back circuit controlling the cathode power supply.

The electron gun emission control was made by modifying a transistor controlled power supply originally manufactured by I.B.M. Figure 7 is a schematic of the circuit used. A zener controlled constant voltage was applied to R_1 which provided a variable reference supply. The total emission current of the electron gun passed through variable resistor R_2 , developing a voltage drop proportional to the emission current. This voltage drop was matched against the reference voltage from R_1 and the difference applied to the base and emitter of transistor T_1 through resistor R_3 in series with the filament. Transistors T_1 , T_2 , and T_3 constituted an extended Darlington circuit and operated to increase the current in the filament if the base of T_1 was positive to the emitter. It is seen that there were two control parameters involved in this circuit. Neglecting R_3 , R_1 and R_2 constituted an emission control. The reference voltage from R_1 would cause the filament current to increase until the emission current caused the voltage drop in R_2 to increase to a value about 0.4 volts less than the reference voltage. This design did not protect the filament from destructively high currents and some filaments were

FIGURE 7
Electron Gun Emission Controller
Circuit.

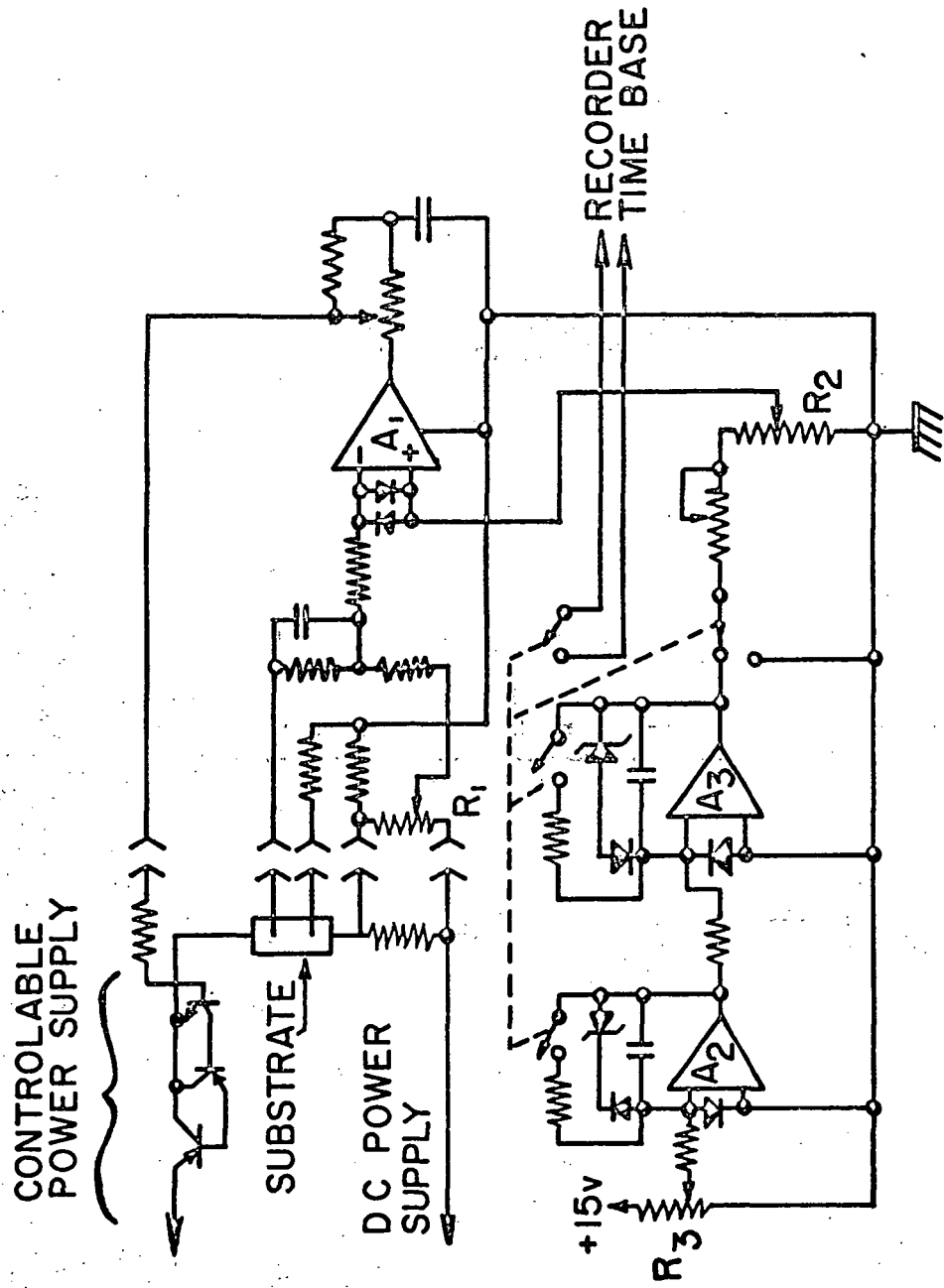


subjected to such. The addition of R_3 provided current limiting control. If there was no voltage drop across R_2 then R_1 and R_3 caused the supply to operate as a constant current source. Filament current developed a voltage across R_3 which opposed the reference voltage from R_1 , thus limiting the maximum current the filament experienced.

c) The Substrate Temperature Programmer. The substrate temperature controller was also made from a modified IBM power supply. This is shown in Figure 8. The substrate was in a bridge circuit that was balanced with R_1 . Two modes of operation were possible. First, with the non-inverting input of control amplifier A_1 grounded, current would be supplied to the substrate until the bridge came to balance, thus R_1 was a temperature setting control. The mode of operation most desired was to provide a linear rise in temperature with time. This could have been most perfectly accomplished by a mechanical drive of R_1 . Providing for an initiation of rise upon command, a variable rise rate, holding at a given temperature for a variable time period, and instantaneous return to room temperature setting would require extensive mechanical design that was judged to be infeasible. Alternatively, an all electronic bridge balancing circuit might have been used but no designs of such could be found and the level of electronic engineering required to design such a circuit was beyond the competence of the experimenter.

The design used was based on the observation that providing a programmed current to the bridge, balanced at room temperature, such as to cause a linear rise in substrate resistance with time, resulted in a bridge output that increased as the square of time. Amplifiers A_2 and A_3 were connected as two integrators in series.

FIGURE 8.
Substrate Temperature Controller
and Programmer Circuit.



The rate of temperature rise was determined by the input voltage from R_3 which was integrated by A_2 . The linearly rising voltage output of A_2 was integrated by A_3 providing an output voltage that increased as the square of time. The fraction of this voltage used for control purposes determined the maximum temperature and was obtained from R_2 . This voltage was fed to the non-inverting input of A_1 , causing the substrate current to increase until the bridge output, connected to the inverting input of A_1 , was equal to it. This design was not without defects, the chief one being that the substrate temperature at a given time after starting the program was a function of the initial substrate temperature and the temperature of the substrate support leads. The system also proved to be badly non-linear. At the time of construction, alternative methods of avoiding the use of a thermocouple on the substrate, such as infra-red detectors or analog computer elements were excessively expensive.

B. Materials Used

1. Substrate Preparation and Characterization

The substrate was made of platinum guaranteed to be 99.99% pure by Engelhard Industries and rolled into ribbon form by the H. Cross Company. The analysis of impurities was not available. The substrate was 1.8 cm X 3 mm X 0.05 mm thick and was welded to 1.5 mm diameter tantalum supports with two 0.05 mm potential leads welded on either side of the center half of the ribbon. The ribbon was heated to about 1200°C in vacuum for several days, then examined by X-ray. The entire flange and substrate support assembly was mounted on the X-ray machine so that the substrate could remain undisturbed.

Three back reflection photographs were taken along the length of the substrate. All three were identical hexagonal star patterns, indicating that the (111) plane was parallel to the surface and that the substrate was wither a single crystal or several crystals with very slight differences in orientation. This phenomenon has been observed by others.³⁸

The substrate was cleaned of carbon by heating to 1200°C in 10^{-5} to 10^{-4} Torr of oxygen for about four hours. This procedure was repeated until only a single flash desorption peak was obtained with carbon monoxide or hydrogen. Since analysis of very high purity platinum used by other workers^{21,39} showed 60 p.p.m. copper as the only detectable impurity, it was likely that some copper may have been present in this substrate. H. B. Lyon and G. A. Somorjai define a clean surface in LEED studies as one in which the concentration of impurities is below the detection limit of the technique.

They further stipulate that:

"There should also be no change in the mass spectrometer trace which is due to the sample surface when it is heated to elevated temperatures at which layers of substrate atoms may be removed by vaporization."

This criterion was met. Heating the substrate resulted in Na, K, Cl, and F emission when it was new. With ageing and prolonged heating the concentration of these elements approached the limit of detectability. Further proof of purity or cleanliness was not possible with the system available.

2. Preparation of Gases

As stated in section IV A2, the gases were obtained from high pressure cylinders. Reagent grade gases were purchased in lecture bottle cylinders from the Matheson Company. These were used directly without further purification. The justification for this was the fact that the system incorporated a mass spectrometer and no impurities were detected with this instrument. This is not to say that there were no impurities, but rather that they were not measurable. The ion pump had a characteristic of re-emitting previously pumped gases when a new gas was admitted to the system. Thus, admission of oxygen to a pressure of 1×10^{-5} Torr caused the argon pressure to rise to 1×10^{-4} Torr. Admission of carbon monoxide to the system which had been at residual pressure for a day or so caused the hydrogen pressure to rise in like amount. This burst of hydrogen would decline within a day to a value approximately the ultimate pressure. In analytical mass spectrometry these difficulties are obviated by not using ion pumps and by sampling at a high pressure in the 10^{-5} Torr range so that the residual gases are of no consequence. The system was seldom taken above 1×10^{-6} Torr because of the pump down time required after such treatment; also, at high pressures chemisorption occurred too quickly to follow with the recording equipment. When the system was taken to high pressures no impurities were observed in the gases used.

Gas mixtures were custom prepared by the Matheson Company and used as received.

C. Techniques of Measurements and Experimental Manipulations

1. Purging of Gas Lines

The first step in all experiments was to insure that the desired gas was admitted to the system. The gas cylinder was connected to the pressure regulator and determined to have a leak tight connection. A rotary vane vacuum pump was connected to the gas manifold via the Hoke valve. The gas cylinder valve was kept closed and the pressure regulator set at an arbitrary high setting. The Hoke valve was opened and the gas lines evacuated. Then the Hoke valve was closed while the gas cylinder valve was opened. This was done to insure that the lines were not under vacuum without active pumping, as this would allow air to leak in through the seals of the pressure regulator. After the gas line was pressurized the gas cylinder valve was closed and evacuation begun again. This procedure was repeated five times. Thereafter the gas lines were kept at a pressure of about 5 p.s.i.g.

2. Pump Speed Determinations

The conductance of the pumping orifice was determined for hydrogen and carbon monoxide only. The gas flow followed the sequential path of leak valve, forechamber, orifice, experimental chamber, and orifice to pump. The first orifice was 1.61 mm in diameter and had a calculated conductance, C , of 0.91 l/s for H_2 and 0.24 l/s for CO. Ionization gauges on both the forechamber and the experimental chamber gave the pressures on either side of the orifice. From these readings the pump speed S could be determined from

$$S = [(P_1/P_2) - 1] C$$

3. Thermodesorption Determination

The first step in running a thermodesorption determination of surface coverage was to obtain the desired pressure of the desired gas and a constant pumping speed. Starting with the system evacuated to its ultimate pressure (4×10^{-10} Torr), the leak valve was opened until the desired pressure was obtained. Since this results in outgassing of other gases from the walls and a change in environment for the ion pump, the pressure would change soon after the leak was set. The leak valve was readjusted frequently for the first half hour and at longer intervals thereafter until the pressure, pump speed, and the mass spectrum were constant. This was usually accomplished in six hours to a day. The substrate was then heated to 1250°C for ten seconds every five minutes for an hour. Then the flash spectra were determined by recording the pressure versus time during a five second rise to 1250°C . Various damping constants were tried until maximum damping without adverse effect on the recorded signal was obtained. The flash spectra were then recorded repeatedly every five minutes until equilibrium was achieved and the traces coincided. The system was then ready to run thermodesorption experiments. The substrate was flashed by raising the temperature to 1250°C in five seconds, holding it at that temperature an additional five seconds, then cooling. Upon cooling, the time was recorded and the substrate was allowed to "rest" for the desired dosing time. At the end of the dosing time the temperature programmer was activated along with the time scan on the X - Y recorder and the pressure was recorded

as a function of time during the period of temperature rise. This gave one datum point. If the dose time was less than five minutes, then the substrate was allowed to rest (so that the substrate support leads could cool) until 4 minutes 50 seconds after the termination of the preceding flash. The procedure was then repeated for the next determination. If the dose time had been five minutes or more then the termination of the flash signaled the beginning of the next dose period.

During the dose periods the leak valve was trimmed to maintain the desired pressure, the recorder zero set was adjusted as necessary and the mass spectrometer mass setting was peaked up.

4. Adsorption Measurements

Setting up for adsorption measurements was similar to thermodesorption procedure. Once the system was at equilibrium at the desired pressure, the detection and recording system was adjusted to give about 3/4 full scale recording at the prevailing pressure. The recorder was set operating in the pressure versus time mode, with the time scan much slower than was used for thermodesorption work. The temperature of the substrate was then raised to about 1250°C and held. The pressure would rise during the thermal cleaning of the substrate, then decline to near the equilibrium value. At this point the substrate heating power was terminated. In this system the area of the substrate was about equal to the area of the pumping port; thus when the substrate cooled, if the sticking probability of the gas were unity, the pressure would decline to about half the equilibrium value, since the effective pumping speed would be doubled. The

sticking probability declined as the substrate was covered with adsorbate, allowing the pressure to rise. When the substrate was completely covered it no longer adsorbed and the pressure returned to the equilibrium value. In general, adsorption determinations were avoided at pressures below 5×10^{-9} Torr CO as more than 1500 seconds would be required for the pressure to return to equilibrium. Long runs tried the stability of the leak valve and ion pump, often resulting in undeterminable equilibrium pressures. Several determinations were made in sequence until successive identical results were obtained.

5. Electron Induced Desorption Determinations

a) Adsorption. An "EID Adsorption" is the process of following surface coverage, upon adsorption of a gas, by observing the EID ion yield from the surface. The system was brought to equilibrium as described previously. During that time the electron gun power supplies and control units were brought to thermal equilibrium. The electron energy was set at the desired value, usually the full supply voltage of 102 volts. The substrate was disconnected from the substrate power supply and a 0-5 microammeter inserted in series between it and the positive side of the electron energy supply. After setting a desired beam current, usually 10^{-6} ampere, the focus control was adjusted for maximum substrate current. The beam current was then readjusted. The only additional attention required by the electron gun system was to readjust the beam current periodically, as it drifted.

The mass spectrometer was tuned to the appropriate mass value and the electrometer and recoding systems set operational. The substrate was thermally cleaned in the manner used for thermodesorption determinations, then cooled. The recording system was started simultaneously with cutting the power to the substrate and the EID ion current was measured versus time. As with other determinations this was repeated until consistent results were obtained.

b) Thermodesorption. An "EID flash" or thermodesorption determination was essentially identical to that described in section IV C3 except that EID ion current was measured instead of pressure. This resulted in a graph of EID ion current versus temperature. The current declined to the background level when the species that was the source of the EID current desorbed from the surface or decomposed.

c) Isothermal Desorption. An "EID Isothermal Desorption" is a determination of the relative surface coverage of EID active species versus time while said species is desorbing from the surface at a fixed temperature. The substrate temperature programmer was deactivated and the temperature of the substrate was controlled by maintaining bridge balance. The bridge balance potentiometer was set at given dial readings and for each the substrate current and voltage was determined. This enabled a calculation of substrate temperature and calibration of the bridge balance potentiometer.

The system was brought to equilibrium, as described under section IV C3, but with the electronics set to determine H_S^+ ion current. The substrate was dosed until maximum H_S^+ current was obtained, then the substrate power supply was activated. This brought the substrate temperature up to the preset value in 0.7 second and desorption

commenced. The H_S^+ ion current was plotted as a function of time after activating the substrate power supply.

PART V
RESULTS

This research involved several experimental techniques and chemical environments. The data from any one experimental technique were inadequate to arrive at the final analysis; therefore compilation of data from several experimental techniques was required. In this paper the results from each experimental technique are presented individually, then in section V I graphical compilations of some data is presented. The discussion section is arranged according to the various chemical systems and calls upon data from the results section as required.

A. Adsorption Experiments

The adsorption technique did not work with hydrogen, owing to its low sticking probability. Carbon monoxide, on the other hand, adsorbed fast enough to produce a large pressure change yielding good "large signal" data. The adsorption kinetics, sticking probability and saturation coverage of carbon monoxide were determined by the adsorption technique.

1. Carbon Monoxide Adsorption from Pure Carbon Monoxide

Figure 1 shows the form of pressure versus time data obtained during adsorption on a freshly cleaned substrate. The area above these curves was subjected to step-wise integration with respect to time to obtain coverage as a function of time. This was plotted as fractional coverage θ , versus carbon monoxide exposure tP_{CO} , as shown in Figure 9.

The coverage as a function of time determinations yielded the rate of adsorption $d\theta/dt$, as a function of the molecular flux to the surface νP , at various fractional coverages. The average results of six determinations at equilibrium pressures of 4×10^{-9} , 8×10^{-9} , and 2×10^{-8} Torr of carbon monoxide are presented in Figure 10.

The slope of the lines in Figure 10 is, by definition, the sticking probability. From these the sticking probability as a function of coverage was determined, as shown in Figure 11. The average initial sticking probability was 0.76.

Determinations at coverages less than 0.20 were unreliable owing to experimental difficulties such as cooling time of the substrate² and outgassing of the substrate supports if the substrate was heated for a sufficient time to obtain steady equilibrium pressure. The maximum surface coverage indicated in Figure 11 is 7×10^{14} molecules cm^{-2} . This is an average value. Redhead, and others, define $\theta = 1$ as the maximum coverage obtained. Noting that the population of platinum (111) sites is 1.5×10^{15} atoms cm^{-2} and that carbon monoxide commonly makes two bonds to a metal surface,²⁴ the value of 7.5×10^{14} molecules cm^{-2} was chosen to define $\theta = 1$. This is not significantly different from the experimental value. The ionization gauge with which the system was calibrated had a stated accuracy of $\pm 10\%$ and the effective area of the substrate could not be ascertained to better than $\pm 10\%$ because of the cold end effect.

The average saturation coverage found was 0.930 and the maximum coverage found in a single determination was 0.970.

FIGURE 9

Carbon Monoxide Coverage on Platinum
(111) as a Function of Torr-Second
Exposure.

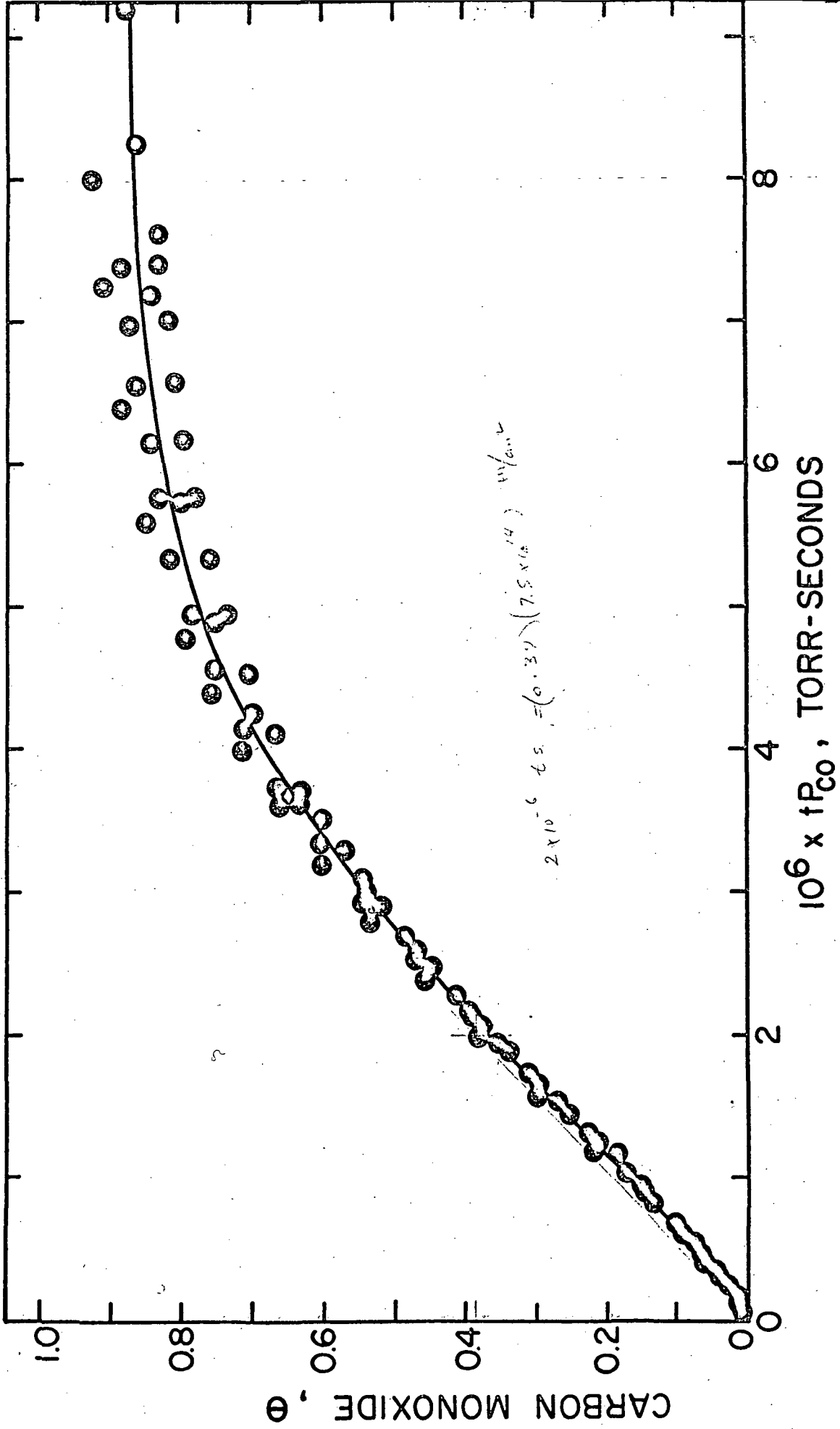


FIGURE 10

The Rate of Adsorption of Carbon
Monoxide Versus the Molecular Flux
to the Surface at Various Fractional
Coverages.

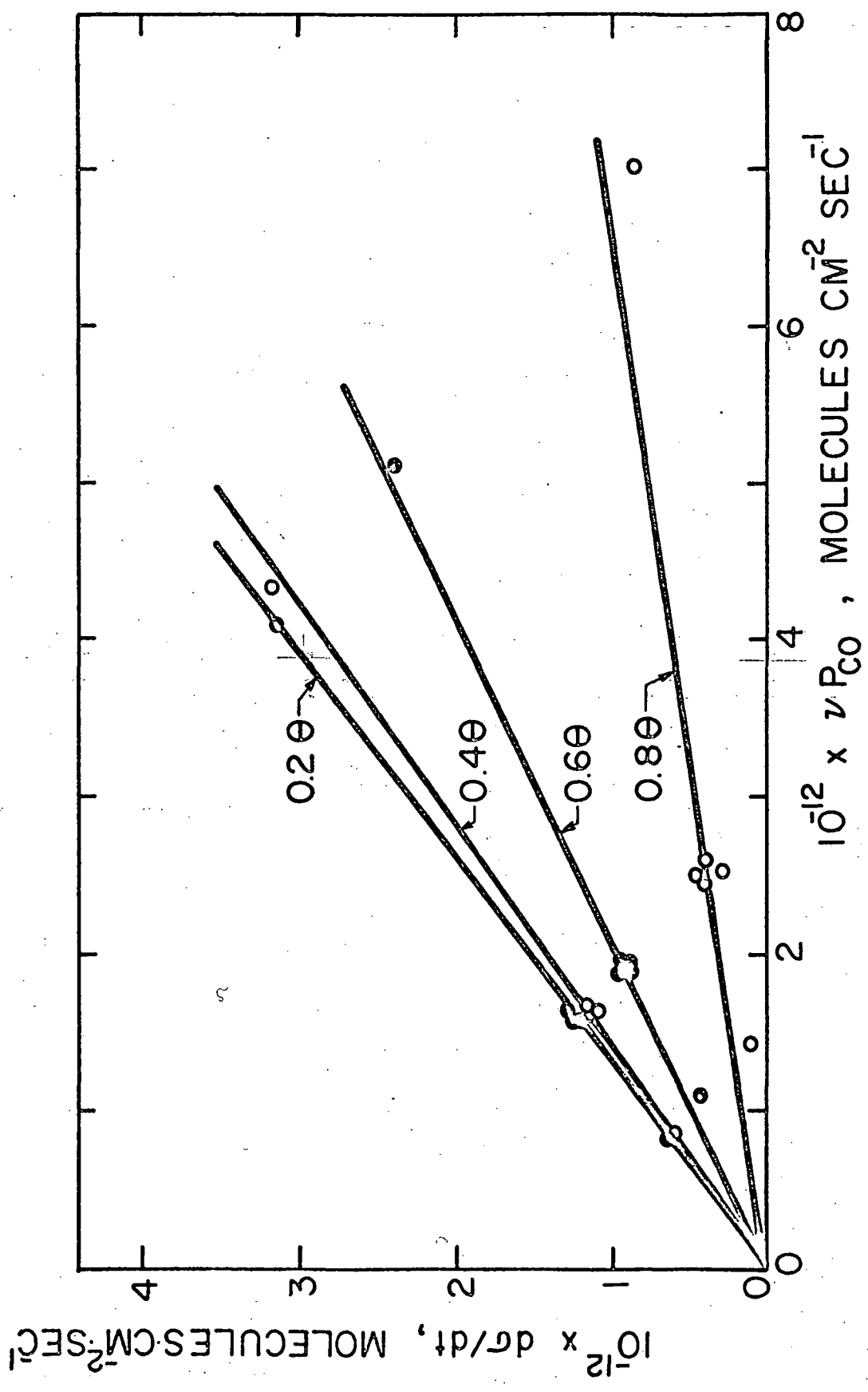
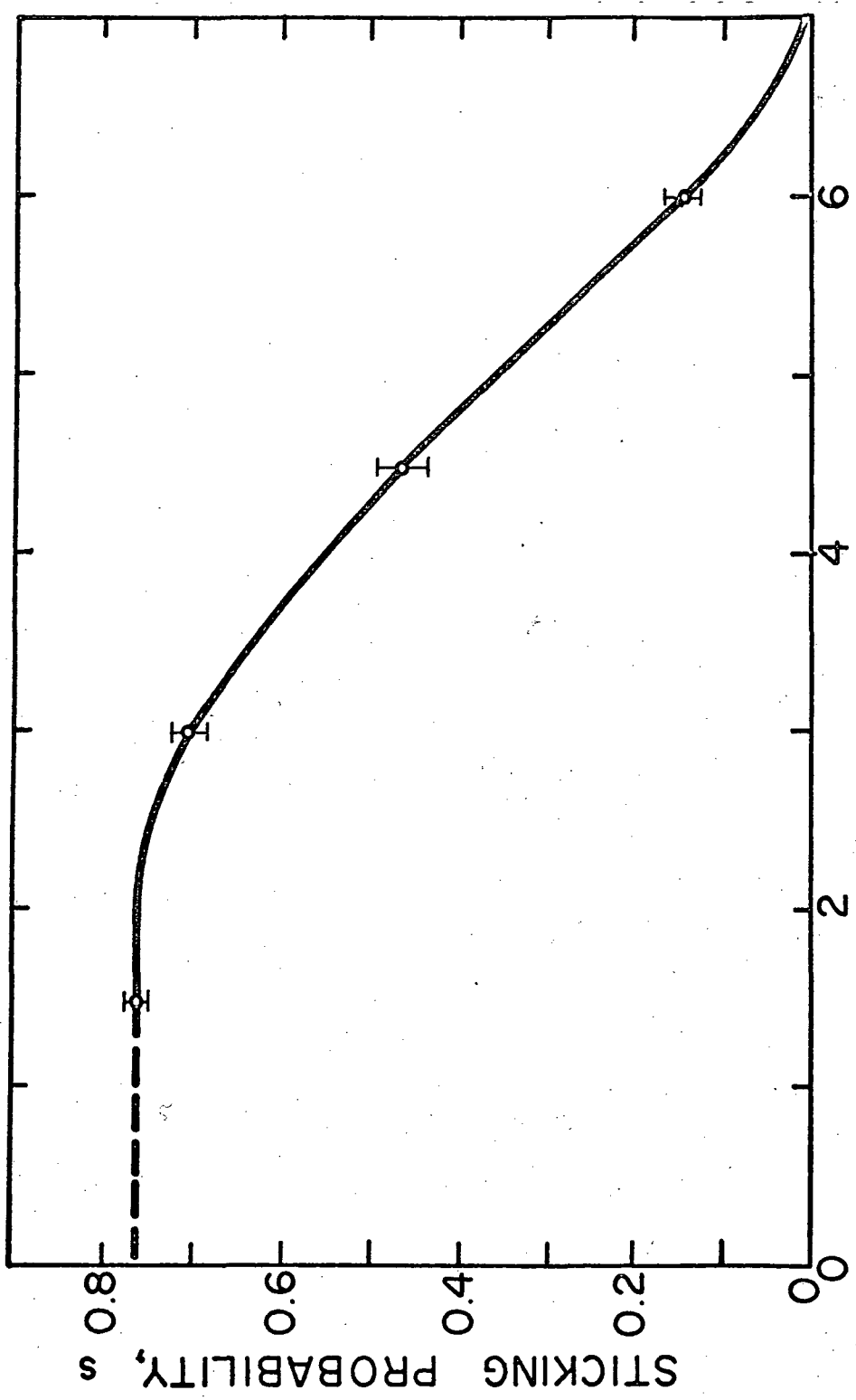


FIGURE 11
The Sticking Probability of Carbon
Monoxide on Platinum (111) as a
Function of Coverage.



10^{14} MOLECULES/CM² CARBON MONOXIDE

2. Carbon Monoxide Adsorption from Mixtures of Hydrogen and Carbon Monoxide

The adsorption of carbon monoxide from mixtures of hydrogen and carbon monoxide at various pressures was determined. The compositions of four such mixtures is given in Table I, page 67. Figure 12 presents the coverage versus dose data for carbon monoxide in these mixtures. The average maximum coverage was 0.43 with an average maximum sticking probability of 0.68.

A single flash determination at 2×10^{-8} Torr Mixture C after 12 hours dose yielded a coverage of 0.528. This was the maximum coverage observed in mixtures.

B. Thermodesorption Experiments

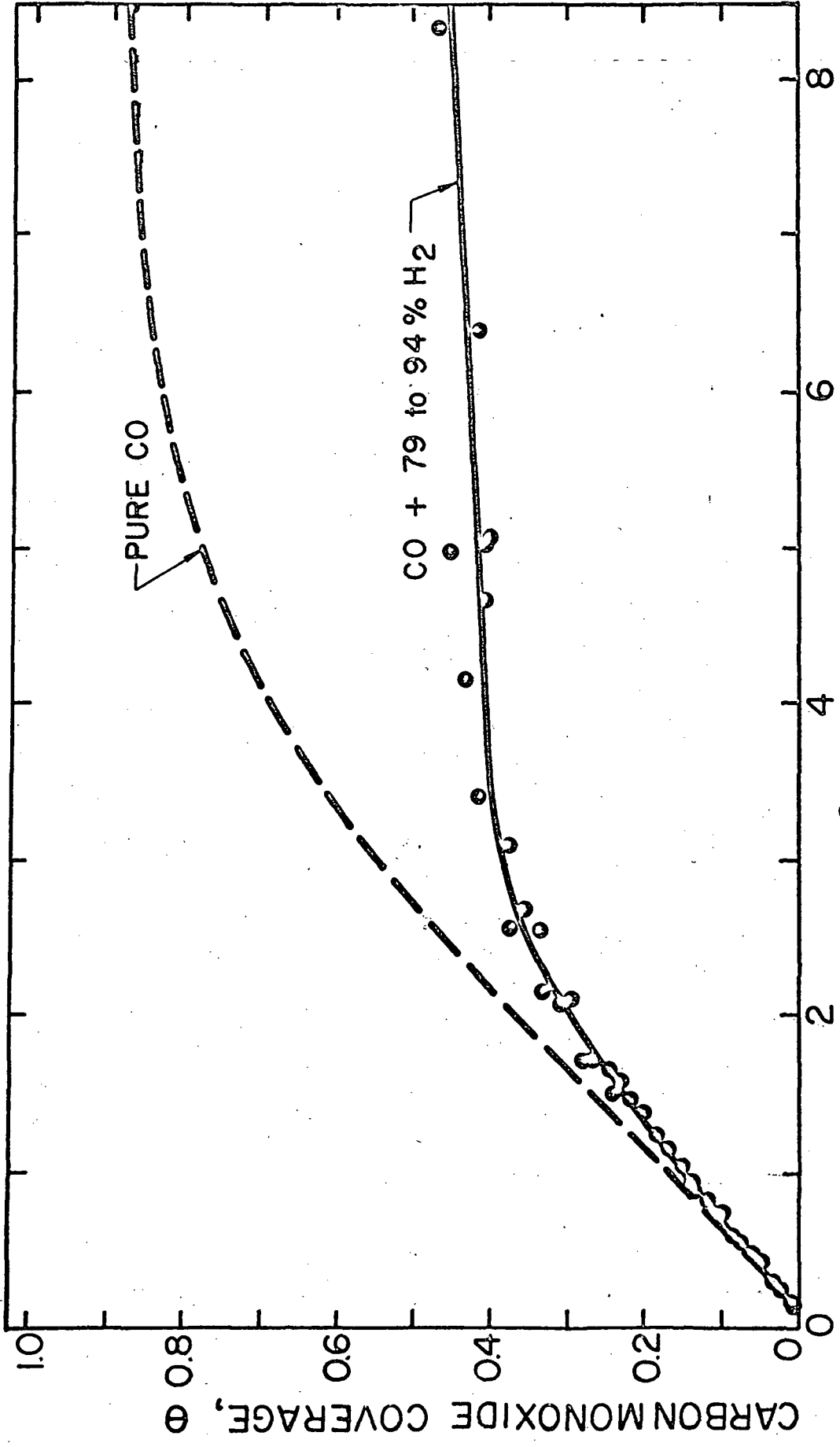
1. Adsorption of Hydrogen from Pure Hydrogen

Thermodesorption of hydrogen resulted in a single desorption peak. Since the thermodesorption spectrum in hydrogen-carbon monoxide mixtures was different from that in pure hydrogen, the desorption peak in pure hydrogen was labeled α - hydrogen. Figure 13 is a copy of a typical result in pure hydrogen. In general the T_p value for α - hydrogen declined with coverage and was in the range of 210°C to 270°C . The desorption curve was more nearly symmetric than that of the first order desorption of CO.

Observed asymmetry is attributed to heating of substrate cold ends and support wires as well as to wall effects, which are usually encountered in systems that experience pressure changes.

The possibility that tailing could be attributed to solubility of hydrogen in the substrate was considered. Ebisuzaki, et al⁴¹

FIGURE 12
Fractional Coverage of Carbon Monoxide
as a Function of CO Exposure in Pure
CO and Mixtures of CO + H₂.



$10^6 \times t P_{CO}$, TORR-SECONDS

PURE CO

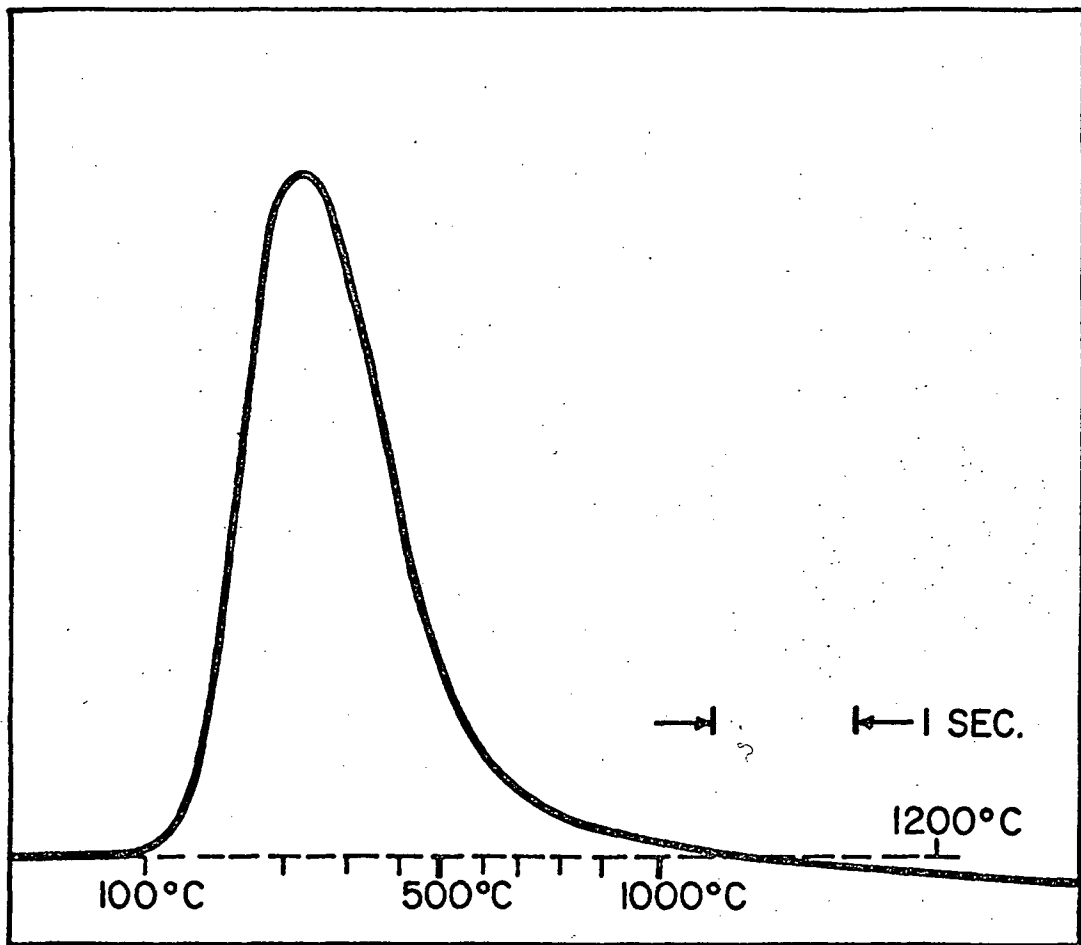
CO + 79 to 94% H₂

CARBON MONOXIDE COVERAGE, θ

FIGURE 13

Thermodesorption Spectrum of Hydrogen from Platinum (111). 2000 Second Dose in 5×10^{-9} Torr Hydrogen.

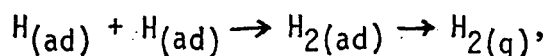
PRESSURE (ARBITRARY) →



TIME, TEMPERATURE →

have determined the solubility and diffusivity of hydrogen in single crystal platinum with the (100) plane parallel to the surface. They found that the diffusivity $D = (6.0 \pm 3.5) \times 10^{-3} \exp(-5.9 \pm 1.0 \text{ kcal/RT})$ in the range of 600°K to 900°K . Although they used an ultra high vacuum system and mass spectrometric detection techniques, the detection sensitivity was inadequate to make determinations at lower temperatures. Assuming the value determined is applicable at 300°K , $D_{300^{\circ}\text{K}} = 3.24 \times 10^{-7}$. For the substrate thickness used in the present work, 0.002 in., this gives a relaxation time $\tau = x^2/\pi^2 D = 7.8$ seconds. Ebisuzaki, et al determined the solubility from permeability and diffusivity measurements to be $S = H/P_t = 1.2 \times 10^{-3} \exp(-11.0 \text{ kcal/RT})$. At 300°K this yields $S = 1.29 \times 10^{-11}$ at 1 atmosphere. Since the solubility of hydrogen in platinum is proportional to the square root of the pressure⁴², the value at 1×10^{-8} Torr is $S = 4.68 \times 10^{-17}$ H/Pt. For the substrate under consideration, the mass was 9.1×10^{-3} g. Thus the number of hydrogen atoms dissolved at 300°K is 1.31×10^3 , an insignificant amount.

No hydrogen atoms could be detected with the mass spectrometer at substrate temperatures below 1230°K . This suggests that desorption is associative,

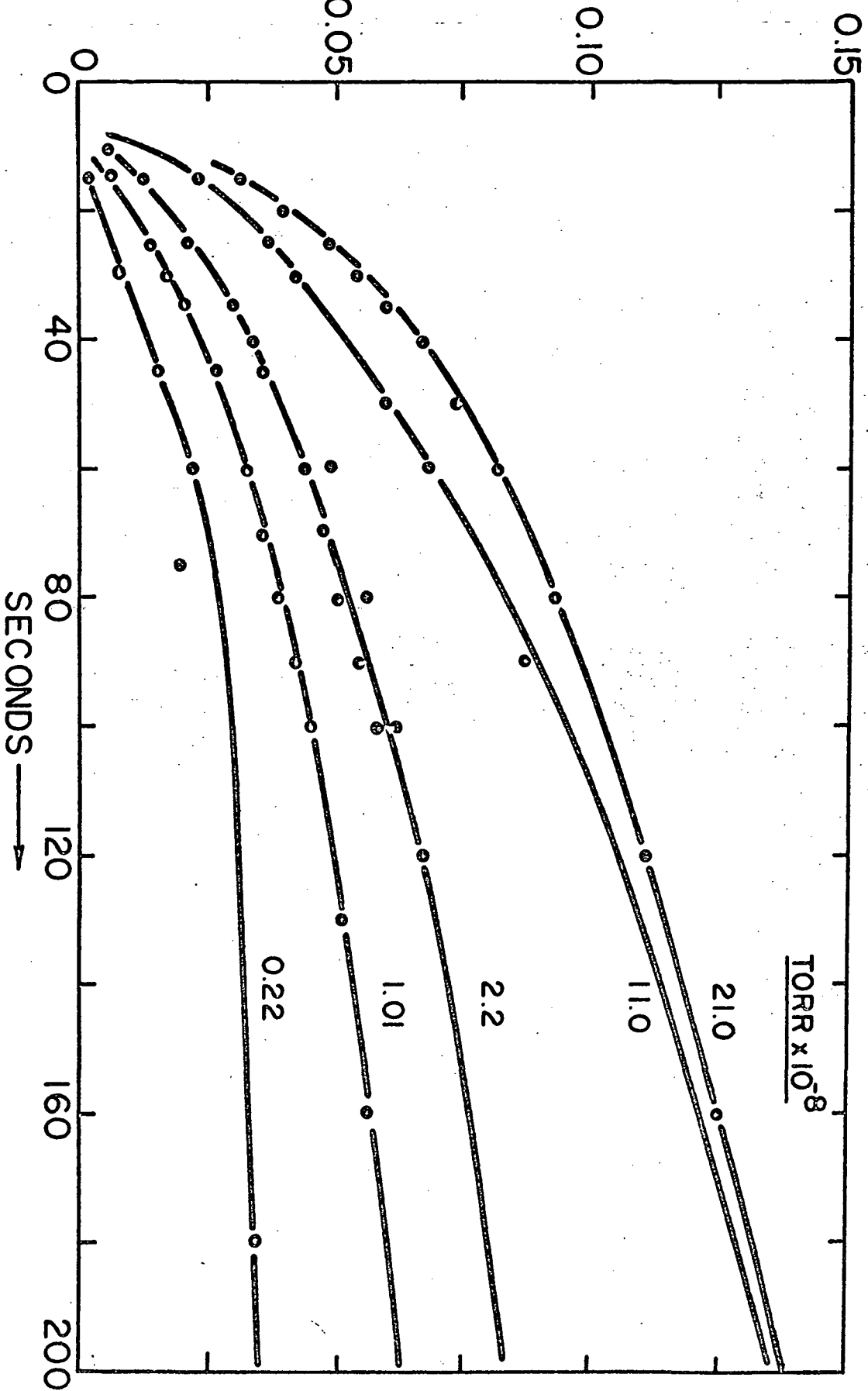


following second order kinetics. Second order desorption of diatomic gases that are dissociated upon adsorption is common.⁴³

The results of the thermodesorption determinations were plotted as fractional coverage, θ , versus time, as shown in Figure 14. In this case, θ is defined as 1.5×10^{15} H/cm², that is, one hydrogen atom per platinum site.

FIGURE 14
Fractional Coverage of Hydrogen as a
Function of Time in Various Pressures
of Hydrogen.

HYDROGEN COVERAGE, θ



In Figure 15 the data are presented as coverage versus Torr-seconds hydrogen exposure, which are proportional to vPt , the Knudsen flow to the surface. As in the case of Wiesendanger's work, the maximum coverage found was $0.2\theta^{28}$. This was attributed to displacement of adsorbed hydrogen by carbon monoxide impurity, and/or competition for sites. The fraction of carbon monoxide present increased as the pressure approached the ultimate pressure (4×10^{-10} Torr) of the system. The extreme case was observed in the 2.2×10^{-9} Torr determination where 3% CO was present. The observation of carbon monoxide desorption after hydrogen dosing confirmed this effect.

The rate of adsorption of hydrogen was directly proportional to the square root of impingement rate, as shown in Figure 16, indicating half order reaction kinetics. This was determined for $\theta = 0.025$ and $\theta = 0.0375$ at five pressures. For each coverage value the data were inadequate at the lowest and highest pressure to determine the slopes accurately, therefore only four points are shown. It is interesting to note that the lines pass through the origin, indicating that the desorption rate of adsorbed hydrogen is insignificant¹ at room temperature.

The data from Figure 16 were used to determine the sticking probability of hydrogen. For the lowest coverage determinable, 0.025 θ , the sticking probability was 7.5×10^{-3} .

After the kinetics of adsorption of hydrogen had been determined to be one half order, the hydrogen coverage data was plotted versus $t(P_{H_2})^{1/2}$ as shown in Figure 17. This resulted in a single smooth curve with the exception of the data obtained at very low pressures and relatively high CO impurity concentration.

FIGURE 15

Fractional Coverage of Hydrogen Versus
Hydrogen Exposure at Various Pressures.

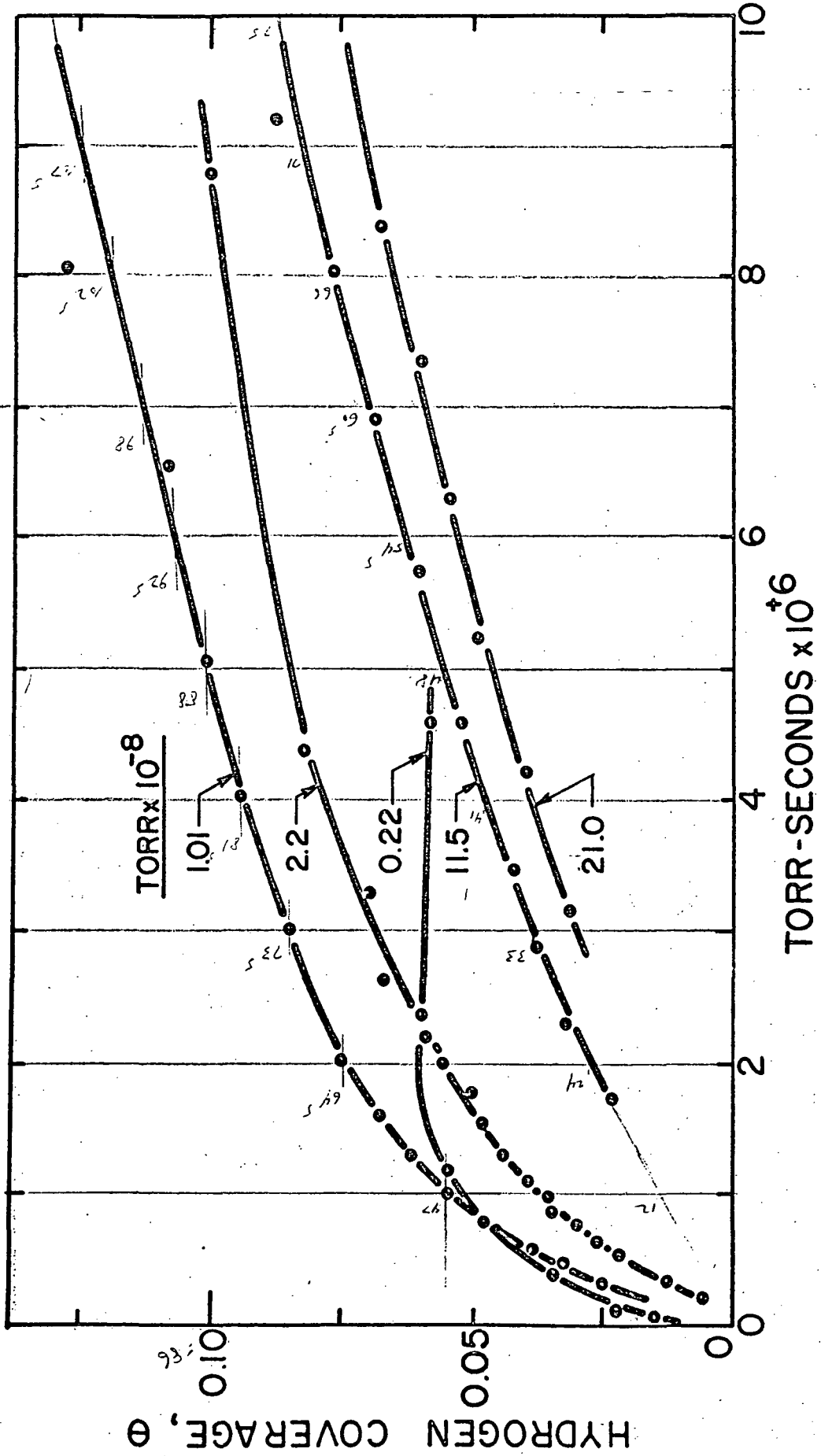


FIGURE 16

Rate of Adsorption of Hydrogen as a
Function of the Square Root of Im-
pingement Rate.

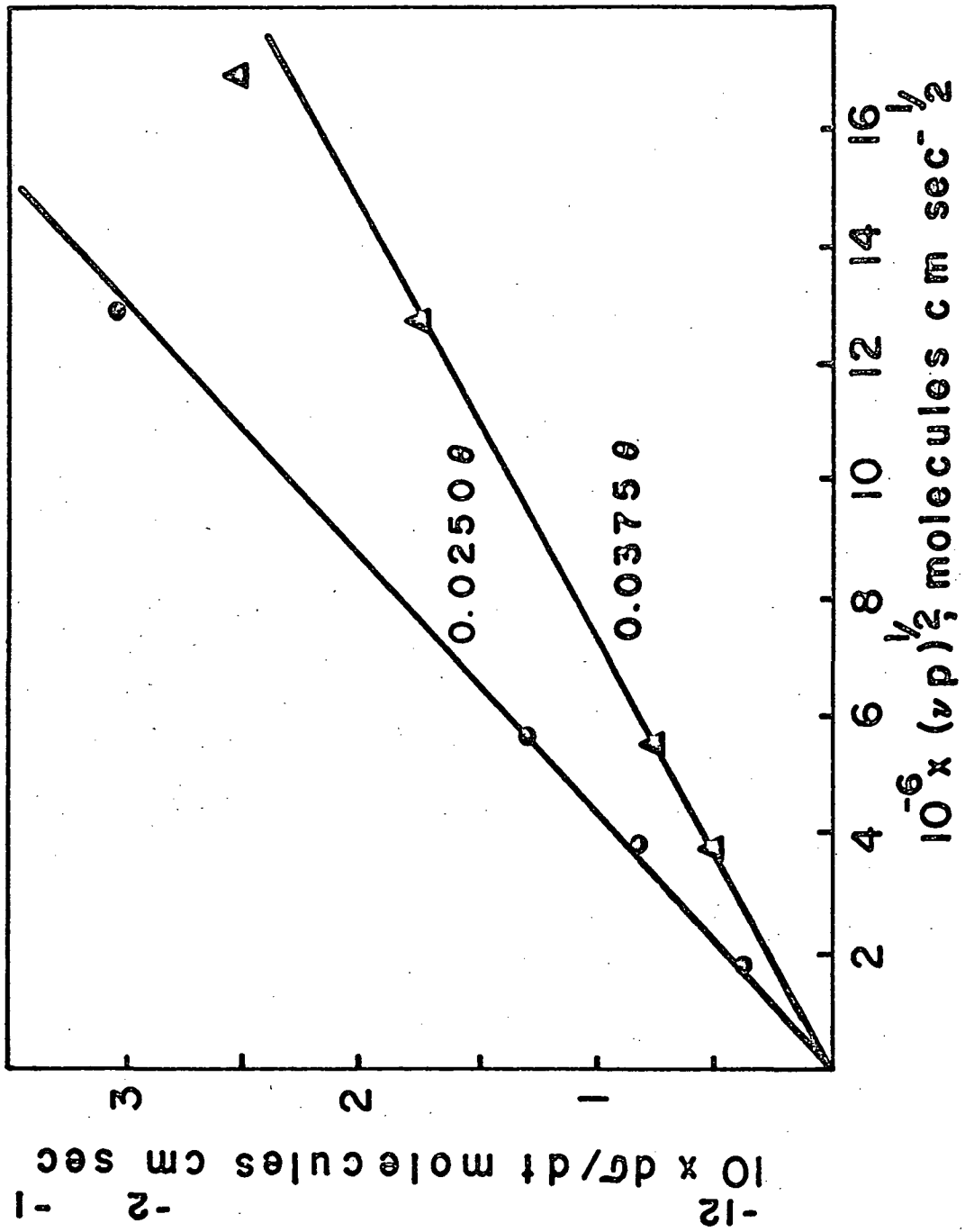
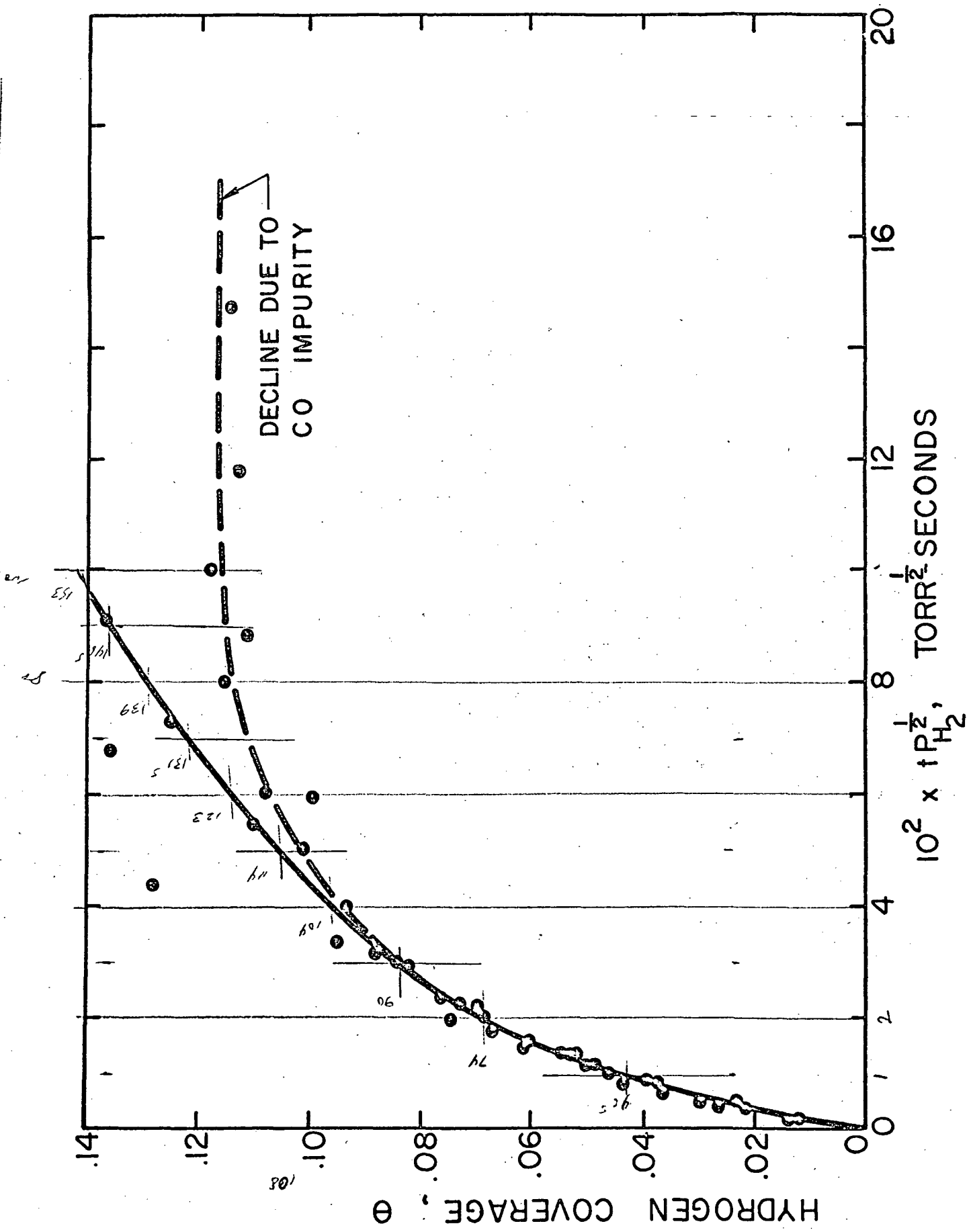


FIGURE 17

Fractional Coverage of Hydrogen Ver-
sus Hydrogen Dose, $t(P_{H_2})^{1/2}$.



2. Effect of Carbon Monoxide and Methane on the Initial Rate of Adsorption of Hydrogen

Thermodesorption measurements of hydrogen coverage for the first 100 seconds in 2.2×10^{-8} Torr hydrogen with varying quantities of impurities added were made to ascertain the effects of impurity gases on hydrogen coverage in the low coverage region. Figure 18 is a plot of coverage versus time with 0.88%, 1.0%, 1.4%, 2.9%, and 6.5% carbon monoxide present. Within experimental error the curves are coincident with the exception of 6.5% carbon monoxide. The desorption spectrum of hydrogen with 6.5% carbon monoxide had a different shape than was obtained with the other mixtures, indicating that the carbon monoxide present was interacting with the hydrogen.

Figure 19 shows that methane had an insignificant effect on initial hydrogen adsorption. Comparing the 33% methane result with the 6.5% carbon monoxide result suggests that methane is not significantly adsorbed.

3. Adsorption of Hydrogen from Mixtures of Hydrogen and Carbon Monoxide

The coverage of hydrogen on platinum in mixtures of hydrogen and carbon monoxide was measured by the thermodesorption technique. The thermodesorption spectrum was different from that in pure hydrogen, exhibiting two desorption peaks. For purposes of identification the single peak obtained in pure hydrogen was named " αH_2 " and the two peaks obtained from mixtures were named " βH_2 " and " γH_2 ", in thermal order of appearance. This is not to be taken as a statement that αH_2 is necessarily different from βH_2 .

FIGURE 18

Effect of Carbon Monoxide on the Initial Stage of Hydrogen Adsorption in 2.2×10^{-8} Torr Hydrogen.

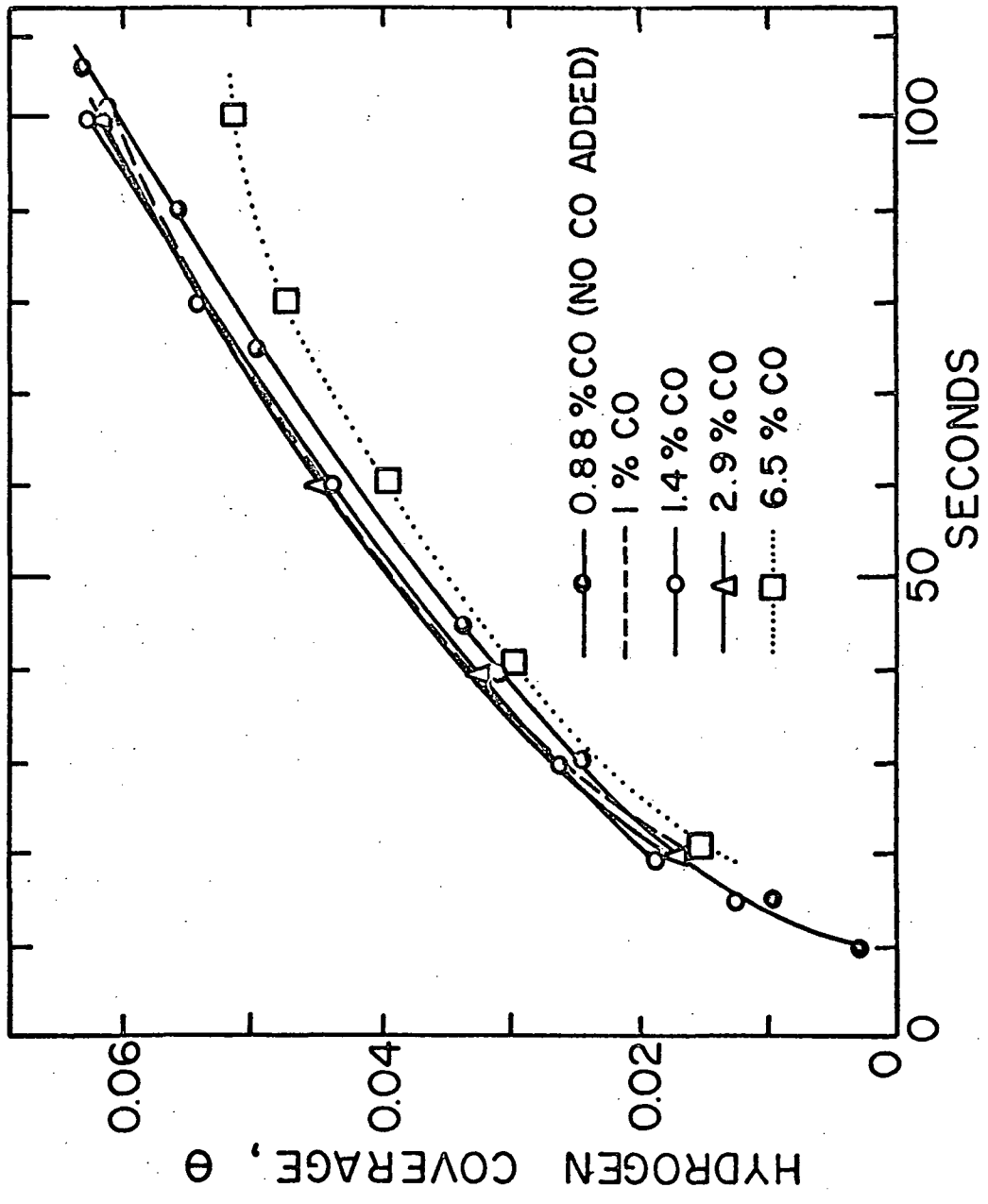
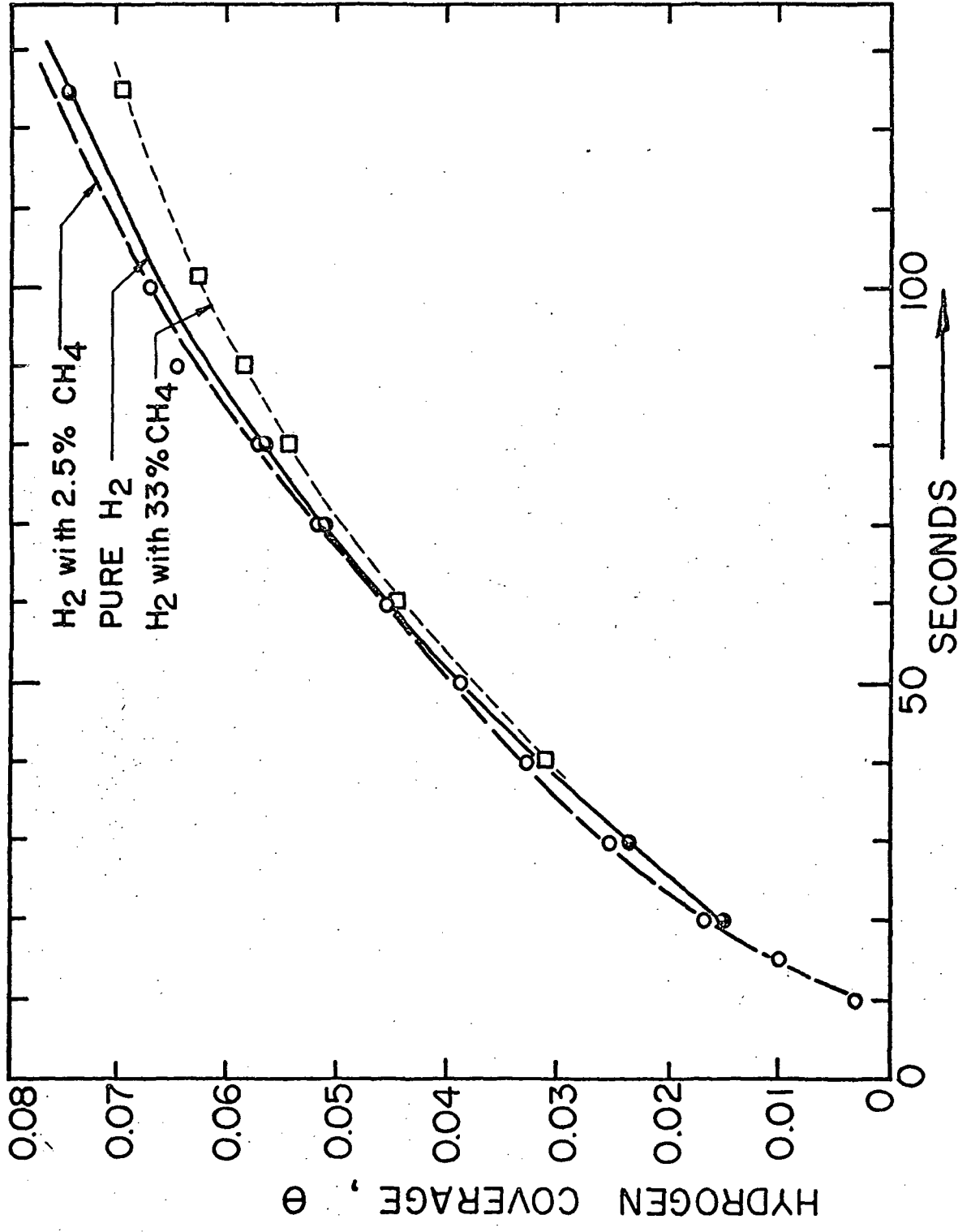


FIGURE 19
Effect of Methane on the Initial
Stage of Hydrogen Adsorption from
 2×10^{-8} Torr Hydrogen.



The indicated T_p usually declined for α hydrogen within the range of 210°C to 270°C. The β hydrogen peaked around 240°C to 290°C and the γ hydrogen peaked around 582°C to 670°C, well above the T_p for carbon monoxide.

Figure 20 is a set of thermodesorption curves from a mixture of 7.8×10^{-9} Torr CO and 3×10^{-8} Torr H_2 , drawn with base lines off set for clarity. The flash rate used was somewhat fast, rising to full temperature of 1075°C in about 5 seconds. This was the maximum flash rate employable consistent with the time constants of the detector system, and was used to enhance the rather low pressure rise resulting from low coverages, 0.01 to 0.05 θ . The substrate was held at full temperature for an additional 5 seconds after the programmed rise, during which time the temperature increased to 1270°C.

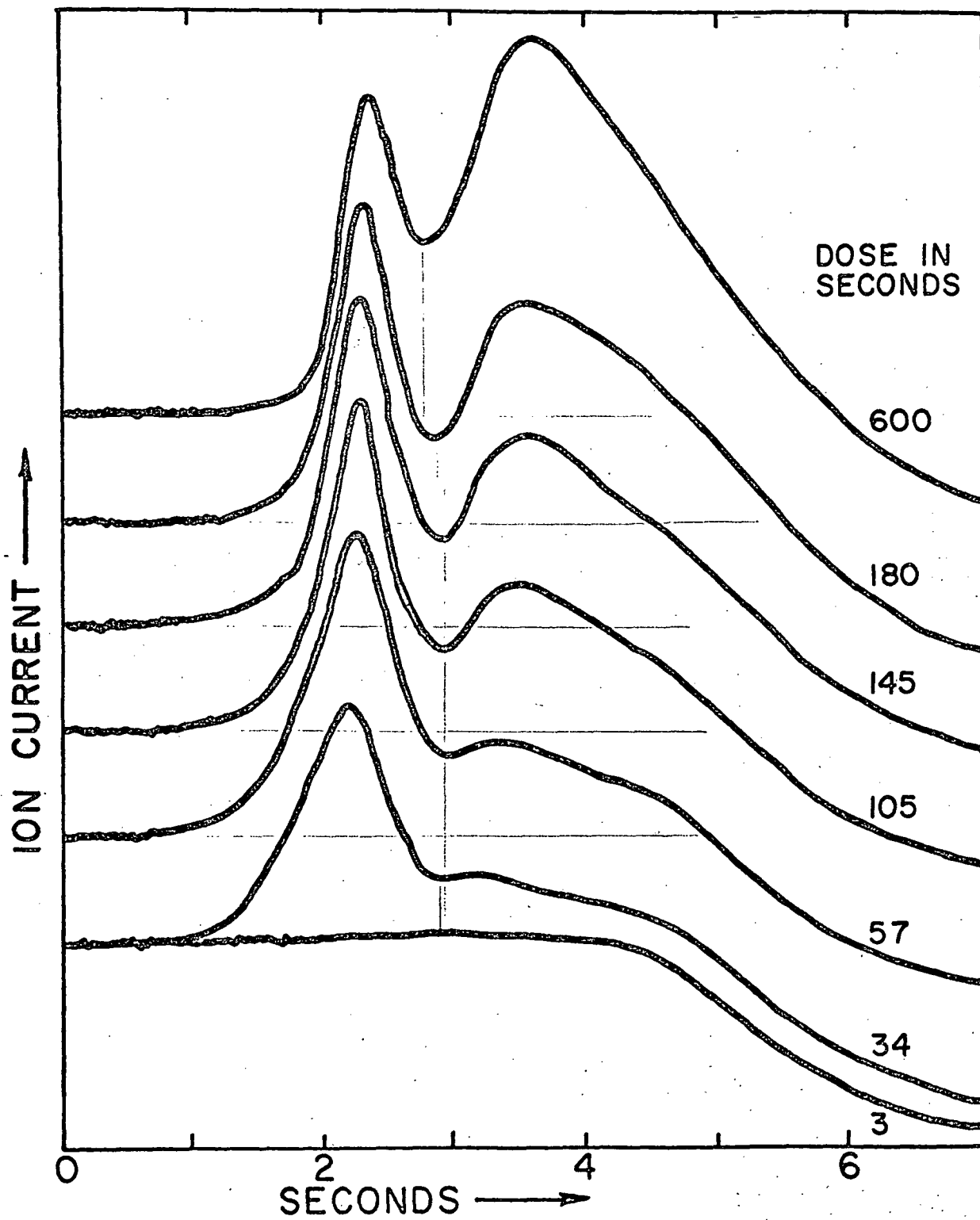
The curve labeled "3 sec." is essentially a base line, as three seconds is not sufficient cooling and dosing time for a measurable amount of hydrogen to be adsorbed. The decrease in H_2 pressure around 920°C is attributed to the reaction



which occurs on hot metals.³⁰ This base line would not consistently fit the curves at higher dosage so the initial pressure was taken as the base line and the area bounded by it and the curve was used to determine coverage. The coverage of each state, β and γ was desired and determined, however these determinations are approximate due to the difficulty of ascertaining the component parts of the curve. At high coverage the γ curve can be extrapolated to the start of the β curve with reasonable certainty, however, at low coverage this is less certain. Changing the starting point of the γ curve according to dose

FIGURE 20

Thermodesorption of Hydrogen from a
Mixture of 2.8×10^{-9} Torr CO and 3
 $\times 10^{-8}$ Torr H₂. Base Lines have
been Offset for Clarity.



would involve subjective opinion. Furthermore, this would accentuate a phenomenon of rise and fall of β hydrogen coverage. Since, it was thought that the β hydrogen rise and fall was directly related to a rise and fall in the EID H_S^+ ion current, this technique approached too closely to "finding what I wanted to find," so it was not used. The γ curve was extrapolated to the starting point of the β curve in all cases.

The resulting determinations of β and γ hydrogen coverage versus time of exposure for three cases are presented in Figures 39, 40, and 41 in the compiled data section. It is observed that the β state coverage rises to a poorly defined maximum, then declines while the γ state shows a monotonic increase after an initial period of rapid rise. The initial rate of adsorption of β hydrogen could not be determined because the β hydrogen coverage maximized less than an order of magnitude above the limit of detectability; also the number of data points obtainable in the low coverage region was inadequate. Comparison with pure (α) hydrogen results at the lowest β hydrogen coverage shows that the rate of adsorption of α hydrogen is greater than that of β hydrogen.

The total hydrogen coverage has been plotted versus hydrogen dose, $t(P_{H_2})^{1/2}$, in Figure 21. The curves labeled a, b, c, and d are for four "systems" (labeled likewise) of pressure and composition. The curves are in two families: a-b from experimental mixture D which was 6 to 7% CO and c-d from experimental mixture C which was about 20% CO. In this case the divergence of coverage with dose is less amongst curves of a family than between families.

The percentage composition is not an adequate basis for comparison of the results. This is a consequence of different adsorption

FIGURE 21

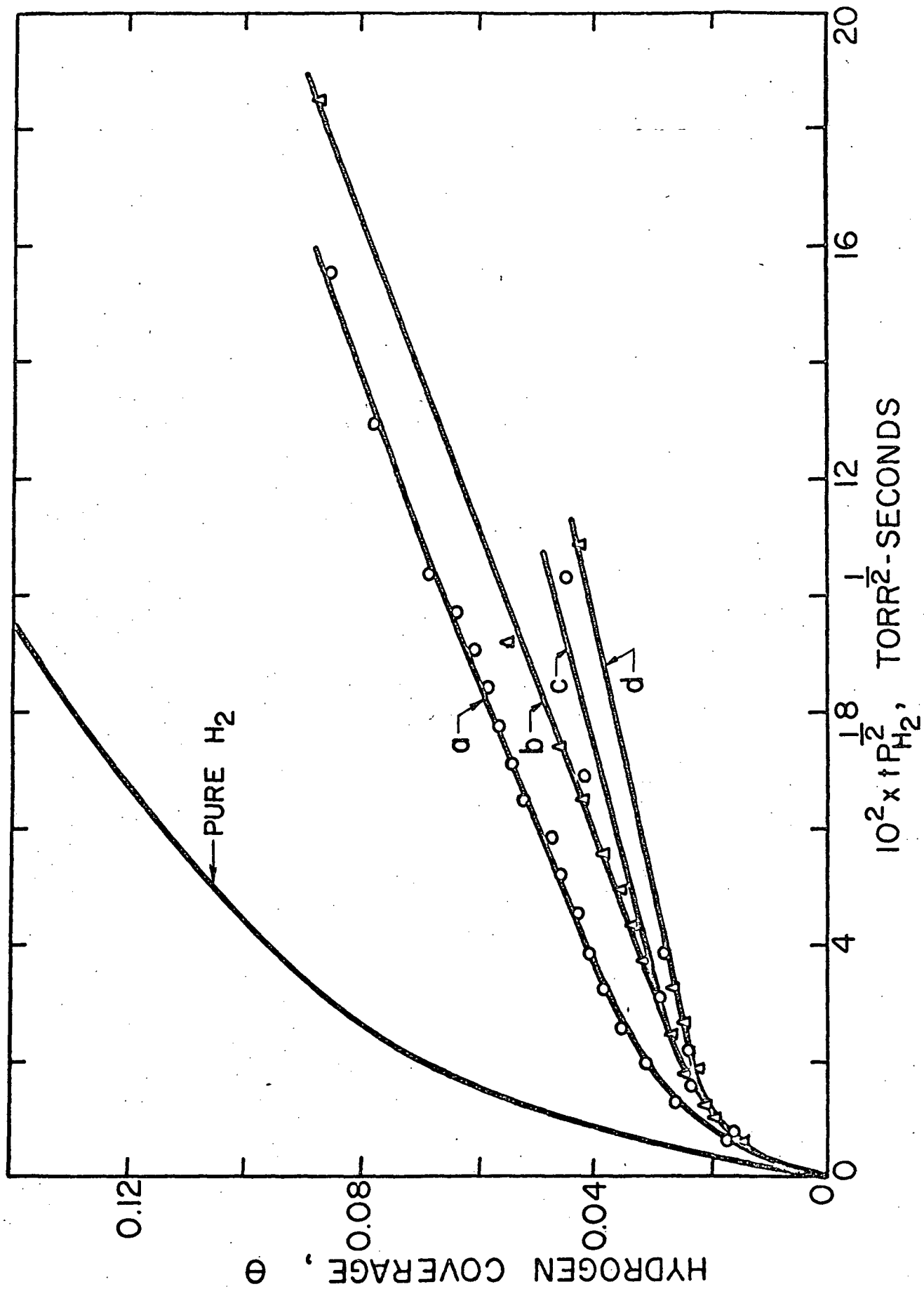
Hydrogen Coverage versus Hydrogen
Dose in Pure Hydrogen and Hydrogen-
Carbon Monoxide Mixtures.

Curve a, 7.7×10^{-8} Torr H_2 and 4.9×10^{-9} Torr CO

Curve b, 9.5×10^{-8} Torr H_2 and 7.5×10^{-9} Torr CO

Curve c, 3.0×10^{-8} Torr H_2 and 7.8×10^{-9} Torr CO

Curve d, 3.3×10^{-8} Torr H_2 and 7.8×10^{-9} Torr CO



kinetics for hydrogen and carbon monoxide. Table I therefore, lists the value of tP_{CO} at $t(P_{H_2})^{1/2} = 0.1$, or the carbon monoxide dosage at constant hydrogen dosage. It is observed that the adsorption of hydrogen is reduced at higher carbon monoxide doses, for a given hydrogen dose. It will be noted that the percentage of carbon monoxide varies, even though the gas was obtained from a tank of mixed gases at high pressure. This is attributed to variations of pump speed for each gas as a function of pressure and history. These variations occurred even over time periods of less than an hour and therefore no determinations could be performed at truly constant composition. As the quantity of gas being leaked into the system is reduced to zero, the composition changes to that of the residual gas at the ultimate pressure, about 25% to 50% carbon monoxide, a few percent of argon, methane, and carbon dioxide, and the remainder of hydrogen. Therefore, mixture determinations were avoided at pressures less than 50 times the residual pressure of 4×10^{-10} Torr in an attempt to obtain constant composition.

The limitations of the thermodesorption technique have been related in the literature.³ This work discovered a new phenomenon which exemplified, more than any other known case, the limitations of the thermodesorption technique. Figure 22 presents some thermodesorption spectra of hydrogen from platinum (111) dosed in a mixture of 1×10^{-7} Torr H_2 and 3.2×10^{-8} Torr CO. These spectra exhibit a decline in pressure during thermodesorption, indicating that the substrate is adsorbing hydrogen. This decline was termed a "pumping peak." The dashed line is the three second dose spectrum, and is used as a base line. Initially, at low dose times, the β hydrogen

TABLE I

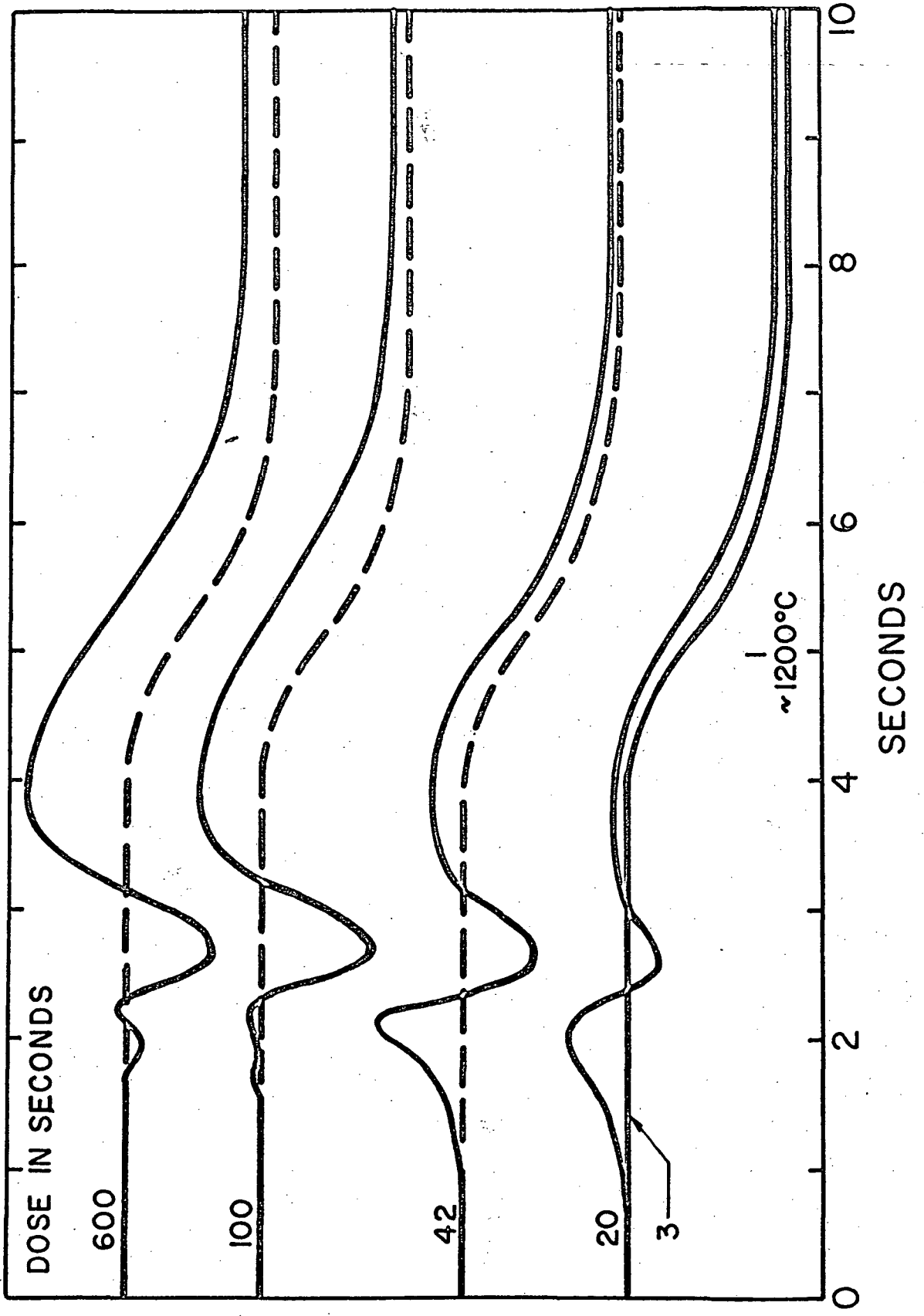
"SYSTEM"	TOTAL PRESSURE (TORR)	HYDROGEN PRESSURE (TORR)	CARBON MONOXIDE PRESSURE (TORR)	PERCENT CARBON MONOXIDE	tP_{CO} at $tP_{H_2}^{1/2} = 0.1$
a	8.1×10^{-8}	7.0×10^{-8}	4.9×10^{-9}	6.0	1.8×10^{-6}
b	1.0×10^{-7}	9.5×10^{-8}	7.5×10^{-9}	7.4	2.4×10^{-6}
c	3.8×10^{-8}	3.0×10^{-8}	7.8×10^{-9}	20.7	4.5×10^{-6}
d	4.1×10^{-8}	3.3×10^{-8}	8.4×10^{-9}	20.2	4.6×10^{-6}

desorbs, then there is pumping by the surface, followed by γ hydrogen desorption. With greater exposure the β hydrogen peak declines and the pumping peak increases. Further exposure results in no β hydrogen desorption and a maximum of pumping, at a temperature that coincides with the carbon monoxide desorption. Finally a second pumping peak appears at a temperature corresponding to the original β hydrogen desorption. At its maximum the initial pumping peak (which was the only pumping peak to appear at some pressures) pumps at about 0.3 l/sec cm^2 . This means about 1% of the impinging molecules are adsorbed or a sticking probability of 10^{-2} . This is nearly the same as that found for pure hydrogen on (111) platinum.

This phenomenon occurred whenever mixtures of hydrogen and carbon monoxide were utilized at high pressures. Explanation on the basis of data available with the present equipment requires much speculation. Two basic possibilities are gas-adsorbate reaction during flash, and diffusion and rearrangement of the adsorbate exposing "ideal sites" for adsorption from the gas phase. The "ideal site" concept is frequently used in the literature but not universally respected. Possibly, with an ideal experimental system, this phenomenon will shed some light on the topic of "ideal sites" in the future. For the present work, it made coverage determinations at these pressures too suspect to attempt an analysis. It is interesting to note that at these high pressures, the characteristics of the electron induced desorption data showed no irregularities. This is because the EID data was obtained during adsorption whereas the desorption phenomenon involves reactions during desorption.

FIGURE 22

Hydrogen Thermodesorption Spectra as
a Function of Dose Time in a Mixture
of 1×10^{-7} Torr H_2 and 3.2×10^{-8}
Torr CO.



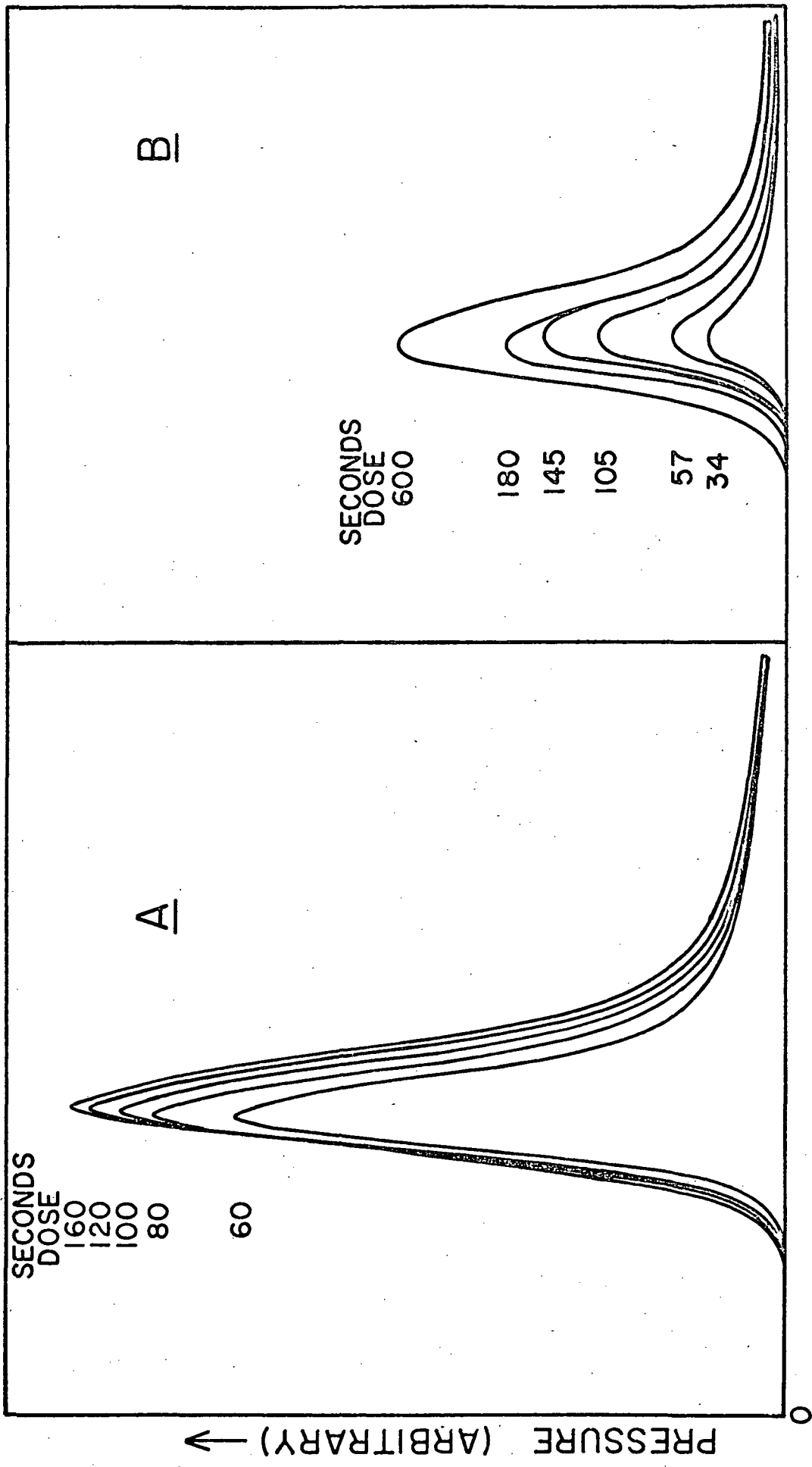
4. Thermodesorption of Carbon Monoxide in Pure Carbon Monoxide and in Hydrogen-Carbon Monoxide Mixtures

The thermodesorption spectrum of carbon monoxide in pure carbon monoxide is presented in Figure 23, part A. There is a single desorption peak at about 400°C. This was referred to as α -CO. The apparent temperature of the peak increased with time of dose, but the true temperature did not. This was an artifact of the temperature programmer. If the substrate support leads were hot then the indicated temperature was below the actual substrate temperature. It was noted that the initial rise is essentially independent of coverage and the temperature of maximum desorption rate is essentially constant. These are characteristic of first order desorption.

Part B of Figure 23 shows the thermodesorption spectrum of carbon monoxide when the substrate is in a mixture of hydrogen and carbon monoxide. The mixture in this case was "system d" in Table I. In this case the curves are more symmetrical and the temperature of the initial rise decreases as the coverage increases, both characteristics of a second order desorption, although the kinetics may be mixed order. Closer examination of the desorption spectrum shows that there are actually two peaks present. This was revealed quite well when examining the CO thermodesorption spectrum while dosing with hydrogen. These peaks were named β -CO, whose T_p is around 365°C and γ -CO whose T_p is about 455°C. The resolution of this doublet was dependent on the pressure of a given mixture, the peaks merging into a single peak at higher pressures. Thermodesorption spectra of carbon monoxide are compared with those of hydrogen for mixture "system C" (Table I) in Figure 42.

FIGURE 23

Thermodesorption Spectra of Carbon Monoxide in a) Pure CO and b) CO + H₂ Mixture.



SECONDS
DOSE

160
120
100
80

60

A

SECONDS
DOSE

180
145
105
57
34

B

PRESSURE (ARBITRARY) ↓

↑ TIME, TEMPERATURE

0

C. The Electron Induced Desorption Spectrum

The bombardment of a metal surface with electrons causes some of the adsorbed gas to desorb as (EID) ions. These ions can be captured and analyzed with a mass spectrometer. When the (111) surface of platinum is exposed to residual gas, the mass spectrum of desorbed ions is typically as shown in Figure 24. The gas phase mass spectrum is shown for calibration purposes. A characteristic of the mass spectrometer and the ion energies obtained resulted in the EID ions appearing 0.5 amu above the corresponding mass in the gas phase. EID ions have been observed to have average energies of 4 to 6eV^{21,33} with a spread from 0 to 10eV. This could account for the width of the O_S^+ peak. The EID ion energy to the mass spectrometer was 25 volts. Peak width as a function of ion energy has not been determined for the monopole spectrometer.

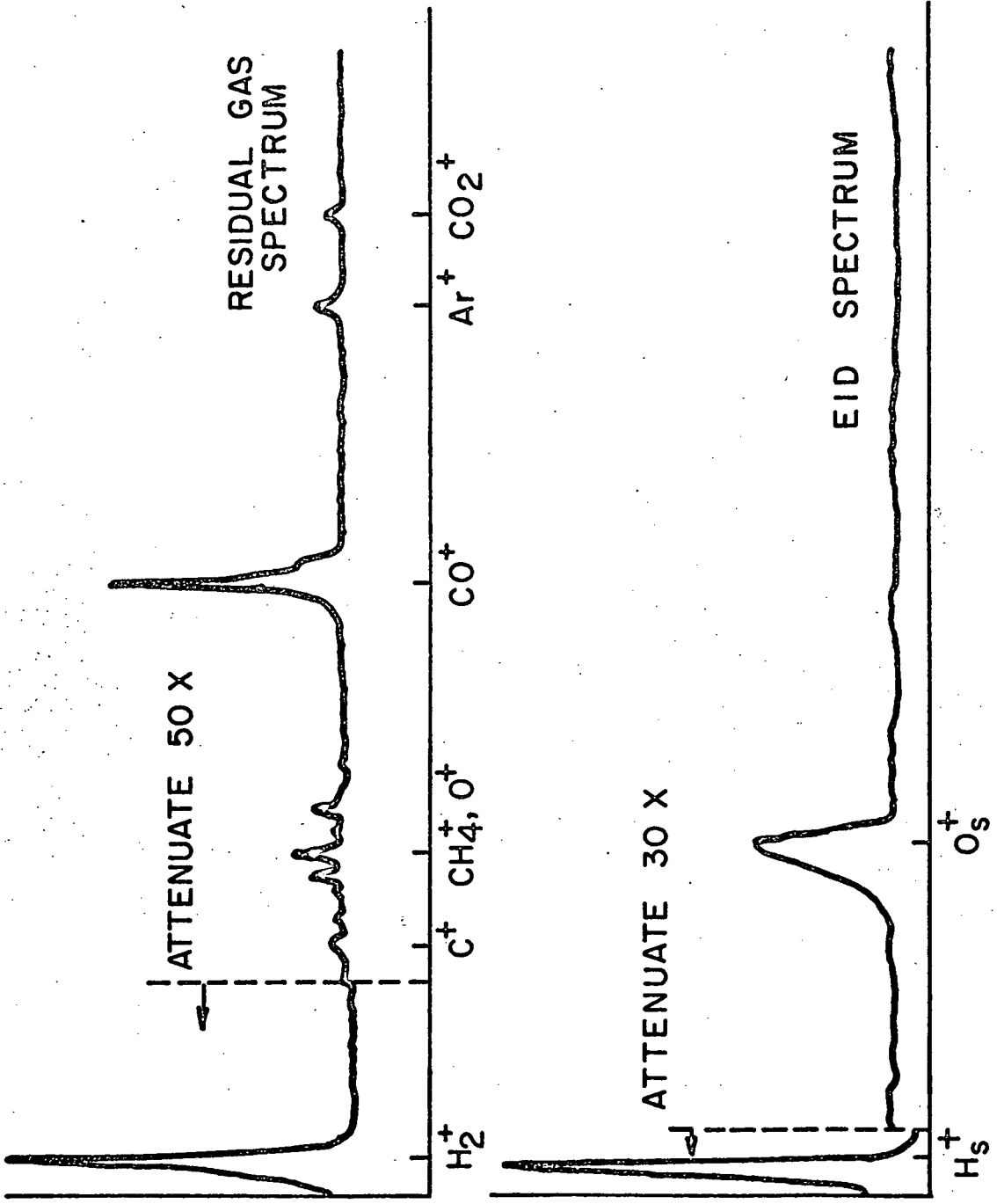
Detection of EID ions other than H_S^+ and O_S^+ was diligently pursued. If the substrate was allowed to "rest" for several weeks and was not heated prior to determining the EID spectrum, then F^{19} , Cl^{35} , and Cl^{37} ions were sometimes observed.

CO_S^+ and C_S^+ were of particular interest. C_S^+ was never detected. CO_S^+ was seemingly detected when high (5×10^{-5} Amp) electron bombardment current was used together with high amplification of the electron multiplier output.

Unfortunately, the signal was not only within the noise level but also had a large component of gas phase CO^+ mixed with it. Evidence that the signal was actually from the gas phase was a direct relation between the signal and the carbon monoxide pressure, and a thermodesorption rise coinciding with the thermodesorption of carbon

FIGURE 24
Residual Gas and EID Spectra.

ION CURRENT (ARBITRARY UNITS)



ATOMIC MASS NUMBER →

monoxide, rather than the decay to zero experienced by EID signals upon thermodesorption. Huber and Rettinghaus²⁹ have obtained CO_S^+ ions on polycrystalline platinum. Their CO_S^+ ion yield was 1.5×10^{-4} that of their H_S^+ ion yield. The system used in the present work gave an O_S^+ ion yield of 1×10^{-2} of the H_S^+ ion yield. As the O_S^+ ion current was less than an order of magnitude above the dark current of the multiplier, one therefore could not expect reliable determinations of CO_S^+ current with this system.

The appearance of O_S^+ when the substrate is being exposed to hydrogen would logically be attributed to CO impurities in the hydrogen atmosphere, however it will be shown later to be associated with adsorbed hydrogen and not simply the result of dissociation of adsorbed carbon monoxide.

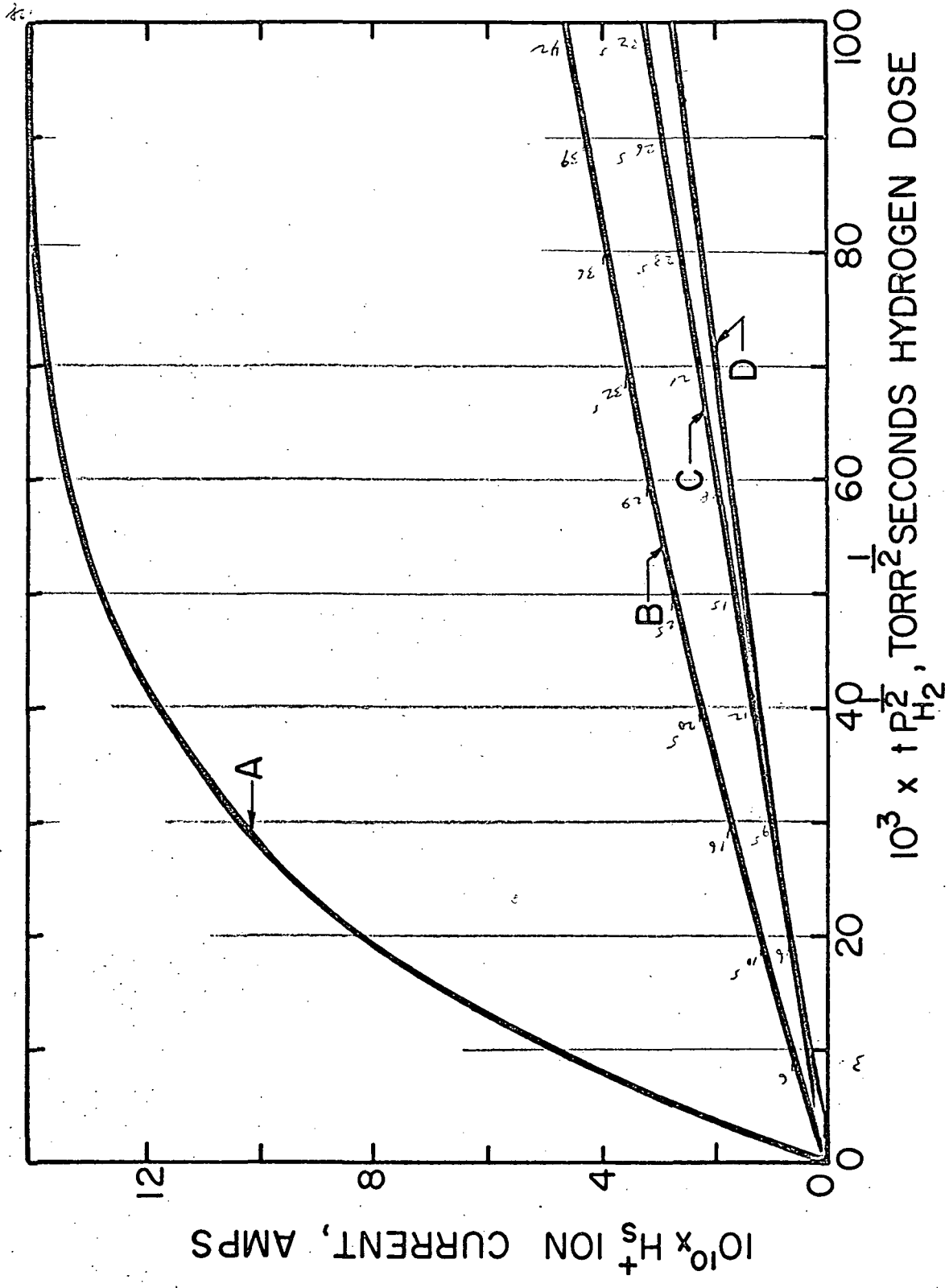
D. Electron Induced Desorbed Ion Study of Surface Coverage

1. Results with Pure Hydrogen Dosing

If the H_S^+ ion originates with adsorbed hydrogen, it should be directly proportional to hydrogen coverage and one would expect the H_S^+ ion current to follow the adsorption of hydrogen. Determinations of H_S^+ ion current versus time in "pure" (99%) hydrogen were obtained directly from the X-Y recorder. The H_S^+ ion current was plotted versus $t(P_{\text{H}_2})^{1/2}$, which has previously been shown to be a function of hydrogen coverage. The result is shown in Figure 25. It is obvious from the figure that the data do not fall on the same curve. Thus no direct relation between H_S^+ ion current and hydrogen coverage was found with pure hydrogen dosing. Careful studies did not reveal any thermodesorption of hydrogen containing species other than hydrogen. This in-

FIGURE 25

EID H_S^+ Ion Current versus Hydrogen Dose in
Various Mixtures of H_2 + CO. Curve A:
 5.7×10^{-10} Torr H_2 , 8.7×10^{-11} Torr
CO; Curve B: 1.0×10^{-8} Torr H_2 , $8.5 \times$
 10^{-11} Torr CO; Curve C: 1.1×10^{-7}
Torr H_2 , 2.9×10^{-10} Torr CO; Curve
D: 2.0×10^{-8} Torr H_2 , 9.6×10^{-11}
Torr CO.



licated that whatever species is responsible for the H_S^+ ion current is dissociated upon thermodesorption.

2. Effect of Carbon Monoxide on the H_S^+ Ion Current

An initial check on the effect of carbon monoxide was made by using the ionization gauge as a source of carbon monoxide. When an ionization gauge is outgassed (cleaned by heating to $1000^{\circ}C$) it releases large quantities of gas, mostly carbon monoxide. A pressure burst to 1×10^{-6} Torr (gauge) is commonly observed.

A hydrogen leak was set to bring the pressure to 2.5×10^{-8} Torr. The ionization gauge was outgassed and the substrate flashed clean. Upon cooling, the H_S^+ ion current increased with time as shown by curve "A" in Figure 26. After 2000 seconds the substrate was flashed clean and the "EID adsorption" repeated. By this time much of the carbon monoxide introduced into the system had been pumped out. Curve "B" in Figure 26 is the second determination. The rate of rise is significantly less than with the added carbon monoxide impurity, suggesting that carbon monoxide is a part of the species producing H_S^+ ions.

If carbon monoxide is involved in the surface reactions, an obvious experiment would be to see if a dose of carbon monoxide could be "titrated" with hydrogen. These results are shown in Figure 27. Carbon monoxide was admitted via a Hoke valve to 1×10^{-8} Torr (gauge) up to a point "a" when it was valved off. The H_S^+ ion current increased sharply until the CO was valved off, then exhibited a much reduced rate of rise. At point "b" the pressure had declined to 3×10^{-9} Torr (gauge). Hydrogen was then admitted via a leak valve to 1×10^{-8} Torr (gauge) at point "c," 5×10^{-8} Torr (gauge) at point "d," 1×10^{-7} Torr

FIGURE 26
EID H_S^+ Adsorptions.

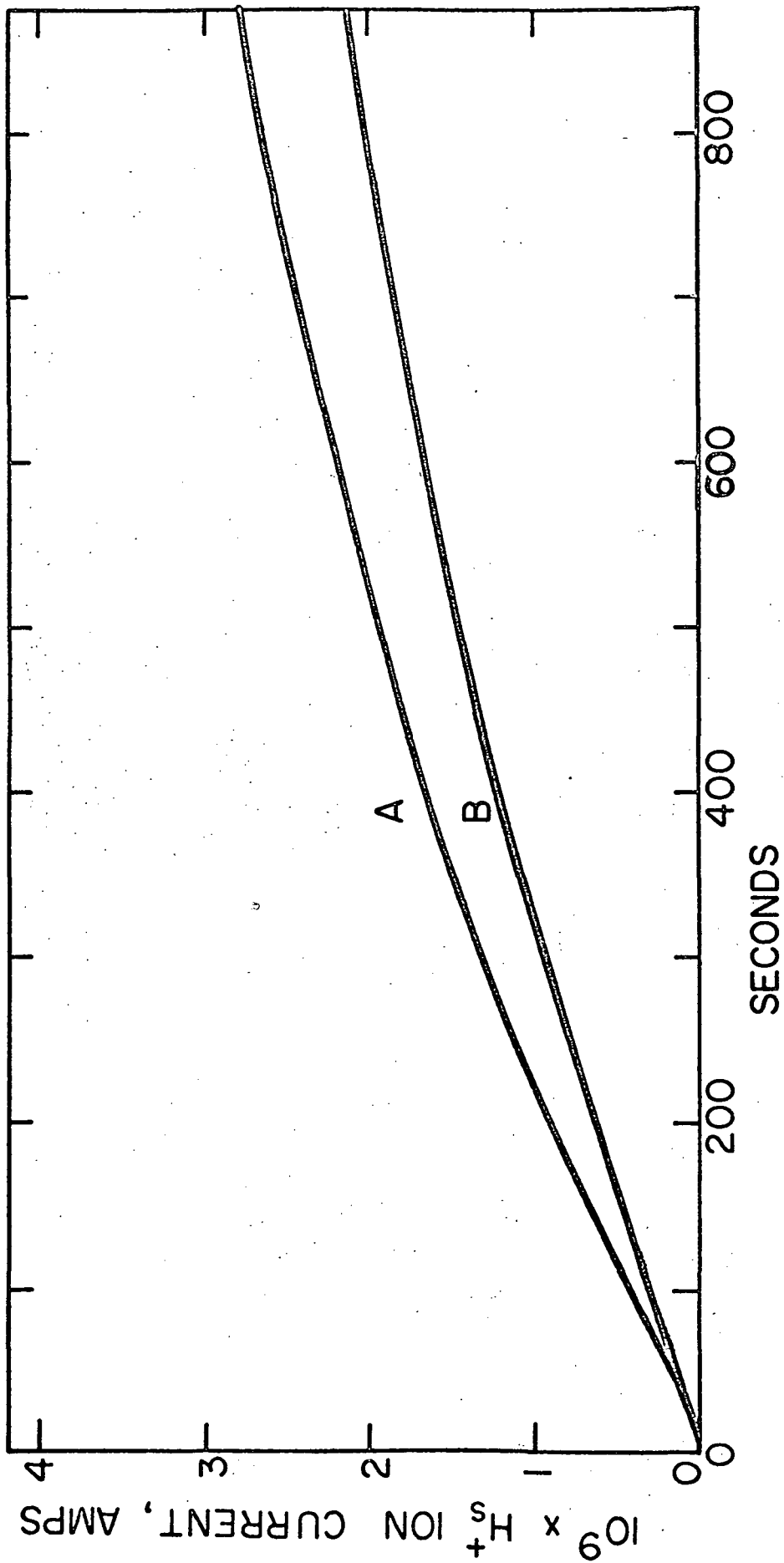
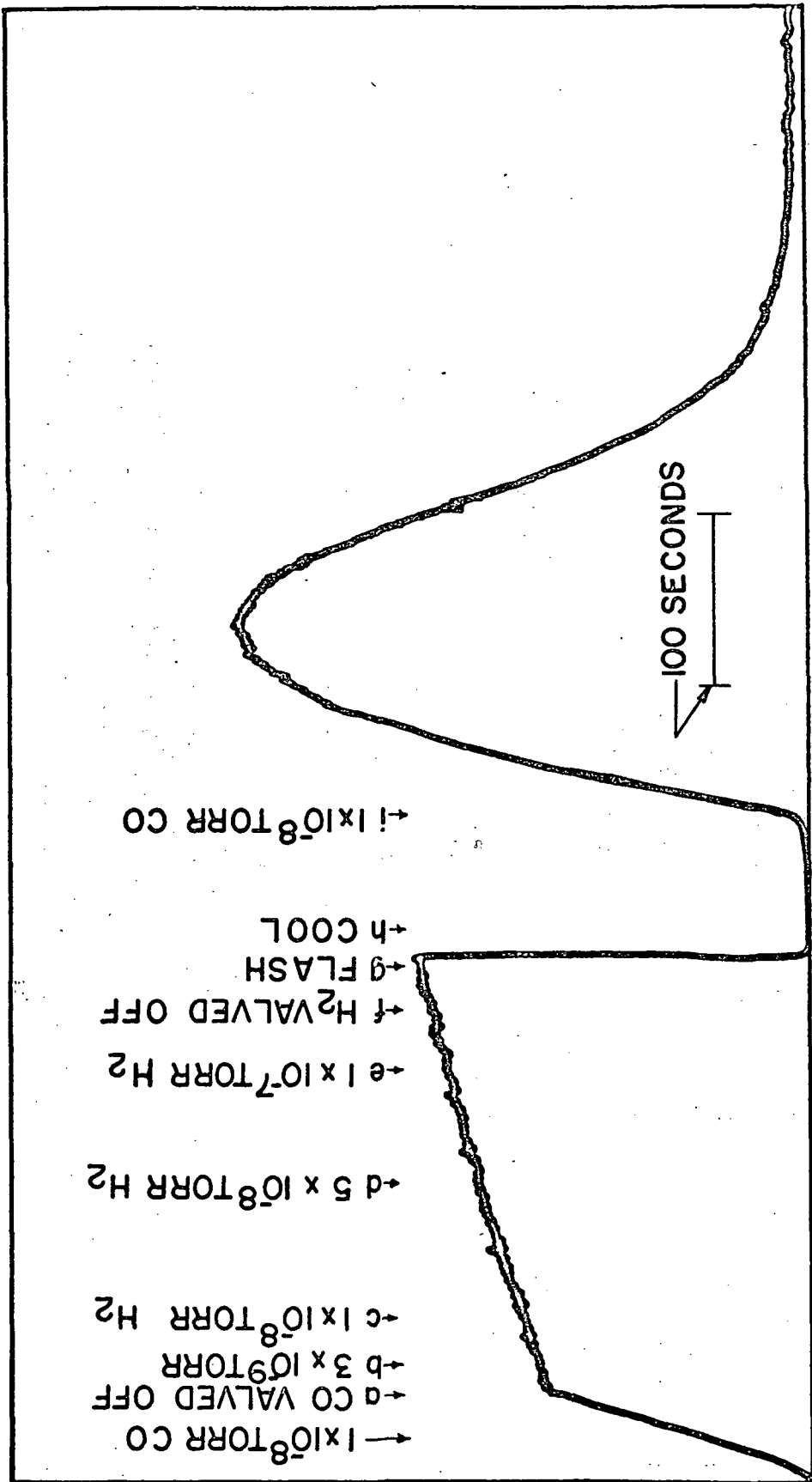


FIGURE 27

EID H_S^+ Ion Current During Various Gas
Exposure Experiments.



H^+ ION CURRENT

TIME

100 SECONDS

1×10^{-8} TORR CO

h COOL

g FLASH

f H_2 VALVED OFF

e 1×10^{-7} TORR H_2

d 5×10^{-8} TORR H_2

c 1×10^{-8} TORR H_2

b 3×10^{-9} TORR

a CO VALVED OFF

1×10^{-8} TORR CO

(gauge) at point "e," and valved off at point "f." It was observed that hydrogen dosing of the surface that had been previously dosed with carbon monoxide plus residual hydrogen, had no discernable effect. The substrate was flashed clean at point "g" and cooled at point "h." In the residual pressure of 1×10^{-9} Torr (gauge) the H_S^+ ion current exhibited a slow rise until carbon monoxide was admitted to 1×10^{-8} Torr (gauge), shown at point "i," whereupon a sharp rise in H_S^+ ion current occurred, followed by peaking and exponential decay.

At first inspection of the data above it seems unreasonable that admitting carbon monoxide alone should have such a large effect on the H_S^+ ion current. It must be noted that the pressures were obtained from an ionization gauge and the gases were named for their apparent source. It was demonstrated, after the experiment above, that admitting carbon monoxide caused the ion pump to emit hydrogen to about half the pressure of the carbon monoxide. This emission of previously pumped gases from the ion pump was frequently observed, consequently quantitative experiments involving sequential dosing with different gases were not practicable.

Further insight into the role of carbon monoxide in producing the H_S^+ ion current is obtained by closer examination of the pure hydrogen data presented in Figure 25. Table II lists the applicable data and some derived results. The carbon monoxide dose, tP_{CO} , at a constant hydrogen dose of $t(P_{H_2})^{1/2} = 0.1$ has been determined and compared with the H_S^+ ion current at this point. The ratio of H_S^+ ion current to tP_{CO} is reasonably constant. This is good indication that carbon monoxide is an essential part of the species providing the H_S^+ ion.

TABLE II

IDENTIFICATION NUMBER	P_{H_2} (Torr)	P_{CO} (Torr)	tP_{CO} at $t(P_{H_2})^{1/2} = 0.1$ (Torr - Sec)	H_S^+ at $t(P_{H_2})^{1/2} = 0.1$ (Amps)	H_S^+/tP_{CO}
1143	2.0×10^{-8}	9.6×10^{-11}	6.8×10^{-8}	2.8×10^{-10}	4.1×10^{-3}
1147	2.7×10^{-8}	1.2×10^{-10}	7.2×10^{-8}	3.1×10^{-10}	3.8×10^{-3}
1150	1.1×10^{-7}	3.0×10^{-10}	8.7×10^{-8}	3.3×10^{-10}	3.8×10^{-3}
1140	1.0×10^{-8}	8.5×10^{-11}	8.3×10^{-8}	4.7×10^{-10}	5.7×10^{-3}
1136	5.7×10^{-10}	8.7×10^{-11}	36.0×10^{-8}	14.0×10^{-10}	3.8×10^{-3}
					4.3 Average

Fig 5
#1143
#1147
#1150
#1140
#1136

Further evidence that carbon monoxide is involved is seen in Figure 28 where the H_S^+ ion current is plotted versus dose of carbon monoxide at a constant hydrogen dose of $t(P_{H_2})^{1/2} = 6 \times 10^{-2}$ Torr^{1/2} seconds. The H_S^+ ion current at a given hydrogen dose is directly proportional to the dose of carbon monoxide.

When the H_S^+ ion current is plotted versus hydrogen dose, $t(P_{H_2})^{1/2}$, at a constant carbon monoxide dose of $tP_{CO} = 3.5 \times 10^{-7}$ Torr-seconds the result is random with no correlation.

Finally it was found that the rate of rise of the EID adsorptions in pure hydrogen was proportional to carbon monoxide pressure. Determining $(dH_S^+/dt)/P_{CO}$ from the determinations presented in Table II, an average value of $(5.7 \pm 1.1) \times 10^{-3}$ amps per second per Torr was found. Thus the EID H_S^+ ion current is related to carbon monoxide adsorption.

3. Effect of Dosing with a Mixture of Hydrogen and Carbon Monoxide

When a mixture of hydrogen and carbon monoxide was admitted to the system and the H_S^+ ion current plotted as a function of time after cleaning, the result shown in Figure 29 was obtained. The substrate was cleaned by heating to 1300°C in a 5 second time interval, holding that temperature for an additional 5 seconds then switching off the heating power. Seven seconds later the substrate was cool long enough for a detectable H_S^+ ion current to result. This time was called t_s . As adsorption of hydrogen and carbon monoxide proceeded, the H_S^+ ion current increased, linearly at first, then at a decreasing rate until the rate of change was zero at a time labeled t_p . After t_p , the current decreased then exhibited an approximately exponential decay.

FIGURE 28

EID H_S^+ Ion Current versus Carbon Monoxide Dose at a Constant Hydrogen Dose of $t(P_{H_2})^{1/2} = 5 \times 10^{-2}$ Torr $^{1/2}$ Seconds in Pure Hydrogen and Residual Gas.

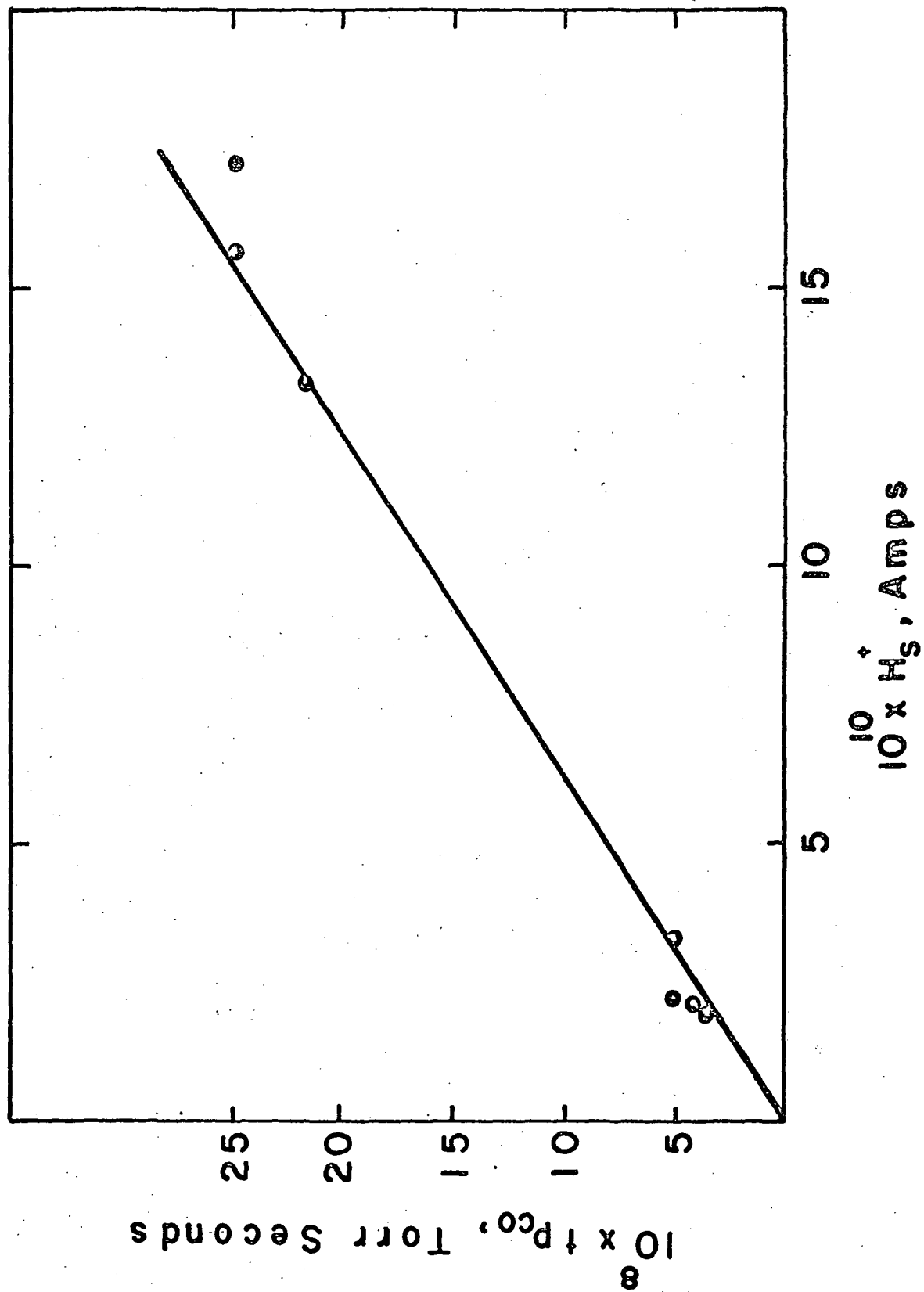
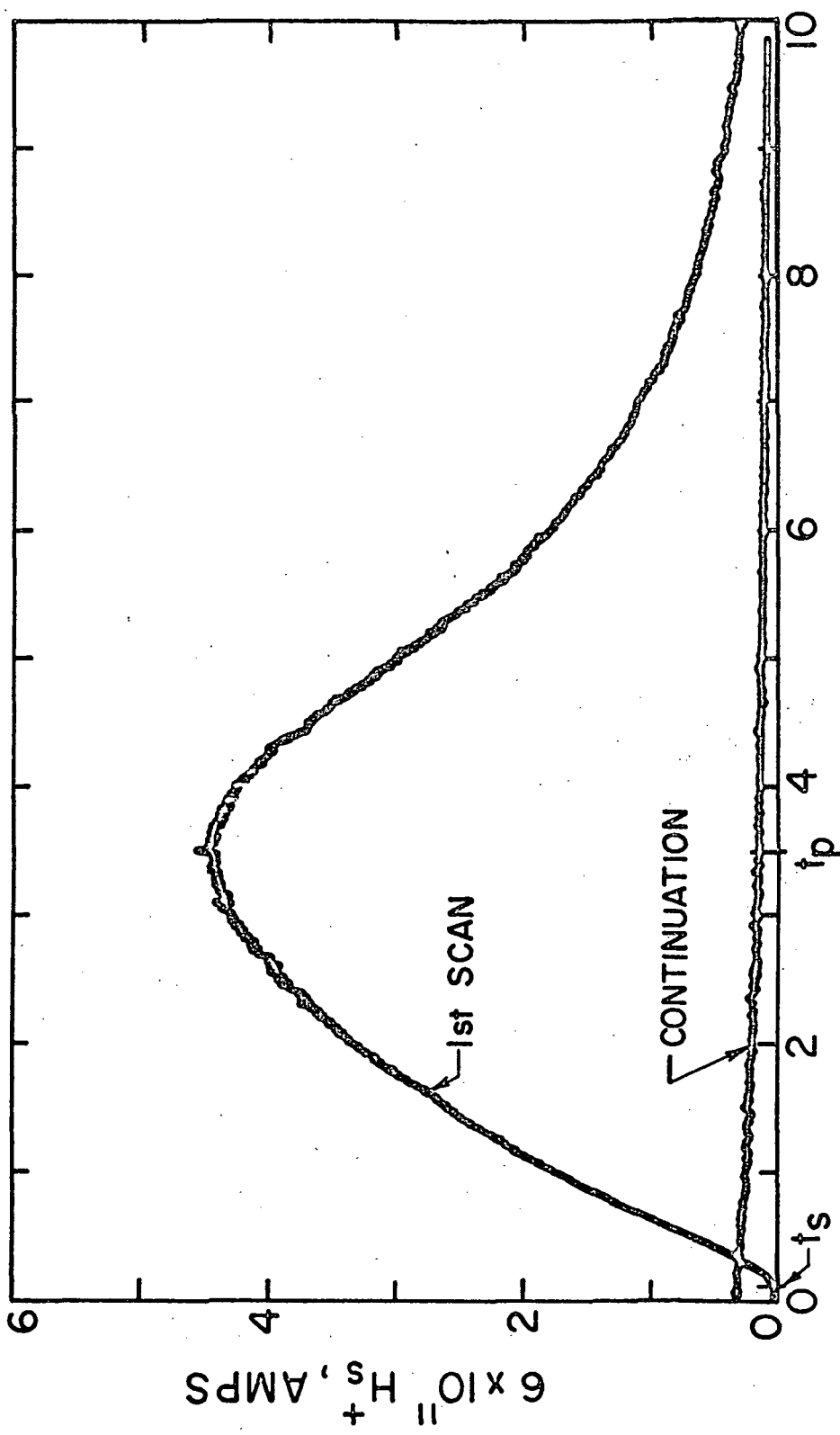


FIGURE 29

EID H_s^+ Ion Current versus Time in a
Mixture of 7.6×10^{-8} Torr H_2 and 4.8
 $\times 10^{-9}$ Torr CO.



50 x t, SECONDS

The value of t_s varied with pressure, mixture and thermal history over the range of 6 to 12 seconds, but usually was within 6 to 8 seconds. Measurements therefore were made from t_s .

Examination of t_p as a function of carbon monoxide partial pressure, shown in Figure 30, reveals that t_p occurred at a constant dose of carbon monoxide for any mixture and pressure. Since carbon monoxide was adsorbed by first order kinetics, this means that t_p occurred at a specific coverage. The line in Figure 30 represents 8.9×10^{-7} Torr-seconds of carbon monoxide dosing. This is equivalent to $0.14\theta_{CO}$ (from Figure 9). This is an approximation since θ_{CO} is a function of H_2 -CO mixture for a given exposure, but comparison with Figure 9 shows that at this coverage the difference is negligible.

Noting that t_p occurred at constant carbon monoxide dose, the EID adsorption curves were normalized with respect to time by plotting H_s^+ ion current versus $(t - t_s) P_{CO}$. This is shown in Figure 31. The apparent delay in the rise of curve D and E resulted from a non-linear rise from t_s at the start of the adsorption. This was attributed to the cool down time of the substrate. As these data are at a relatively high pressure, a significant dose, t_p , occurred during this time. It is observed that the rate of decay is proportional to the carbon monoxide dose. The rate of decay is therefore a function of carbon monoxide pressure, being higher at higher pressures.

The coverage of carbon monoxide exceeded that of hydrogen during most of the EID adsorptions run in mixed gases, as is seen in Figures 39, 40, and 41. Under the conditions of an excess of carbon monoxide, the H_s^+ ion current is proportional to the hydrogen dose. This is seen

FIGURE 30
Time to Maximum EID H_5^+ Ion Current in
 $H_2 + CO$ Mixtures as a Function of Car-
bon Monoxide Pressure.

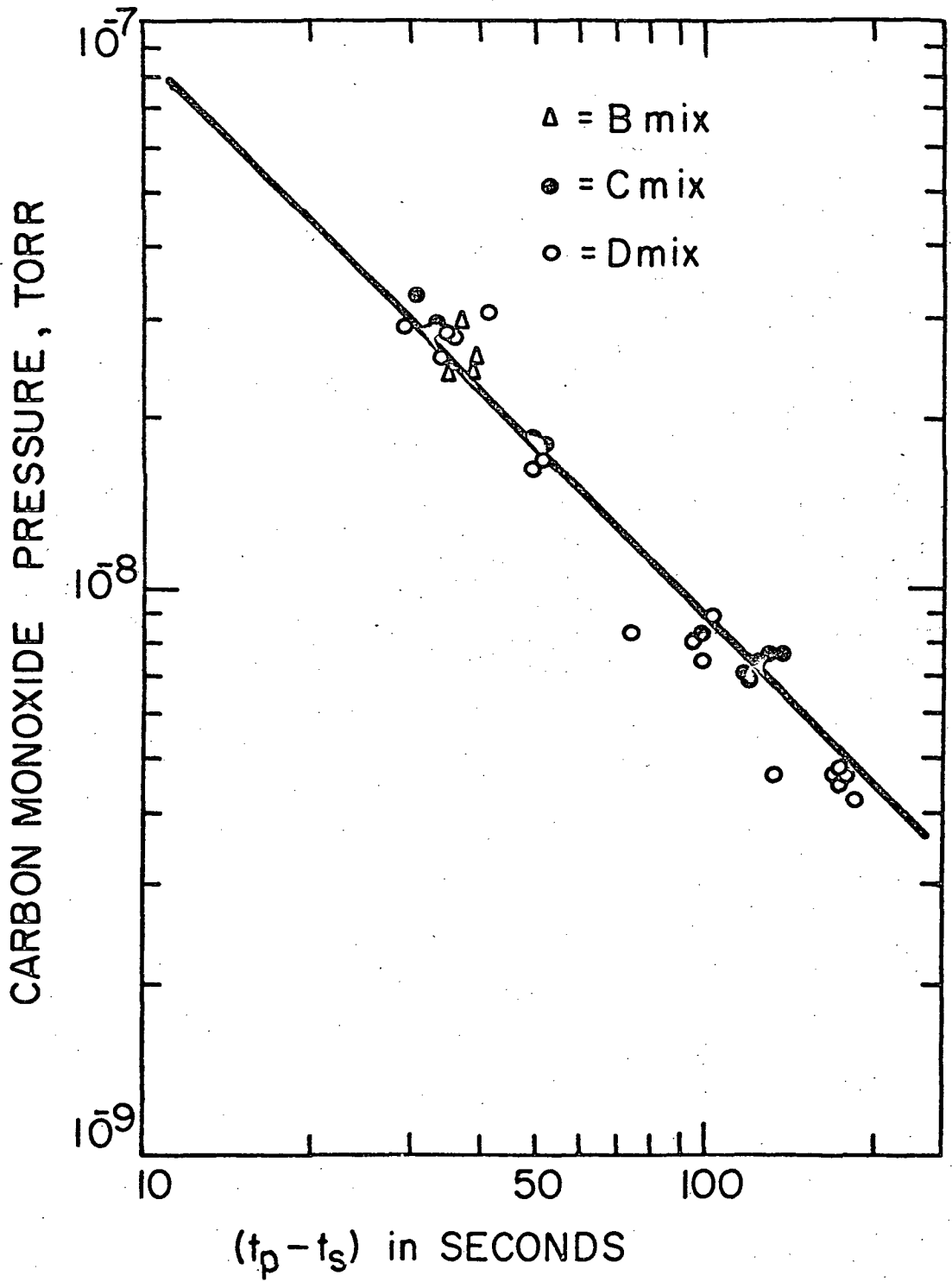
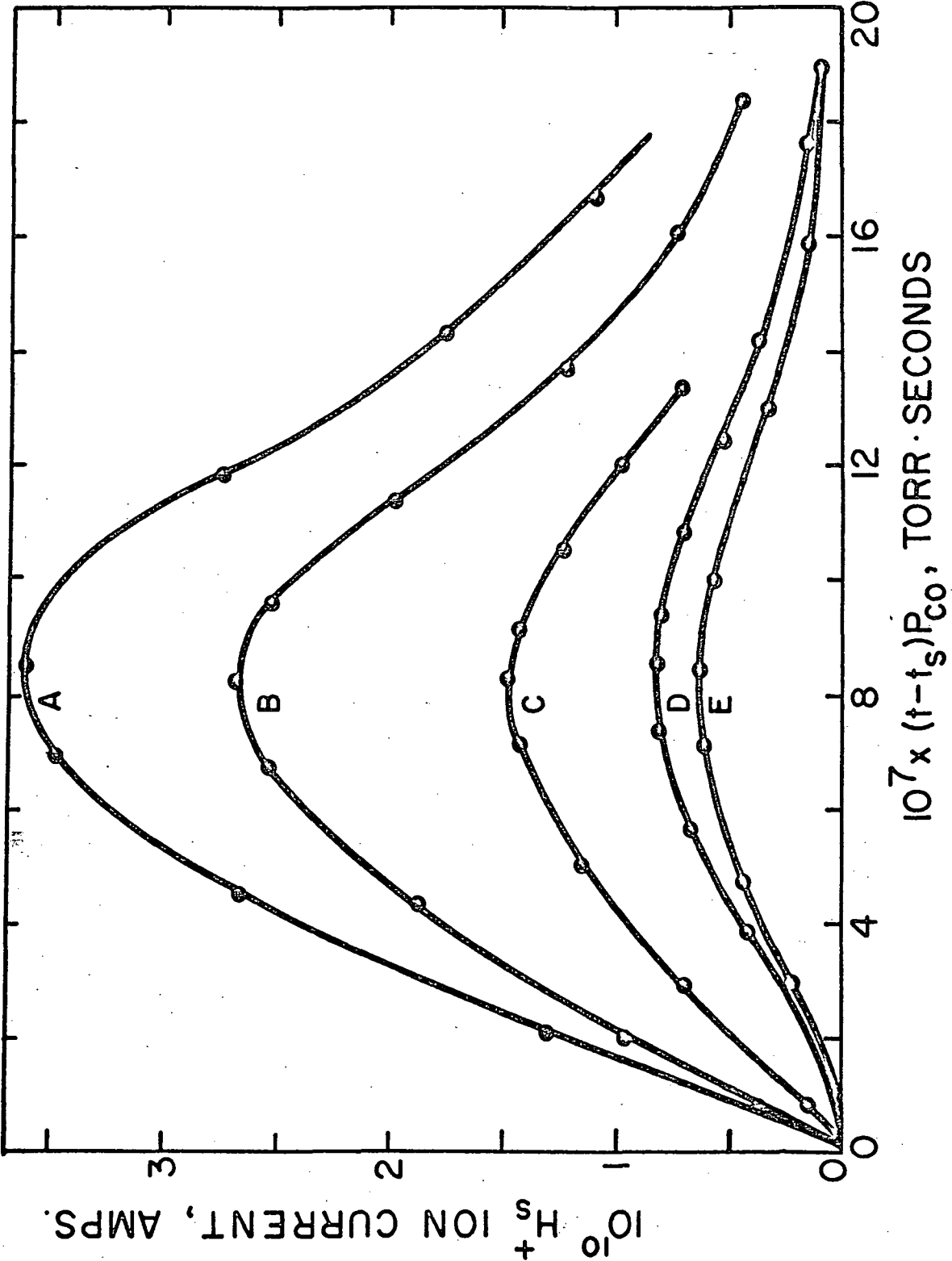


FIGURE 31

EID H_2S^+ Adsorptions Normalized with
Respect to Carbon Monoxide Dose.



in Figure 32 in which the H_S^+ ion current is plotted against hydrogen dose $t(P_{H_2})^{1/2}$. The time used to determine hydrogen dose was the time required to achieve a carbon monoxide dose of 8×10^{-7} Torr-seconds at the prevailing CO pressure, thus data was obtained at approximately constant coverage of carbon monoxide.

A similar plot to Figure 32, relating H_S^+ ion current to tP_{CO} at a constant dose of hydrogen resulted in random points.

Since the H_S^+ ion current is proportional to $t(P_{H_2})^{1/2}$ at constant coverage of carbon monoxide, the effect of CO coverage on the H_S^+ ion yielding species could be shown by plotting the "normalized EID species concentration," $H_S^+/t(P_{H_2})^{1/2}$, versus dose of CO. This is shown in Figure 33. The entire curve is in the region of linear carbon monoxide adsorption at its highest sticking probability and the CO coverage is greater than the hydrogen coverage throughout. It is seen that carbon monoxide coverage does not affect the normalized EID species concentration initially but with increasing CO coverage the normalized concentration is reduced. This will be discussed in section VI C.

Finally, it was found that the rates of rise of the EID adsorptions were a function of hydrogen pressure. Considering the kinetics of hydrogen adsorption, as developed in section VI C

$$d\theta_{H^*}/dt = k P_{H_2}^{1/2} (1 - \theta_{H^*})$$

we see that at given coverage of hydrogen the rate of hydrogen adsorption is proportional to $P_{H_2}^{1/2}$. Determining $(dH_S^+/dt)/P_{H_2}^{1/2}$, an average value of $(9.15 \pm .30) \times 10^{-9}$ Amps per second per Torr^{1/2} was found, using the initial rate of rise. Thus the rate of rise of the H_S^+ ion current was proportional to the rate of hydrogen adsorption.

FIGURE 32

EID H_S^+ Ion Current as a Function of
Hydrogen Dose, $t(P_{H_2})^{1/2}$ at a Constant
Carbon Monoxide Dose of $tP_{CO} = 8 \times$
 10^{-7} Torr Seconds.

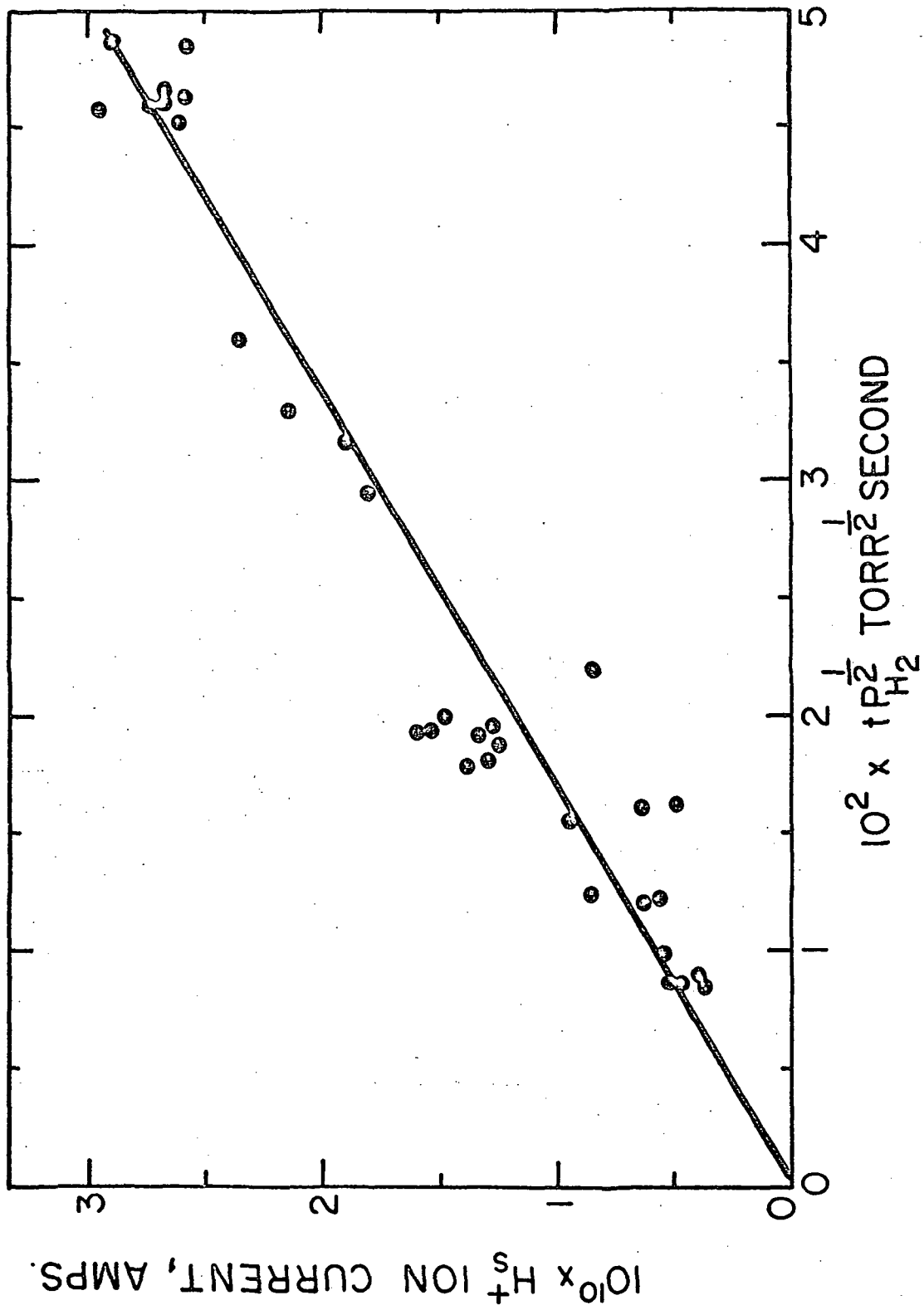
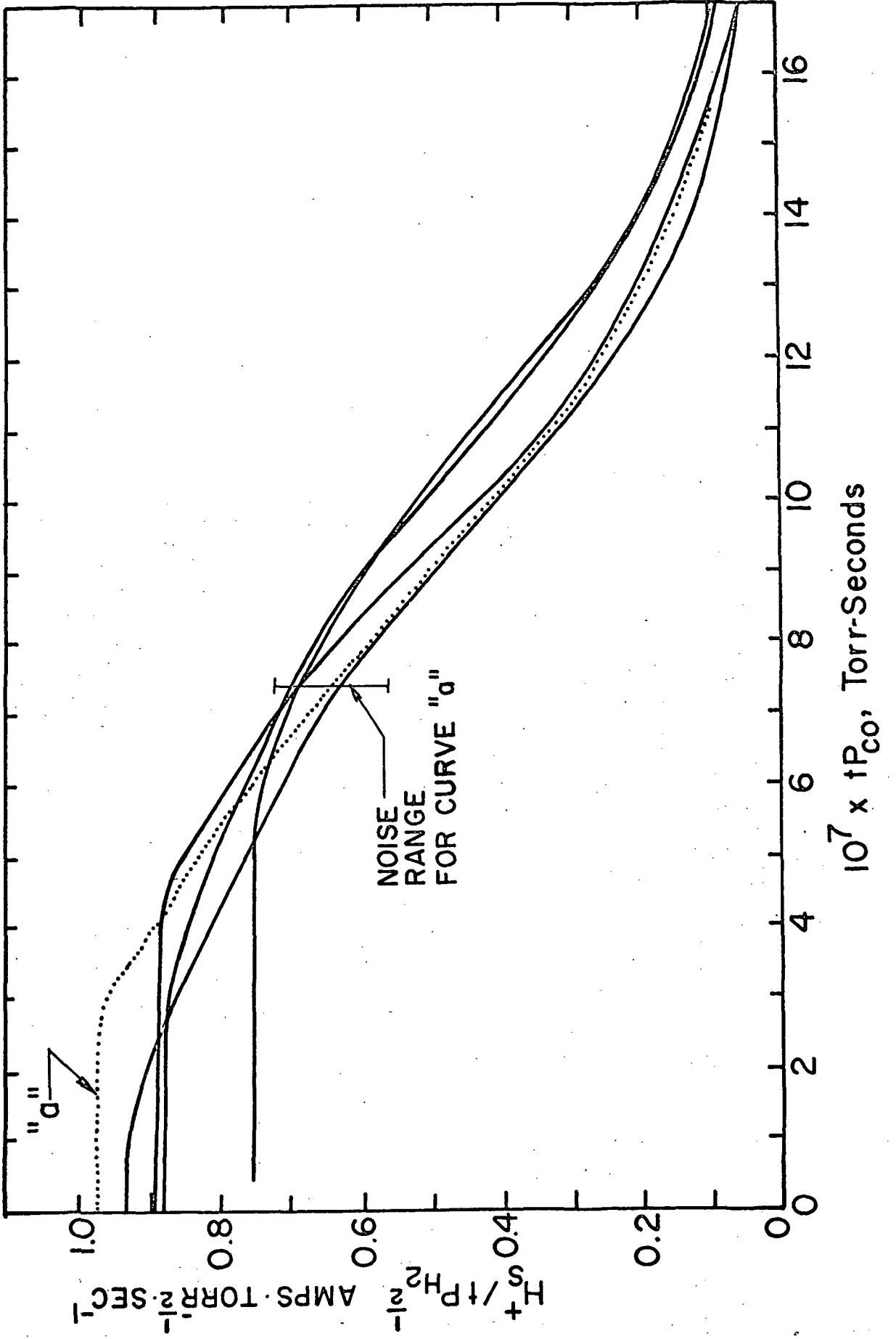


FIGURE 33
Normalized EID Species Concentration
as a Function of Carbon Monoxide Dose.



In summary, it has been found that:

a) In "pure" hydrogen where the hydrogen coverage exceeds the carbon monoxide coverage:

- 1) H_S^+ current is not related to $t(P_{H_2})^{1/2}$ at constant tP_{CO} .
- 2) H_S^+ current increases linearly with tP_{CO} at constant $t(P_{H_2})^{1/2}$.

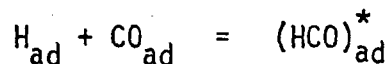
Therefore, H_S^+ current is directly proportional to carbon monoxide coverage.

b) In mixtures of hydrogen and carbon monoxide where carbon monoxide coverage exceeds hydrogen coverage:

- 1) H_S^+ current is not related to tP_{CO} at constant $t(P_{H_2})^{1/2}$.
- 2) H_S^+ current increases linearly with $t(P_{H_2})^{1/2}$ at constant tP_{CO} .

Therefore, H_S^+ current is a function of hydrogen coverage.

This leads to the hypothesis that the H_S^+ ion current comes from a species containing both hydrogen and carbon monoxide. This could form by



where $(HCO)^*$ will be referred to as the surface complex. This will be explored further in the discussion section.

4. Effect of Electron Beam Current

The electron beam current was variable up to $50\mu A$ and was measured with a $0-5\mu A$ D'Arsonval meter between the substrate and its bias supply. This imposed the limitation that $1\mu A$ was the lowest current that could be measured with $\pm 10\%$ accuracy. The beam current exhibited an occasional drift from 0.8 to $1.2\mu A$ when the current was set at $1\mu A$. This drift was corrected between determinations.

The H_S^+ ion current was observed as a function of electron beam current in residual gas after a near equilibrium signal was obtained. An electron current of $1\mu A$ produced a decay in the H_S^+ ion current of 1% per minute, while larger currents produced proportionately greater effects. Decreasing the current after a period of high current bombardment caused a return of the H_S^+ signal to the equilibrium value associated with the lower current. EID adsorptions were run with the beam on continuously and then repeated with intermittent beam current. If the beam current was $1\mu A$ or lower, the two determinations coincided. Hydrogen and carbon monoxide adsorptions and thermodesorptions were performed with and without electron bombardment during the adsorptions. The results were identical.

Considering the limitations of beam current measurements, the effect of the beam observed, and the need for H_S^+ ion signals of sufficient amplitude to conveniently measure, the expedient value of beam current was $1\mu A$. This amounts to 10^{-5} amp/cm² or 6×10^{13} electrons sec⁻¹ cm⁻², or 4×10^{-2} monolayer per second if each electron caused an event. Huber and Rettinghaus report a H_S^+ yield of 2×10^{-5} ion per electron, or a maximum removal rate of 8×10^{-7} monolayer per second for the experimental system used in this work. This value is one or two orders of magnitude low as it neglects EID neutrals, which were not determined by Huber and Rettinghaus.

In the case of adsorption in a mixture of hydrogen and carbon monoxide the H_S^+ ion current exhibited rise, peaking and decay to an equilibrium value. To determine the effect of the electron beam on this phenomenon, identical runs were made using $10\mu A$ and $1\mu A$ beam currents. These were plotted as normalized H_S^+ ion current versus tP_{CO} .

Figure 34 shows that up to 13×10^{-7} Torr-sec carbon monoxide exposure the curves virtually coincided, being well within the limits of experimental variation, as comparison with Figure 31 reveals. In Figure 31 it is seen that the time constant of decay, at $1\mu\text{A}$ beam current, was a function of carbon monoxide pressure and $\tau P_{\text{CO}} = \text{constant}$ where τ is the decay constant. Figure 34 shows that the decay constant was identical at either $1\mu\text{A}$ or $10\mu\text{A}$ up to 13×10^{-7} Torr-sec CO. At high coverage the curves do diverge since the beam did cause some desorption. The near equilibrium levels at 2×10^{-6} Torr-sec CO exposure were not proportional to the beam currents involved. The decay of the H_S^+ ion current was therefore the result of CO exposure and not electron bombardment.

E. Electron Induced Desorbed Ion Behavior During Thermodesorption

Raising the temperature of a surface may cause an adsorbate to desorb. If the adsorbate was yielding EID ions, then the surface ion current will decline as the substrate is heated. This is shown for H_S^+ ion current in Figure 43 and 44.

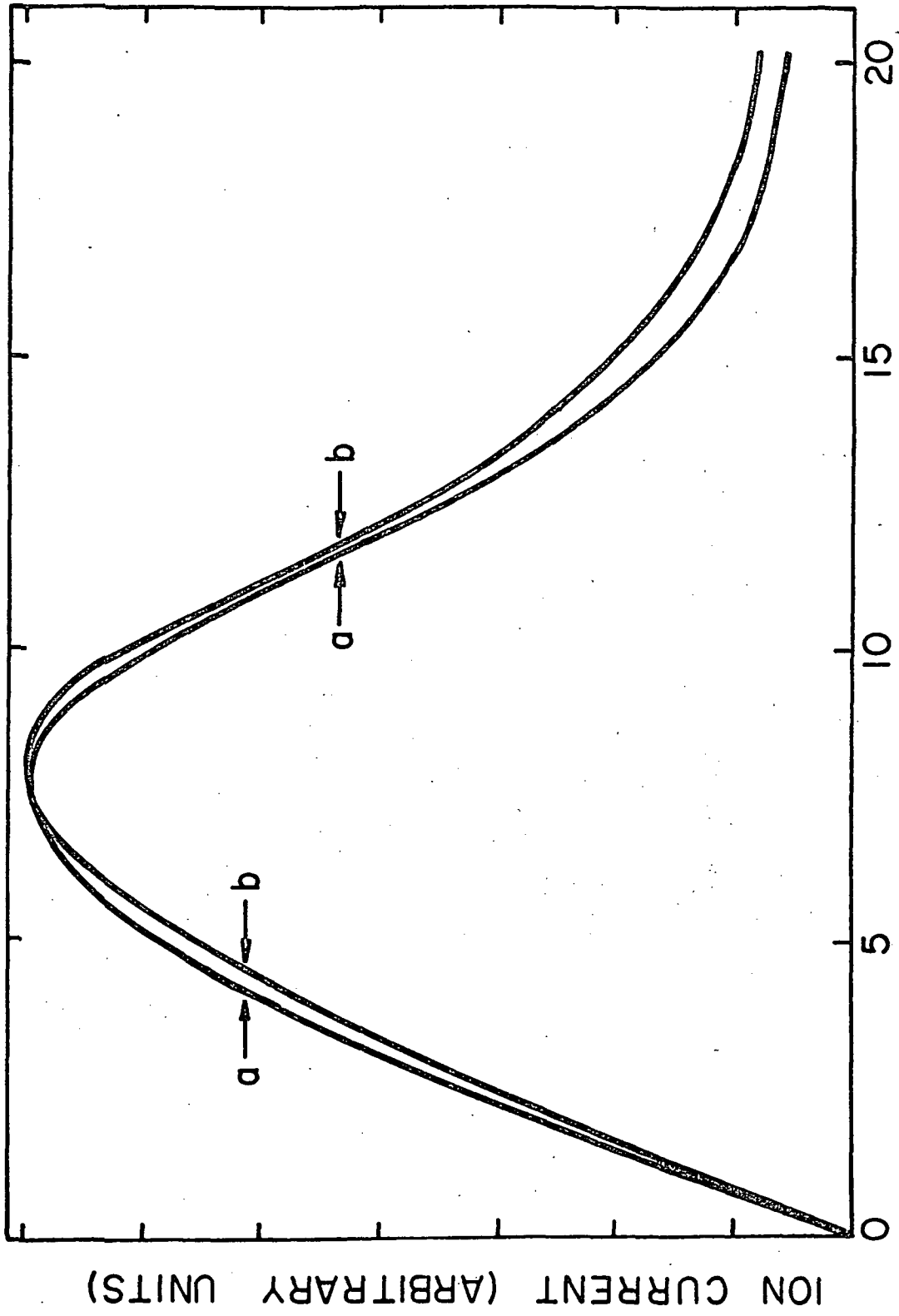
The rise in H_S^+ ion current prior to the decline is attributed to "thermal enhancement of electron induced desorption cross section" by Menzel.⁴⁴ This results from the increase in average bond length between substrate and adsorbate as the magnitude of thermal vibration increases. This lengthening of the bond reduces the amount of Auger neutralization, thus increasing the yield of EID ions. This thermal enhancement was regularly observed with the bias settings used. Alternative bias settings were found that caused the opposite of thermal enhancement - a slight continuous decline in signal until the rapid decline to zero at

FIGURE 34

Effect of Electron Bombardment Current on the H_S^+ Ion Current Behavior.

Curve A = 10^{-5} amp

Curve B = 10^{-6} amp



$10^7 \times t P_{CO}$ TORR - SECONDS

ION CURRENT (ARBITRARY UNITS)

the temperature of desorption. Thus, although discovered prior to Menzel's paper, this was considered to be a characteristic of the system and not a genuine physical phenomenon.

Comparing the EID flash results with the thermodesorption spectra of hydrogen in hydrogen-carbon monoxide mixtures, as shown in Figure 44 reveals that the H_S^+ ion current decays at a temperature corresponding to the β hydrogen peak. The significance of this will be seen in the Discussion part.

Pure hydrogen dosing resulted in an EID H_S^+ ion current (due to CO impurity) but the current did not correlate with hydrogen coverage and the EID flash temperature was notably different from the T_p of pure (α) hydrogen thermodesorption.

F. Electron Induced Desorbed Ion Observation of Isothermal Desorption

If a substrate, covered with adsorbed gas, is quickly brought to a fixed temperature of appropriate value, the gas will desorb and the surface coverage will decline according to the applicable rate law. The EID technique enables a direct measurement of the coverage versus time during such an isothermal desorption. This type of determination was performed on the H_S^+ ion current in residual gas dosing. The substrate was dosed until the maximum H_S^+ ion current was attained. The substrate power supply was then switched on with the bridge balance pre-set to the desired temperature. This resulted in a power surge through the substrate until the pre-set temperature was reached, which required less than 0.7 second. The H_S^+ ion current exhibited an exponential decay.

The decay of the H_S^+ ion current was subjected to kinetic order tests. These are presented in Figure 35 which shows that the decay is first order.

The isothermal desorptions were performed at a series of temperatures. For a first order decay from an original concentration C_0 ,

$$\ln C_0/C = kt$$

where C is the instantaneous concentration, t is time and k the reaction rate constant. The stay time is the time required for the concentration to decay to $1/e$ of its original value. Thus $\tau_a = 1/k$. Plotting $\log \tau_a$ versus $1/T$ should produce a line yielding ΔE but a curve resulted instead. This was corrected by subtracting from τ_a the response time of the recording system. A current source was fed to the recording system, then switched off. The resulting decay in response has an average time constant of 0.599 second. Subtracting 0.6 from the τ_a values resulted in a linear plot of $\log (\tau_a - 0.6)$ versus $1/T$. Utilizing

$$E_d = -R \Delta 2.303 \log (\tau_a - 0.6) / \Delta(1/T)$$

gave an E_d for decomposition value of 31 kcal/mole. Now stay time

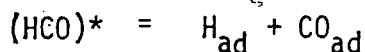
$$\tau_a = \tau_0 e^{\Delta E_d/RT}$$

where $\tau_0 = 1/\nu$ and ν = frequency factor which is commonly 10^{10} to 10^{13} sec^{-1} . Thus

$$\log \tau_0 = \log \tau_a - \Delta E_d/2.3RT$$

and τ_0 was found to equal 1.4×10^{-13} which is an acceptable value.

Since as discussed later, $(HCO)^*$ is probably the EID active species, the E_a calculated may be that of dissociation of the species by



rather than desorption of the species.

FIGURE 35

Test for Order of Isothermal H_S^+ Decay.

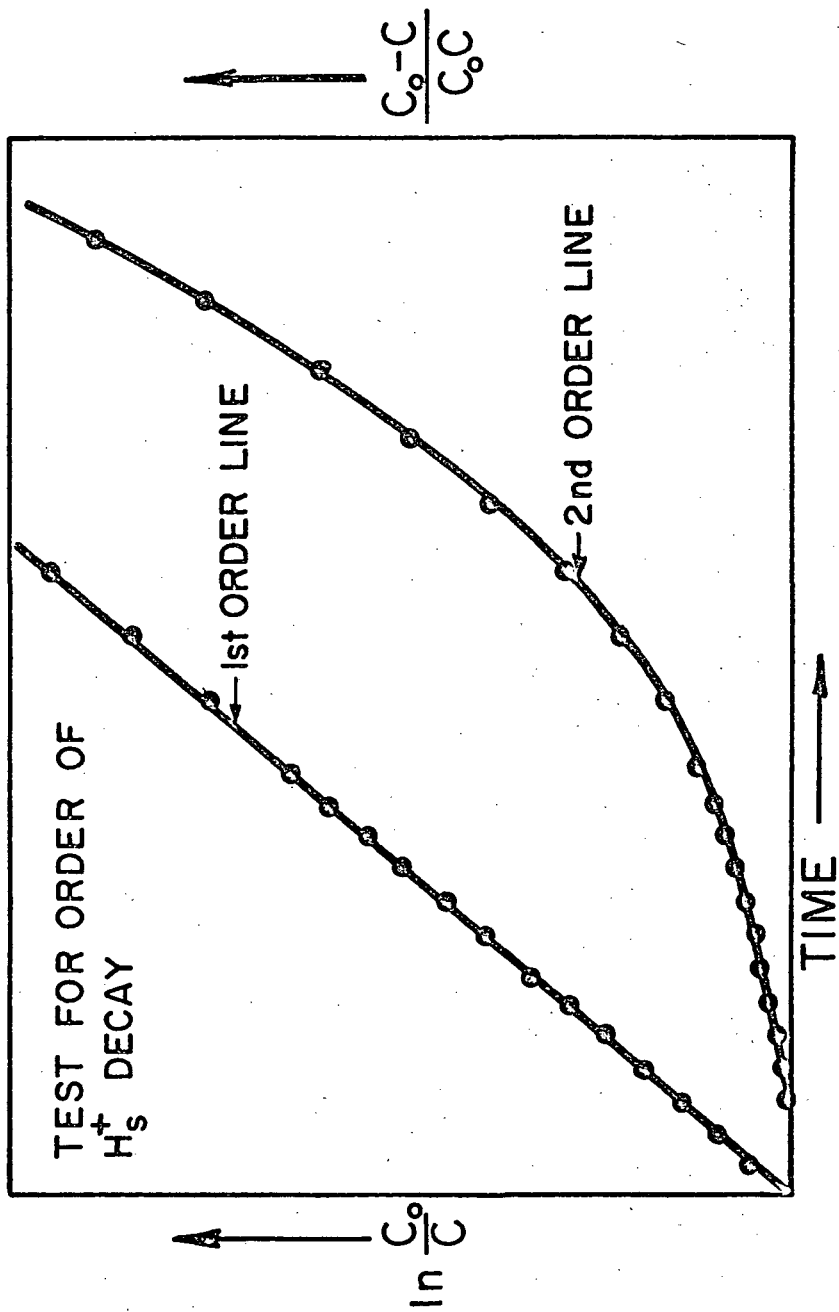
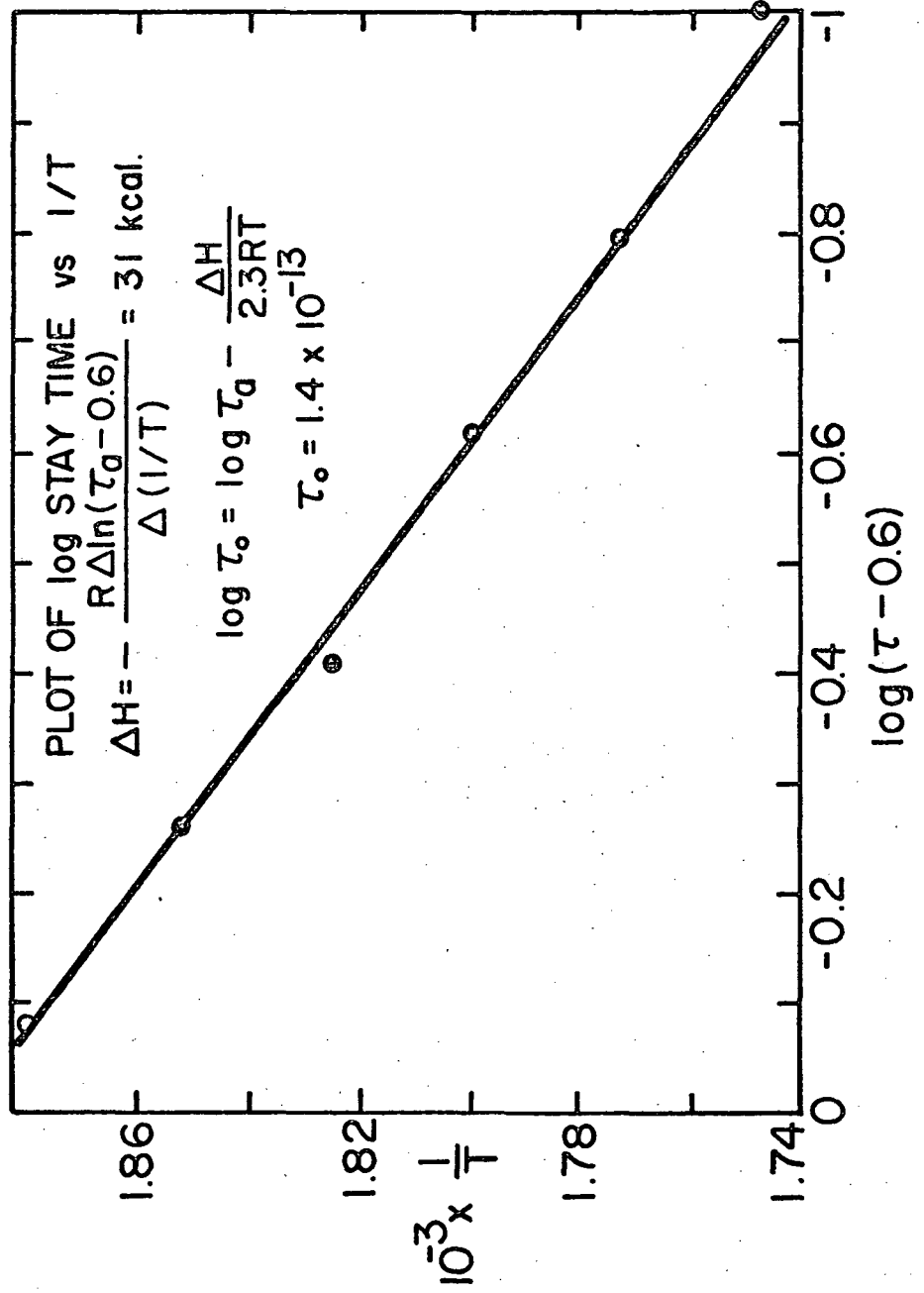


FIGURE 36

Plot of Log Stay Time versus Reciprocal Temperature.



G. The Electron Induced Desorbed O_S^+ Ion

Studies of the O_S^+ ion were complicated by low signal to noise ratio. The dark current or zero signal output of the system was about 20% of the maximum O_S^+ ion current. Figure 37 illustrates the adsorption and thermodesorption characteristics of the species under study while examining the H_S^+ and O_S^+ ion currents produced by electron bombardment. The O_S^+ ion current was consistently two orders of magnitude lower than the H_S^+ ion current.

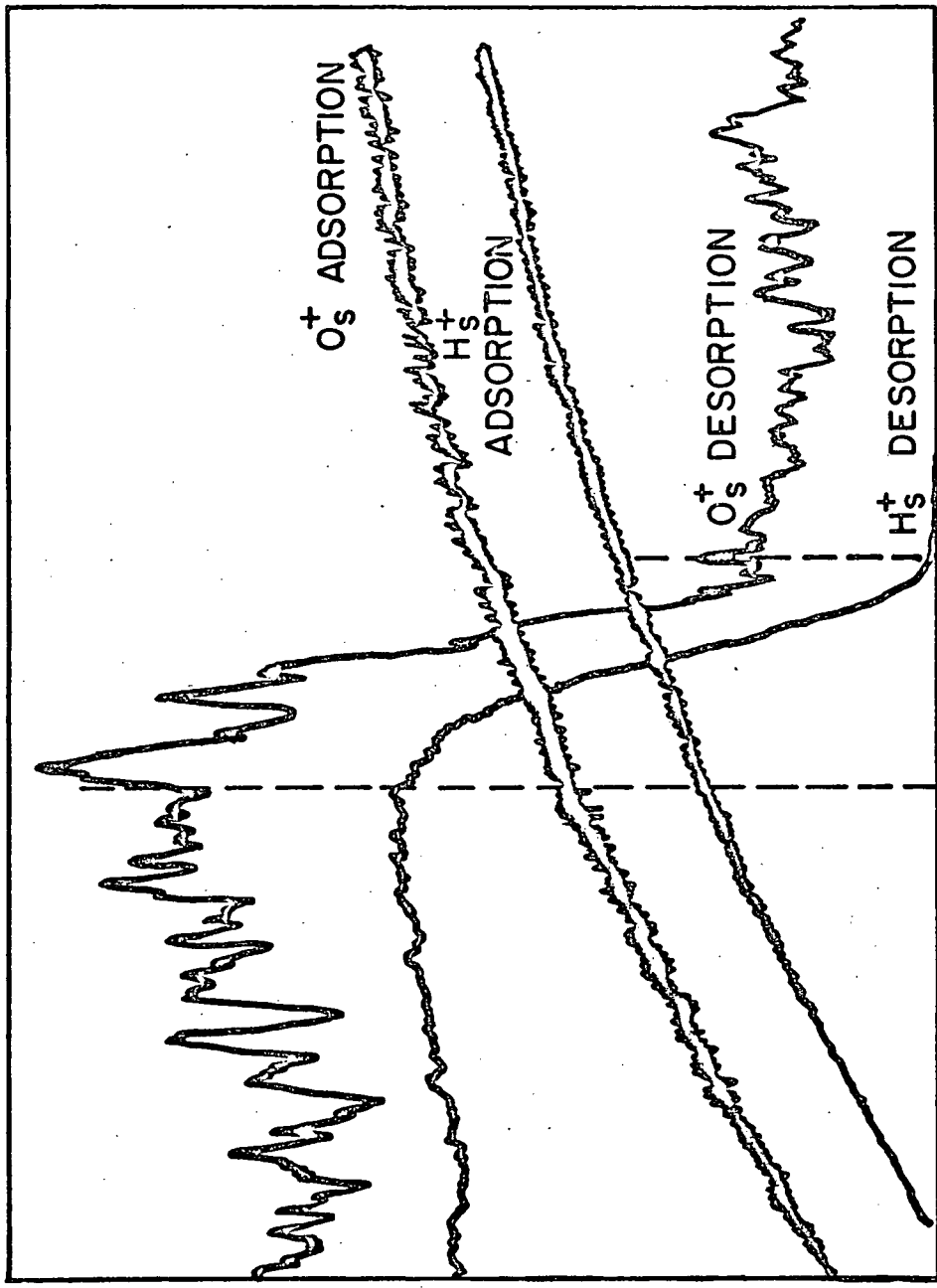
The O_S^+ ion signal could not be obtained with pure CO dosing of the substrate. Tungsten and other transition metals adsorb carbon monoxide and yield EID O_S^+ ions by the dissociation of strongly bound CO. The energy of desorption of CO from platinum is less than that of most other transition metals, a fact used to explain the observation of CO_S^+ by Huber and Rettinghaus.²⁹ It is estimated that the system used in this work had about 10^{-3} the ion collection efficiency of Huber and Rettinghaus's system. They found the CO_S^+ ion yield to be about 10^{-4} of the H_S^+ ion yield. Since this work found the O_S^+ ion yield to be 10^{-2} of the H_S^+ ion yield, then certainly if the O_S^+ ion came from adsorbed CO, Huber and Rettinghaus would have observed it. Dosing with pure carbon monoxide, Huber and Rettinghaus were not able to detect O_S^+ ions.

The present work indicated that when EID adsorptions were studied, the kinetics of the curves for H_S^+ and O_S^+ coincided within experimental error. In mixtures there was the same peaking and decay phenomenon as was found for H_S^+ . Thermodesorption determinations exhibited identical desorption temperatures for H_S^+ and O_S^+ , as best as could be measured under the limitations of the system.

These observations suggest that the source of the O_S^+ ion is the same as that of the H_S^+ ion. The low magnitude of the O_S^+ ion current made it impractical to study it in the same detail as the H_S^+ ion.

FIGURE 37

Adsorption and Desorption Kinetics of
the H_s^+ and O_s^+ Ion Currents.



ION CURRENT (ARBITRARY UNITS)

TIME, TEMPERATURE →

O^+ ADSORPTION

H^+

ADSORPTION

O^+ DESORPTION

H^+ DESORPTION

For the purpose of comparison, the O+ and H+ curves are vertically offset.

H. Experiments with Formaldehyde

No EID experiments with complex molecules had been published at the time of this work. Since hydrogen and carbon monoxide can form formaldehyde, an experiment with formaldehyde was indicated for obtaining evidence to confirm or compliment the data from hydrogen-carbon monoxide mixtures.

Figure 38 abstracts the salient features of many runs. The formaldehyde decomposed on the hot substrate when it was thermally cleaned. The essential mechanics were that the formaldehyde molecules adsorbed on the hot platinum, then either desorbed or decomposed to hydrogen and carbon monoxide. When the substrate was cooled, the stay time of the adsorbed formaldehyde increased, thus increasing the probability of decomposition. As can be seen in Figure 38, the formaldehyde pressure dropped, owing to adsorption. Simultaneously the hydrogen and carbon monoxide pressures increased during the first six seconds of cool down time of the substrate. The rise in hydrogen pressure, which was measured at mass 2, could be attributed to the cessation of the atomization of hydrogen by the hot substrate. The mass 28 peak, labeled CO on the graph, can be attributed to both CO and CH₂O. Since the mass 30 peak, labeled CH₂O, shows an immediate decline upon cooling, the CO component of mass 28 is responsible for the initial rise. Thus, while the substrate was cooling the efficiency of formaldehyde decomposition increased while the substrate was still too hot to adsorb hydrogen or carbon monoxide. After the substrate was cool both hydrogen and carbon monoxide were adsorbed and the H_S⁺ ion current increased to a peak value then exhibited a decay, similar to the behavior in mixtures of hydrogen and carbon monoxide. After the

decay of the H_S^+ ion current carbon monoxide was evolved approximately in proportion to the adsorption of formaldehyde while the hydrogen pressure continued to decline. Through the entire run formaldehyde was adsorbed. Thermodesorption failed to positively indicate the desorption of formaldehyde. This does not appear to be the case if one observes the rise of the CH_2O curve upon flashing in Figure 38. It is necessary to observe the mass spectrum with rapid scanning during thermodesorption to observe that the mass 29 and 30 peaks are superimposed on the tail of the mass 28 peak. Mass 28 is both carbon monoxide and formaldehyde and with the particular mass spectrometer used it "tailed off" badly toward the high mass side.

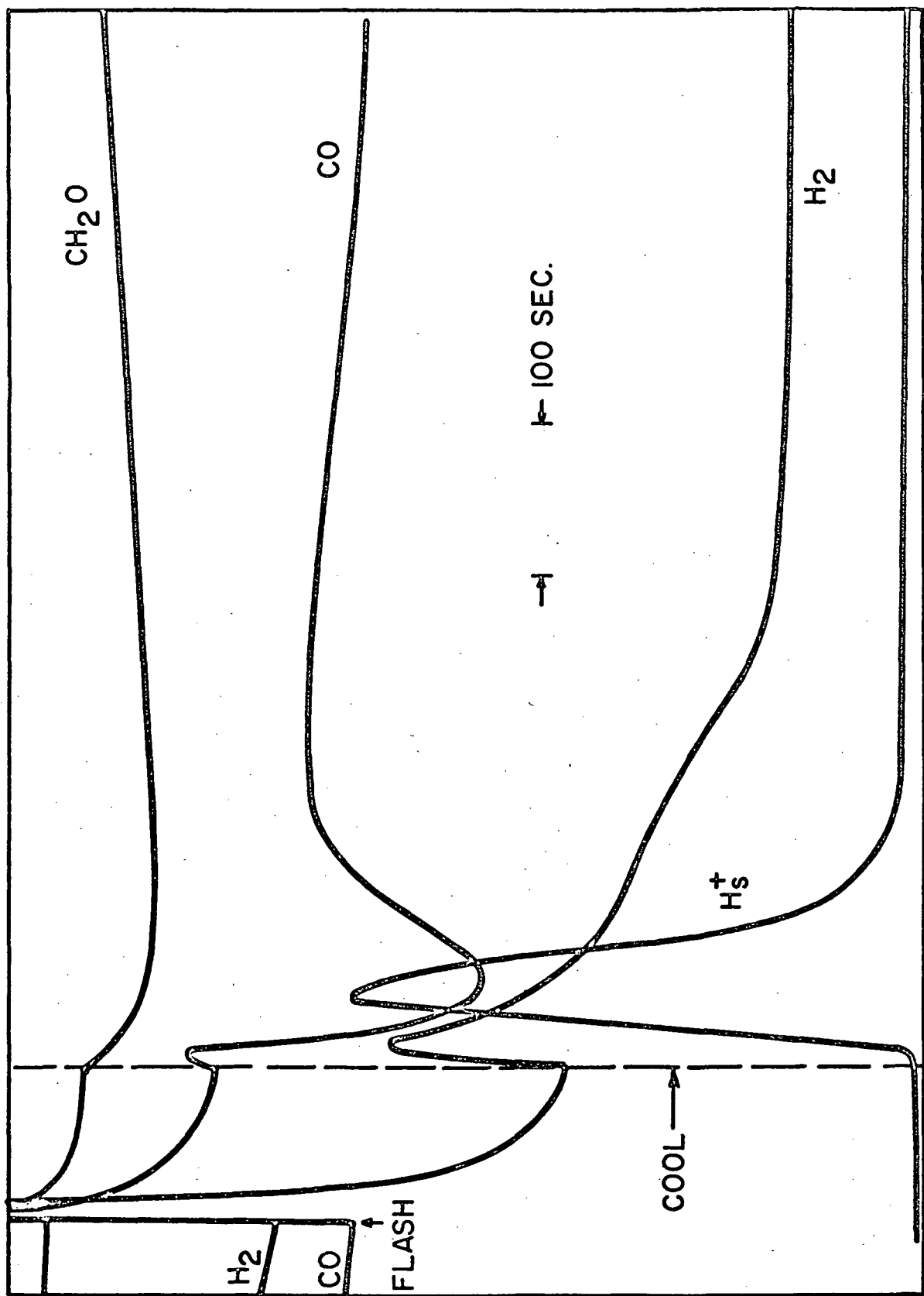
The ion currents of mass 28, 30, and 2 were 11×10^{-9} , 5.5×10^{-9} and 2.1×10^{-9} amp respectively before the substrate was cleaned. If the electron gun filament was turned off, the mass 28 peak was about 1/3 its magnitude when the electron gun was on. This indicated that a considerable amount of formaldehyde was decomposed by the filaments of the electron gun, ionization gauge, and mass spectrometer as well as by the substrate when it was thermally cleaned. This high background of hydrogen and carbon monoxide made experiments with pure formaldehyde impossible.

The effect of electron bombardment was determined by running a plot of H_S^+ ion current versus time with continuous and with intermittent bombardment periods. The two results were identical, indicating that the source of H_S^+ ion is not significantly affected by the electron beam.

The adsorption of formaldehyde throughout the runs, even after the H_S^+ ion current decayed, seemed to indicate that CH_2O is not the

FIGURE 38

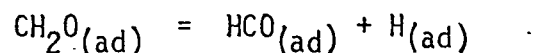
Hydrogen, Carbon Monoxide, Formalde-
hyde and H_2S Adsorption versus Time.



ION CURRENT (ARBITRARY UNITS)

TIME

source of H_S^+ . Partial decomposition of the formaldehyde



is probable considering the observations. This lends strength to the view that $(HCO)^*$ is the source of H_S^+ .

I. Graphical Comparison of Data

The nature of this investigation is such that one needs to view many different data simultaneously in order to analyze and understand the total system. To facilitate this, data from thermodesorption, adsorption and EID studies have been compiled on single graphs rather than presenting them individually in the preceding parts. These compiled data follow.

FIGURE 39

Composite Graphs of Carbon Monoxide, β ,
 γ , and Total Hydrogen Fractional Coverages
and the EID H_S^+ Ion Current versus Time in
a Mixture of 3.3×10^{-8} Torr Hydrogen and
 8.4×10^{-9} Torr Carbon Monoxide (System
"d", Table I).

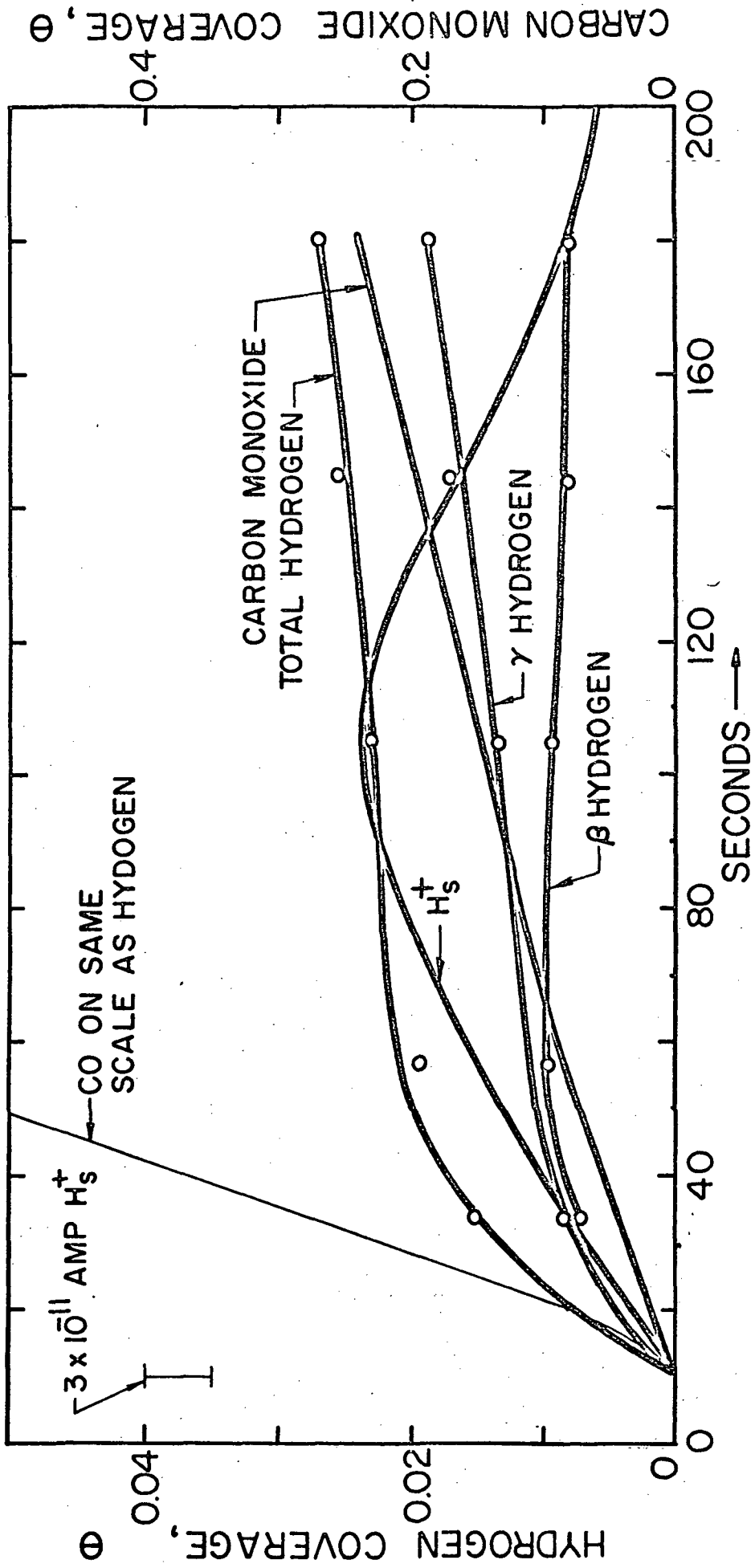


FIGURE 40

Composite Graphs of Carbon Monoxide, β , γ , and Total Hydrogen Fractional Coverages and the EID H_S^+ Ion Current versus Time in a Mixture of 7.7×10^{-8} Torr Hydrogen and 4.9×10^{-9} Torr Carbon Monoxide (System "a", Table I).

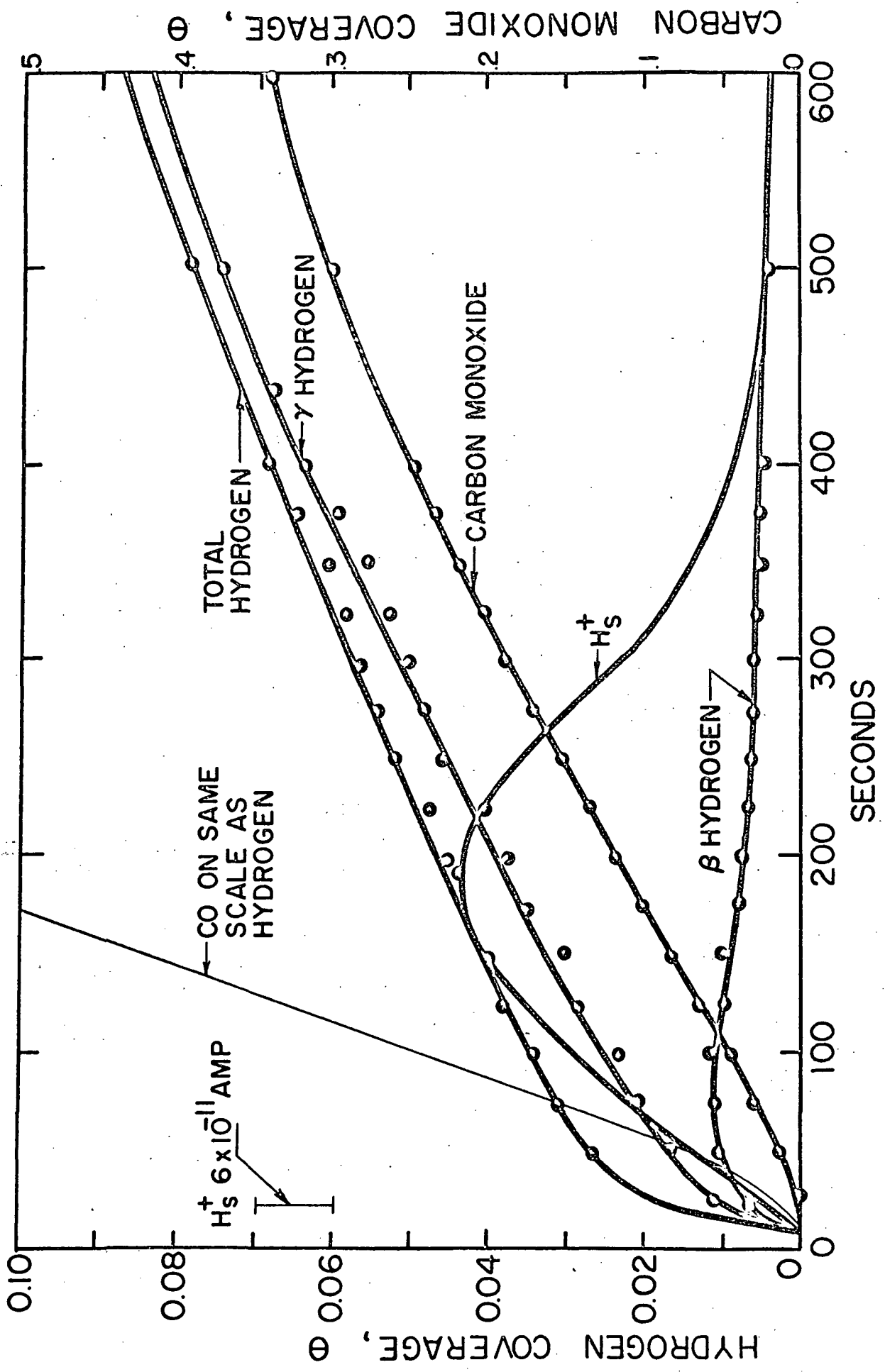


FIGURE 41

Composite Graphs of Carbon Monoxide, β , γ , and Total Hydrogen Fractional Coverages and the EID H_S^+ Ion Current versus Time in a Mixture of 9.5×10^{-8} Torr Hydrogen and 7.5×10^{-9} Torr Carbon Monoxide (System "b", Table I).

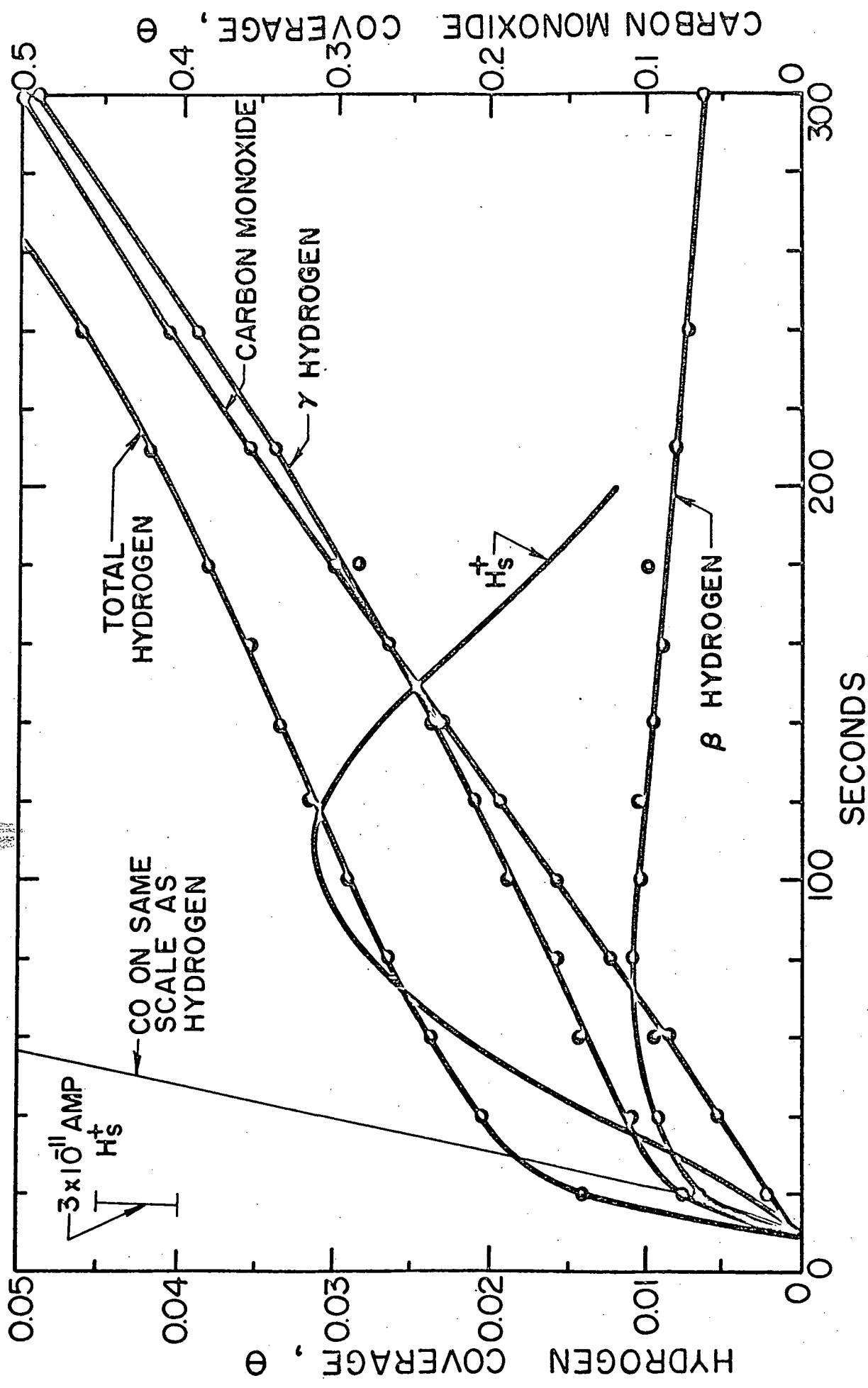


FIGURE 42

Thermodesorption Spectra of Hydrogen
and Carbon Monoxide from a Mixture of
 3×10^{-8} Torr H_2 and 7.8×10^{-9} Torr
CO (System "c", Table I).

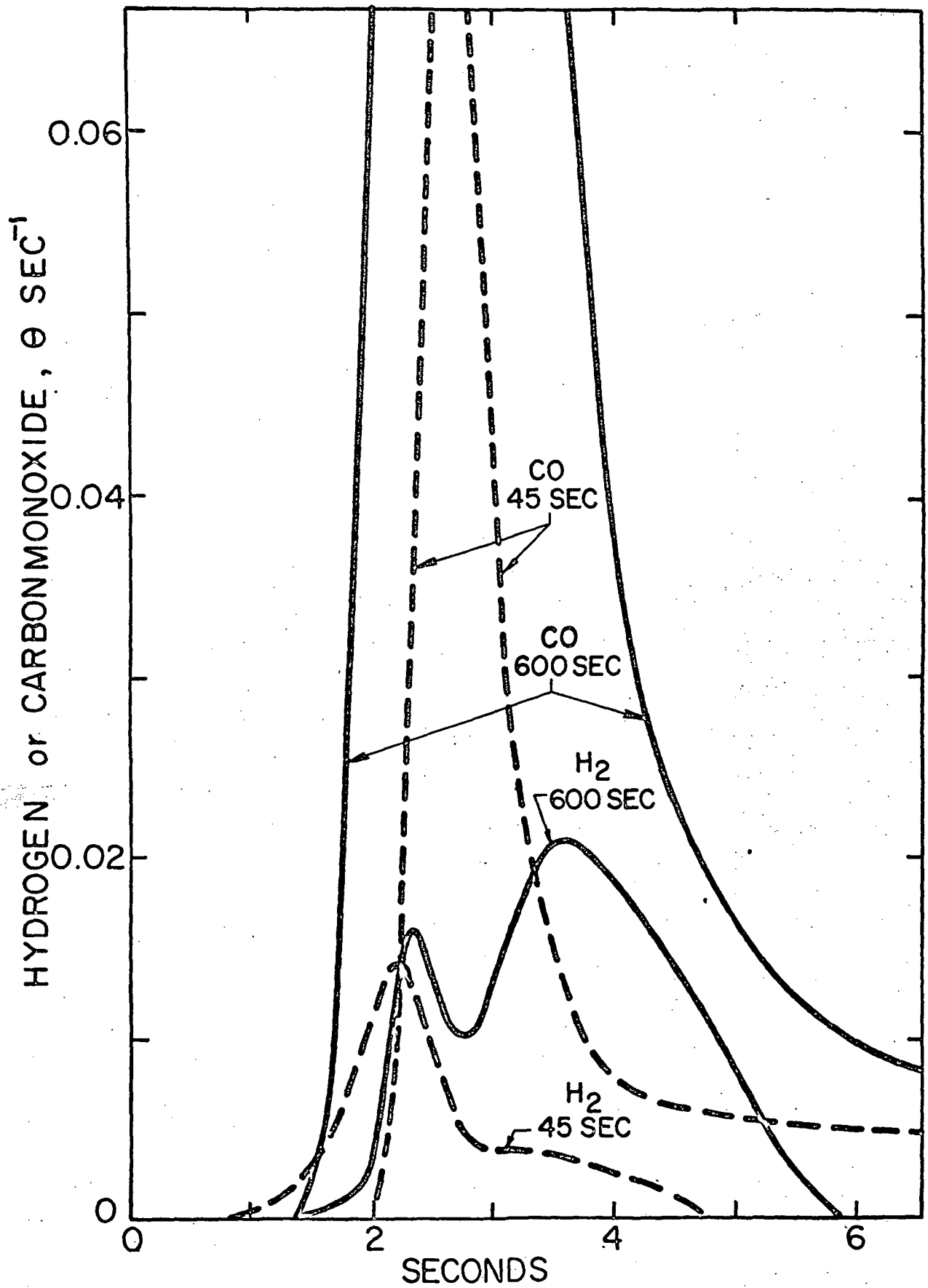


FIGURE 43

Hydrogen, Carbon Monoxide, and H_S^+
Thermodesorption Spectra in a Mix-
ture of 1×10^{-7} Torr H_2 and $3.2 \times$
 10^{-8} Torr CO. The 42 Second Dose
Time Resulted in Maximum H_S^+ Current.

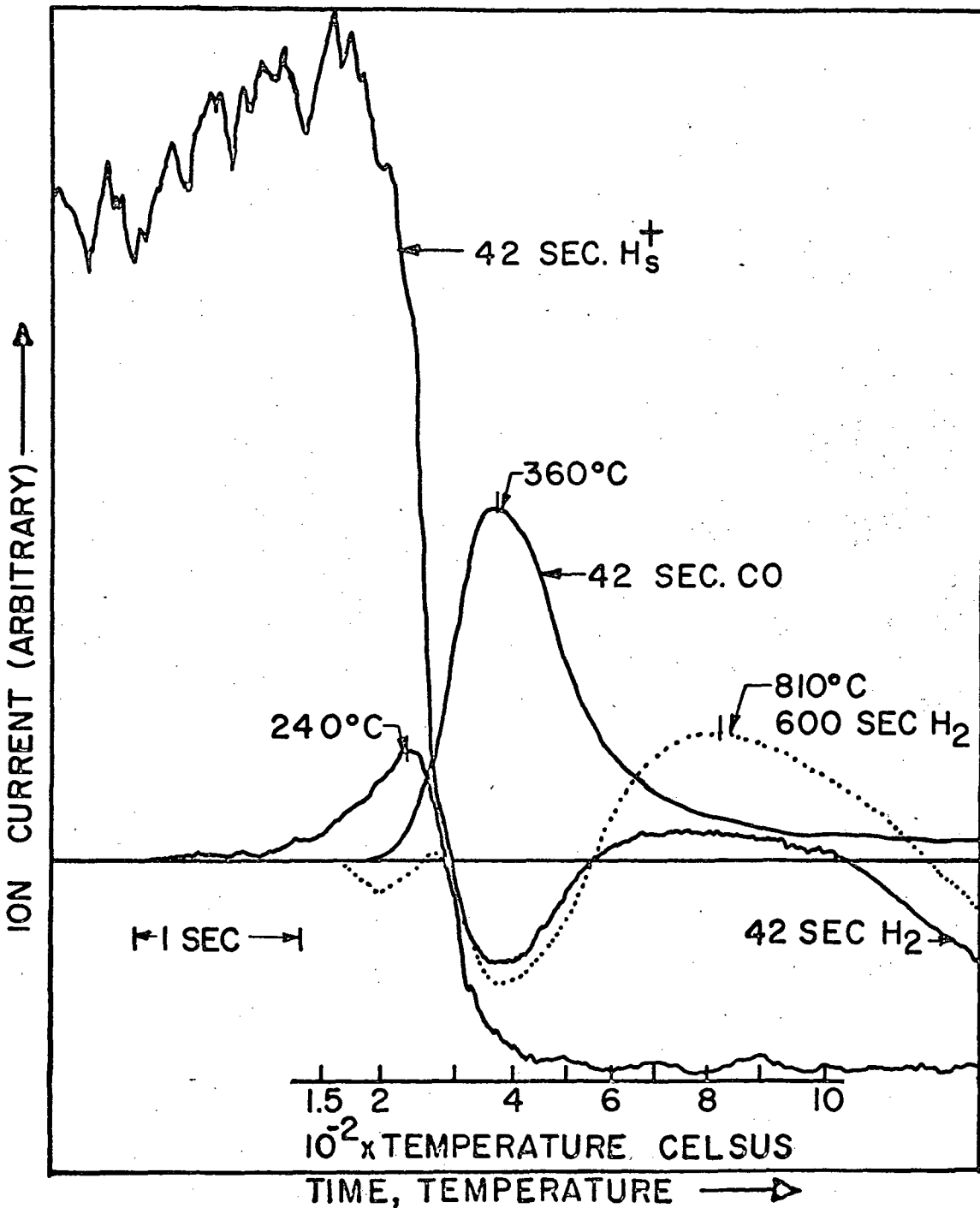
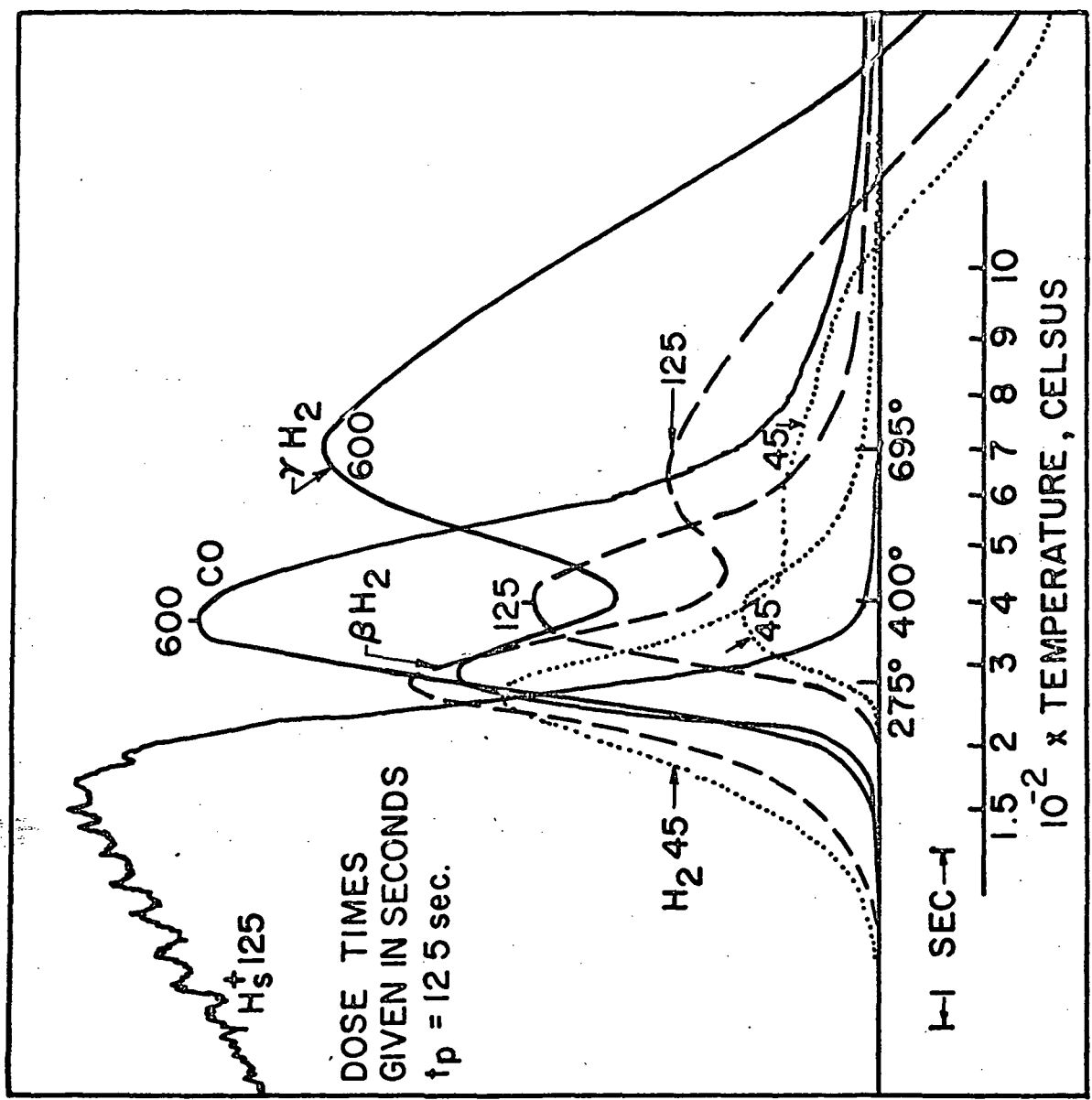


FIGURE 44

Thermodesorption Spectra for Hydrogen,
Carbon Monoxide, and the H_S^+ Ion Current
in a Mixture of 3×10^{-8} Torr H_2 and 7.8
 $\times 10^{-9}$ Torr CO (System "c", Table I).

ION CURRENT —



PART VI
DISCUSSION

A. Chemisorption of Pure Carbon Monoxide

The adsorption and desorption kinetics of carbon monoxide have always been found to be first order. It was not surprising therefore to find that the carbon monoxide coverage data described a smooth curve when plotted versus tP_{CO} as in Figure 9. Verification that the adsorption process was of the first order with respect to the concentration of molecules in the gas phase was shown by Figure 10. The rate of adsorption was linear in the impingement rate and passed through the origin, indicating insignificant evaporation rate during the adsorption process. If the adsorption had been other than first order, then P in the term vP would have to have been taken to a power other than the first to obtain a straight line.⁴⁵

The sticking probability was nearly constant at 0.76 in the range of 0.20 to 0.30 in all determinations. It could not be determined for coverages below 0.20. This constancy, observed on most metals, is interpreted to indicate that physisorption occurs first, followed by either desorption or chemisorption.⁴⁶

Gavrilyuk⁴⁷ has derived a theoretical expression for the sticking probability:

$$s = [c/1 + \exp (E_a/RT)] - [\sigma_c/\tau_0 \exp - (E_d/RT)]$$

where c = physisorption condensation coefficient

E_a = activation energy of adsorption to the chemisorbed state

E_d = activation energy of desorption from chemisorbed state

σ_c = coverage in chemisorbed state

τ_0 = nominal vibration time of an adsorbed molecule

This expression is in good agreement with experimental results of CO on W(113). Assume that E_a is constant at low coverage; then since $\sigma_c = 0$ at $t = 0$, this would predict a constant sticking probability from zero coverage up to the point where the coverage dependent term becomes significant. If we assume that the same principle applies to CO on Pt (111), then it is reasonable to extrapolate the highest s value determined to zero coverage, as shown in Figure 11.

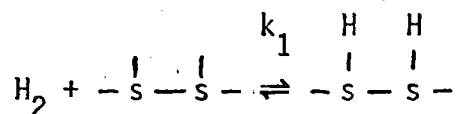
Isotopic exchange measurements by Madey, et al⁴⁸ and field emission studies by Menzel and Bomer⁴³ suggest that the high energy bound state, "Beta CO," of carbon monoxide on tungsten lies flat with both the C and O bonded to tungsten sites. The low energy bound state, "Alpha CO," involves a single bond from carbon to a single metal site. The "Beta CO" state induces the formation of new sites which adsorb CO in the more weakly held "Alpha CO" state.⁵⁰

In this work, only one adsorption state of CO was observed on the Pt (111) surface exposed to pure CO, as shown in Figure 23a. (The term α -CO, used in this paper, refers only to CO adsorbed from pure CO gas and is not related to the "Alpha CO" state referred to in the literature.) The alternative possibility to "Alpha CO" and "Beta CO" states is "Virgin CO" in which the carbon makes two bonds, one to each of two metal sites. Since the maximum coverage determined was one CO per two sites, the adsorption state is either of the "Beta CO" or "Virgin CO" type. The "Virgin CO" state is obtained by dosing at low temperatures, 100^oK. At 270^o-350^oK "Virgin CO" on tungsten either desorbs or converts to "Beta CO." Room temperature dosing of tungsten always produces "Alpha" and "Beta" states.⁴⁹

The presence of only a single adsorption state of CO on Pt (111) at room temperatures together with the occupation of two sites per CO molecule, suggests that carbon monoxide adsorbs on platinum (111) with the "Beta CO" structure in which the CO molecule is lying flat on the surface.

B. Chemisorption of Pure Hydrogen

The chemisorption of hydrogen is usually accompanied by dissociation into the atomic state. Laidler⁵¹ and others have assumed first order hydrogen adsorption on dual sites with simultaneous dissociation



proposing that

$$d\theta/dt = k_1 P_{\text{H}_2} (1 - \theta)^2 \quad (15)$$

where $(1 - \theta)$ is squared to account for dual sites. Integrating equation (15) yields

$$\begin{aligned} d\theta/(1 - \theta)^2 &= k_1 P_{\text{H}_2} dt \\ [1/(1 - \theta)] - 1 &= k_1 P_{\text{H}_2} t \\ \theta &= 1 - [1/(k_1 t P_{\text{H}_2}) + 1] \end{aligned} \quad (16)$$

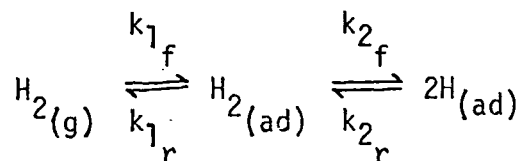
Defining exposure ϵ , as $\epsilon = tP$, which is proportional to Knudsen flow to the surface, this becomes

$$\theta = 1 - [1/(k\epsilon) + 1] \quad (17)$$

so that at constant exposure the coverage is constant. While this may be the case for some metals, it was not found to be true on platinum (111).

If it is assumed that hydrogen is adsorbed molecularly and then undergoes slow dissociation, a different result is obtained. Consider

the consecutive reactions



and assume that:

a) Reaction k_{1f} is faster than k_{2f} , therefore reaction k_{2f} is rate controlling

b) Pair sites are required for H_2 adsorption and therefore sites available to H_2 are $(1 - \theta_{\text{H}})^2$

c) Equilibrium conditions are maintained during adsorption.

It is known that in general, at equilibrium

$$\sigma = s\dot{I}\tau_a = s\nu P_{\text{H}_2} \tau_a$$

where σ = number of adsorbed molecules,

\dot{I} = impingement rate,

ν = specific arrival rate,

τ_a = stay time,

and s = sticking probability.

Assuming rapid equilibrium between the gas phase and dual sites available for hydrogen molecule adsorption,

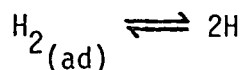
$$\sigma_{\text{H}_2(\text{ad})} = s\nu P_{\text{H}_2} \tau_a (1 - \theta_{\text{H}})^2$$

or

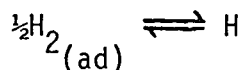
$$\theta_{\text{H}_2(\text{ad})} = s(\nu/\sigma_s) P_{\text{H}_2(\text{g})} \tau_a (1 - \theta_{\text{H}})^2 \quad (17)$$

where θ_{H_2} is the fractional coverage of the substrate by the physisorbed species and the term $(1 - \theta_{\text{H}})$ removes from this area the portion covered by chemisorbed hydrogen atoms. This term must be squared to account for

the requirement of pair sites for hydrogen molecule adsorption. The dissociation of hydrogen is given by



or



so

$$d\theta_H/dt = k_2 (\theta_{H_2})^{\frac{1}{2}}$$

Substituting θ_{H_2} from equation (17)

$$\begin{aligned} d\theta_H/dt &= k_2 s(\theta) [(v/\sigma_s) P_{H_2} \tau_a (1 - \theta_H)^2]^{\frac{1}{2}} \\ &= k_2 s(\theta) [(v/\sigma_s) P_{H_2} \tau_a]^{\frac{1}{2}} (1 - \theta_H) \end{aligned} \quad (18)$$

Integrating:

$$\begin{aligned} d\theta_H/(1 - \theta_H) &= k_2 s(\theta) \{(v/\sigma_s) P_{H_2} \tau_a\}^{\frac{1}{2}} dt \\ -\ln(1 - \theta_H) &= k_2 s(\theta) \{(v/\sigma_s) P_{H_2} \tau_a\}^{\frac{1}{2}} t \\ \theta_H &= 1 - \exp [-k_2 s(\theta) \{(v/\sigma_s) \tau_a\}^{\frac{1}{2}} P_{H_2}^{\frac{1}{2}} t] \end{aligned}$$

It will be noted that the sticking probability is an unknown function of coverage; therefore the equation cannot be properly integrated.

This precludes an analytical fit with the data, however the trend of dependence on various parameters can be predicted. Treating the sticking probability as a constant, and gathering constants:

$$\theta_H = 1 - \exp - (k_2 (P_{H_2})^{\frac{1}{2}} t), \quad (19)$$

or in terms of exposure,

$$\theta_H = 1 - \exp - (k_2 (P_{H_2})^{-\frac{1}{2}} \epsilon). \quad (20)$$

Figures 14, 15, and 17 fit the predictions of these equations when P , t , ϵ , and $(P^{\frac{1}{2}}t)$ are held constant.

The differential form, equation (4), may be written

$$d\sigma/dt = k_2 (vP_{H_2})^{1/2} (1 - \theta_H) \quad (21)$$

predicting the linear relation between $d\sigma/dt$ and $(vP_{H_2})^{1/2}$ at constant coverage as shown in Figure 16.

Hydrogen was thus found to adsorb by half order kinetics to a maximum coverage of 0.200, assuming one hydrogen atom per platinum site. This value may well not be the maximum possible, since carbon monoxide impurity interfered, as other workers have found.⁵² The proposed two step adsorption reaction is also in agreement with recent FEM studies by Lewis and Gomer.²⁷ They found that at 300°K to 500°K H₂ was not rapidly accommodated but diffused great distances before being dissociatively chemisorbed.

A few percent of carbon monoxide or methane had little effect on the initial rate of adsorption at short dose times but a very great effect was noted at the longer times required for significant hydrogen coverage. The low initial sticking probability of 7.5×10^{-3} and the even lower probability at higher coverages aggravated the problem of obtaining a high coverage of hydrogen before competition for sites by carbon monoxide set in.

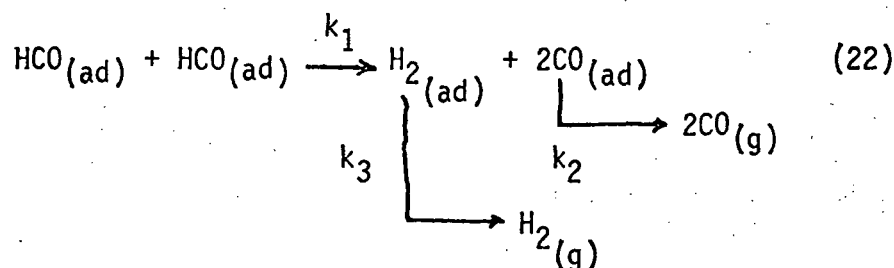
A problem peculiar to hydrogen may be observed in Figure 13. At high temperatures, the pressure declined below the equilibrium value. Wiesendanger attributed this to dissociation of hydrogen molecules on hot substrates. Since the mass spectrometer was set to mass 2 the reduction of H₂ pressure is easily noted. This phenomenon is also observable with an ionization gauge because the system walls adsorb the atomic hydrogen readily.²⁸

C. The Interaction of Adsorbed Hydrogen
and Carbon Monoxide

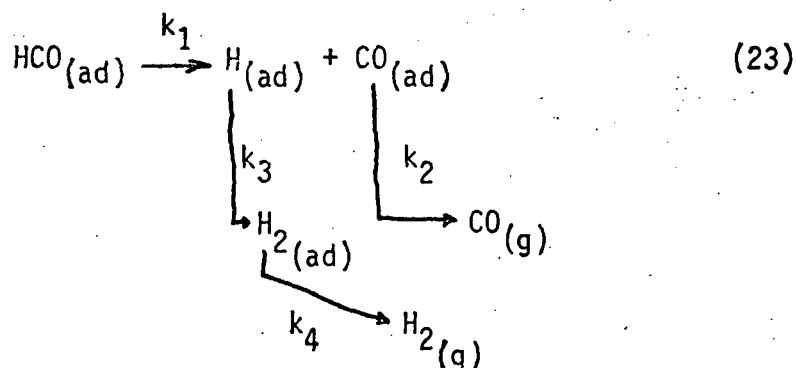
Hydrogen has little effect on the initial coverage of carbon monoxide, as was seen in Figure 12. This is also evident from the initial sticking probabilities of 0.76 in pure CO and 0.68 in hydrogen-carbon monoxide mixtures. These values are not accurate to better than 10%, thus they could be identical.

The relative effect of hydrogen and carbon monoxide upon one another can be noted by comparing the data at $t(P_{H_2})^{\frac{1}{2}} = 2 \times 10^{-2}$ in Figure 21 with the equivalent range of $tP_{CO} = 0.92 \times 10^{-6}$ to 0.35×10^{-6} in Figure 12. (This is the range of tP_{CO} values for which $t(P_{H_2})^{\frac{1}{2}} = 2 \times 10^{-2}$.) The adsorption of carbon monoxide deviates from the pure carbon monoxide values only slightly while the adsorption of hydrogen in mixtures deviates significantly from that in the pure gas. Higher hydrogen coverages, about $\geq 0.05\theta$, have sufficient influence to limit carbon monoxide adsorption to about one half the coverage in the pure state. This effect is greater than can be explained by competition for sites. This reduction of carbon monoxide coverage in the presence of hydrogen is in contrast to the behavior on zinc alloy at 200 Torr where hydrogen and carbon monoxide mutually enhance the adsorption of one another, forming a species of stoichiometric formula CH_3O .⁵³ It should be noted that this mutual enhancement occurs on methanol synthesis catalysts which are sp metals or alloys of sp metals or basic metal oxide mixtures. Platinum, being a transition metal, is a d metal and is a well known dehydrogenating catalyst.^{54,55} The formation of CH_3O would therefore not be expected.

The effect of hydrogen on the carbon monoxide thermodesorption spectra was shown in Figure 23. An analytical determination of desorption kinetics was not possible due to inadequate accuracy and reproducibility of the temperature programmer. In theory the desorption kinetics could have been estimated from thermodesorption peak shapes, but this is considered tenuous in practice. An adequate comparison could be made, however, to surmise that the desorption kinetics of carbon monoxide in mixtures was other than first order. Considering carbon monoxide alone, this would be difficult to explain, however, postulating that hydrogen and carbon monoxide combined to form a surface complex, the CO thermodesorption spectra would be the result of the decomposition of that complex, and not the desorption of isolated CO molecules. The reaction may be proposed:



If k_1 is the rate limiting step, then second order desorption of both hydrogen and carbon monoxide would be apparent. Another possibility is the unimolecular decomposition of HCO:

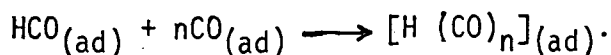


This could appear as first, second, or mixed order, according to the values of the rate constants.

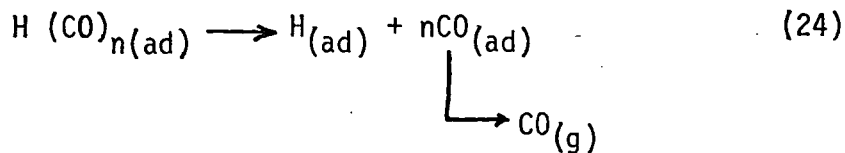
The carbon monoxide desorption spectra in mixtures exhibited two desorption peaks, labeled β -CO and γ -CO, whose T_p values were below and above that of α -CO from pure CO exposure. At higher pressures it was difficult to resolve these peaks, probably because all three occurred. It is probable that β -CO and γ -CO are not the result of desorption of isolated CO molecules but rather the result of surface reactions during thermodesorption, such as equations (22) and (23).

One of the difficulties of thermodesorption studies is the speculative nature of the interpretations, particularly if the desorbed gas is not the species that was on the cold surface, but a decomposition product of a surface species. Here we have a case where EID studies can clarify the results of thermodesorption studies, or at least eliminate some of the speculative possibilities. As was seen in section V F, the isothermal decay of the H_s^+ ion signal is first order. If it is assumed that the H_s^+ ion signal comes from a surface complex of hydrogen and carbon monoxide $(HCO)^*$ (this will be discussed later), then reaction (22) must be eliminated as a possibility. Reaction (23) could be first order in the decomposition of $(HCO)^*$ while being of higher order with respect to the desorption of carbon monoxide.

As will be discussed later, there is support for the formation of a higher order complex of hydrogen and carbon monoxide,



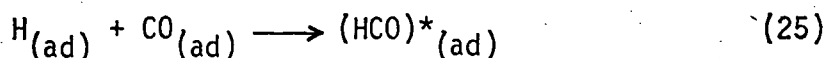
The decomposition of $[H(CO)_n]_{(ad)}$ would require more energy than the decomposition of (HCO) , so the reaction



is attributed to the higher energy γ -CO peak, and reaction (23) is assigned to the lower energy β -CO peak.

Electron induced desorption of surface species resulted mostly in H_S^+ ions with a low yield of O_S^+ ions. The O_S^+ ion current exhibited the same behavior as the H_S^+ ion current indicating that the two originated from the same source. The rate of increase of H_S^+ ion current was proportional to the carbon monoxide pressure when hydrogen was present in excess, as described in section V D2. The H_S^+ ion current was also proportional to the hydrogen dose, $t(P_{\text{H}_2})^{1/2}$, when carbon monoxide was present in excess on the surface, related in section V D3.

This led to the hypothesis that the H_S ion came from a surface complex, $(\text{HCO})^*$, where the asterisk indicates an EID active species. These observations suggest the possible equilibrium reaction



If hydrogen is present in excess, then the quantity of $(\text{HCO})^*$ will be dependent on the quantity of carbon monoxide. If carbon monoxide is present in excess, then the quantity of $(\text{HCO})^*$ will be dependent on the quantity of hydrogen.

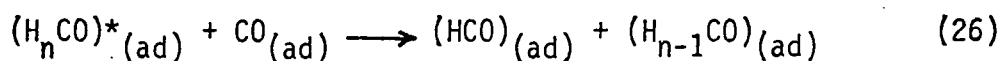
When a clean substrate was introduced to a mixture of hydrogen and carbon monoxide, the H_S^+ ion current increased, peaked, and exponentially decayed. (See Figures 39, 40, and 41) The initial rate of rise was proportional to the square root of hydrogen pressure, indicating that hydrogen adsorption was involved in producing the EID active species. The decline in the H_S^+ ion current had a time constant inversely pro-

portional to the carbon monoxide pressure, as can be seen in Figure 31.

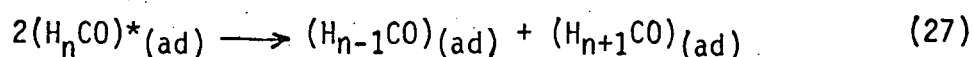
This is interpreted to mean that carbon monoxide is involved in the elimination of the H_s^+ ion current as well as in its production.

There are two basic possible reasons for a decrease of an EID signal: a) a reduction in the population of the species and b) a change in the nature of the bonding of the species to the surface. An adsorbate is attached to the surface by London dispersion forces, covalent bonding, electrostatic bonding, or a combination of these. In the case of chemisorption, measurements of surface potential difference or work function changes, suggest that an adsorbate, by donating or accepting electrons, changes the electronic density around its site. This influence extends out several sites away.⁵² Thus, the nearest neighbor site to an adsorbed species will have altered electronic structure and may bond to an adsorbate differently. If this alteration is such as to increase its binding energy, thus decreasing the adsorbate-adsorbent distance, then Auger neutralization of any EID ion formed will increase, consequently decreasing the EID yield, or cross section.³³

If the surface complex contains more than one hydrogen, $(H_nCO)^*(ad)$, then the population of the species can be reduced by the reaction

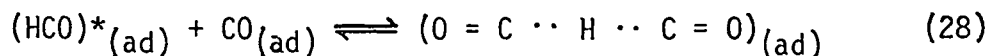


This would indicate that (HCO) is not the species producing H_s^+ ions. Since platinum is a dehydrogenating catalyst, formation of (H_nCO) is less likely than formation of (HCO) . This is also indicated by increased rate of decomposition of formaldehyde when the substrate was cooled. One could also propose a disproportionation reaction

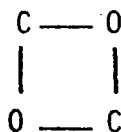


however, the rate of reaction would not be a function of carbon monoxide pressure.

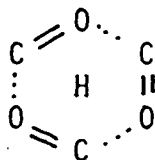
Assuming the EID active species to be $(\text{HCO})^*$, its concentration could be reduced by interaction with carbon monoxide:



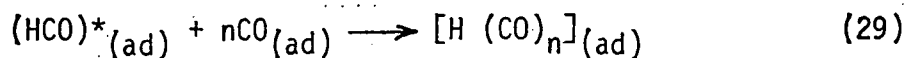
This fits the kinetic requirements of a reaction involving carbon monoxide that removes $(\text{HCO})^*$. The product contains hydrogen that would be bound to the surface more strongly than hydrogen in $(\text{HCO})^*_{(\text{ad})}$. This "tying down of the hydrogen" action can be carried further. It is known that adsorbed CO molecules can interact with the carbon of one molecule bonding to the oxygen of another.⁵⁰ The surface structure



is believed by Yates and Madey to be responsible for the exchange of oxygen isotopes when CO is adsorbed on tungsten. It is also well recognized that a six member ring is unusually stable and is frequently an intermediate structure in reactions. This leads to the extreme possibility of the structure



where the bonding of hydrogen is not specified. Such a structure is certainly hypothetical. The reaction of equation (28) however, should be modified to



to account for the possible subsequent steps.

Figure 33 presented a plot of $H_S^+ / t(P_{H_2})^{1/2}$ versus tP_{CO} . The quotient $H_S^+ / t(P_{H_2})^{1/2}$ should be constant if adsorbed hydrogen is the H_S^+ producing species. This could be interpreted as a reduction in cross section resulting from the influence of carbon monoxide. If adsorbed carbon monoxide was reducing the cross section by associating with the hydrogen, one would expect the decline to begin immediately, especially since this entire curve is in the region of linear carbon monoxide adsorption at its highest sticking probability and the CO coverage is considerably greater than the hydrogen coverage. Alternatively if the H_S^+ producing species is formed from hydrogen and carbon monoxide, then the concentration of $(HCO)^*$ would increase, as seen in the plots of H_S^+ versus time. Since this is now being normalized with respect to hydrogen, the term should remain constant, as it does for a considerable time. The decrease in $H_S^+ / t(P_{H_2})^{1/2}$ now must be regarded as the result of a decrease in $(HCO)^*$ population, which could have been effected by the association or combination of $(HCO)^*$ with CO, as described in equation (29) producing an EID inactive species.

The thermodesorption spectra of hydrogen from mixtures of hydrogen and carbon monoxide (Figure 20) indicated that hydrogen filled a low energy bound state first, then filled and transferred to a high energy bound state. If it were assumed that the hydrogen gas desorbed came from isolated adsorbed hydrogen atoms, then interpretation would be difficult indeed. It is generally accepted that in the case of multiple binding states, the high energy state fills first, followed by the lower energy states.

It is more reasonable to assume that the desorption spectra originated with surface reactions involving hydrogen containing species,

especially since these "multiple state" spectra were only obtained when carbon monoxide was present on the surface. Thus it will be assumed that an adsorbed hydrogen atom adjacent to an adsorbed carbon monoxide molecule, interacts with it. For simplicity, and as a starting point, the first stage of interaction was symbolized as $(\text{HCO})^*$, and was considered to be the EID active species.

Making a comparison of the EID flash results with the hydrogen (in mixture) thermodesorption spectra, as shown in Figure 44, we see that the H_S^+ ion current decays at a temperature corresponding to the βH_2 peak. It was stated previously that the αH_2 thermodesorption peak was not necessarily different from the βH_2 peak. This possibility had to be acknowledged because the temperature ranges overlap and a specific assignment of a T_p cannot be made in the case of second order thermodesorption. The α hydrogen is adsorbed atomic hydrogen, not associated with anything. It is proposed that β hydrogen is adsorbed atomic hydrogen associated with carbon monoxide. As seen in Figure 44, at low dosages, there is a component of the β peak that begins desorption at low temperatures. As the dosage increased the peak shifts to higher temperatures and the starting temperature shifts upward to the starting temperature of the H_S^+ desorption, which was essentially constant. This upward shift of starting temperature with increasing coverage is not characteristic of first or higher order desorption. Now if the initial stage of desorption of the β peak consisted of an α hydrogen component, this anomaly would be elucidated. In the early stages of adsorption a significant amount of unassociated atomic (α) hydrogen was present and upon desorption revealed itself as the initial rise in the β peak. At longer dose times, more carbon

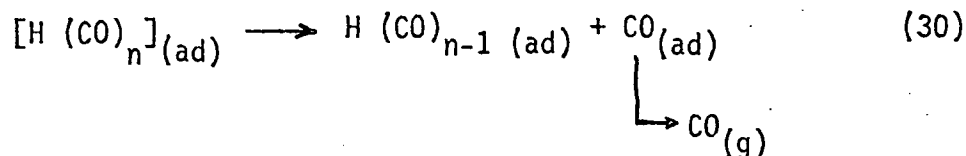
monoxide was on the surface and more hydrogen was associated into (HCO)* leaving less in the α state. This resulted in less α component and more β component in the first desorption peak. As the β component increased, the temperatures of βH_2 desorption and H_s^+ desorption approached a common value.

The identification of the β hydrogen peak with the proposed EID H_s^+ ion producing species (HCO)* posed the problem that $\theta_{\beta\text{H}_2}$ does not follow the H_s^+ ion current upon adsorption. It must be recognized that the H_s^+ ion current was measured upon adsorption, while $\theta_{\beta\text{H}_2}$ was deduced from desorption measurements. It is established that species in a low energy binding state can undergo transition to a higher energy state during the thermodesorption process.² In other words, the thermodesorption technique failed to provide accurate coverage data for each surface species. The H_s ion current therefore, is presumed to indicate the relative surface coverage of the β hydrogen producing species.

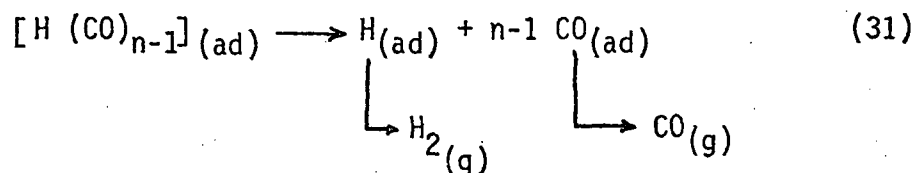
The high temperature desorption peak of hydrogen, (γ), probably results from a higher degree of hydrogen-carbon monoxide association, $[\text{H}(\text{CO})_n]$ as proposed in equations (24) and (29). Although the T_p for γ hydrogen is greater than that of γ carbon monoxide, Figure 42, which has been drawn so that equal areas under any curve represent equal coverages, revealed that the coverage of carbon monoxide is greater than that of hydrogen throughout desorption.

In addition to a heterogeneous surface we must consider that various reactions of unknown nature are occurring upon thermodesorption, as revealed by the "pumping peaks." This phenomena could be explained by the "ideal site" theory or by surface rearrangements, a more comprehensible concept that seems to have more credibility. Taking these con-

siderations into account, it is quite possible for reaction (24) to occur over a wide range of temperatures with the major fraction giving the peak of the carbon monoxide desorption by

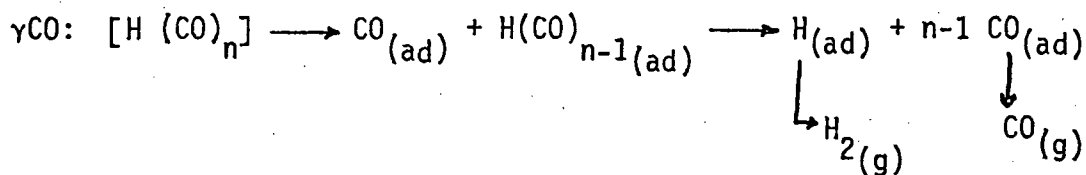
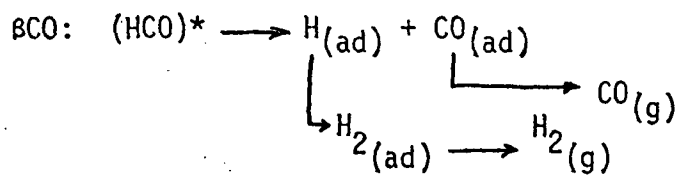


and the remainder decomposing to give the hydrogen peak and the carbon monoxide tailing

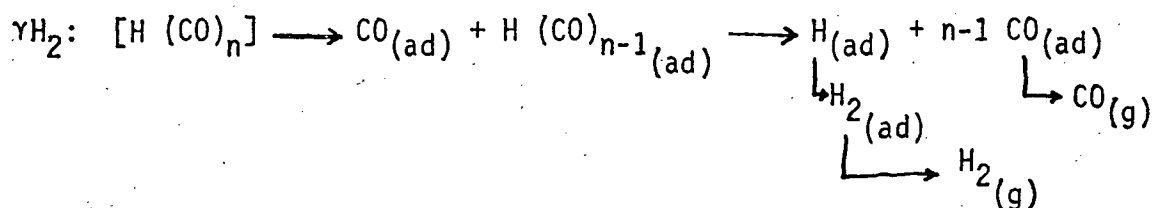
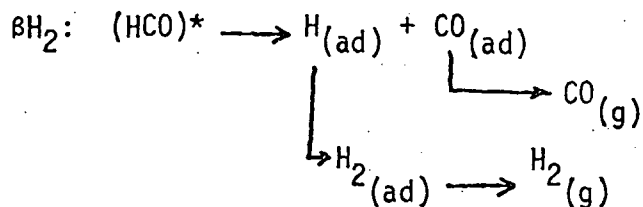


In summary, when the EID studies are combined with the thermodesorption studies, the assignments made to the thermodesorption spectra are:

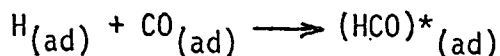
α CO: pure CO desorption



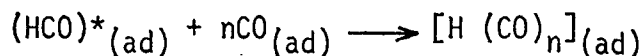
α H₂: pure H₂ desorption



The formation of the EID H_S ion producing species is probably



and the destruction of the EID species upon further adsorption reactions is probably



in addition to the influence on cross section of induced heterogeneity.

When the adsorption of hydrogen and carbon monoxide are compared with the EID H_S^+ adsorption spectra an overall pattern of interaction can be seen. The adsorption of carbon monoxide causes immediate deviation of hydrogen adsorption from that in the pure state (Figure 2]) while causing an increase in H_S^+ flux owing to association with the hydrogen (Figure 3] and equation 25). At a time called t_p the rate of formation of $(HCO)^*$ is equalled by a second reaction, removing $(HCO)^*$ (equation 29). Also at this time the adsorption rate of carbon monoxide starts deviating from that of pure CO (Figure 12) as $H(CO)_n$ is formed. This suggests that the electronic interaction of CO with the substrate is such as to inhibit the adsorption of hydrogen. Since CO combines with adsorbed atomic hydrogen the inhibition reaction would have to be an interaction of either CO or $(HCO)^*$ with physisorbed hydrogen molecules diffusing along the surface. The product of the second stage of interaction causes an inhibition of the adsorption of carbon monoxide. This could be either by electronic effect or by competition for sites, since the $H(CO)_n$ structure would have a different steric effect than the CO molecule alone.

PART VII

CONCLUSIONS

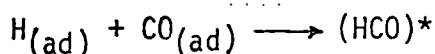
A. Summary of Results

The adsorption of carbon monoxide on platinum (111) has been found to obey first order kinetics with a sticking probability of 0.76. The maximum coverage of CO was one half the number of sites, suggesting that each CO molecule is bound to two surface sites.

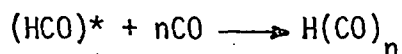
The adsorption of hydrogen on platinum (111) has been found to obey half order kinetics. The behavior obeyed a two step adsorption process, confirming Lewis and Gomer's FEM studies of physisorption as hydrogen molecules followed by slow dissociative chemisorption. The maximum sticking probability found was 7.5×10^{-3} and the maximum observed coverage was $0.2\theta_H$.

The coadsorption of hydrogen and carbon monoxide was found to result in attenuated adsorption of each gas. This did not appear to be mutual, but rather carbon monoxide or a reaction product of hydrogen and carbon monoxide (HCO)*, reduced the rate of hydrogen adsorption while a second reaction product $H(CO)_n$, appeared responsible for the attenuation of carbon monoxide adsorption.

The electron induced desorbed H_S^+ ion was found to originate from a hydrogen-carbon monoxide surface complex. It was accompanied by EID O_S^+ ion emission that duplicated the H_S^+ ion characteristics. The behavior of the EID H_S^+ ion current elucidated some surface reactions that occurred during thermodesorption. During coadsorption the reaction



produced the source of the H_S^+ and O_S^+ ions and the reaction



resulted in the destruction of the EID active species. The H_S^+ ion current was, therefore, a proportional measure of the surface concentration of a reaction intermediate.

B. Significance of Work

The EID phenomenon has been used before to elucidate thermodesorption results when wall effects were interfering. In this work however, it has been shown to be invaluable in the interpretation of surface reactions occurring during thermodesorption. It was also discovered that the H_S^+ ion signal is a measure of the concentration of a surface complex, $(HCO)^*$, indicating that the EID phenomenon can be used to study reaction intermediates. Techniques for observing reaction intermediates are sorely needed in the field of catalysis and it is indicated that this technique should be explored further in systems involving complex chemical species.

The discovery of the "EID observation of isothermal desorption" technique opens a new avenue of approach to determining the activation energy of desorption or decomposition of surface species. In this work, the H_S^+ ion current resulted from a molecular surface species $(HCO)^*$, thus the energy of decomposition was obtained. This could not have been done by gas phase measurements as the decomposition products might not have desorbed. Other systems in which the EID signal is the result of a single species such as H, O, CO, etc. could well utilize the isothermal desorption technique for stay time and energy of desorption determinations. Not only is the problem of non-ideal temperature programming obviated but problems caused by walls adsorb-

ing the desorbed gas are also eliminated since only surface concentration is being measured. The credit for this idea should be given to Dr. J. B. Hudson.

In summary, this research has established a new experimental technique, extended the utility of an old technique, implicating its unused potential, and obtained some useful scientific and engineering data.

PART VIII

L I T E R A T U R E C I T E D .

1. J. A. Becker and C. D. Hartman, *J. Phys. Chem.* 57, 156, (1953).
2. P. A. Redhead, *Trans. Faraday Soc.* 57, 641 (1961).
3. P. A. Redhead, *Vacuum* 12, 203 (1962).
4. D. Menzel, *Surf. Sci.* 14, 340 (1969).
5. A. W. Smith and S. Aranoff, *J. Appl. Phys.* 32, 411 (1961).
6. J. A. Dempster, *Phys. Rev.* 11, 316 (1918).
7. Y. Ishidawa, *Rev. Phys. Chem. Japan* 15, 83 (1942).
8. R. H. Plumlee and L. P. Smith, *J. Appl. Phys.* 21, 811 (1950).
9. D. Lichtman, *J. Vac. Sci. Technol.* 2, 70 (1965).
10. J. R. Young, *J. Appl. Phys.* 31, 921 (1960).
11. G. E. Moore, *J. Appl. Phys.* 32, 1241 (1961).
12. D. A. Degras, L. A. Petermann and A. Schram, *Natl. Symp. Vacuum Technol., Trans.* 9, 497 (1962).
13. L. A. Peterman, "Gas Desorption Efficiency Under Electron Bombardment" (2nd International Symposium on Residual Gases in Electron Tubes, Milan, Italy, 1963).
14. P. Marmet and J. D. Morrison, *J. Chem. Phys.* 36, 1238 (1962).
15. W. D. Davis, *Natl. Symp. Vacuum Technol., Trans.* 9, 363 (1962).
16. P. A. Redhead, *Vacuum* 13, 253 (1963).
17. P. A. Redhead, *Can. J. Phys.* 42, 886 (1964).
18. D. Menzel and R. Gomer, *J. Chem. Phys.* 41, 3311 (1964).
19. C. W. Tucker, Jr., *Surf. Sci.* 2, 516 (1964).
20. A. E. Morgan and G. A. Somorjai, *Surf. Sci.* 12, 405 (1968).
21. R. Lewis and R. Gomer, *Nuovo Cimento Suppl.* 5, 506 (1967).
22. T. Sugita, S. Ebisawa, and K. Kawasaki, *Surf. Sci.* 11, 159 (1968).
23. R. P. Eischens, W. A. Pliskin and S. A. Francis, *J. Chem. Phys.* 22, 1786 (1954).

24. G. C. Bond, "Catalysis by Metals" Academic Press, London, 1962.
25. P. O. Hayward and B. M. W. Trapnell, "Chemisorption" Butterworths, London, 1964.
26. J. C. P. Mignolet, J. Chem. Phys. 54, 19 (1957).
27. R. Lewis and R. Gomer, Surf. Sci. 17, 333 (1969).
28. H. U. D. Weisendanger, J. Cat. 2, 538 (1963).
29. W. K. Huber and G. Rettinghaus, J. Vac. Sci. Technol. 7, 289 (1970).
30. R. A. Pasternak and H. U. D. Wiesendanger, J. Chem. Phys. 34, 2062 (1961).
31. D. Lichtman, F. N. Simon and T. R. Kirst, Surf. Sci. 9, 325 (1968).
32. D. P. Williams and R. P. H. Gasser, Surf. Sci. 25, 265 (1971).
33. T. E. Madey and J. T. Yates, Jr., J. Vac. Sci. Technol. 8, 525 (1971).
34. P. A. Redhead, Nuovo Cimento Suppl. 5, 586 (1967).
35. C. K. Crawford and C. E. Woodward, Tech. Report 175, Laboratory for Insulation Research, M.I.T. Nov. 1962.
36. J. R. Pierce, "Theory and Design of Electron Beams" Van Nordstrand, N. Y., 1949.
37. V. E. Cosslett, "Introduction to Electron Optics" Oxford, 1950.
38. G. E. Moore, S. Datz and E. H. Taylor J. Cat. 5, 218 (1966).
39. R. Lewis and R. Gomer, Surf. Sci. 12, 157 (1968).
40. H. B. Lyon and G. A. Somorjai, J. Chem. Phys. 46, 2539 (1967).
41. Y. Ebisuzaki, W. J. Kass and M. O'Keefee, J. Chem. Phys. 49, 3329 (1968).
42. D. P. Smith, "Hydrogen in Metals" University of Chicago Press, 1948.
43. J. L. Robins, W. K. Warburton and T. N. Rhodin, J. Chem. Phys. 46, 665 (1967).
44. D. Menzel, Surf. Sci. 14, 340 (1969).
45. G. Ehrlich, J. Chem. Phys. 34, 29 (1961).
46. P. A. Redhead, J. P. Hobson and E. V. Kornelsen, "The Physical Basis of Ultrahigh Vacuum" Chapman and Hall, N. Y. (1968).

47. V. M. Gavriilyuk, Proc. Acad. Sci. USSR: Phys. Chem. Section 141, 938 (1961).
48. T. E. Madey, J. T. Yates and R. C. Stern, J. Chem. Phys. 42, 1372 (1965).
49. D. Menzel and R. Gomer, J. Chem. Phys: 41, 3329 (1964).
50. T. E. Madey and J. T. Yates, J. Vac. Sci. Technol. 8, 525 (1971).
51. K. J. Laidler, "Chemical Kinetics," McGraw Hill, N. Y., 1965.
52. R. Culver, J. Pritchard and F. C. Tompkins, Z. Elektrochim. 63, 741 (1959).
53. S. Tsuchiya and T. Shiba, J. Cat. 4, 116 (1965).
54. A. A. Balandin, Adv. Catalysis 10, 96 (1958).
55. J. H. Sinfelt, H. Hurwitz and R. A. Shulman, J. Phys. Chem. 64, 1559 (1960).

APPENDIX B

Kinetics of the Reaction of Oxygen with Clean and
Sulfur Pre-Contaminated Nickel
Single Crystal Surfaces

by

Paul H. Holloway

KINETICS OF THE REACTION OF OXYGEN WITH CLEAN AND WITH
SULFUR PRE-CONTAMINATED NICKEL SINGLE CRYSTAL SURFACES

by

Paul H. Holloway

A Thesis Submitted to the Graduate

Faculty of Rensselaer Polytechnic Institute

in Partial Fulfillment of the

Requirements for the Degree of

DOCTOR OF PHILOSOPHY

Major Subject: Materials Science

Approved by the
Examining Committee:

John B. Hudson, Thesis Advisor

George S. Ansell, Member

Russell J. Diefendorf, Member

David J. Duquette, Member

Philip M. Zaretski, Member

Rensselaer Polytechnic Institute
Troy, New York

, August 1972

(For graduation June 1973)

TABLE OF CONTENTS

	Page
List of Tables.....	v
List of Figures.....	vi
Acknowledgement.....	xi
Abstract.....	xii
I Introduction.....	1
II Electron Interactions with Adsorbates and Adsorbents...	4
(A) Elastically Scattered Electrons (LEED).....	6
(B) Inelastically Scattered Electrons.....	13
(C) Electron Induced Desorption.....	20
III Historical Review.....	24
(A) Clean Surfaces.....	24
(B) Results for Oxygen on Clean Nickel Surfaces.....	27
(C) Summary of Oxygen Interacting with Clean Nickel.....	38
(D) Surface Reactions on Pre-Contaminated Surfaces..	40
(E) Statement of the Problem.....	41
IV Experimental Equipment and Procedure.....	43
(A) Vacua and Specimen Chamber.....	43
(B) Substrate Configuration and Temperature Control.....	47
(C) Experimental Techniques.....	50
(D) Ion Bombardment.....	66
(E) Data Collection Techniques.....	68
(F) Analytical Definitions.....	71
V Results.....	73
(A) Oxygen on Clean (100) Nickel Surfaces.....	73
(B) Oxygen on Clean (111) Nickel Surfaces.....	114
(C) Oxygen on Nickel (111) Pre-Contaminated with Sulfur.....	125

VI Discussion.....	137
(A) Oxygen on Clean Nickel Surfaces.....	137
(B) Oxygen/Sulfur Surface Reaction.....	190
(C) Future Efforts.....	197
VII Summary.....	200
VIII Literature Cited.....	206
IX Appendix I.....	215

LIST OF TABLES

		Page
Table 1	Surface structures due to oxygen on nickel as determined by LEED.....	29
Table 2	Mass spectrometer peak heights of various gases relative to oxygen peak height.....	53
Table 3	Average selected nickel, oxygen, carbon, and sulfur AES peak heights for clean, sulfur saturated, and oxygen saturated surfaces.....	81
Table 4	Origin and energies of peaks observed in the inelastically scattered electron energy spectrum.....	82
Table 5	Work function changes versus secondary emission coefficient, oxygen coverage, and temperature on (100) nickel.....	96
Table 6	Adsorption energies calculated from changes of the secondary emission coefficient at various temperatures.....	103
Table 7	Conditions for which the oxygen coverage increased beyond the saturation value.....	104
Table 8	Values of the island growth parameter.....	159

LIST OF FIGURES

		Page
Figure 1	Energy distribution of secondary electrons from solids. (a) Number of electrons with an energy E. (b) Derivative of the number of electrons with an energy E.....	7
Figure 2	Condition for constructive interference between scattered electrons.....	9
Figure 3	Possible arrangements of adsorbent and adsorbate surface molecules. (a) Atomic arrangement and unit mesh for the (111) surface of nickel. (b) Atomic arrangement and unit mesh for the (100) surface of nickel. (c) Unit mesh of a p(2 x 2) structure on (111) nickel. (d) Unit mesh of a c(2 x 2) structure on (100) nickel.....	10
Figure 4	LEED patterns observed from (a) clean (111) nickel, (b) clean (100) nickel, (c) (111) nickel with a p(2 x 2) structure, and (d) (100) nickel with a c(2 x 2) structure. (Filled circles are nickel diffraction spots; open circles are extra diffraction spots.).....	11
Figure 5	Schematic representation of the Auger process	16
Figure 6	Photograph of the experimental system and associated electronics.....	44
Figure 7	Schematic cross-section of the UHV specimen chamber for surface analysis.....	46
Figure 8	Schematic of the substrate assembly.....	48
Figure 9	Typical spectrum of residual gases.....	54
Figure 10	Experimental configuration for LEED.....	55
Figure 11	Experimental configuration for AES.....	58

	Page	
Figure 12	Experimental configuration for EID. (a) Total ion current mode. (b) Mass spectrometer mode.....	63
Figure 13	Experimental configuration for retarding potential measurement of work function changes.....	65
Figure 14	Experimental configuration for ion bombardment.....	67
Figure 15	Temperature dependent, reversible segregation of carbon on nickel (100).....	74
Figure 16	Typical AES spectrum from 0 to 1000 V from "clean" nickel.....	76
Figure 17	Typical AES spectrum from 0 to 70 eV from "clean" nickel. (2 VPP modulation voltage)..	78
Figure 18	Carbon versus oxygen AES peaks for nickel (100) exposed to CO.....	79
Figure 19	Typical AES spectrum from 0 to 1000 eV from an oxygen saturated surface.....	83
Figure 20	Oxygen concentration versus short exposures for (100) nickel. Δ - 147°K; $\bar{\Gamma}$ - 302°K; \ominus - 373°K; \square - 398°K; \diamond - 423°K; ∇ - 302°K, C = 0.54 μ V/ μ A; \circ - 302°K, IB.....	84
Figure 21	Oxygen concentration versus long exposures for (100) nickel. Δ - 147°K; $\bar{\Gamma}$ - 302°K; \circ_x - 373°K; \square - 398°K; \diamond - 423°K; ∇ - 302°K, C = 0.54 μ V/ μ A; \circ - 302°K, IB.....	86
Figure 22	Oxygen sticking coefficient versus oxygen coverage on (100) nickel.....	89
Figure 23	Carbon AES peak heights versus oxygen concentration for (100) nickel.....	92

	Page	
Figure 24	Changes in secondary electron peaks between 0 and 70 eV as a function of oxygen coverage on (100) nickel. (1 VPP modulation voltage; oxygen coverage in $\mu\text{V}/\mu\text{A}$).....	93
Figure 25	Secondary emission coefficient versus changes of the work function for oxygen on (100) nickel (positive denotes increased work function; negative denotes decreased work function).....	97
Figure 26	The secondary emission coefficient (solid lines) and the true secondary electrons peak height (dotted line) versus oxygen coverage on (100) nickel.....	99
Figure 27	Ranges and maximum intensities of LEED patterns versus oxygen coverage on (100) nickel.....	107
Figure 28	LEED pattern showing diffuse NiO plus unexplained diffraction spots. (a) Photograph of LEED patterns. (b) Schematic identifying diffraction spots. ($\theta_0 = 0.87 \mu\text{V}/\mu\text{A}$; 86V)...	109
Figure 29	LEED patterns showing that the sequence (a) NiO ($\theta_0 = 0.87 \mu\text{V}/\mu\text{A}$; 86V), (b) $c(2 \times 2)$ ($\theta_0 = 0.30 \mu\text{V}/\mu\text{A}$; 68V), and (c) $p(2 \times 2)$ ($\theta_0 = 0.15 \mu\text{V}/\mu\text{A}$; 74V) structures are observed with decreasing surface coverage...	113
Figure 30	Oxygen coverage versus short exposures for (111) nickel. \diamond - 147°K; \bullet - 302°K; ∇ - 366°K; Δ - 423°K.....	116
Figure 31	Oxygen coverage versus long exposures for (111) nickel. \diamond - 147°K; \bullet - 302°K; ∇ - 366°K; Δ - 423°K.....	117
Figure 32	Oxygen sticking coefficient versus oxygen coverage on (111) nickel.....	119

- Figure 33 Changes in secondary electron peaks between 0 and 70 eV as a function of oxygen coverage on (111) nickel (2 VPP modulation voltage; oxygen coverage in $\mu\text{V}/\mu\text{A}$)..... 121
- Figure 34 Secondary emission coefficient (solid lines) and true secondary electrons peak height (dotted line) versus oxygen coverage on (111) nickel..... 122
- Figure 35 Ranges and maximum intensities of LEED patterns versus oxygen coverage on (111) nickel..... 124
- Figure 36 LEED pattern due to sulfur in a $(5\sqrt{3} \times 2)$ structure on (111) nickel. (74V)..... 127
- Figure 37 LEED pattern due to sulfur in a $(8\sqrt{3} \times 2)$ structure on (111) nickel. (78V)..... 128
- Figure 38 AES spectra from 0 to 1000 V showing (a) sulfur saturated surface, (b) oxygen/sulfur reaction 50% complete, and (c) reaction nearly to completion..... 130
- Figure 39 Relative coverages of oxygen and sulfur with sulfur in the $(5\sqrt{3} \times 2)$ structure. \square No. 1 (302°K); \blacktriangle No. 2 (305°K); \blacksquare No. 3 (303°K); \bullet No. 4 (373°K); \blacktriangledown No. 5 (233°K). The variation of oxygen coverage is shown only for No. 2..... 132
- Figure 40 Relative coverage of oxygen and sulfur with sulfur in the $(8\sqrt{3} \times 2)$ structure. (302°K; 2 runs)..... 133
- Figure 41 LEED pattern from a $(5\sqrt{3} \times 2)$ sulfur structure and increased background intensity due to oxygen; reaction is 60% complete. (74V)..... 135
- Figure 42 Oxygen AES peak height versus IB time for (100) and (111) nickel surfaces. (Solid lines are calculated curves, filled circles are data points. Time scale for data from (111) surface multiplied by 0.5.)..... 142

Figure 43 Schematic of oxide island growth on the surface of a metal..... 153

ACKNOWLEDGEMENT

The author wishes to express his appreciation to Dr. John B. Hudson for his continued encouragement and advise. Discussions with members of the Surface Studies group and faculty of the Materials Division were very helpful. Support from NASA for this work by a Traineeship and by Research Grant Number NGR-33-018-066 is gratefully acknowledged.

ABSTRACT

The reaction of oxygen with clean (111) and (100) nickel surfaces and a (111) surface pre-contaminated with sulfur has been studied using LEED, AES, and EID. The variation of work function was investigated by a secondary electron technique and by the retarding potential method. A calibration was established between the oxygen AES peak and the oxygen coverage, and inelastic scattering of oxygen Auger electrons was accounted for.

The reaction of oxygen with clean nickel proceeds by the formation of dissociatively chemisorbed surface structures, followed by nucleation and growth of NiO islands which cover the surface. Chemisorption kinetics are Langmuirian until coverages of 0.34ML on the (111) and 0.25ML on the (100) surfaces. Beyond 0.34ML on the (111) surface, NiO nucleates and grows until a saturation coverage of 1.8 layers of NiO. Adsorption beyond 0.25ML on the (100) surface occurs into the chemisorbed layer until NiO nucleates at a temperature dependent coverage between 0.3 and 0.4 ML and grows to form a saturated surface at 2.0 layers of

NiO. For both orientations, the work function is increased by the chemisorbed structure but decreased by oxide formation. The $p(2 \times 2)$ chemisorbed structures on both faces were associated with 0.25ML coverage, but due to NiO formation, the $c(2 \times 2)$ structure on the (100) surface never fully developed.

A model to describe NiO growth which assumes that the perimeter sites of oxide islands are active growth sites was shown to describe the experimental data. The rate of NiO formation was limited either by surface diffusion or by both surface diffusion and oxygen capture of physisorbed oxygen. The reaction rate increased with decreasing temperature and the negative activation energy and oxide island density were determined to be 1.4 kcal/mole and $1 \times 10^{11} \text{ cm}^{-2}$, and 1.5 kcal/mole and $6 \times 10^9 \text{ cm}^{-2}$ for the (111) and (100) surfaces, respectively. Coherence broadening of the NiO diffraction patterns provided direct experimental evidence for oxide islands on the surface.

Broadening and energy shifts of the 60eV Auger peak and a new peak at 12eV, both associated with NiO formation, were interpreted in terms of band structure changes upon oxidation.

Increases of NiO coverage after saturation were associated with a reversibly adsorbed ionic or polar oxygen species with an adsorption energy between 12 and 25 kcal/mole.

The study of sulfur pre-contaminated (111) nickel surfaces indicated that sulfur surface structures with $(5\sqrt{3} \times 2)$ and $(8\sqrt{3} \times 2)$ symmetries could be produced by heating in vacuum at 1023 to 1073 °K. Oxygen caused removal of the sulfur at temperatures near 300°K and the only reaction product was SO_2 . The reaction rate between oxygen and the $(8\sqrt{3} \times 2)$ sulfur structure was analyzed in terms of the growth of oxide islands using the model described above. The $(5\sqrt{3} \times 2)$ data were not amenable to analysis.

PART I

INTRODUCTION

The interactions between gas molecules and solid surfaces are important to many common processes. For example, the adsorption and desorption of molecules are important to component design and performance for vacuum and space applications, and to the success of catalyzed reactions. The solid phases which result from oxidation processes are important to component performances in applications such as surface lubrication, metal bonding, electrical contacts, solid state devices, and structural components. Yet, a good understanding of the basic phenomena underlying the gas/surface interaction has not been achieved, primarily due to experimental difficulties in characterizing the solid surface and the gas adsorbed on, or incorporated in these surfaces.

Recently a number of sophisticated experimental techniques, such as Auger electron spectroscopy (AES)¹, low energy electron diffraction (LEED)², and electron induced desorption (EID)³, have been developed for surface research. These techniques are based on interactions between electrons and solids, and in combination with

mass spectrometry and ultra-high vacuum (UHV) techniques, have now made it possible to better characterize the solid surface and study the gas/surface interactions. Parameters such as surface cleanliness and structure, adlayer concentrations and binding, and gas phase reactants and products can begin to be characterized in order to describe the surface reactions. The present study has used these techniques to describe the reaction between oxygen and clean (100) and (111) nickel single crystal surfaces and a (111) nickel surface pre-contaminated with sulfur.

In the case of oxygen on clean nickel surfaces, the clean surface and the initiation of oxide formation has been studied in detail. The oxygen has been shown to form a chemisorbed oxygen structure followed by nucleation and growth of nickel oxide islands which cover the surface. After achieving a saturation coverage of oxide, further adsorption of oxygen only occurs if an ionic species which assisted ionic transport is present. Kinetic expressions to describe these processes are presented, and the relevance to the theories of low temperature oxidation is discussed.

For the surface reaction between oxygen and sulfur, the initial structure and quantity of sulfur on the surface has been determined. It was shown that oxygen causes removal of this sulfur as SO_2 and that the kinetics were consistent with formation of oxygen-rich regions, with the surface reaction proceeding at the perimeter of these regions.

Before describing the results in detail, the interaction between electrons and solid surfaces, and previous work on gas/surface interactions, with particular emphasis on the nickel/oxygen system will be discussed.

PART II

ELECTRON INTERACTIONS WITH ADSORBATES AND ADSORBENTS

To understand the results obtained by LEED, AES, and EID techniques, it is necessary to discuss the complex interactions between electrons (with energies less than 2000eV) and a solid.

Impinging electrons are scattered elastically or inelastically by the solid, and can cause changes in the electronic state of atoms or molecules at the surface. It has been observed that electron bombardment may cause desorption of adsorbate molecules³, and that the rate of electron induced desorption (EID) is specific to the adsorption state. Since knowledge of the adsorption state can provide important information about the gas/surface interaction, EID is useful for studying the surface. Additionally, it may influence the reaction being studied and must necessarily be considered when electron beam techniques are used^{1,4}.

Beyond causing changes on the surface, impinging electrons may be reflected or cause secondary electrons to be raised to energy states above the Fermi level; these "hot" secondary electrons may suffer further inelastic

collisions which cause more "hot" electrons. A portion of these cascading electrons will be scattered within a range close to the surface and in a direction such that they will surmount the surface barrier and result in electrons external to the sample. The energy distribution⁵ of these electrons is shown in Figure 1a, where $N(E)$ is the number of electrons with an energy E and the primary electrons have an energy E_p . Three regions are denoted in the figure; region I corresponds to the elastically scattered primaries. Historically, region II has been termed the rediffused primary region and, III, the true secondary region. This distribution has been well known for some time, with only recent recognition that secondary electrons provide information about the surface of the solid. The information is specific to the surface because electrons with well defined energies provide the information and the inelastic scattering mean-free-path for these electrons is on the order of 10\AA or less⁶. Thus, electrons originating deep in the solid will lose energy and be eliminated from observation. The information provided by secondary electrons as well as by EID will be discussed in a more detailed fashion.

A. Elastically Scattered Electrons (LEED)

The elastically scattered electrons in region I, Figure 1a, may be scattered coherently or incoherently. Electrons exhibit a wave nature and those scattered coherently produce a diffraction pattern as shown in 1928 by Davisson and Germer⁷. This was subsequently applied to surface work by Farnsworth and co-workers (see e.g. references 8 and 9) using a Faraday cage detection technique. They demonstrated⁹ that LEED patterns are normally dominated by the first two atom layers. In the early 1960's, a group at Bell Laboratories^{10,11} used a fluorescent screen display technique (described in the experimental section) which increased the convenience and popularity of LEED.

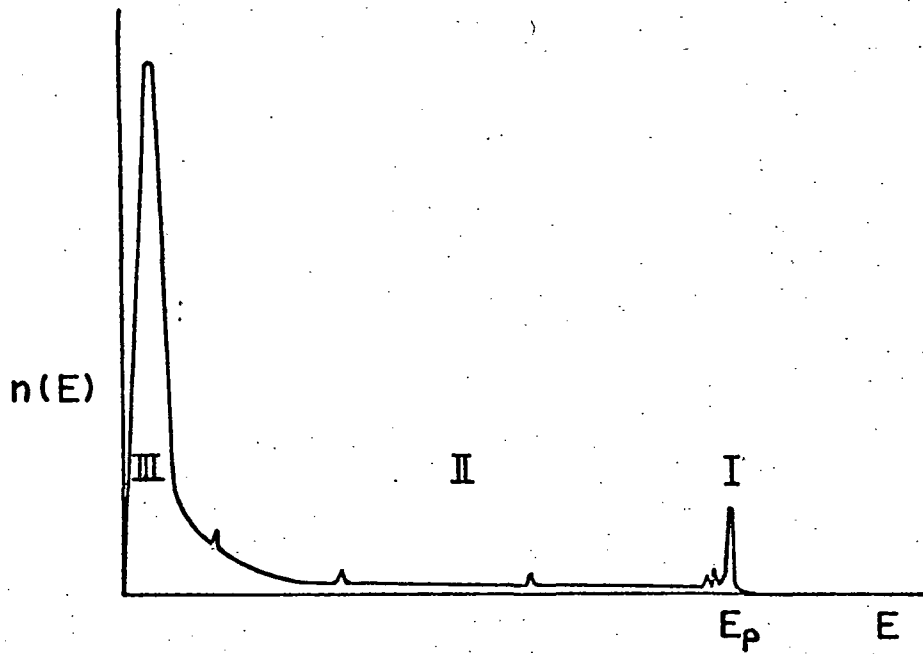
The theory, experimental arrangements, experimental results, and applications of LEED have been reviewed by several authors^{2,12,13,14}. The wavelength, λ , associated with low energy electrons is given by:

$$\lambda = \left(\frac{150}{V} \right)^{1/2} \text{ \AA} \quad (1)$$

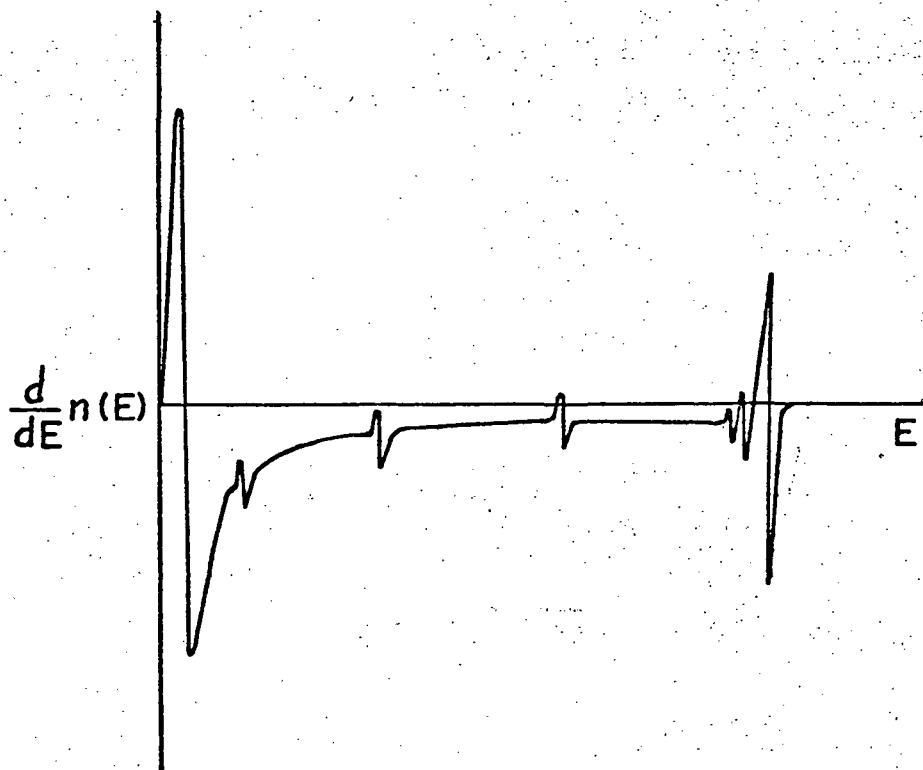
where V is in volts. The condition for constructive interference from surface atom arrays is shown in Figure 2.

Figure 1 Energy distribution of secondary electrons from solids.

- (a) Number of electrons with an energy E .
- (b) Derivative of the number of electrons with an energy E .



(A)



(B)

This condition is:

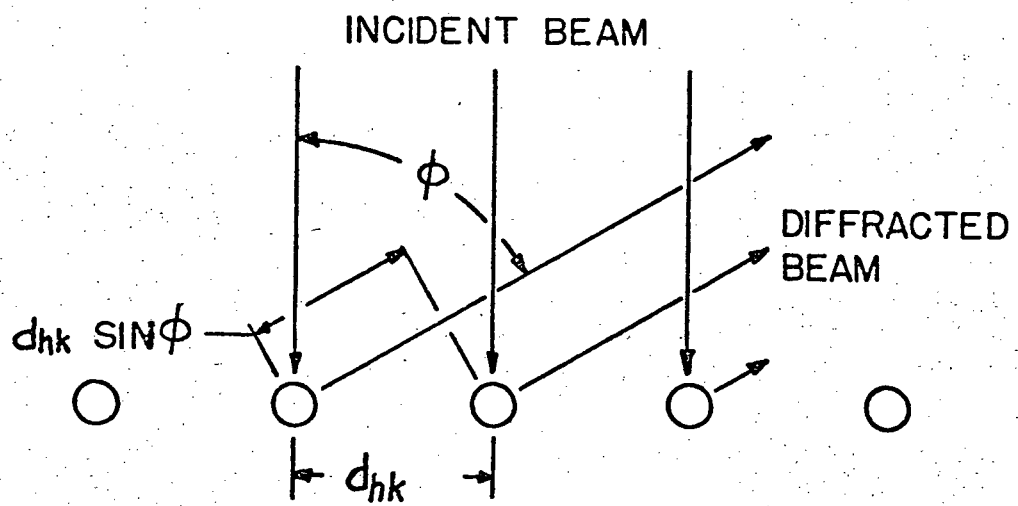
$$n \lambda = d_{hk} \sin \phi \quad (2)$$

for normally incident beams where d_{hk} is the separation of hk atom rows, n is the order of diffraction, and ϕ is the angle between the incident and backscattered beams.

The conventions for surface crystallography have been discussed by Wood¹⁵. It is convenient to define a unit mesh (analogous to a unit cell) based on the substrate bulk crystal structure. These are shown in Figure 3a and 3b for (111) and (100) nickel. The respective diffraction patterns from these mesh are shown in Figure 4a and 4b.

Adsorbed gases have often been found to form structures on the surface with a periodicity related by integers to the unit mesh. These are called surface structures or surface nets and are denoted with respect to the unit mesh. Thus, a structure equivalent to the unit mesh is denoted as $p(1 \times 1)$ or simply (1×1) . A surface structure twice the size of a unit mesh is denoted $p(2 \times 2)$ if it is primitive, or $c(2 \times 2)$ if it is centered. Examples of a $p(2 \times 2)$ structure on (111) nickel and a $c(2 \times 2)$ structure on (100) nickel are

Figure 2 Condition for constructive interference between scattered electrons.



$$n\lambda = d_{hk} \sin \phi$$

Figure 3 Possible arrangements of adsorbent and adsorbate surface molecules.

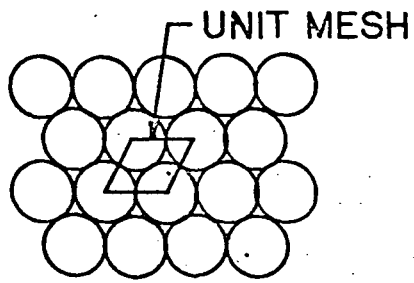
(a) Atomic arrangement and unit mesh for the (111) surface of nickel.

(b) Atomic arrangement and unit mesh for the (100) surface of nickel.

(c) Unit mesh of a p(2 x 2) structure on (111) nickel.

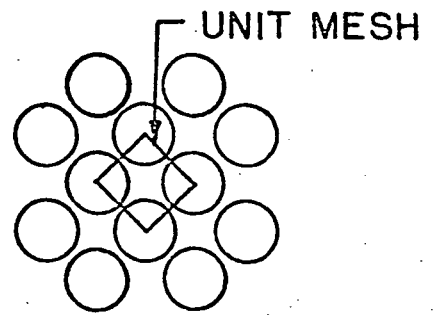
(d) Unit mesh of a c(2 x 2) structure on (100) nickel.

(111)

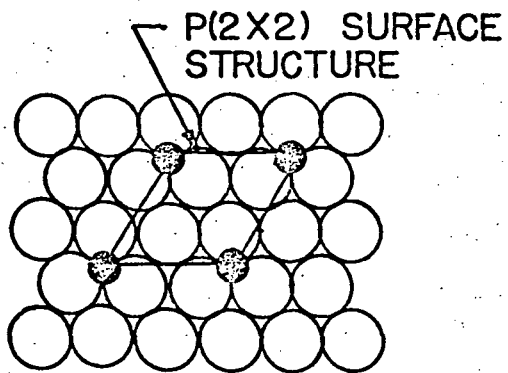


(A)

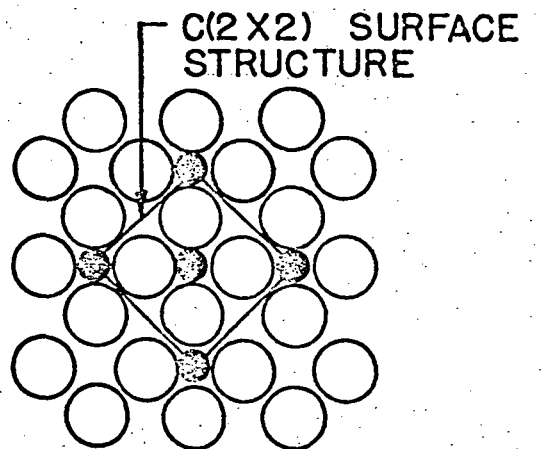
(100)



(B)



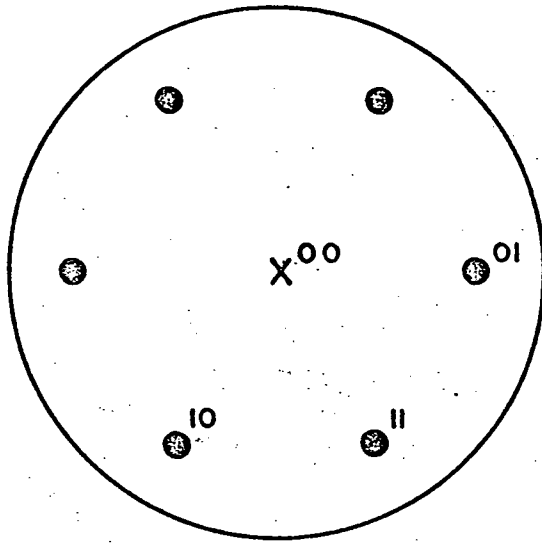
(C)



(D)

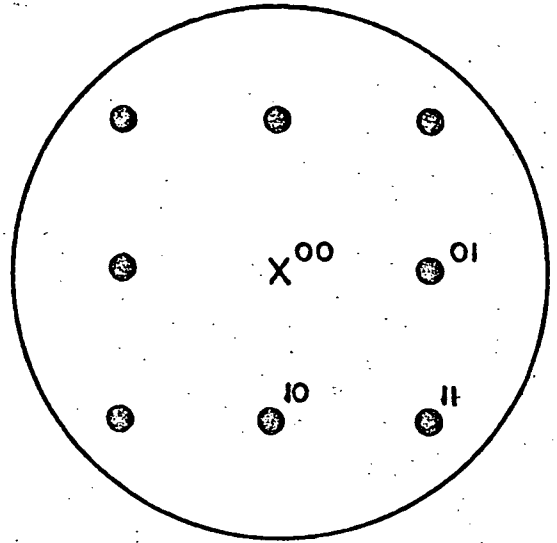
Figure 4 LEED patterns observed from (a) clean (111) nickel, (b) clean (100) nickel, (c) (111) nickel with a $p(2 \times 2)$ structure, and (d) (100) nickel with a $c(2 \times 2)$ structure. (Filled circles are nickel diffraction spots; open circles are extra diffraction spots.)

(111)



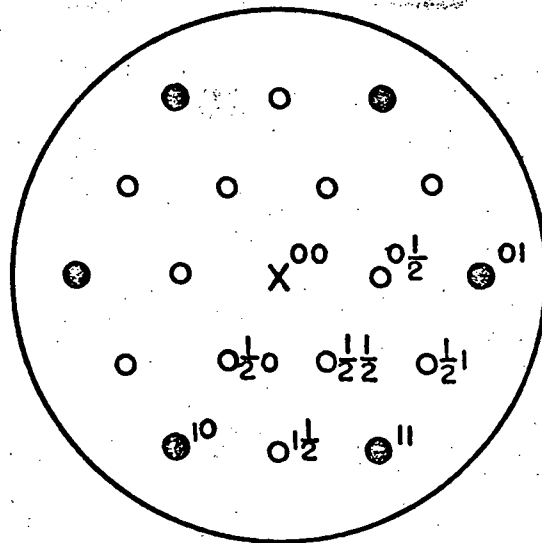
(A)

(100)



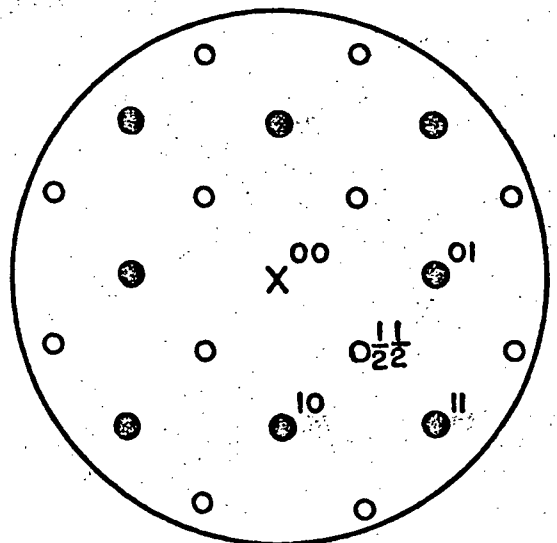
(B)

P(2X2)



(C)

C(2X2)



(D)

shown in Figure 3c and 3d, respectively. The diffraction patterns are shown in Figure 4c and 4d. At times, the surface net is rotated in relation to the unit mesh.

For a 30° rotation this is designated by $R30^\circ$, e.g.

$(\sqrt{3} \times \sqrt{3})R30^\circ$.

Considering the intensity of diffracted beams versus electron wavelength, the Laue condition normal to the surface would be completely relaxed if electrons were totally scattered by the first molecular layer. The diffracted intensity would then be essentially uniform over small ranges of wavelength. Since the electrons penetrate but only for short distances beyond the first layer, the Laue condition is intermediate between two and three dimensional diffraction. The diffracted intensity is modulated by interference between parallel layers and theoretically this yields information on atomic species and position. To date, theoretical analysis of the intensity has not been satisfactory and, as we shall see, controversy exists concerning the location of adsorbate molecules. (For example, the $p(2 \times 2)$ and $c(2 \times 2)$ structures shown in Figure 3c and 3d are only two of several possible structures which

could give the same LEED patterns^{2,12}.)

The diffracted intensity may still be useful in analyzing the distribution of material on the surface. If the domain size of a surface structure is small enough, the diffraction conditions may be relaxed causing a broadening of the diffraction spots. The coherence width for these electrons is on the order of $10^2 - 10^3 \text{ \AA}$, and circular domains smaller than this cause uniform circular diffuseness of the spots. Similarly, small lengths in one direction can cause streaking of the spots. Both conditions can also be caused by disorder of the scattering centers.

B. Inelastically Scattered Electrons

LEED was the first modern surface technique to be used extensively with the inelastically scattered electrons being ignored. A number of investigators^{16,17,18} showed at approximately the same time that LEED optics could be used as a retarding field electron energy analyzer and subsequently, more information has been obtained from the inelastic electrons. The structure immediately below the elastic peak in the secondary electron energy spectrum, Figure 1, is due to electrons

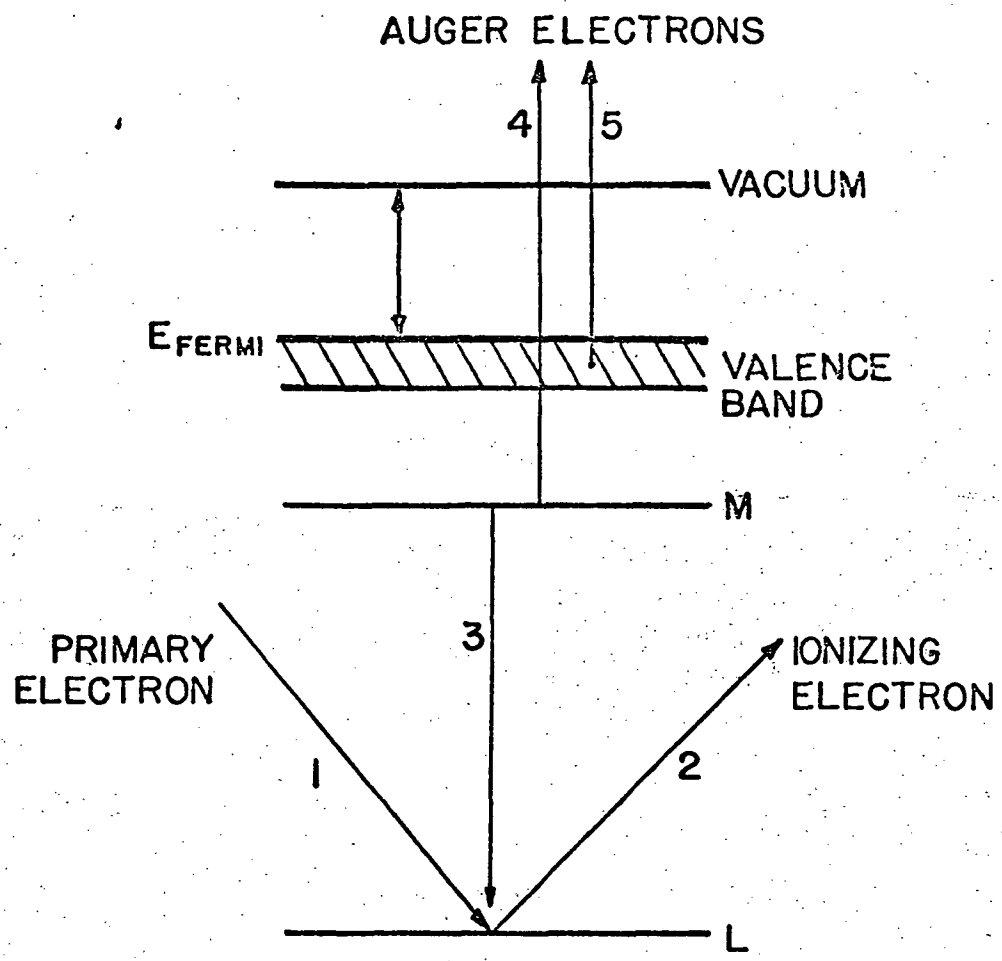
losing discrete quantities of energy to surface and bulk plasmon excitations and/or to interband and intraband transitions. These losses are characteristic of a given solid and consequently are called characteristic losses. They have been discussed in detail by Klemperer and Shepard¹⁹ and Raether²⁰. More recent discussions on characteristic losses²¹ and gains²² and ionization losses²³ at energies removed from the primary peak are also available. While characteristic losses hold some potential for surface studies²⁰, they are mentioned here only to aid interpretation of the secondary electron spectrum and will not be discussed further.

1) Auger Electron Spectroscopy. Within regions II and III of the secondary electron energy distribution (Figure 1) are shown peaks (exaggerated in magnitude) which represent secondary electrons generated by the Auger process and are commonly referred to as Auger electrons. An Auger electron is an electron emitted during the decay of an ionized atom to a lower excited state. The physics of the Auger process has been discussed by Burhop²⁴ and by Bergstrom and Nordling²⁵. The process is depicted in Figure 5. A primary electron

(step 1 of Figure 5) may cause an initial ionization by ejection of a relatively tightly bound electron (step 2) of a surface atom. Subsequently (e.g. step 3) an electron from a higher bound state may fill this lower energy vacant state and the released energy may cause ejection of either a photon or an Auger electron (as shown by step 4). The sum of the probabilities of photon and Auger electron ejection is equal to unity. However, for a transition energy less than approximately 1000eV, the probability of releasing an Auger electron is close to one while the probability of photon release is close to zero.

By convention, Auger transitions are denoted by ~~three~~ electron shell designations, e.g. LMM, where the first letter denotes the level of the vacant state caused by the initial ionization, the second letter refers to the original level of the electron which fills the initial vacant state, and the last letter denotes the level from which the Auger electron originates. Thus the Auger process shown by 1-2-3-4 in Figure 5 is an LMM transition while that by 1-2-3-5 is an LMV transition, where V stands for valance band. For sufficient energy

Figure 5 Schematic representation of the Auger process.



separation, subshell designations must be used with this scheme. The Auger transitions give a "fingerprint" of the emitting element, and transition energies may be roughly calculated from existing tables of atomic energy levels (e.g. Bearden and Burr²⁶) and making corrections for energy level shifts caused by ionization of the emitting atom¹. In addition to element identification, the possibility exists of analyzing chemical states of the elements through peak shifts and shape changes^{1,27,28}.

Lander²⁹ was the first to suggest that Auger electrons could be used in surface analysis, but it remained for Harris³⁰ to show that differentiation of the secondary electron energy distribution makes the technique feasible. Differentiation reduces the effect of the large background shown in Figure 1a and allows amplification of the Auger peaks. Thus rather than working with $N(E)$ vs. E , $dN(E)/dE$ vs. E , shown in Figure 1b, is used. For retarding field analysis, differentiation is accomplished electronically by modulating the retarding voltage and detecting the second harmonic of this modulation as described by Palmberg¹⁸. There have been recent reviews on the progress of and prospects for AES

by Chang¹ and Dooley and Haas²⁷.

Although the qualitative ability of AES is well documented by these reviews, quantitative calibration is a very significant problem, especially when the element being studied has a concentration distribution normal to the surface. Several investigators have shown that the peak to peak height of the derivative of an Auger peak is proportional to coverage, at least up to one monolayer¹. Palmberg and Rhodin⁵ have investigated multilayer effects and, for uniform coverage, observed exponential decay of Auger signals with depth of origin below the surface. Escape depths were on the order of 4 to 10 Å and were energy dependent. Gallon³¹ has developed a finite layer model for signal versus depth of origin, but this relies on experimental data for the primary and secondary mean free paths and this is not generally available. Thus, quantitative calibration of AES beyond a monolayer has not been generally accomplished.

2) True secondary electrons. The true secondary region is defined by convention to be the region between 0 and 50 eV. This is dominated by a large peak caused by true secondary electrons and has a maximum at about

2eV, a full width at half maximum of about 10eV, and a high energy tail which extends out to about 50eV. There are smaller characteristic loss and Auger peaks in this region, but they may not be detectable because of the high background.

True secondary electrons result from primary electrons creating secondaries which in turn create tertiaries and so on, until a cascade of electrons with decreasing energy is obtained. Theories of secondary emission have been developed and discussed by several authors^{4,32,33}, but in general the physical parameters required to apply the theories are unknown. The true secondary peak has not been used to date for surface analysis, but will be used in this study to characterize work function changes due to oxygen adsorption. The important physical parameters which determine true secondary emission are the Fermi energy, work function, penetration depth of primary electrons, and escape depth of true secondary electrons. For low surface coverage, changes of the work function caused by adsorbed oxygen are expected to have a large effect on changes of true secondary emission compared to the changes caused by

the other important parameters. Since more than 95% of the total secondary emission current is due to true secondary electrons, both the secondary emission coefficient, δ , (defined to be the ratio of secondary electron current to primary electron current) and the area under the true secondary peak should reflect variations in the work function. This is supported by studies of adsorption of metal on metal in which changes in δ were directly correlated with changes in work function^{18,34,35}. As the work function increased, δ decreased and vice versa. The correlation between secondary emission and work function variations must necessarily be qualitative since we have neglected electron mean-free-path variations and Fermi energy shifts, but the correlation should be sufficient to compare work function trends in the present study to previous work.

C. Electron Induced Desorption

For establishing validity of any experimental result, the perturbing influence of the experimental techniques on the studied process must be considered. Cracking of poly-atomic molecules by energetic electrons

is well known and expected to occur on surfaces. In addition, impinging electrons may cause desorption or conversion to other binding states of surface molecules. We will discuss these effects further.

These effects have been termed EID and have been reviewed by Redhead, et.al.³, and Madey and Yates³⁶. It is easy to show that the upper limit of direct energy transfer from impinging electrons is about 1eV, but EID has been observed for states with a binding energy of as much as 6eV, therefore the process is caused by electronic excitation. Redhead³⁷ and Menzel and Gomer³⁸ simultaneously postulated equivalent mechanisms for EID. They postulated that ionization of surface molecules occurred with a cross-section near that for gas molecules (approximately 10^{-16} cm^2), and this raised the molecule to a state where desorption from the surface could occur. Due to the close proximity of the ion and surface, Auger or resonance neutralization was very probable, therefore the molecule might follow any of four paths. If neutralization did not occur, it might desorb as an ion. If neutralization did occur, it might still desorb, but as a neutral. After neutralization, it might readsorb

in the original state, or it might return to another adsorption state. These possibilities have been discussed in detail^{3,36,37,38}.

There are several ways to investigate EID³⁶. The material leaving the surface may be detected, e.g. by a mass spectrometer or by collecting desorbed ions. The material remaining on the surface may also be measured, e.g. by the field emission microscope or by AES. AES appears to be a particularly powerful technique since it may be quantitative in certain instances and is capable of determining fragmentation. Its disadvantages are that primary voltages higher than optimum are required³ and signal from adsorption states without an EID yield may mask those states which do experience EID. EID will be characterized in this study by measuring decreases in AES peaks with electron bombardment.

To describe the EID effect, cross-sections may be defined and measured for each of the adsorption states. The ionic cross-section, Q_j^+ , describes desorption of only ions from the j th state, while the total cross-section, Q_j^T , for the j th state includes desorption of ions and neutrals as well as conversion to other states. The ionic

cross-section is given by:

$$Q_j^+ = \frac{i_j^+}{I^- \sigma_j} \quad (3)$$

where I^- is electron current, i_j^+ is the ion current from the j th state, and σ_j is the ad-population of the j th state. Since the ad-population in the j th state is not generally known, Q_j^+ is more difficult to determine than Q_j^T . Redhead³⁷ has shown that Q_j^T may be determined, assuming Q_j^T is independent of σ_j , by:

$$i_j^+ = i_0^+ e^{-t/\tau} ; \tau = \frac{e}{J^- Q_j^T} \quad (4)$$

where i_0^+ is the initial ion current at zero time, e is the ionic charge, and J^- is the electron current density.

Reported EID cross-sections have been collected by

Redhead^{3,39} and partially by Madey and Yates³⁶.

PART III

HISTORICAL REVIEW

A. Clean Surfaces

1) Cleaning techniques. If a nickel surface is "cleaned" by conventional solvents, then placed in vacuum, AES will commonly show N, O, Ca, K, F, S, and heavy C contamination; very poor or no LEED patterns will be observed. After sufficient heating in UHV, AES generally reveals high carbon and/or sulfur concentrations and sulfur induced LEED patterns are observed⁴⁰; i.e. simply heating nickel in UHV will not produce an atomically clean surface. (Clean must be defined in terms of AES detectibility limits which are estimated to be about 0.02ML for C, S, and O¹.)

The sulfur results from segregation from the bulk to the surface^{30,40,41}, and carbon results from bulk segregation and adsorption of CO and CO₂ residual gases^{40,42,43,44}.

Additional cleaning techniques are required and have been reviewed^{45,46}, but the most popular for nickel is ion bombardment. This is generally accomplished using argon ions with less than 600eV energy, current

densities of 10^{-6} to 10^{-5} amps/cm², and bombardment times of about 15 minutes. The surface damage caused by this bombardment can be removed by a subsequent anneal. Farnsworth and Tuul⁴⁸ have concluded that annealing at 1023°K for fourteen hours will remove this damage in nickel. This is consistent with Rantanen, et.al.⁴⁹, who report that 500eV argon ions embedded in nickel are all released by a temperature and time of 898°K and six minutes, and with annealing studies for gold which show bombardment damage is removed by annealing at a homologous temperature of 0.4⁵⁰ (1023°K is a homologous temperature of 0.6 for nickel).

Annealing may cause segregation of additional carbon and/or sulfur to the surface. This may be eliminated by cyclic bombardment and annealing to deplete the bulk concentrations. Usually ion bombardment is accomplished with the substrate at room temperature; some investigators have bombarded at elevated temperatures to ensure diffusion and therefore depletion of bulk impurities^{43,44}.

Another method for cleaning nickel is by chemical reactions between adsorbed surface species and gases in the system. Germer and MacRae⁵¹ have used oxygen at

1×10^{-6} torr with the nickel at 773°K to remove unspecified impurities. The residual oxygen was then removed by hydrogen (1×10^{-7} torr) with the nickel at 473°K. Riwan⁴¹ has used oxygen to remove sulfur from nickel surfaces at elevated temperatures. Both Harris³⁰ and Sickafus⁴⁰ have reported reduced sulfur concentrations after exposing the surfaces to oxygen-containing atmospheres, but the kinetics of this oxygen/sulfur reaction were not studied. Oxygen chemical reaction has been shown to remove carbon^{40,44}, but this may be complicated by a temperature dependent, reversible segregation of carbon in nickel^{42,43,44}.

It was initially stated that simply heating nickel is not sufficient to clean it. However, when the bulk carbon and sulfur concentrations are sufficiently low, heating may cause dissolution of oxygen, leaving a clean surface.

Recent studies using AES have shown that, in general none of the above techniques alone will yield a clean surface in every instance. Tracy⁴⁴ has recently reported a simultaneous ion bombardment and oxygen chemical cleaning technique. We will report in this study, a sequential technique of ion bombardment and chemical

cleaning. In both cases, AES was used to define when the surface was clean.

2) Maintaining a clean surface. The dominant residual gases in a diffusion pumped vacuum system are CO and CO₂. CO presents the greatest problem since it adsorbs rapidly on nickel^{52,53} and experiences self-oxidation^{6,54}, i.e. $2\text{CO} \rightarrow \text{C} + \text{CO}_2$. To control this problem, residual pressures are reduced to the 10^{-10} torr range and the time between cleaning the surface and performing the experiment is minimized.

3) Structure of clean nickel surfaces. The observed structure of clean nickel surfaces is that expected from termination of the bulk metal lattice⁵⁵. This is shown in Figure 3a and 3b for (111) and (100) nickel, respectively.

B. Results for Oxygen on Clean Nickel Surfaces

1) Low-energy electron diffraction. There have been many investigations of the interaction of oxygen on relatively clean nickel surfaces and those for the (100) and (111) faces are referenced in Table 1. Since one cannot characterize the kinetics and other aspects of the oxygen reaction or determine whether a surface is

atomically clean by using only the LEED technique, it seems desirable to re-examine the interaction using LEED in combination with AES and EID techniques.

As indicated in Table 1, $p(2 \times 2)$ and $c(2 \times 2)$ surface structures have been observed on the (100) face with increasing oxygen exposure until at long exposures, a NiO diffraction pattern was observed. For the (111) face, a $p(2 \times 2)$ structure has been observed and MacRae⁵⁵ reported that this was followed by a $(\sqrt{3} \times \sqrt{3})R30^\circ$ structure without subsequent formation of NiO at room temperature. Becker and Hagstrum⁷⁰ have also observed a $(\sqrt{3} \times \sqrt{3})R30^\circ$ structure, while Park and Farnsworth⁶⁹ and Bauer⁶⁴ reported that only a NiO pattern was observed subsequent to the $p(2 \times 2)$ structure at room temperature. Apparently Germer, et.al.^{72,73}, and Bauer⁶⁴ obtained the $(\sqrt{3} \times \sqrt{3})R30^\circ$ only after heating while Edmonds and Pitkethley⁴ observed it as a result of beam dissociation of CO_2 adsorbed on the (111) face. MacRae^{63,65,71} has reported that NiO in the form of pyramids exists on the (111) face after heating. It is obvious that the sequence of surface structures beyond the $p(2 \times 2)$ structure on the (111) face is in doubt.

Although LEED has clearly established the

TABLE I

Surface Structures Due to Oxygen on Nickel as Determined
by LEED

Face	Structure	Reference
(100)	p(2 x 2)	2, 11, 48, 55, 56, 57, 58, 59, 61, 62, 63, 64, 66, 67
	c(2 x 2)	2, 11, 48, 55, 56, 57, 58, 59, 61, 62, 63, 64, 66, 67, 68
	NiO	11, 48, 56, 57, 58, 65, 66, 67
(111)	p(2 x 2)	55, 63, 64, 69, 70
	($\sqrt{3} \times \sqrt{3}$)R30°	2, 4, 55, 64, 70, 72, 73
	NiO	2, 63, 64, 65, 69, 71

existence of surface structures for many adsorbates on many different metals, the scattering species for these structures are sometimes in doubt. Based on diffraction spot intensities, reconstruction of the surface to a nickel-oxygen layer (as opposed to a layer of oxygen chemisorbed on top of the nickel lattice) has been proposed for the observed surface structures (see e.g. references 55, 56, and 75). Following May and Carroll⁷⁶, we define a reconstructed layer as a surface alloy, one atom thick, with the special property that the metal atoms have separations which are exact multiples of those of the substrate surface. May¹² has summarized the rather extensive number of observations concerning reconstruction and Becker and Hagstrum⁷⁰ have reported more recent experimental results supporting reconstruction. Bauer^{2,64,79}, among others has challenged some of the evidence for reconstruction and recent results by Lewis and Gomer⁸⁰ with the field ion microscope have indicated that reconstruction may not be as general as originally postulated. Thus, the matter is undecided.

While the concept of surface structures is almost totally a result of LEED, the established concept

of nucleation and island growth has only been re-emphasized by LEED results. This has been discussed by May¹² in connection with surface reactions between adsorbed gases. In addition, Tracy and Blakely⁸¹ have applied the concept to oxygen adsorbing on clean tungsten surfaces. This concept has also found limited applications in catalysis¹² and ultra-thin film oxidation^{82,83}. Nucleation and growth of oxide islands will be discussed in detail below, and used to analyze experimental data from the present study.

2) Auger electron spectroscopy. There have been no reported studies of the oxygen/nickel reaction using AES. AES has been used in several studies to investigate contamination of nickel^{30,40,43,44}. The capabilities of AES for measuring the kinetics of reactions have been established by studies on other systems¹.

3) Electron induced desorption. Young⁸⁴ has reported that oxygen ions are released when heavily oxidized (and possibly contaminated) nickel surfaces are bombarded with 90eV electrons, but other EID parameters were not measured. Klopfer⁸⁵, using polycrystalline nickel, has observed desorbed oxygen ions with an ionic cross-section of $1 - 2 \times 10^{-21} \text{ cm}^2$, and desorbed neutral

O_2 molecules with a total cross-section of $1.5 - 2 \times 10^{-19} \text{ cm}^2$. This was true for oxygen coverage from 7.5×10^{14} to 4×10^{16} oxygen molecules/cm². Desorption of neutral atomic oxygen was not detected.

4) Work function. Changes of the work function during oxygen adsorption on nickel has been studied a number of times. Farnsworth and coworkers^{56,69,86} have measured changes of work function due to oxygen on nickel single crystals and attempted a correlation with LEED patterns. For the (100) surface⁵⁶, they observed an increase in the work function to a broad maximum between maximum intensities for the p(2 x 2) and the c (2 x 2) structures. A subsequent decrease to below the value for clean nickel was associated with NiO formation. For the (111) surface^{69,86} an increase in work function was associated with the p(2 x 2) surface structure, but the subsequent behavior was not reported. MacRae⁵⁵ reported similar increases in the work function due to surface structures on the (111) surface.

Work function changes have been used in several investigations to characterize oxygen adsorption on evaporated polycrystalline nickel films. Roberts⁷⁸ and

Roberts and Wells⁸⁸ have observed work function behavior similar to that for single crystals for slow adsorption rates, i.e., the work function initially increased, then decreased to below the value for pure nickel. However, for continued adsorption on evaporated films, the work function increased again to above the clean surface value. This effect has not been reported for single crystal work. Roberts and Wells⁸⁸ and Delchar and Tompkins⁸⁹ have both observed a decrease in the work function upon warming towards room temperature a surface saturated with oxygen at 77°K. Delchar and Tompkins also observed work function decays with short time constants after dose-wise adsorbing oxygen onto nickel. All of these effects have been used to argue for reconstruction of the surface; however, May and Germer⁷⁴ suggest the effects may be artifacts peculiar to vapor deposited films.

Several reservations about the use of vapor deposited films are obvious. Contamination of the films is probable and no method of monitoring is generally used. High defect concentrations are present in films formed by vapor deposition, and a complete anneal is not usually performed. This could affect the transport mechanisms

(e.g. high vacancy concentrations could increase the rate of bulk diffusion) and indeed, sintering of the vapor deposited films is commonly observed during adsorption of oxygen⁹⁰. Finally, the surfaces of deposited films are very rough and very reactive, and non-uniform distribution of adsorbed oxygen, especially during dose-wise gas additions, may account for some transient behavior. Although some of these factors may be of importance, evidence will be presented to show that these peculiar variations of work functions may be partially accounted for by adsorbed oxygen species.

5) Calorimetry and oxygen uptake methods.

Horgan and King^{91, 92} have measured the sticking coefficient versus oxygen coverage on deposited polycrystalline nickel films using a Wagener flow technique. At 293°K and 373°K, the sticking coefficient, s (defined to be the probability that an impinging gas molecule will stay on the surface), decreased rapidly from an initial value of one to a minimum of about 10^{-2} , increased with increasing coverage to a broad maximum at 10^{-1} , then rapidly decreased to a value less than 10^{-3} . Beyond this point, s decreased exponentially with increasing

coverage. Horgan and King interpret their results as initial molecular adsorption (decreasing θ) followed by reconstruction (θ at a plateau versus coverage) and finally, classical thin film oxidation.

Calorimetric data for oxygen adsorbed on deposited nickel, reported by Brennan, et.al.⁹⁰, and Brennan and Graham⁹³, was cited to support Horgan and King's conclusion that oxygen initially adsorbed non-dissociatively. Brennan and Graham have reported a heat of adsorption of 77 kcal/mole at 77°K and 110 kcal/mole at 300°K. Brennan, et.al., have also reported 110 kcal/mole as the heat of adsorption of oxygen on nickel at 300°K. This value is close to the heat of formation of NiO⁹⁰. However, both sets of investigators report (without comment) that the heat of adsorption at low coverage and at 300°K is less than 110 kcal/mole, and on the basis of these data, the conclusion of non-dissociative adsorption was drawn. Cerny⁹⁴ has also reported initially low heats of adsorption at low coverages for several metals and suggests that the effect is an artifact. Thus the conclusion of non-dissociative adsorption during the initial adsorption of oxygen on nickel is not well supported.

Klopfer⁸⁵ has also investigated the sticking coefficient versus oxygen coverage on a polycrystalline substrate cleaned both by ion bombardment and by chemical reactions. His results at room temperature were very similar to those of Horgan and King's in that s initially decreased, passed through a minimum to a broad maximum, then decreased again as the oxygen coverage increased.

In all four of these studies, an estimate of the total oxygen uptake was made. The calorimetry studies indicated about two monolayers of oxygen were taken up before the heat of adsorption dropped to a very low value. Both Horgan and King and Klopfer concluded that the sticking coefficient decreased below 10^{-3} at about one monolayer of oxygen, but that several monolayers were taken up after the sticking coefficient decreased below this value. This slow uptake to several monolayers of oxygen was observed with oxygen pressures on the order of 10^{-5} to 1 torr. We shall see that higher oxygen pressures are a prerequisite for this uptake at room temperature. However, because the surface oxygen concentration is not measured directly in any of the above methods and because the true surface areas of deposited films are

hard to determine, the accuracy of these reported oxygen coverage values is difficult to judge.

Another study of significant interest to the present investigation has been reported by Orr⁸³ and partially by Rhodin, et.al.⁸². In this case, the formation of an oxide on deposited magnesium films was studied by the Wagener flow technique. The reaction rate, as characterized by the sticking coefficient, was initially observed to be slow, increased as the oxygen coverage increased, then decreased to low values at a coverage of approximately three monolayers. This behavior was postulated to result from nucleation and growth of MgO islands with the perimeter being the active growth site for lateral island growth. A model was proposed which related the kinetics of island growth to the rate at which oxygen molecules reached the perimeter; three limiting cases of oxygen transport were considered: (1) limit by impingement rate, (2) limit by surface diffusion of physisorbed oxygen, and (3) limit by the rate of incorporation of oxygen into MgO islands. The data were shown consistent with reaction rates limited by either surface diffusion or oxygen capture, and electron microscopic analysis of the oxide indicated

crystallite sizes consistent with the calculated density of oxide islands on the surface. We will discuss the model in more detail below and expand the treatment in order to apply it to the reaction between oxygen and nickel surfaces.

6) Field ion microscope (FIM) and field emission microscope (FEM). Although these techniques might be expected to contribute significantly to adsorption studies, the probability of field induced artifacts is so significant^{80,95} that the interpretation of results is in doubt and the few reported studies^{96,97,98} will not be discussed in detail.

C. Summary of Oxygen Interaction with Clean Nickel

It is obvious from the preceding discussion that no one technique can answer all the questions concerning the nickel/oxygen interaction. We will discuss the connection between the separate observations and point out where clarification is desired. To accomplish this, it is convenient to use the LEED work as a reference, since experimental conditions were best controlled in these studies.

Initially LEED shows the formation of surface structures (for submonolayer coverage) which are consistent

with the adsorption of oxygen on sites which maximize the coordination number of the adsorbed oxygen. This is accomplished by very rapid oxygen adsorption and causes an increase in the work function. Uptake methods show that the rate of adsorption decreases monotonically during this stage. On the basis of LEED data, this initial increase of oxygen on the surface must be associated with chemisorption of oxygen. However, it is uncertain whether these changes occur by classical planar adsorption (of either molecular or dissociated oxygen) or reconstructive adsorption.

Beyond this initial rapid increase in oxygen coverage a reaction region in which the sticking coefficient is about 10^{-2} is observed, but the connection between results by different techniques becomes more confusing and uncertain. In some cases, LEED indicates subsequent surface structures thereby indicating further chemisorption. Data taken by uptake and work function methods have been analyzed by postulating that oxygen penetrates below the nickel surface during this region causing an increase in the sticking coefficient with increasing oxygen coverage. The surface phase resulting from this penetration is unspecified and LEED does not always indicate an NiO

pattern at long exposures.

Based on coverage data from the oxygen uptake methods, an ultra-thin film oxidation stage follows when the sticking coefficient decreases below 10^{-3} , but this is not well supported by LEED studies.

The relation between the above observations will be clarified by the present study. In addition, the kinetics of the reaction, which have not been investigated or interpreted, will be discussed.

D. Surface Reactions on Pre-Contaminated Surfaces

There have been few studies of surface reactions which were conducted in UHV using well characterized surfaces. May¹² has discussed some of those reported. Most studies have dealt with simple reactions using LEED as the primary investigative technique with various gas phase techniques as secondary methods. In some instances, incubation periods have been attributed to nucleation^{12,99}, and in some cases island morphology of second phases on the surface has been observed¹².

There have been few studies in which the surface concentrations of reacting species have been measured directly by AES. Bonzel¹⁰⁰ has reported such an investigation of the reaction of oxygen with sulfur on a copper

(110) surface, and since we will be concerned with a similar reaction in this study, we will discuss Bonzel's work in some detail. The study was concerned with temperatures in the range of 883-1103°K and the only reaction product observed was SO₂. The results were analyzed in terms of a Langmuir-Hinshelwood mechanism¹⁰¹ which postulates that for the reaction to occur, both species must be adsorbed on the surface and occupy adjacent sites. Bonzel proposed that oxygen dissociated on sites free of sulfur and that near 883°K the reaction rate was proportional to the concentration of atomic oxygen, while near 1103°K, the rate was proportional to the square of this concentration. The important requirements for this reaction to proceed then, were dissociation of oxygen and the occurrence of adsorbed atomic oxygen and sulfur on adjacent sites. We shall see a similar situation in the present study.

E. Statement of the Problem

The above review of the literature clearly reveals that a complete and consistent description of the interaction of oxygen with nickel surfaces has not been achieved. LEED and work function data have permitted

partial characterization of the reaction, but there is as yet no direct information on the surface oxygen coverage and the kinetics of the reaction have not been described. In addition, there is little or no information available on the effect that other adsorbed molecules have on the course of the nickel/oxygen interaction. Therefore, the major objectives of the present study were to:

(1) Establish a calibration relating the AES oxygen signal to the quantity of oxygen on the surface and thus achieve a direct measure of the oxygen coverage.

(2) Establish connections between the data obtained by LEED, AES, EID, and work function changes.

(3) Describe the kinetics of the reaction of oxygen with nickel surfaces.

(4) Investigate the sequence of the reaction of oxygen with clean nickel surfaces. In particular, to describe the transition between chemisorbed oxygen and oxygen in a nickel oxide structure, and to determine when and if the present theories of low-temperature oxidation are expected to apply.

(5) Investigate the reaction between species adsorbed on a surface, to identify the parameters important to the surface reaction, and to describe the kinetics of such a reaction.

PART IV

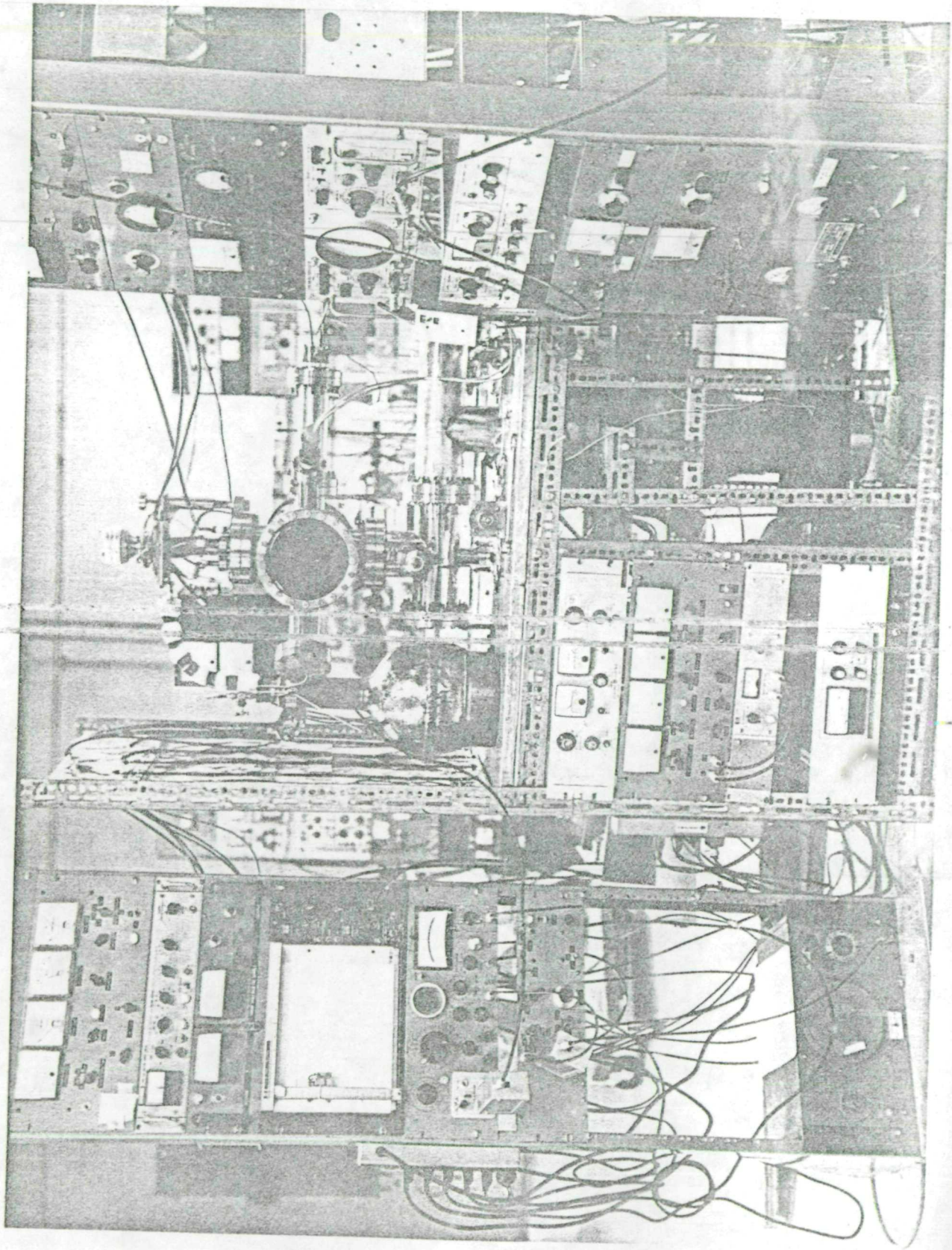
EXPERIMENTAL EQUIPMENT AND PROCEDURE

A. Vacua and Specimen Chamber

The ultra-high vacuum system, shown in Figure 6, was constructed predominantly of 304 stainless steel with copper sealed UHV flanges and a few glass components. Vacuum was achieved and maintained by an NRC VHS-4 oil diffusion pump using Convalex-10 pump oil. The system was roughed and backed by a Welch Model 1376 mechanical vacuum pump separated from the diffusion pump by a VEECO Coaxial foreline trap. The diffusion pump was separated from the system by a Granville-Phillips 6 inch Cryosorb liquid nitrogen cold trap. The cold trap liquid nitrogen level was automatically maintained from a pressurized dewar using a temperature-sensing resistor to open a solenoid valve and time-delay relay set for the proper fill time. A lower limit temperature-sensing resistor could interrupt power to the diffusion pump in case of low liquid nitrogen levels.

The pumping system was connected to the specimen chamber by two four inch diameter TEE sections. A Bayard-Alpert gauge (General Electric Model 22GT102 with

Figure 6 Photograph of the experimental system and associated electronics.

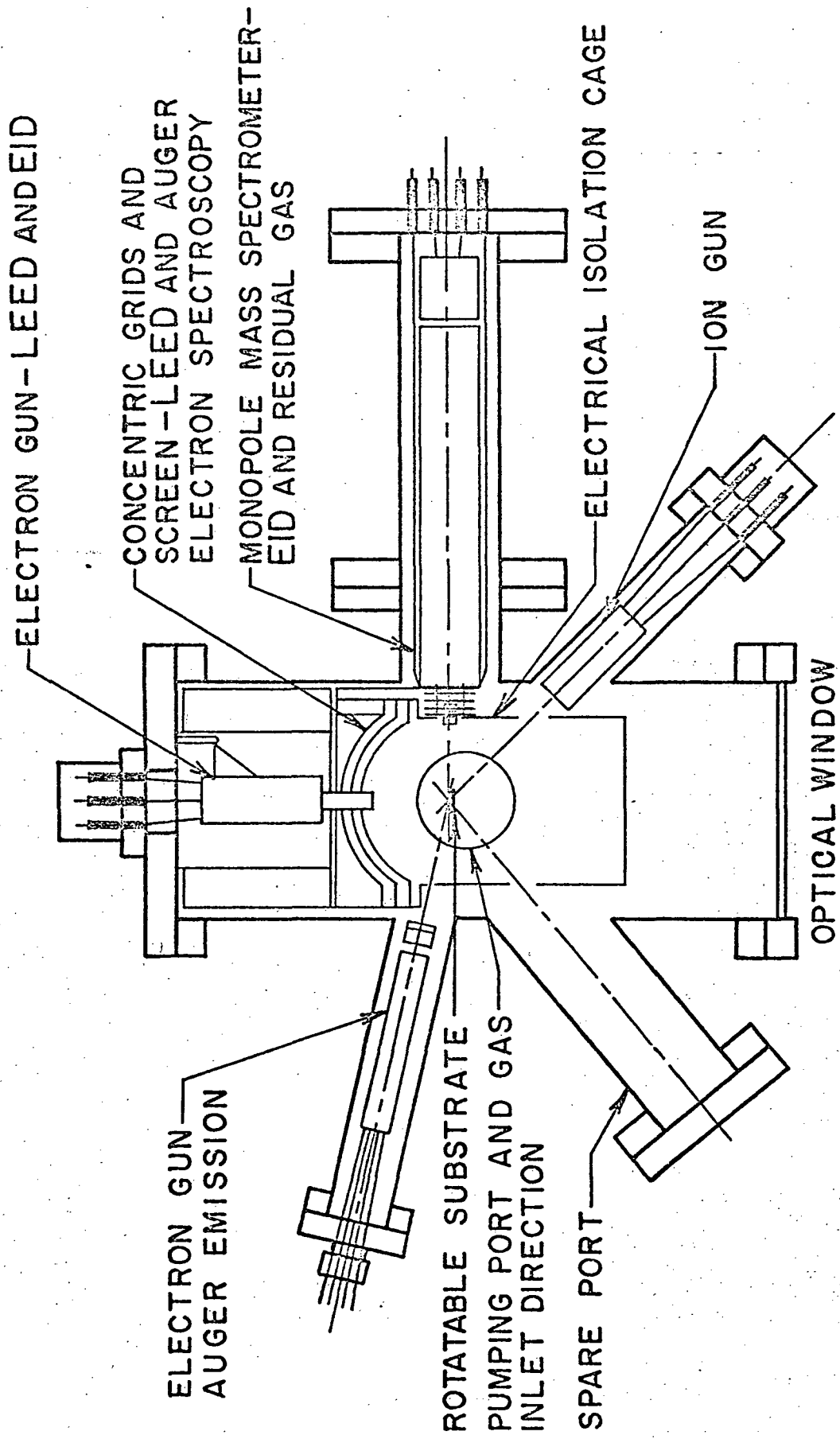


associated power supply Model 22GC100) located on the second TEE was situated so it was left on while the system and the gauge were being baked. The gas inlets for both oxygen and argon were located on the second TEE which in turn connected to the specimen chamber. This chamber, shown in schematic cross-section in Figure 7, housed the ion gun, mass spectrometer, electron optics (three grids and fluorescent screen), electron guns for LEED and AES, and the specimen.

All of the vacuum system, except the cold trap and vacuum pumps, was baked at a maximum temperature of 513°K for more than 18 hours to reach the ultra-high vacuum range. Air circulation during baking insured that the temperature within the oven was uniform to within 20°C, exclusive of the area connected to the cold trap. This procedure reduced the system residual pressure to 3×10^{-10} as indicated by the ion gauge; it is suspected that this limit was affected by the low pressure limit of the gauge and control. After thorough component outgassing, the ion gauge indicated 5×10^{-10} torr with both electron guns and the mass spectrometer turned on and the substrate at room temperature.

The ion gauge was used to indicate total pressure,

Figure 7 Schematic cross section of the UHV specimen chamber for surface analysis.



ULTRA-HIGH VACUUM SPECIMEN CHAMBER FOR SURFACE ANALYSIS

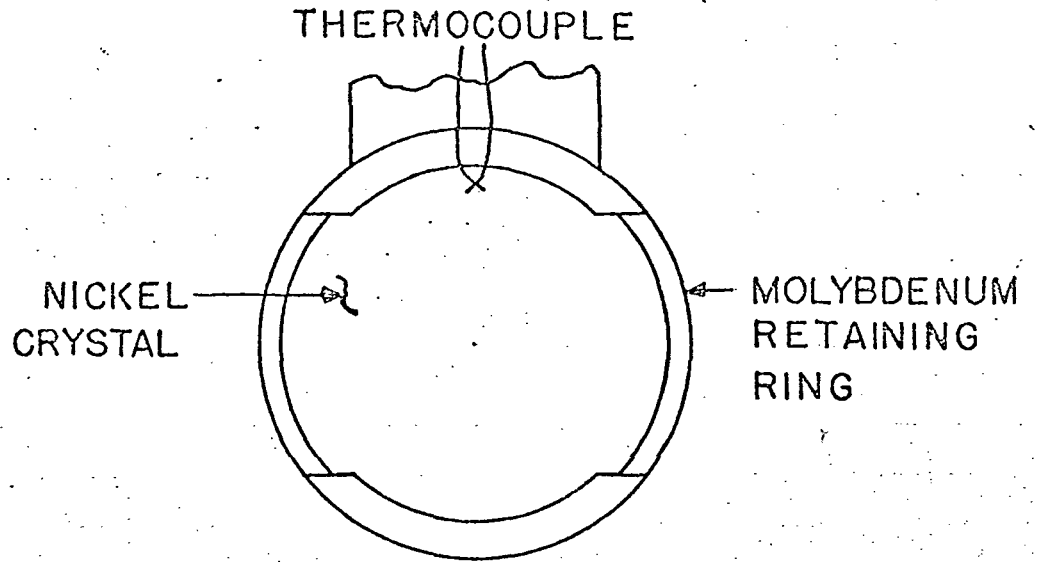
but the 32 AMU mass spectrometer peak was used to control oxygen exposures. This eliminated error due to wall and filament gas reactions as discussed by Redhead, et.al.^{31,39}

Research grade oxygen (99.995+% pure) in break seal flasks from Air Products, Inc. was introduced through a bakeable Varian Variable Leak Valve. Prepurified grade argon (99.998% pure) from Matheson Gas Products, used for ion bombardment and mass spectrometer calibration, was stored in a one liter flask between two Granville-Phillips Type C UHV valves. Before filling this flask, the inlet line was evacuated by a mechanical pump through a liquid nitrogen cold trap and backfilled at least three times. Titanium was generally deposited on the walls of the flask before filling to getter-clean the argon before it was used for ion bombardment. The argon leak rate into the system was controlled by the second Type C valve.

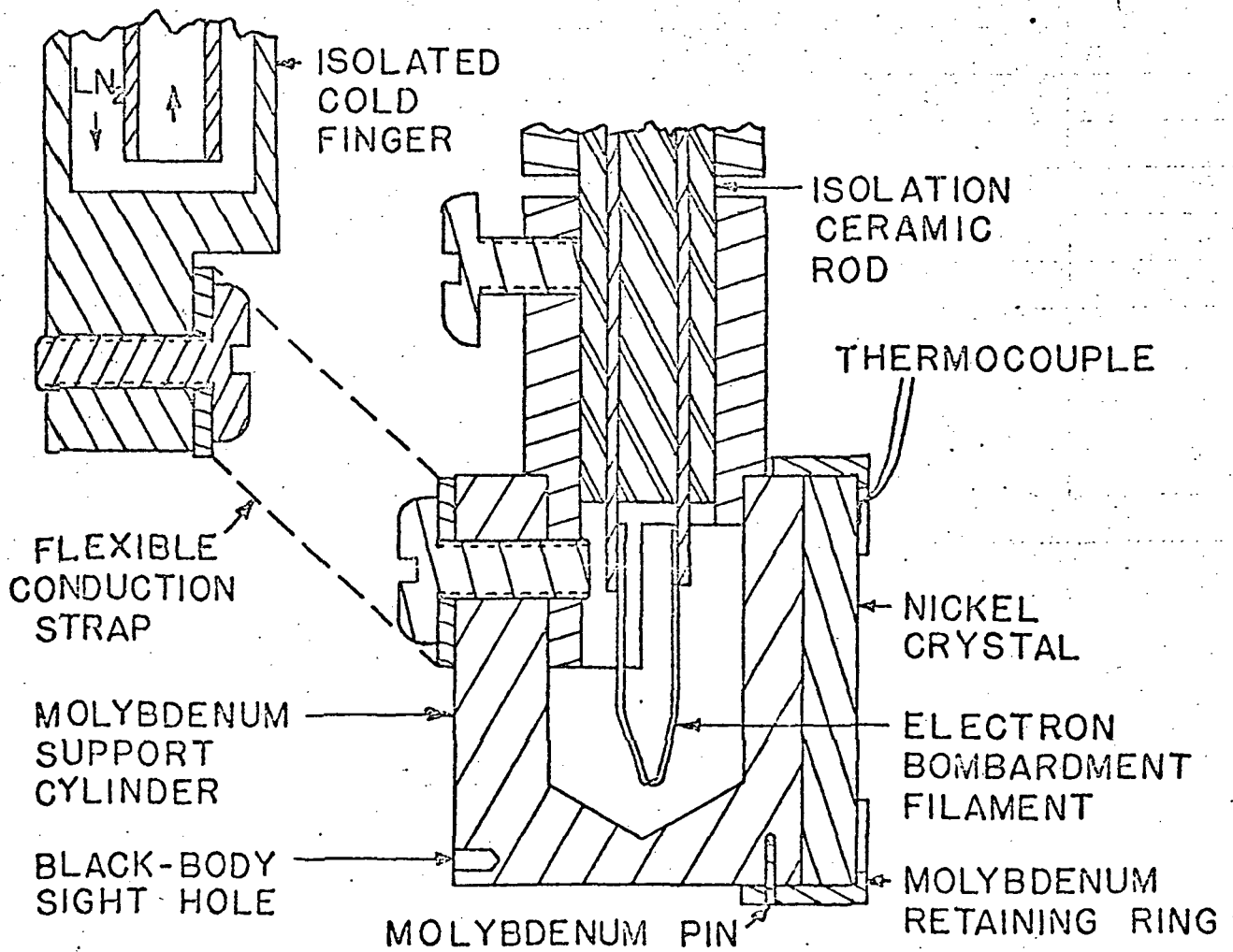
B. Substrate Configuration and Temperature Control

The substrate assembly is shown in Figure 8 and described in detail elsewhere¹⁰². The nickel substrate (Semi-Elements, Inc.) was a disk 9.5mm in diameter and 0.15mm thick and was specified to be 99.99+% pure. This was mounted on a molybdenum cylinder and pinned in place with a molybdenum retaining ring. Heating was

Figure 8 Schematic of the substrate assembly.



FRONT VIEW



SIDE SECTION VIEW

accomplished by electron bombardment from a 0.125mm tungsten filament which was totally enclosed by the mounting cylinder to prevent electron and photon leakage. The temperature was measured by a 0.076mm W-3%Re, W-25%Re thermocouple spot-welded to the nickel substrate. The temperature could also be checked by using an optical pyrometer and the black-body sight hole. The temperature was controlled by using the thermocouple output as a feed-back signal to control the circuit supplying filament power. This procedure is described in detail elsewhere¹⁰³.

The substrate was electrically isolated (to facilitate alignment and to identify artifact in the AES spectrum¹⁰⁴) and thermally isolated by the alumina support rod. To reduce the subsequent cool-down time after heat treating, an electrically isolated liquid nitrogen cold finger was incorporated into the system. It was a 6.35mm diameter stainless steel tube with an inner nylon conductor 3.2mm in diameter, and was thermally coupled to the substrate by a flexible copper strap (Figure 8). This cold finger also allowed investigations at substrate temperatures below ambient. This entire substrate assembly was mounted on a manipulator with x, y, z, and rotary motion.

C. Experimental Techniques

1) Gas phase mass spectrometry. The mass spectrometer used in this study consisted of a General Electric RF Monopole mass filter section followed by a ten stage electron multiplier. The output was amplified by an electrometer and displayed on a scope or x-y recorder. The ion source configuration was with one exception, that commonly used (see Figure 12) and consisted of focus and drawout electrodes plus an ionization cage with a thoriated iridium filament to supply ionizing electrons. The exception was that an extractor electrode was placed close to the open-ended ionization cage to improve the capture efficiency of the mass spectrometer for ions generated by EID at the substrate and to repel ions formed in the ion cage toward the analyzer section. During gas phase operation, the electrodes were biased as follows: (1) ion energy = 35V, (2) draw-out = -245V, (3) focus = 50V, and (4) extractor = 50V.

As reported, the mass spectrometer was used to measure oxygen pressures during experiments. The mass spectrometer was calibrated for both oxygen and argon against an outgassed and oxygen saturated ion gauge, thus

the calibration could be checked at the end of each experimental run by using argon and the ion gauge. The calibration of the ion gauge supplied by General Electric was assumed to be accurate and a correction based on the number of electrons in oxygen versus nitrogen was applied to obtain the true oxygen pressure¹⁰⁵. Based on variations of ion gauge sensitivities reported by Dushman and Lafferty¹⁰⁶, the measured pressure is estimated to be within 15% of the true pressure.

It was found that high oxygen pressures, which resulted in high electron multiplier currents, caused considerable fluctuation in the mass spectrometer calibration. This effect was minimized by reducing the electron ionization current to 0.1 ma or 1.0 ma at appropriate pressures. In addition, the mass spectrometer was turned off once the pressure was stabilized at the desired value. Under these conditions the mass spectrometer calibration change during a single run was normally less than 3%.

In order to study the interaction of oxygen with nickel, it is important to maintain low partial pressures of other gases in the system. The gas composition relative to oxygen versus total system pressure (estimated by the ion gauge) is shown in

Table 2 where the all peaks are referenced to $m/e = 32(O_2) = 100\%$. Although the absolute partial pressures of CO (28 AMU) and CO_2 (44 AMU) increased, the relative partial pressures decreased with increasing oxygen pressure. The relative pressures are about 1.5% at 10^{-9} torr oxygen but decrease to 0.1% at 10^{-6} torr oxygen.

The pumping speed of the system was calculated to be about 300 l/sec and recovery to 5×10^{-9} torr occurred in approximately 2 seconds and to less than 1×10^{-9} torr in about 120 seconds. A typical spectrum of residual gases is shown in Figure 9.

2) Low-energy electron diffraction. The experimental configuration used for LEED is shown in Figure 10. The filament voltage (and therefore the electron energy) was supplied by a Fluke 415B regulated power supply modified for isolated output and was typically between 30 and 200 V. The electron gun was a VEECO LEG-2 with a lanthanum hexaboride filament. Since the gun power supply was isolated, the current leaving the gun and going to ground could be continuously monitored and was shown to be equal to the current striking the sample. This current was typically 1 to 4 μA and will henceforth be termed the gun current. This current was regulated

TABLE 2

Mass Spectrometer Peak Heights of Various Gases Relative
to Oxygen Peak Height

m/e =	16	18	28	40	44	P _{total}
	8.2%	.5%	1.8%	.85%	1.3%	6×10^{-9}
	8.5	.096	.45	-	.38	7×10^{-8}
	8.4	.051	.15	-	.21	5×10^{-7}
	8.1	.028	.075	-	.16	6×10^{-6}

Figure 9 Typical spectrum of residual gases.

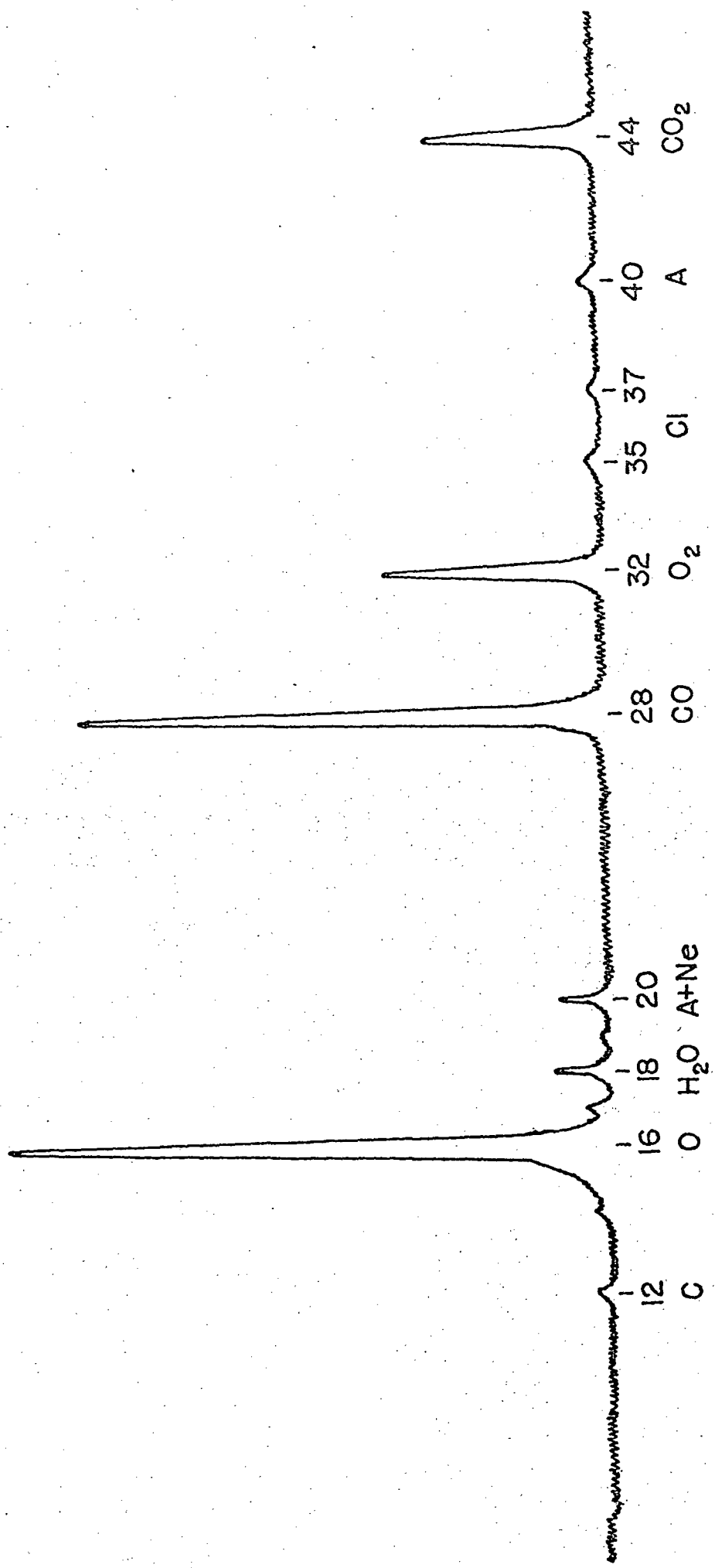
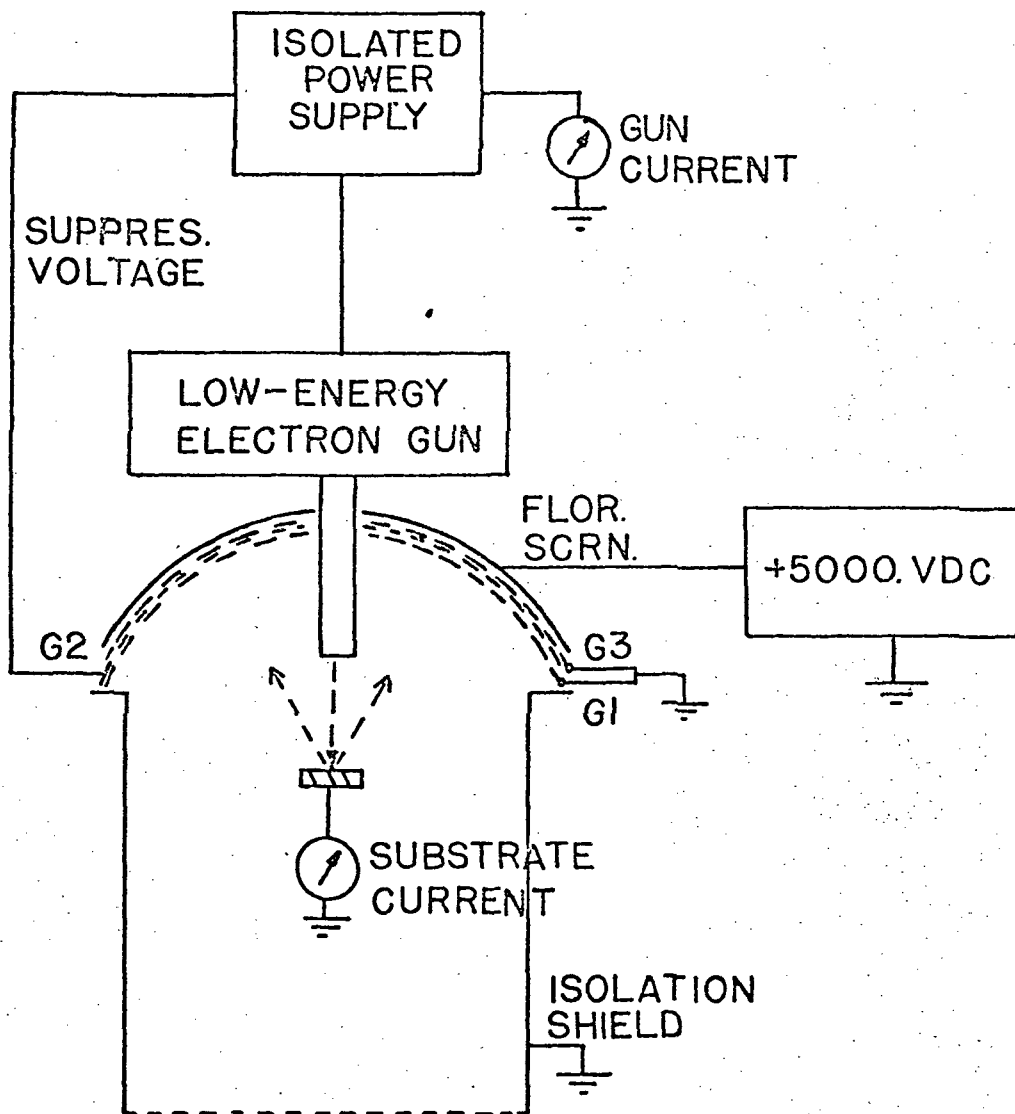


Figure 10 Experimental configuration for LEED.



by feed-back regulating the current between the filament and grid. Slow gun current drifts were still observed, but these were compensated manually in order to maintain a constant current output.

The substrate was positioned at the center of curvature of the grids and fluorescent screen and was grounded through an ammeter, thus the substrate current could be continuously monitored. Grid 1 and the isolation shield were grounded to eliminate stray electric fields which would distort the flight path of electrons and therefore the energy analyzing characteristics of grid 2. The filament voltage was applied to grid 2 and could be varied $\pm 15\text{VDC}$ about this potential in order to suppress the inelastically scattered electrons. The fluorescent screen was elevated to $+5000\text{ VDC}$ by a Spellman Model RHR 5PN 30 power supply, and grid 3 was grounded to prevent penetration of this voltage through grid 2. Elastically scattered electrons, which could surmount the energy barrier presented by grid 2, were accelerated to 5000 eV to cause fluorescence when they struck the screen. This technique of diffraction pattern display is known as the post-acceleration technique. The patterns were recorded photographically using a Crown-

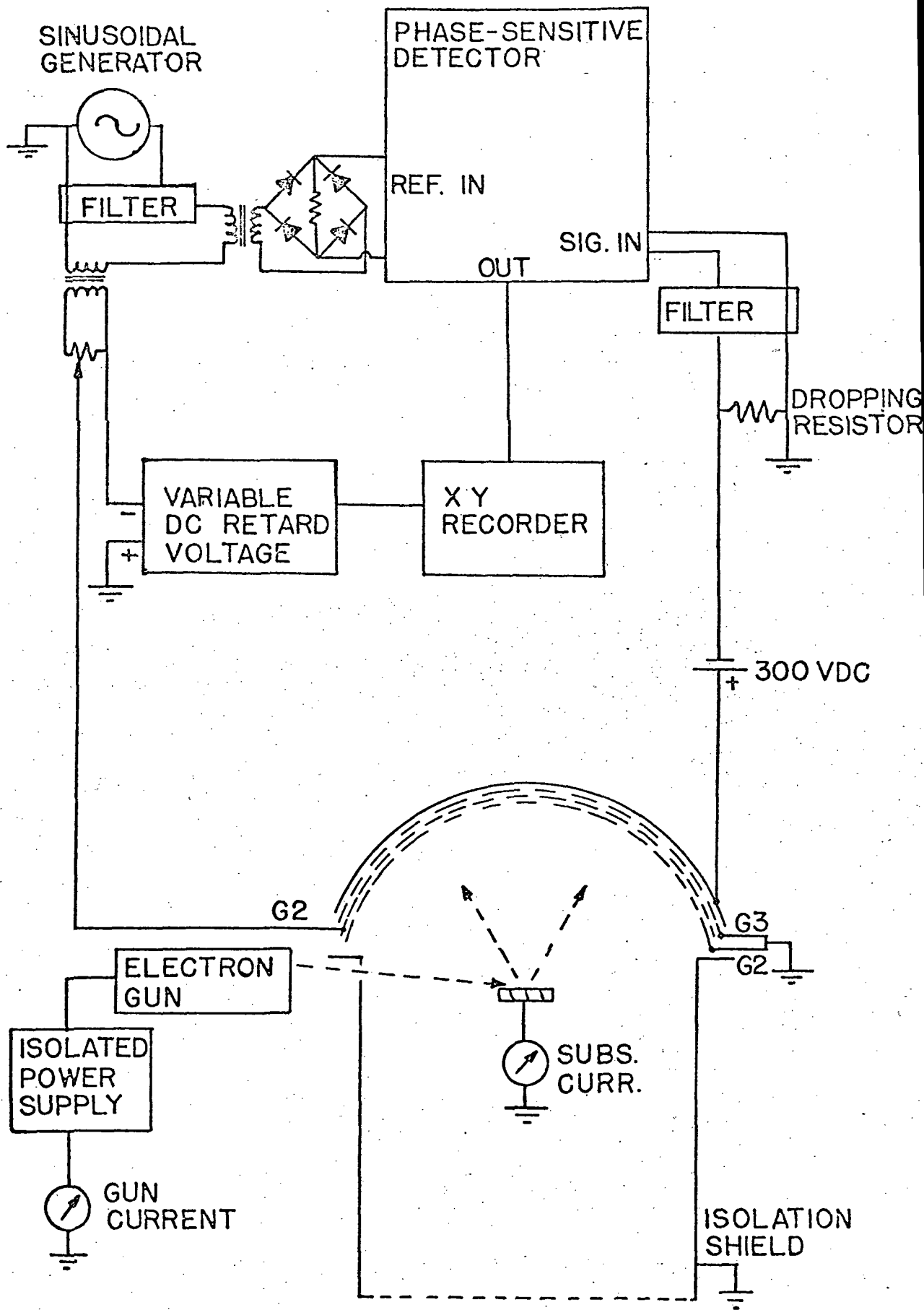
Graflex camera and 4 x 5 Polaroid film.

Small increases in carbon and calcium (285eV AES peak) on the nickel surfaces were sometimes observed after LEED analysis. This probably resulted from desorption of the elements from the LEED grids and/or fluorescent screen during LEED operations.

3) Auger electron spectroscopy. The experimental configuration used for AES is shown in Figure 11. As for LEED, the filament voltage was supplied by the modified Fluke 415B supply. The electron gun was a Superior Electronics Model 3K/5U modified with an inert, replaceable thoriated iridium filament¹⁰⁷. This filament was preferred over the original tungsten filament due to better placement and gun current, and preferred over a lanthanum hexaboride filament due to poisoning of the latter in oxygen atmospheres.

To increase the AES signal¹⁰⁸, the primary beam struck the sample at a 15° glancing angle. The gun power supply, as with LEED, was isolated, the filament to grid current was regulated, and the gun current could be continuously monitored and maintained constant. The substrate current could also be continuously monitored,

Figure 11 Experimental configuration for AES.



and grid 1 and the isolation shield were maintained at ground to eliminate stray fields. A negative voltage from a programmable Spellman Model RHR 5PN 30 power supply was impressed on grid 2, which acted as a retarding field energy analyzer.

At the same time, a 1000 Hz sinusoidal signal from a Hewlett-Packard Model 200D Audio Oscillator was passed through a passive bandpass filter centered at 1000Hz (TT Electronics Model K17) to reduce signal distortion. The filter output was used to drive an audio transformer which supplied a full wave rectified signal to the reference channel of a phase-sensitive detector, and also impressed a sinusoidal voltage across a ten turn potentiometer. This potentiometer was used to apply a variable sinusoidal voltage on top of the DC retarding voltage on grid 2. Therefore, the secondary electron current passing through grid 2 and collected on the fluorescent screen was modulated over a small energy range and created a voltage upon passing through the one megohm dropping resistor. A voltage could also be induced across this resistor by capacitive coupling between grid 2 and the fluorescent screen. Grid 3 was

grounded to suppress this coupling and thus prevent swamping the secondary electron current signal.

As discussed by several authors^{1,18,109}, the fundamental of the modulated signal is proportional to the energy distribution of electrons, i.e. to $N(E)$ in Figure 1a. The second harmonic is proportional to $dN(E)/dE$, shown in Figure 1b. We are concerned with $dN(E)/dE$ and therefore are interested in the 2000 Hz^c component of the modulated signal. Thus, the dropping resistor voltage was applied to a passive bandpass filter (TT Electronics Model K17) centered at 2000 Hz and the output applied to the input channel of the phase-sensitive detector (Princeton Applied Research, HR-8 Lock-In Amplifier). This amplifier vastly improved the signal to noise ratio by frequency and phase considerations of the input and reference signals¹¹⁰. The HR-8 produced a DC voltage output which was plotted versus retarding potential giving a $dN(E)/dE$ versus E curve as shown in Figure 1b.

A motor-driven potentiometer (Helipot Model 939) in the resistance programmed Spellman supply, was swept to obtain the energy distribution of Figure 1. Different sweep rates were obtained by step-wise variation of the

drive motor voltage.

The primary voltage for AES was 1500V and the gun current was 20 μ A unless otherwise specified. The modulation voltage was 8 VPP (volts peak to peak) for the 0-1500V region unless otherwise specified; 1 to 2 VPP modulation voltages were used in the 0-80V region.

To investigate the 0-80V region, the AES experimental configuration was as previously described except that the Spellman output voltage was divided to one tenth of its original value. Zero electron energy was established by measuring the potential on grid 2. Low energy electrons were observed which did not originate from the nickel sample. They were distinguished from the electrons originating at the substrate by negatively biasing the sample. This increased the energy of electrons from the substrate by an amount equal to the bias voltage.

4) Electron induced desorption. AES was used to study EID in this investigation. The experimental arrangement was as previously described with the various peaks being measured with time of electron bombardment. In addition, variation of the secondary emission coefficient was used to study EID. Primary electron energy for the AES arrangement was 1500V; currents up

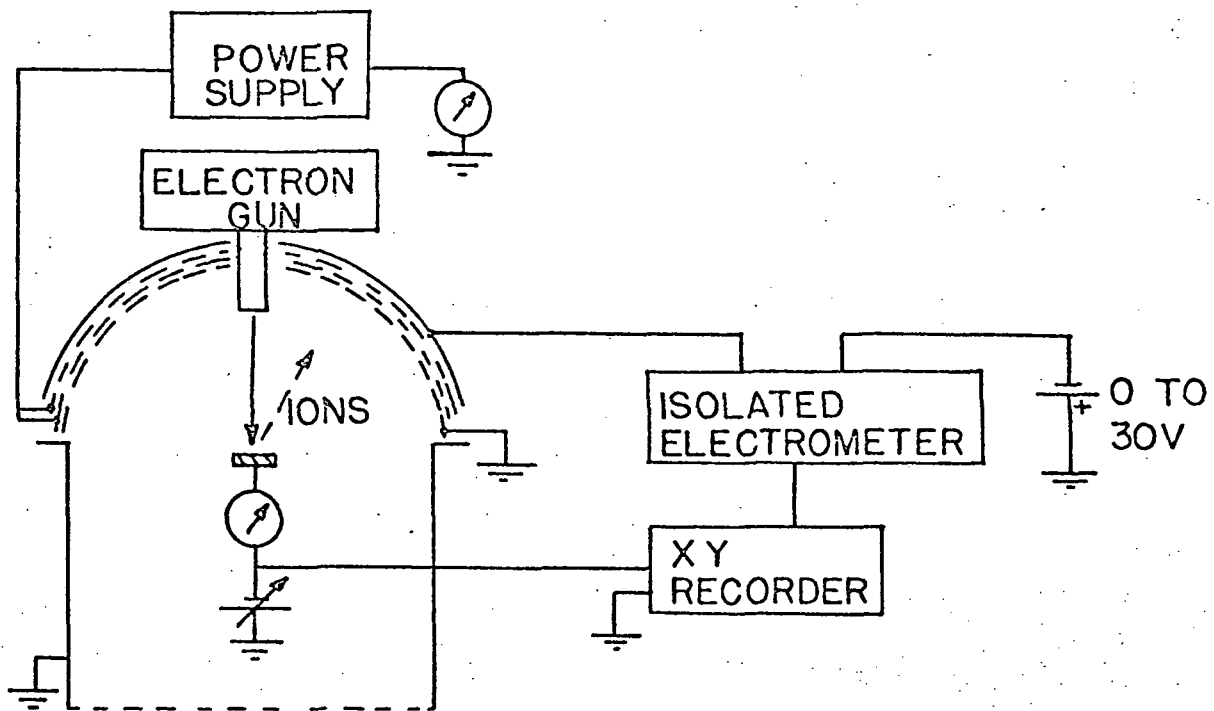
to 40 μA , and modulation voltages up to 16 VPP were used.

The system was capable of investigating the ionic species desorbed during EID both by collecting the total desorbed ion current and by mass spectrometric detection of the ions. The experimental configurations for the respective modes are shown in Figure 12a and 12b. The validity of the experimental setup was established by measuring EID of oxygen from the molybdenum support cylinder (Figure 8). No signal from nickel could be detected by the mass spectrometer arrangement and the total ion current collected was only about 10^{-13} A per μA of gun current for 100eV primary electrons. (The gun current was limited to below 4 μA .) Although variation of the substrate potential indicated that ions were being desorbed, variation of the potentials applied to grid 1, the fluorescent screen, and the isolation shield indicated extraneous contributions to the ion signal, and the data are not judged trustworthy and will not be reported.

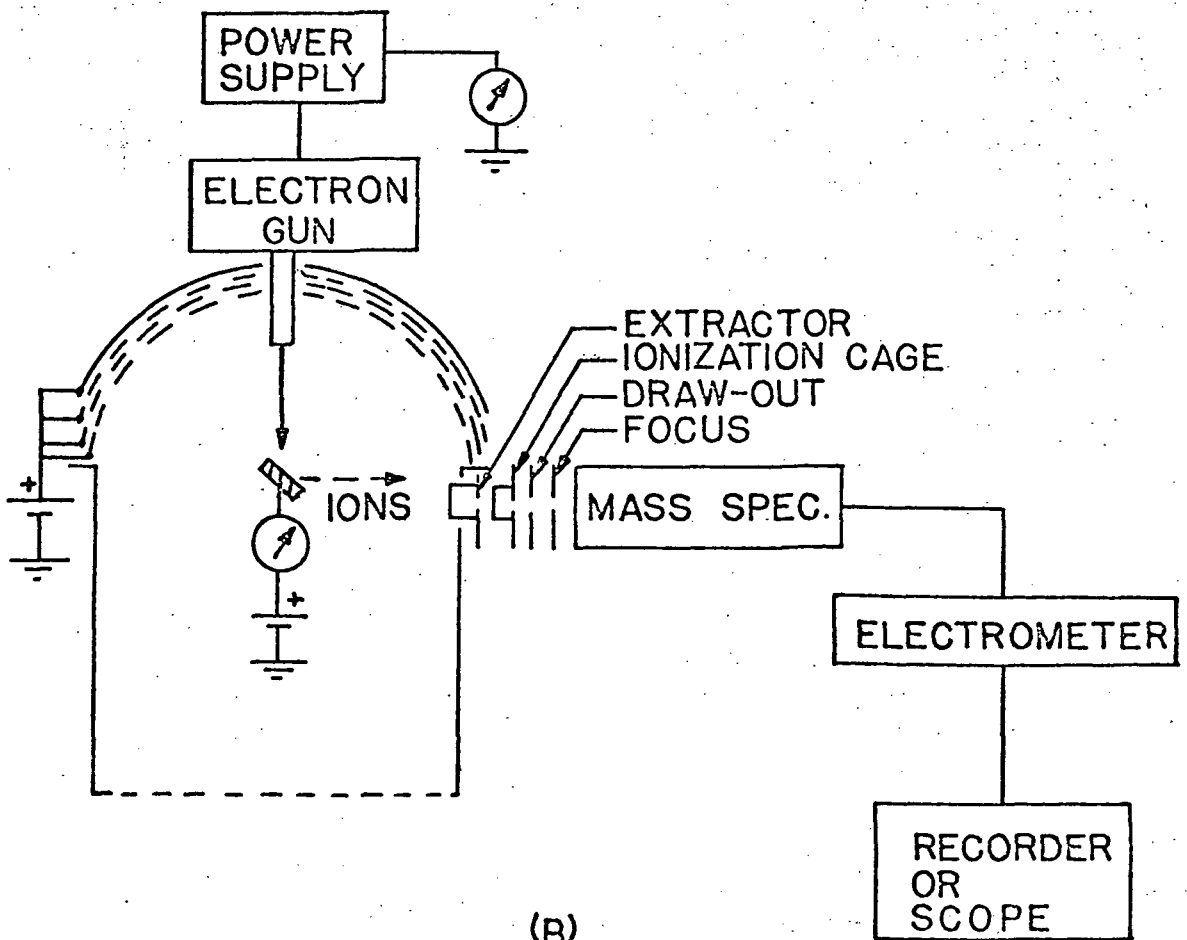
5) Work function. The variation of work function with oxygen coverage was investigated by two methods. The first method was by observing changes in the emission of secondary electrons. These changes

Figure 12 Experimental configuration for EID.

- (a) Total ion current mode.
- (b) Mass spectrometer mode.



(A)



(B)

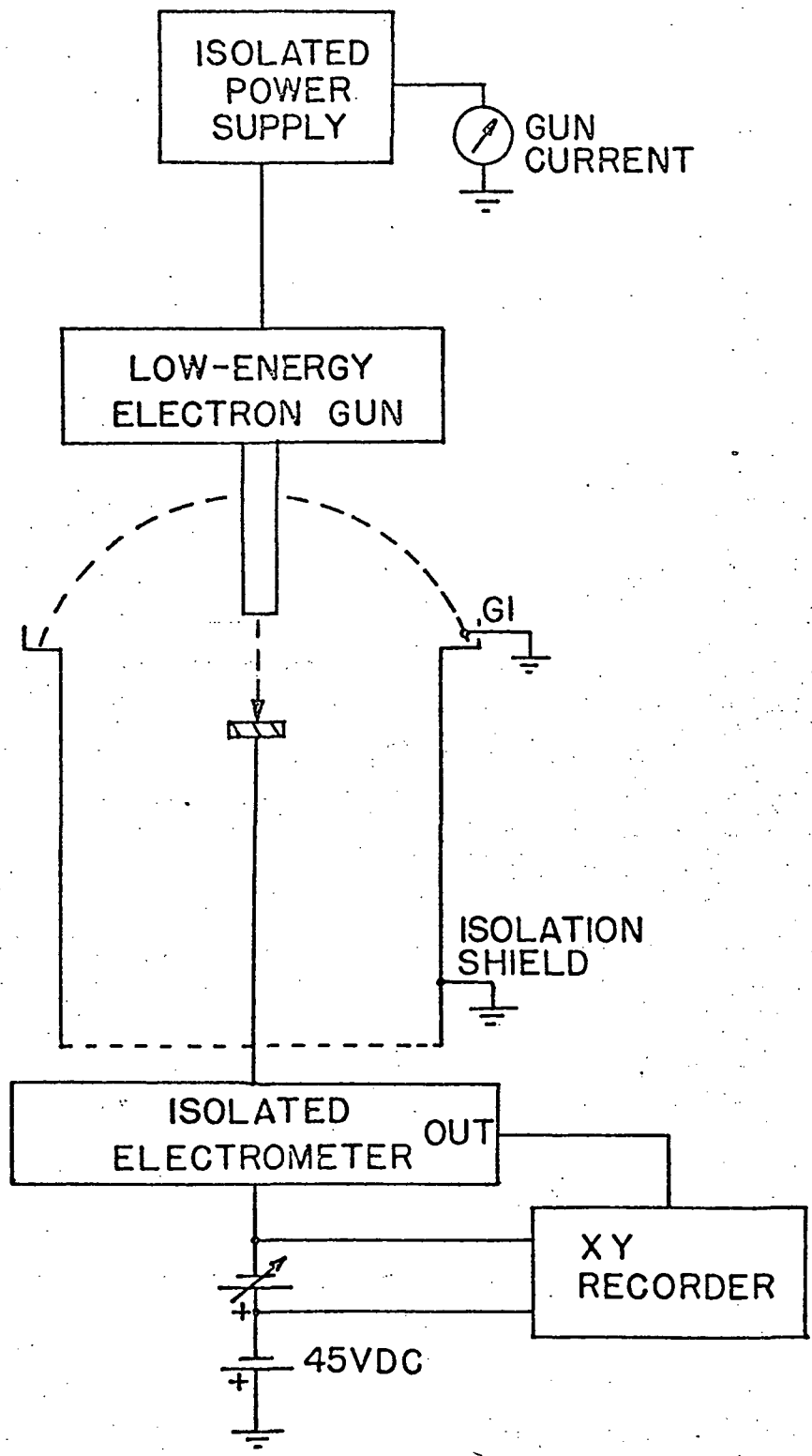
were characterized by measuring the secondary emission coefficient and by measuring the true secondary electron peak height. The experimental configuration for both measurements was the same as that for AES (Figure 11). A 20 μ A beam of 1500eV primary electrons from the AES gun struck the substrate. Since the substrate was connected to ground through an ammeter, the current to ground, i_s , could be measured. The secondary emission coefficient, δ , was calculated by

$$\delta = \frac{i_p + i_s}{i_p} \quad (5)$$

The true secondary peak height was measured with the AES configuration for the 0-80eV region discussed previously.

The second method for measuring work function changes was the retarding potential method¹¹¹, using the experimental configuration shown in Figure 13. The LEED gun was used for this experiment with an electron energy of 51eV. Grid 1 and the isolation shield were grounded to eliminate electric fields. The substrate current was measured by an isolated Keithley 602 Electrometer biased to a potential of approximately -48 VDC. This potential was varied from -46 VDC, the voltage at which

Figure 13 Experimental configuration for retarding potential measurement of work function changes.



all the 51eV electrons were collected on the substrate, to -51 VDC, the voltage at which none of the 51eV electrons were collected on the substrate. As the oxygen coverage changed parallel curves of substrate current versus bias voltage were obtained with shifts equal to changes in the work function.

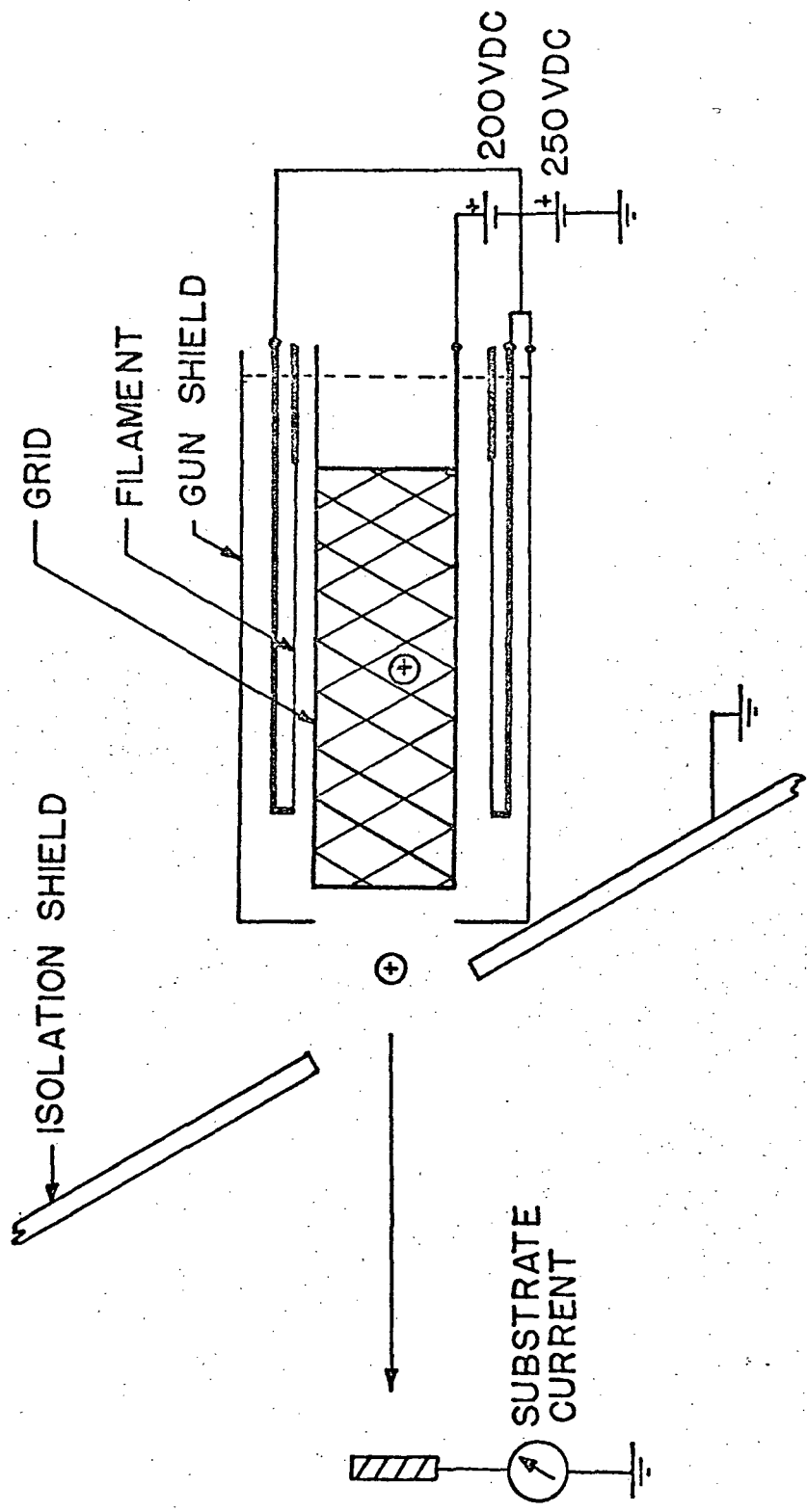
D. Ion Bombardment

The primary cleaning technique was ion bombardment (IB) with the experimental arrangement shown in Figure 14. During bombardment, the sample was rotated 135° to face the ion gun. A continuously pumped argon gas pressure of 5×10^{-5} torr was maintained during bombardment. Ions were created within the nickel grid using 200eV electrons from tantalum filaments. The ions were accelerated out of this region by the 450V potential and produced a current of 7 μ A on the substrate, i.e. a current density of approximately 10^{-5} amps/cm². A negative bias of 50 VDC on the substrate had little effect and generally was not used. Following IB, the substrate was usually annealed at 1023°K for 15 minutes.

IB was used to remove gross contamination, as when the surface was saturated with oxygen or after bake-out.

Figure 14 Experimental configuration for ion bombardment.

2



For the (111) oriented sample, cyclic IB and annealing were sufficient to reduce the sulfur concentration to undetectable limits and leave carbon and oxygen peaks which were small and resulted from adsorption of residual CO, CO₂, and O₂ at room temperature. However, for the (100) oriented sample, a large carbon peak was observed after IB and annealing and an additional cleaning technique was used. This will be discussed in the results section as will the production of sulfur-rich (111) nickel surfaces.

Ion bombardment was sometimes used to investigate the depth distribution of adsorbates. The bombarding procedure was the same in this case, but bombardment times and argon pressures were carefully controlled. Between intervals the sample was rotated to face the electron optics for AES and LEED analyses.

E. Data Collection Techniques

To reduce the time required to change between the various techniques in this study, a switching box, located near the signal sources to reduce noise pickup, was used. A change between LEED and AES could be accomplished in 30 seconds.

1) Oxygen on clean surfaces. Prior to a run, an AES spectrum (0-1000V) was taken to ensure cleanliness and a residual gas spectrum was taken for control. In many cases these were taken while the sample was cooling toward room temperature and in some cases, times of 30 minutes may have elapsed between taking the AES spectrum and starting the experiment. In these cases, the AES spectrum was spot checked for surface cleanliness and additional cleaning performed if necessary. The reaction was then studied using LEED, AES, or EID. The possibility of electron beams affecting the reaction was checked by varying the amount of gun current with time, experiments run with and without beams and hot filaments present, and by moving the beam over the surface at the end of an experiment. After establishing that there were no beam effects, LEED and AES were observed continuously or intermittently (after pumping down to residual pressure) but primarily intermittently during the run. LEED patterns were always photographed at residual pressures. EID was always studied with intermittent exposure. The general behavior of the reaction was first established by the AES technique. Subsequently, cross-references were established between techniques during a single run.

After a run was complete, reference AES (0-1000V) and residual gas spectra were taken and the mass spectrometer calibration checked against the ion gauge using argon.

The oxygen pressure, as monitored by the mass spectrometer, was varied both between runs and during a given run to check the dependency of the reaction on the oxygen pressure. The pressure range was generally from 2×10^{-9} to 1×10^{-6} torr oxygen, but some exposures to 10^{-4} torr were made.

2) Nickel surfaces pre-contaminated with sulfur.

For the surface reaction between oxygen and sulfur, electron beams and hot filaments in the presence of gas-phase oxygen were observed to increase the reaction rate, so the experimental techniques were modified slightly.

Reference AES and residual gas spectra were taken before and after a run and the mass spectrometer calibration was checked after a run. During the run, the electron gun filaments and the ion gauge filament were off when gas phase oxygen was in the system. The mass spectrometer emission current was 0.1 ma and the filament was used no more than was necessary when gas phase oxygen was present. LEED and AES analysis were performed only after pumping down to residual pressures. There

were no observable effects of electron beams or hot filaments on the reaction with only residual gases in the system.

The oxygen pressure range used in this part of the study was 3×10^{-8} to 3×10^{-6} torr.

F. Analytical Definitions

We will deal with a number of quantities and terms which are not well defined by convention or by the literature, therefore we state explicitly how they are used in this study.

The term adsorbed will be used to denote a concentration of a species in the surface region. There is no connotation as to how the species is bound in the region. The term monolayer (ML) is only used to denote a quantity of adsorbed species normalized to the theoretical atomic density of a specified crystallographic plane of nickel. The term coverage refers to the concentration of oxygen in the surface region and will be used to denote both absolute amounts of oxygen and quantities of oxygen normalized to a specified saturation concentration of oxygen. For experimental data, oxygen exposure (oxygen pressure x time) will be expressed in Langmuirs (L)

where $1L = 10^{-6}$ torr-sec. Finally, the Auger peak heights will be expressed with units (V/ μ A) where volts refer to the signal magnitude measured by the HR-8 amplifier; this is normalized to unit analyzing current by dividing by the measured gun current.

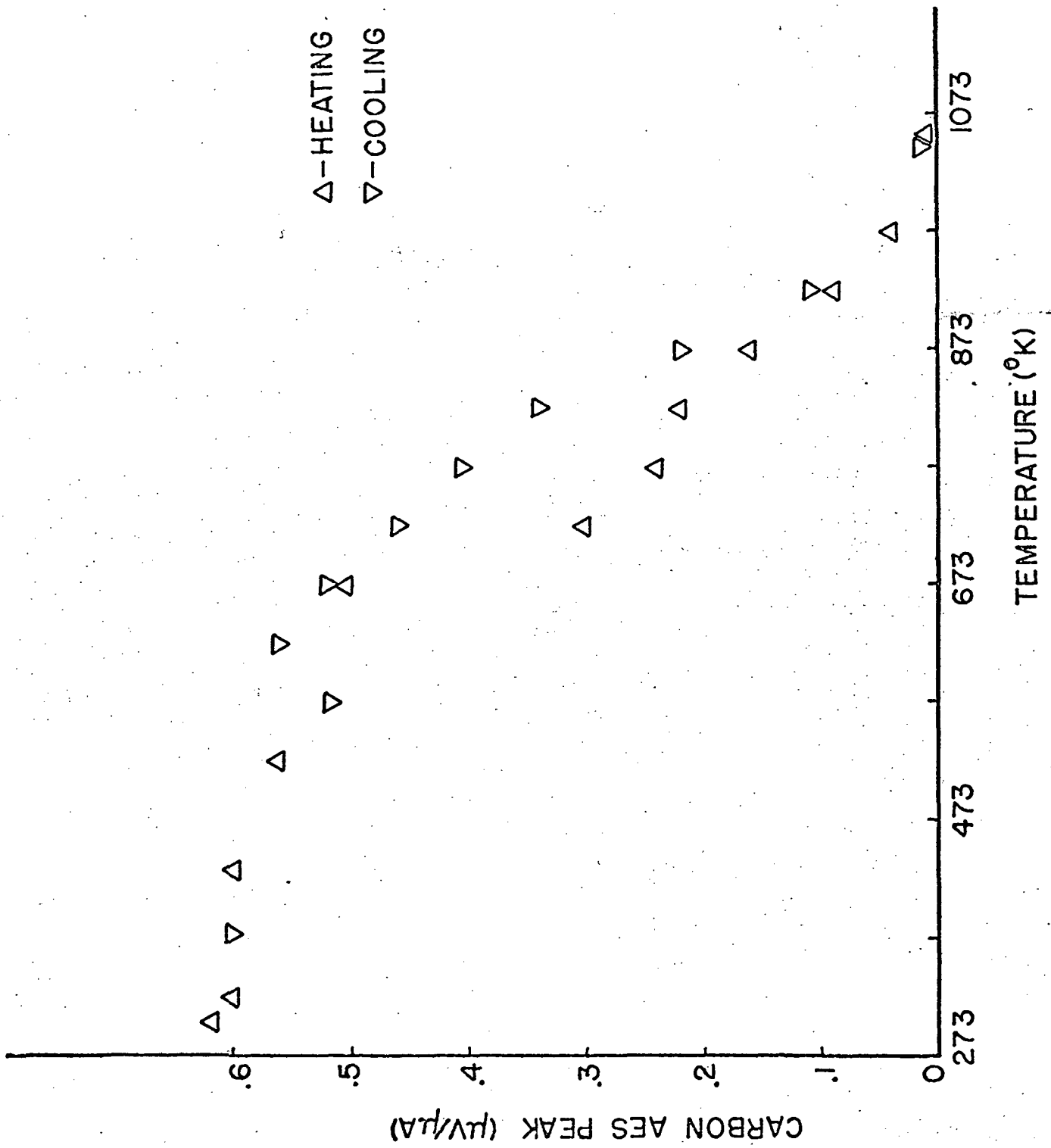
PART V

RESULTS

A. Oxygen on Clean (100) Nickel Surfaces

1) Clean (100) surfaces. The primary cleaning technique of IB and annealing left a high carbon concentration on the (100) surface. Although the magnitude varied, initially the peak was $0.6\mu\text{V}/\mu\text{A}$. Based on the oxygen calibration obtained (see below) and results for CO adsorption on platinum which showed a carbon to oxygen peak ratio (1570V primaries) of 1.35^{112} , it is estimated that this represents 0.6ML of carbon. This carbon exhibited a temperature dependent reversible segregation between the surface and bulk, which complicated the cleaning procedure. Carbon concentration versus temperature is shown in Figure 15. The most effective method to eliminate the carbon was to IB, anneal at 1023°K , lower the substrate temperature to 948°K , and backfill with 5×10^{-9} torr oxygen. A surface reaction apparently occurred to remove carbon as CO_x . AES was used to make sure that carbon was removed before pumping back to residual pressures, and to ascertain that all oxygen had dissolved before the substrate was allowed to cool. Cooling was initially

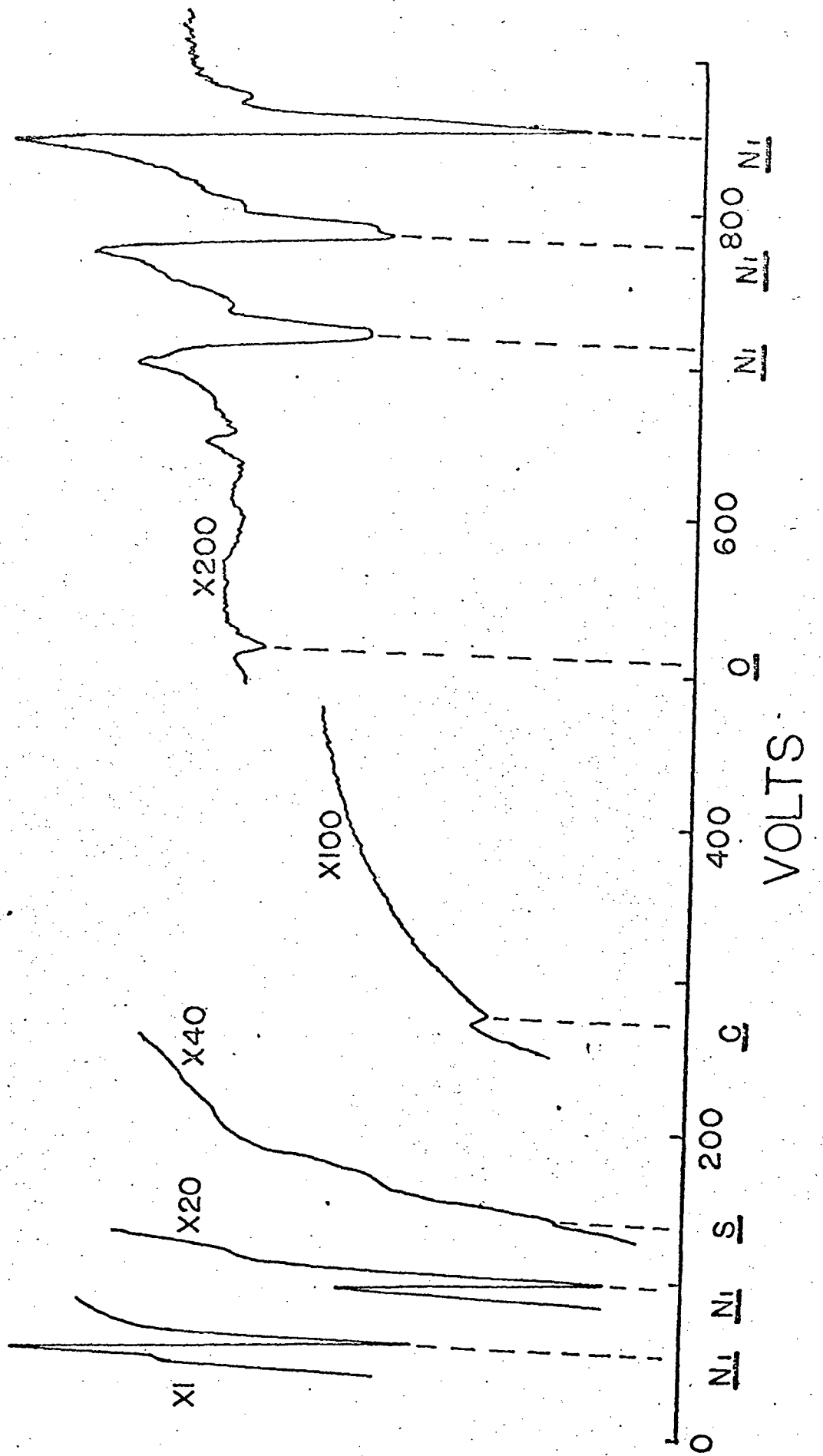
Figure 15 Temperature dependent, reversible segregation of carbon on nickel (100).



by radiational heat loss but the rate at low temperatures was increased by using the liquid nitrogen cold-finger. However, the cold-finger was not used until the residual pressure decreased below 10^{-9} torr, thereby minimizing the amount of gas pumped by the cold finger and the subsequent gas burst when it was warmed. Even with this cleaning procedure, carbon and oxygen peaks were generally observed (Figure 16) before the run was started. Presumably these peaks were caused by adsorption of residual CO, CO₂, and O₂ and some temperature induced carbon segregation during cooling. Therefore a truly atomically clean surface was not generally obtained for these studies. The average value of residual carbon and oxygen peaks, shown in Table 3, indicate average initial coverages of .095ML and .025ML, respectively. Atomically clean surfaces could be obtained momentarily by using extreme care or elevated temperatures (to prevent CO and CO₂ adsorption and to permit oxygen and carbon dissolution).

To investigate whether or not CO adsorption could produce these residual peaks and to attempt a calibration for the amount of carbon on the surface, the surface was cleaned and the ion gauge outgassed. Outgassing caused a gas pressure estimated to be

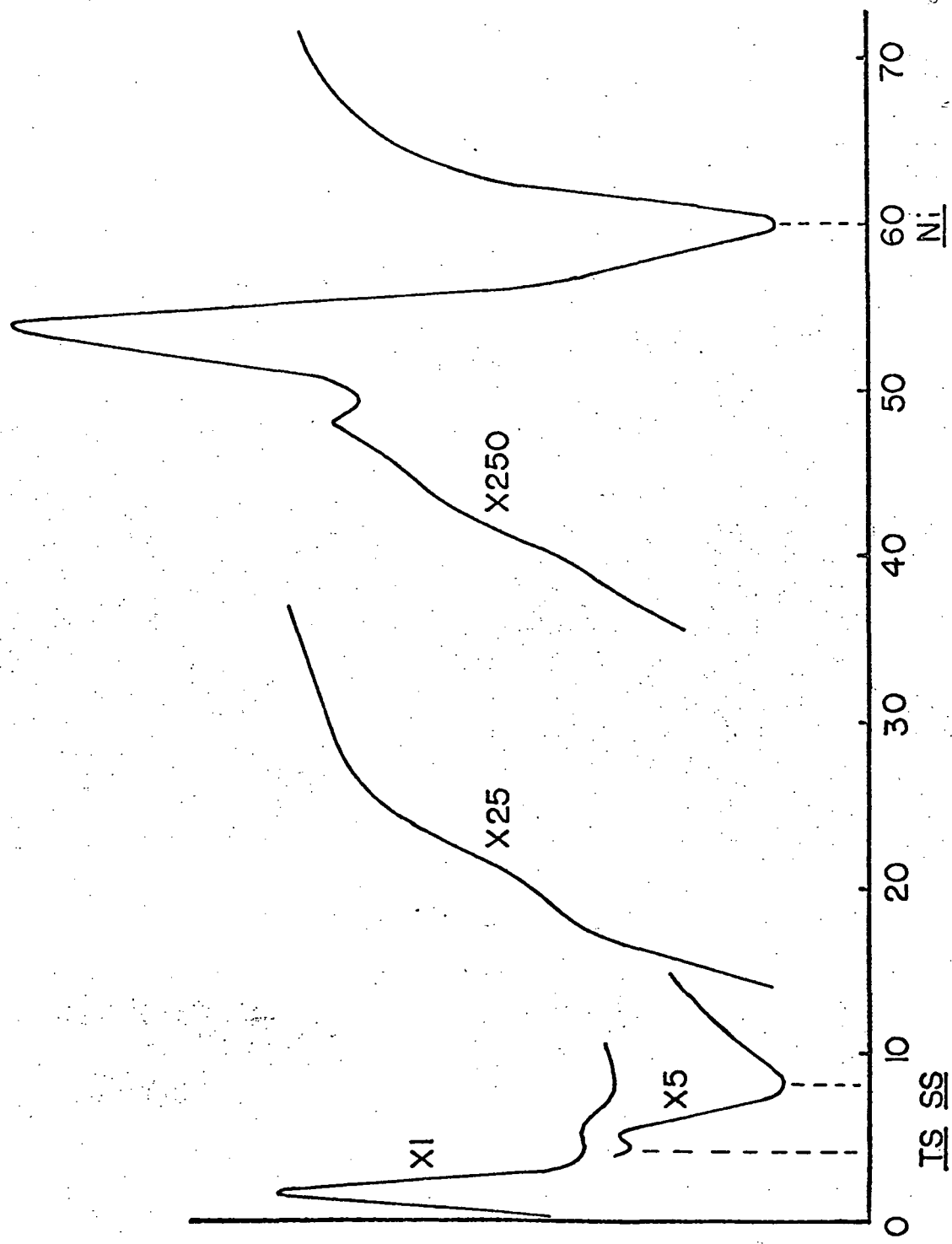
Figure 16 Typical AES spectrum from 0 to 1000V from
"clean" nickel.



10^{-7} to 10^{-8} torr which was composed predominantly of CO; some CO_2 and O_2 were also present, at least initially. The resulting carbon and oxygen AES peaks are plotted in Figure 18 and indicate an initial region where both increased, followed by a region in which only carbon increased. This occurred in the absence of the AES beam and indicates the reaction $2\text{CO} \rightarrow \text{C} + \text{CO}_2$ occurred on the surface. Others have reported self-oxidation of CO on nickel on the basis of LEED⁴ and flash work⁵⁴. Thus CO can cause a carbon peak. The oxygen peak may be due to adsorbed CO or due to interaction of the relatively clean surface with the residual O_2 and/or CO_2 .

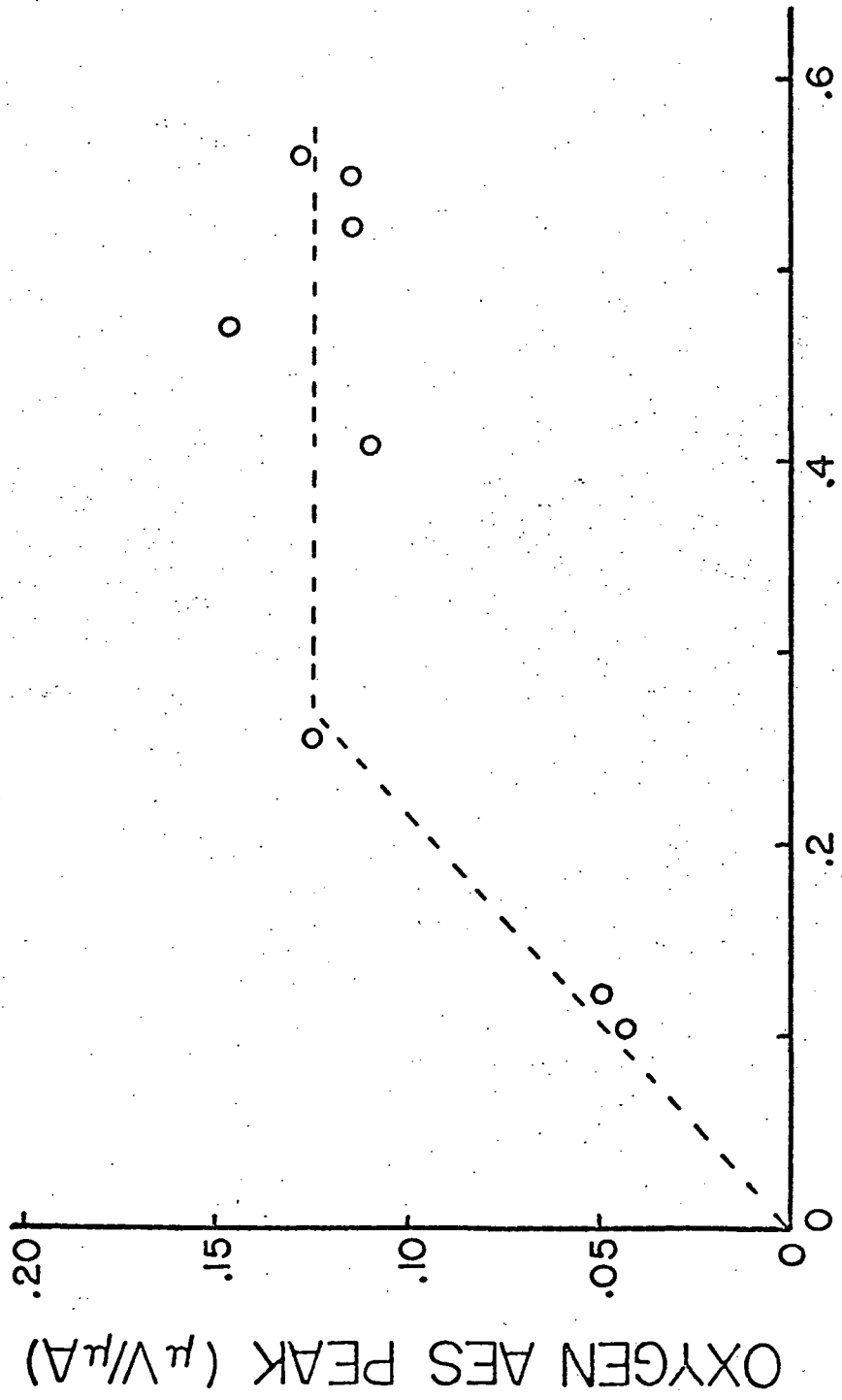
The peaks observed in the inelastically scattered electron energy spectrum are shown in Figure 16 and 17 for the range 0-1000V and 0-70V, respectively. The observed energies and the peak origins are shown in Table 4, where we have defined the peak energy by the voltage of the maximum negative derivative. The LEED pattern for the clean surface was that expected by the termination of the bulk nickel lattice on a (100) plane and the pattern is shown schematically in Figure 4b.

Figure 17 Typical AES spectrum from 0 to 70eV from
"clean" nickel (2 VPP modulation voltage).



VOLTS

Figure 18 Carbon versus oxygen AES peaks for nickel (100) exposed to CO.



CARBON AES PEAK ($\mu\text{V}/\mu\text{A}$)

OXYGEN AES PEAK ($\mu\text{V}/\mu\text{A}$)

Residual carbon did not lead to new patterns, even at coverages up to 0.6ML, but did slightly increase the background at high coverages.

2) Inelastically scattered electrons below oxygen saturation. Upon introducing oxygen into the vacuum chamber, the oxygen peak at 507eV increased in size until saturation was reached, beyond which the signal increased only under special circumstances described later. A typical spectrum at saturation, shown in Figure 19, indicates two additional peaks on the low energy side of the main energy peak. The average peak heights at saturation are shown in Table 3. The energy and origin of all three oxygen peaks are listed in Table 4 where the origin is assigned on the basis of energy levels reported by Bearden and Burr²⁶ with a correction for the ionized state as suggested by Chang¹.

The magnitude of the oxygen AES peak is shown versus exposure in Figures 20 and 21 for short and long exposures, respectively. The oxygen coverage initially increased rapidly with exposure, slowed for awhile, then increased again until the saturation value was reached.

By varying the oxygen pressure between 2×10^{-9} and 2×10^{-6} torr both during a single run and between

TABLE 3

Average selected nickel, oxygen, carbon, and sulfur AES peak heights for clean, sulfur saturated, and oxygen saturated surfaces.

Surface Condition	Ni-60eV ^a	Ni-103eV ^a	Ni-843eV ^a	O-507eV ^a	C-269eV ^a	S-150eV ^a
Clean (100) Ni	6.1x10 ²	1.8	.37	.019	.09	.0
Oxidized (100) Ni	2.2x10 ²	.24	.25	.87	.02	.0
Clean (111) Ni	5.9x10 ²	1.9	.35	.019	.04	.0
Oxidized (111) Ni	1.7x10 ²	.15	.20	.89	.04	.0
Sulfur-rich (111) Ni	3.3x10 ²	1.0	.20	.00	.004	92. (8 $\sqrt{3}$ x 2)
Oxidized sulfur-rich (111) Ni	1.2x10 ²	.083	.15	.62	.036	88. (5 $\sqrt{3}$ x 2)

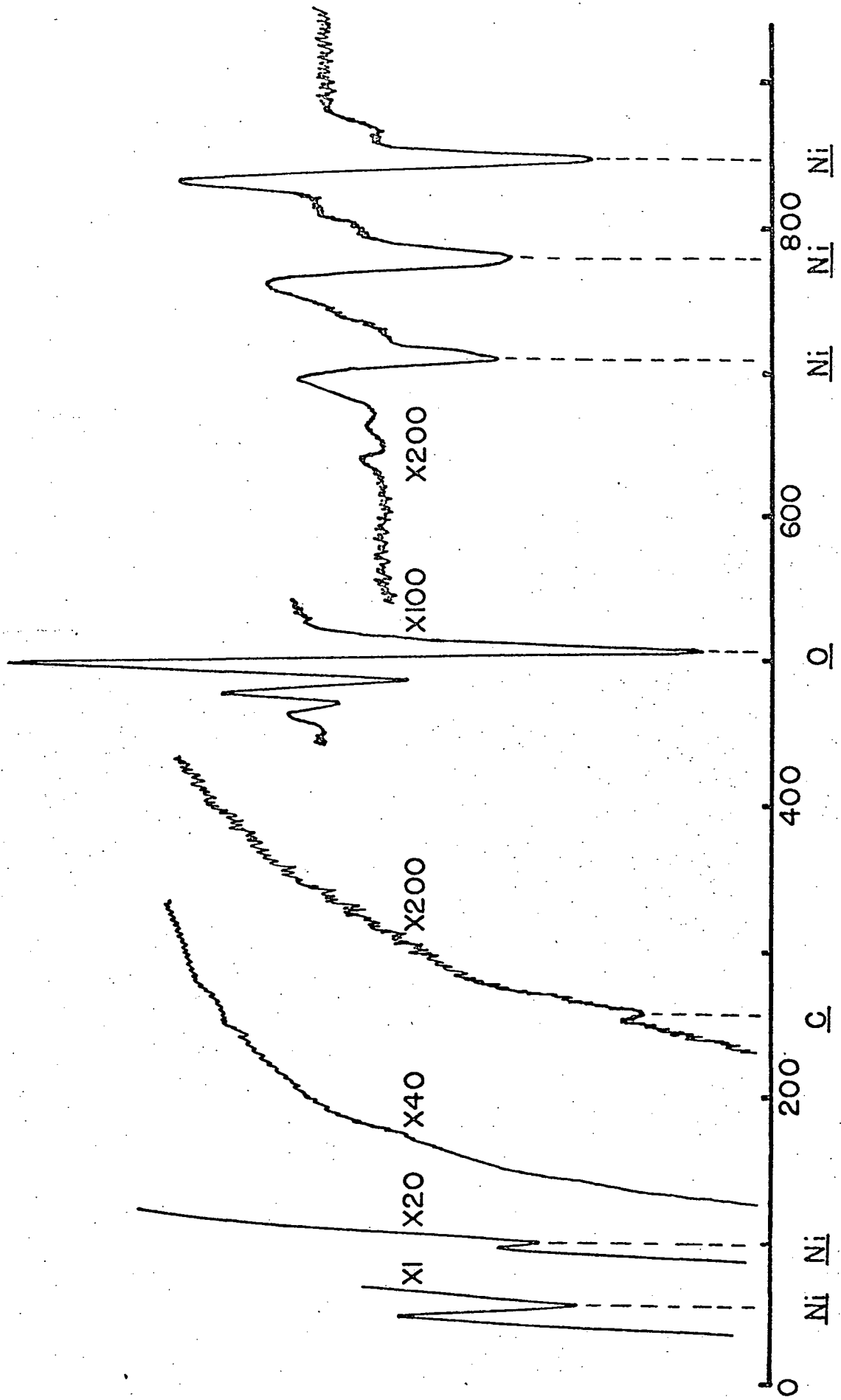
a Dimensions are $\mu\text{V}/\mu\text{A}$ indicating the magnitude of detected signal normalized to unit analyzing current.

TABLE 4

Origin and energies of peaks observed in the inelastically scattered electron energy spectrum.

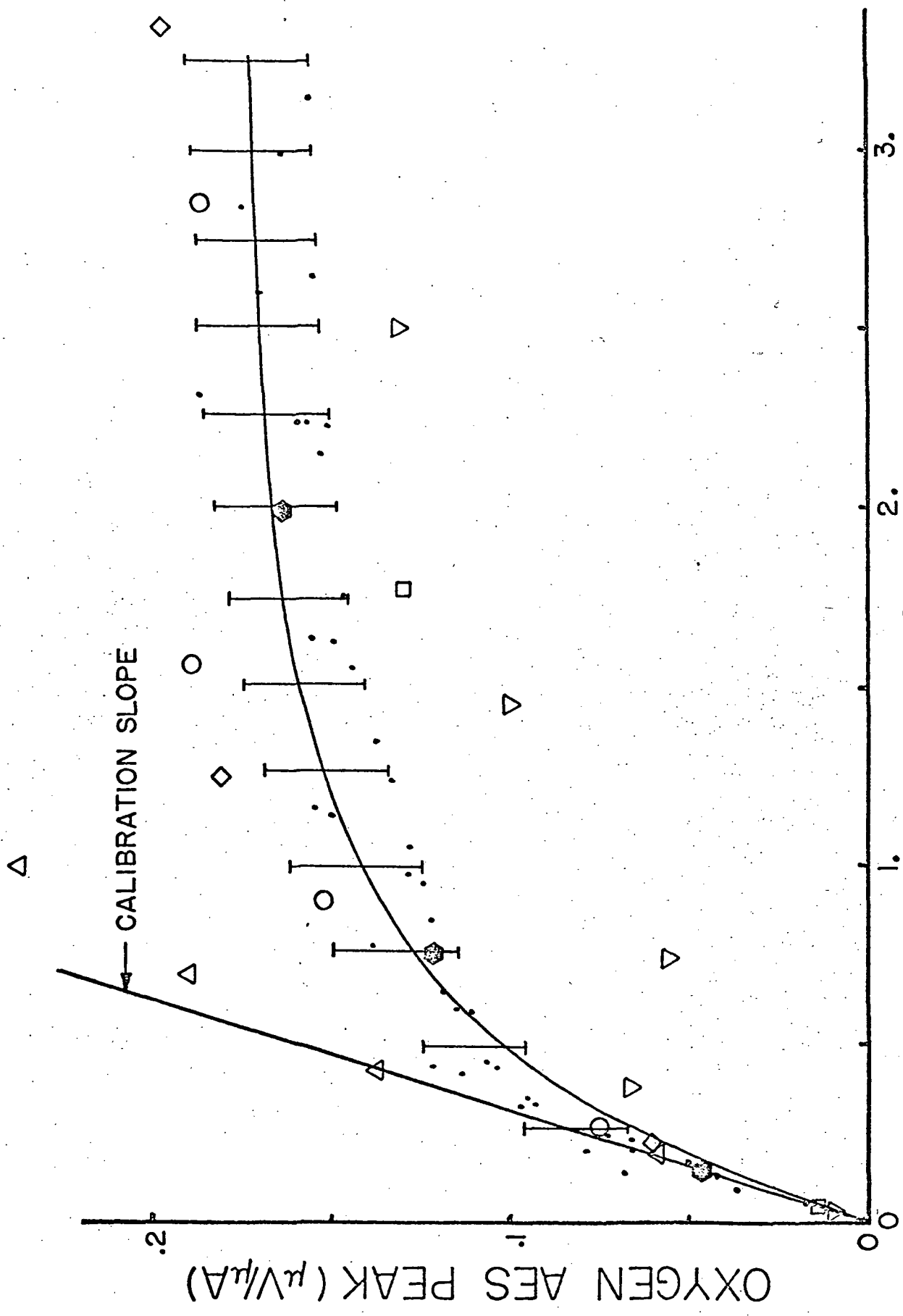
Observed Energy (eV)	Origin
<u>Nickel</u>	
8 (100 surface)	Surface State
12 (111) surface)	Surface State
49	Plasma Loss from $M_{2,3}^{VV}$
57	M_3^{VV}
60	M_2^{VV}
103	M_1^{VV}
655	$L_3^{M_1 M_{2,3}}$
680	$L_2^{M_1 M_{2,3}}$
704	Plasma Loss from $L_3^{M_{2,3} M_{2,3}}$
710	$L_3^{M_{2,3} M_{2,3}}$
728	$L_2^{M_{2,3} M_{2,3}}$
772	Plasma Loss from $L_3^{M_{2,3} V}$
776	$L_3^{M_{2,3} V}$
843	L_3^{VV}
860	L_2^{VV}
<u>Oxygen</u>	
12	$O_{NiO, NiO}$
472	L_1^{VV}
487	$KL_1 L_1$
507	$KL_1 L_{2,3}$
	$KL_{2,3} L_{2,3}$
<u>Sulfur</u>	
139	$L_3^{M_1 M_{2,3}}$
150	$L_3^{M_{2,3} M_{2,3}}$

Figure 19 Typical AES spectrum from 0 - 1000eV from an oxygen saturated surface.



VOLTS

Figure 20 Oxygen concentration versus short exposures
for (100) nickel. Δ - 147°K; $\bar{\Gamma}$ - 302°K;
 \odot - 373°K; \square - 398°K; \diamond - 423°K; ∇ - 302°K,
 $C = 0.54 \mu\text{V}/\mu\text{A}$; \circ - 302°K, IB.



OXYGEN AES PEAK ($\mu\text{V}/\mu\text{A}$)

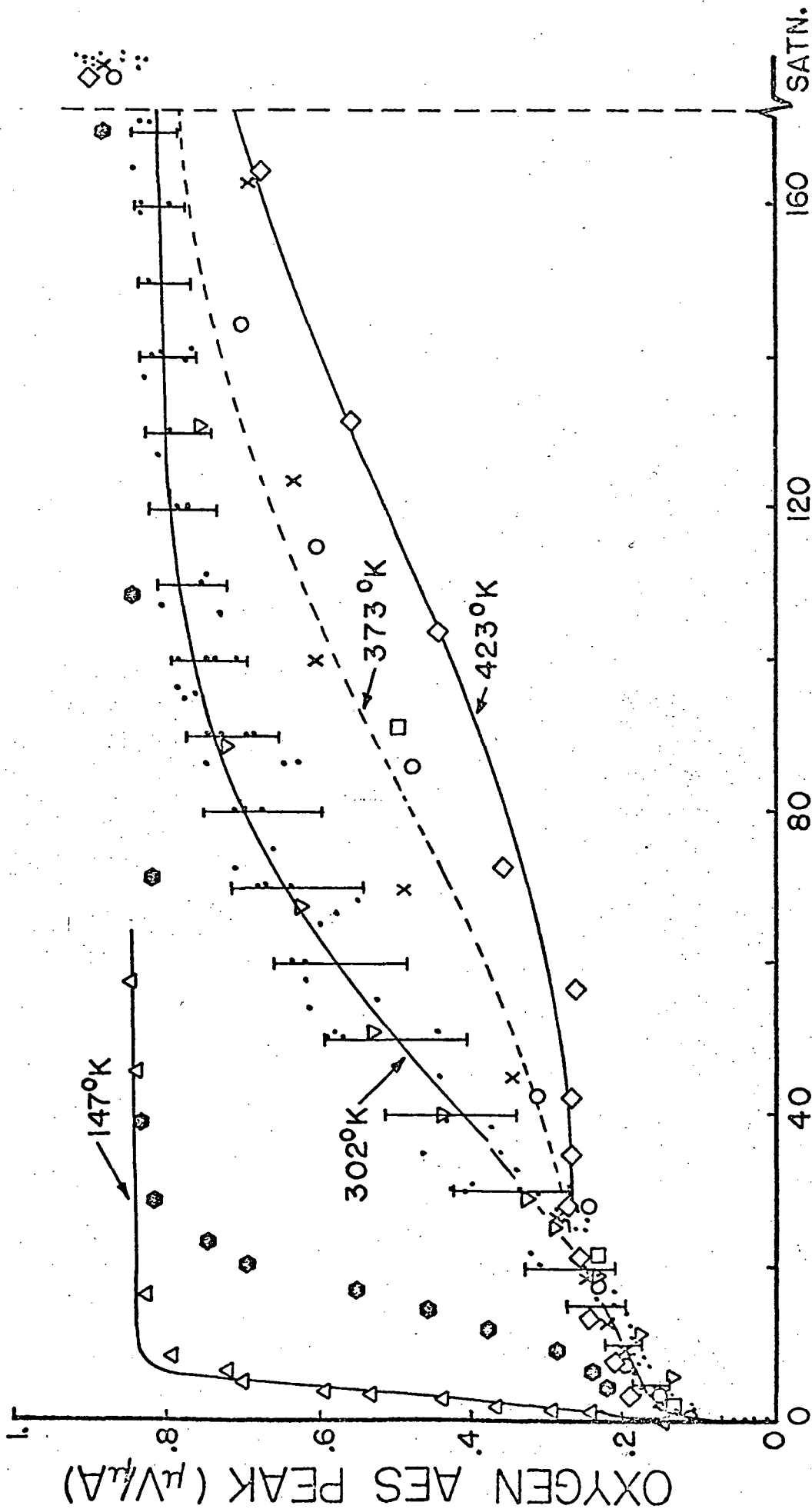
EXPOSURE $\times 10^6$ (TORR-SEC)

CALIBRATION SLOPE

several runs, it was demonstrated that, within experimental error, the exposure parameter was the controlling parameter for the reaction and this will be used throughout the study. The curve shown in Figure 21 for oxygen coverage versus exposure at 302°K (thirteen runs) has appreciable scatter as indicated by the scatter bars. The origin of this scatter is uncertain, but it probably arises largely from error in calculating exposure values, and to some extent to system alignment variation and noise which causes peak height variations between and during runs. (The noise level was approximately $0.012\mu\text{V}/\mu\text{A}$ for the instrument.) To reduce scatter due to system alignment error, all data were corrected by a factor equal to the sum of the 60eV, 103eV, and 843eV nickel peaks divided by the sum of the average of these peaks. Although this factor was up to a 10% correction, the scatter was not significantly reduced. The average values of the nickel peaks are given in Table 3 to facilitate comparison between this and future work.

Increasing the temperature slowed the reaction at coverages below saturation as shown in Figure 21, but did not significantly affect the reaction during the initial rapid adsorption (Figure 20). Decreasing the temperature to 147°K increased the reaction rate significantly.

Figure 21 Oxygen concentration versus long exposures
for (100) nickel. Δ - 147°K; $\bar{\Gamma}$ - 302°K;
O, X - 373°K; \square - 398°K; \diamond - 423°K; ∇ - 302°K,
C = 0.54 $\mu\text{V}/\mu\text{A}$; \odot - 302°K, IB.



OXYGEN AES PEAK ($\mu\text{V}/\text{\AA}$)

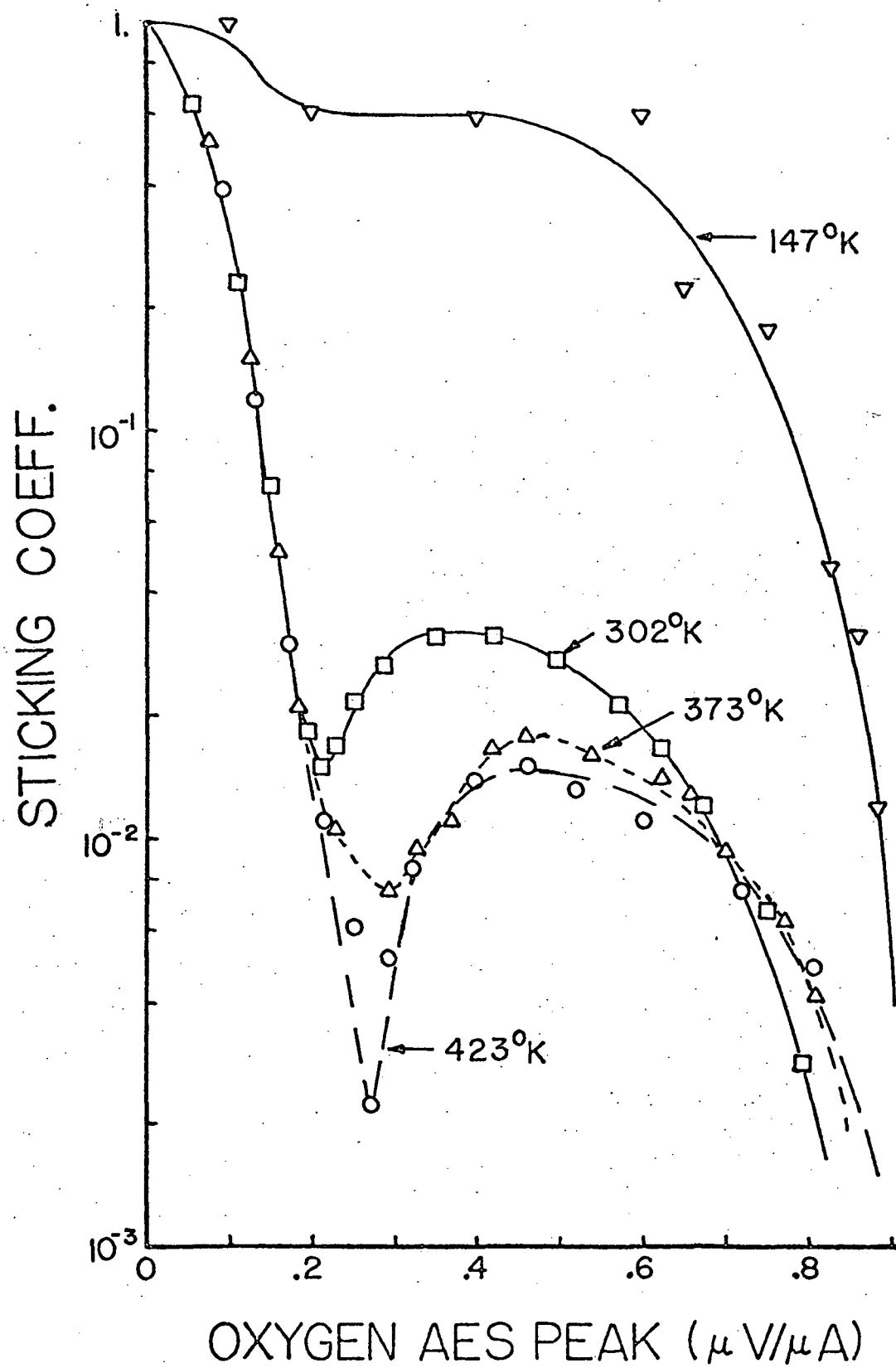
EXPOSURE $\times 10^6$ (TORR-SEC)

We would like to quantify the oxygen AES peak versus the amount of oxygen on the surface, bearing in mind the previous discussion on AES calibration. To accomplish a calibration, we consider the initial sticking coefficient for oxygen on nickel. LEED data indicate an initial sticking coefficient of unity⁵⁵, as do data by Horgan and King^{91,92}. Assuming that the maximum initial slope, shown in Figure 20, corresponds to unity sticking coefficient, a calibration constant of 4.3×10^{-16} ($\mu\text{V}/\mu\text{A})/(\text{atoms}/\text{cm}^2)$ was calculated (including data for (111) nickel reported below). On this basis, the apparent saturation concentration of oxygen is 1.2ML of oxygen atoms, i.e. greater than one layer. On the basis of this coverage plus other evidence discussed below, a depth distribution of the oxygen is expected and inelastic scattering, i.e. absorption, of Auger electrons must be carefully considered. Since the absorption effects depends on the oxygen surface morphology, we will delay discussion of such effects until after the reaction sequence has been described. Some conclusions from this discussion will be anticipated; in particular, it will be concluded that there are no absorption effects for oxygen coverages below $0.3 \mu\text{V}/\mu\text{A}$.

For low oxygen concentrations, we shall therefore indicate monolayer-equivalent values of the coverage. At saturation the true surface concentration is less than 15% greater than the uncorrected oxygen AES peak would indicate.

Since a calibration has been established between the oxygen AES peak and the coverage, and since we have anticipated that corrections for absorption effects will be relatively small, the derivative of the adsorption curves (Figure 21) may be calculated, thus yielding the sticking coefficient versus oxygen coverage for (100) nickel (Figure 22). At 302°K, the sticking coefficient, s , initially decreased rapidly to a minimum of 10^{-1} , increased to a broad plateau at 2×10^{-1} , then decreased to below 10^{-3} . The minimum occurred at slightly greater than 0.22 $\mu\text{V}/\mu\text{A}$ coverage (0.32ML) while the decrease below 10^{-3} occurred at 0.87 $\mu\text{V}/\mu\text{A}$ coverage. Decreasing the temperature increased s at high coverages; increasing the temperature decreased s , except in the initial rapid adsorption region. This behavior of s versus coverage is very similar to that reported by Horgan and King^{91,92} and by Klopfer⁸⁵.

Figure 22 Oxygen sticking coefficient versus oxygen coverage on (100) nickel.



Although the relative partial pressure of CO and CO₂ were low at residual pressures and during exposure of the sample to oxygen, accumulation of C on the surface from adsorption of CO and CO₂ plus the residual carbon left after cleaning sometimes resulted in surface carbon concentrations up to 0.15ML. This is shown in Figure 23. To determine the effect of carbon on the reaction rate of oxygen with nickel, a large concentration of carbon (.54 μ V/ μ A or .55ML) was produced by IB and annealing at 1023°K for a few hours. (No sulfur was detected after this treatment.) The concentration of carbon on this surface versus oxygen coverage is shown in Figure 23. Oxygen coverage versus exposure for this surface is shown in Figures 20 and 21 and indicates that the oxygen coverage in the initial rapid adsorption region was lower than on a clean surface, but the adsorption behavior beyond this region was normal.

To explore further the carbon which accumulated when oxygen reacted with nickel, the (100) surface was exposed until the carbon coverage maximized at an oxygen coverage of about 0.2 μ V/ μ A. The substrate was then flash heated and the CO and CO₂ peaks observed mass spectrometrically. Only a CO peak was observed, at

about 623°K and subsequently AES indicated the carbon peak had disappeared. Thus the accumulated carbon was in the form of CO which desorbed at 623°K. We will later discuss the significance to the oxygen/nickel reaction of both of the above experiments.

In order to check the possible effects of ion bombardment induced defects on the oxygen/nickel reaction, a clean surface was produced and was ion bombarded for five minutes at 302°K. The secondary electron spectrum after bombardment showed 0.36 $\mu\text{V}/\mu\text{A}$ (0.36ML) of carbon, 0.07 $\mu\text{V}/\mu\text{A}$ (0.1ML) of oxygen, and a peak due to occluded argon which could still be detected after oxygen saturation. This bombardment treatment significantly increased the reaction rate of oxygen with nickel after the initial rapid adsorption region as shown in Figures 20 and 21. However, a similar five minute IB of a clean surface, carried out at 473°K, had no detectable effect on the oxygen/nickel reaction at 302°K; the data were well within the scatter for other 302°K data, even though occluded argon was detected by AES.

3) Low energy secondary electron spectrum.

The secondary electron spectrum from 0 to 80 eV was investigated during oxygen interaction and significant

Figure 23 Carbon AES peak heights versus oxygen concentration for (100) nickel.

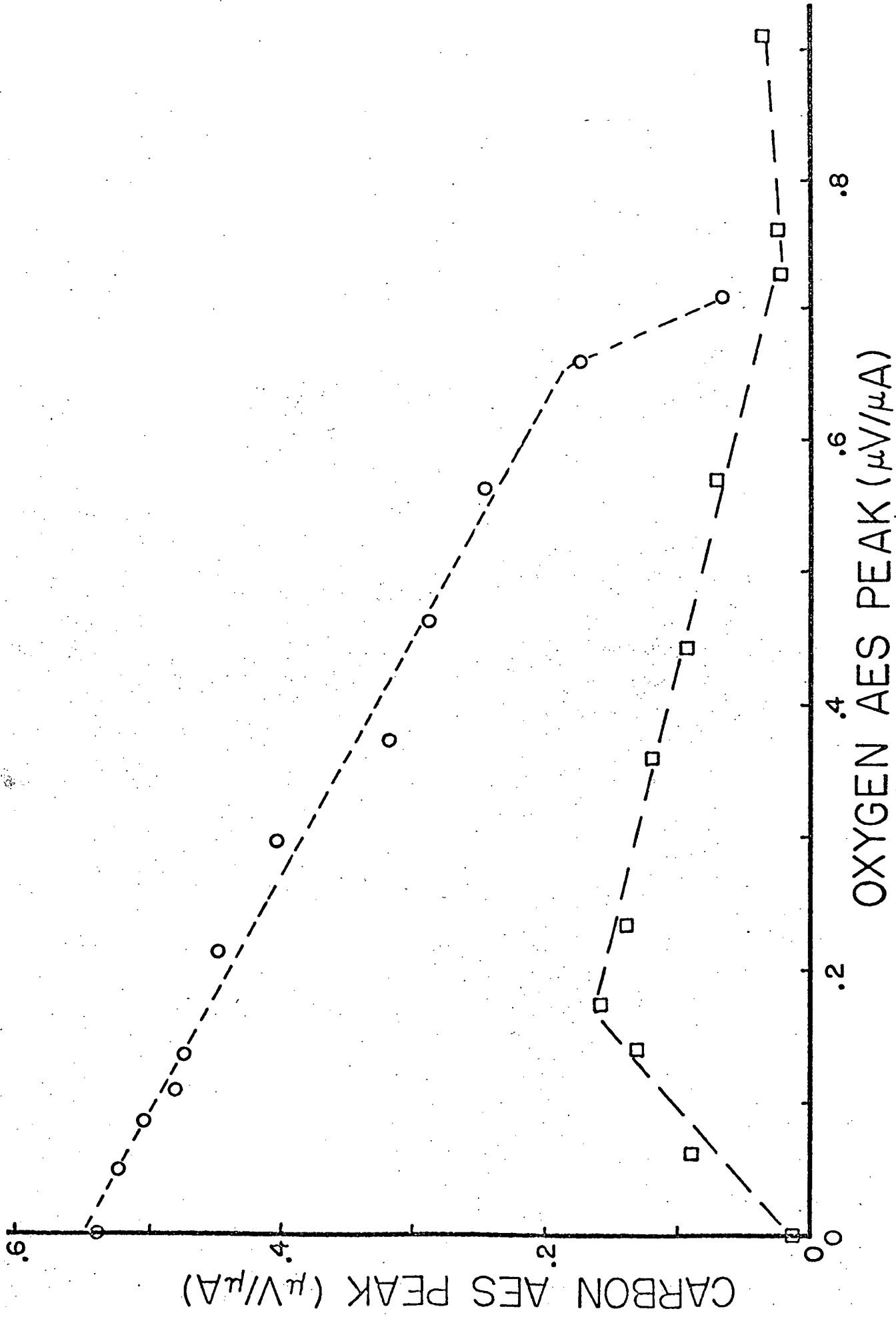
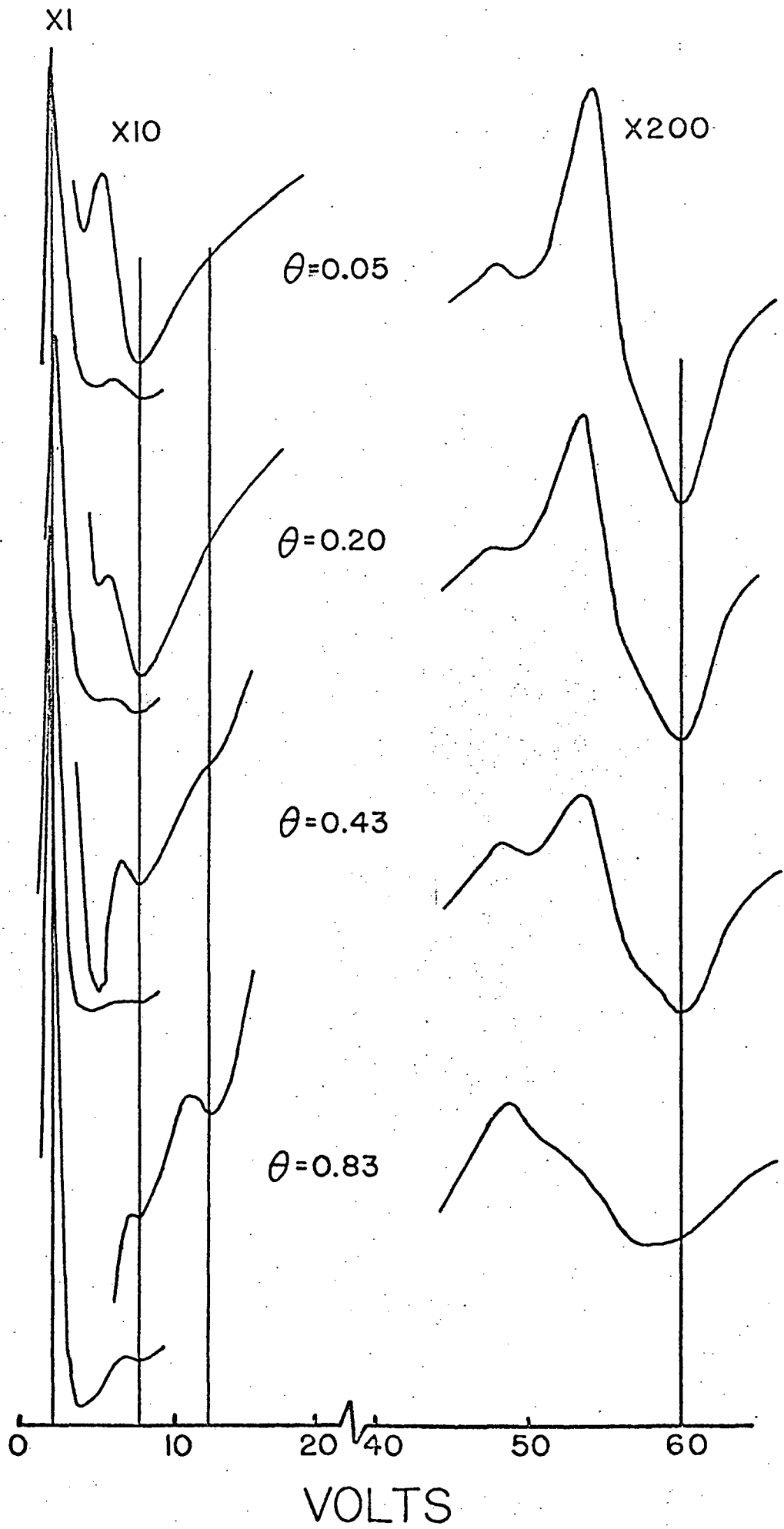


Figure 24 Changes in secondary electrons peaks between 0 and 70 eV as a function of oxygen coverage on (100) nickel (1 VPP modulation voltage; oxygen coverage in $\mu\text{V}/\mu\text{A}$).



changes were observed. The spectrum from 0-70eV for a clean surface, shown in Figure 17, had a peak due to true secondary electrons near zero energy, a peak at 8eV, and a nickel peak at 60eV. (The slope changes shown in Figure 17 at 20, 28, and 40 eV are not believed to be caused by the nickel substrate since they did not respond to oxidation as did the other peaks.) Spectra from 0-70eV with increasing oxygen coverage are shown in Figure 24. For the clean surface, the true secondary peak has a maximum positive derivative at 1.6eV and a width between derivative maxima of 2.3eV. During the initial rapid increase in oxygen coverage, the true secondary peak height remained almost constant while the maximum positive derivative and the width between derivative maxima increased. Above $0.3\mu\text{V}/\mu\text{A}$ oxygen coverage, the peak height increased, and at saturation oxygen coverage the maximum positive derivative had decreased to 1.1eV and the peak width decreased to 1.8eV. The 8eV peak from the clean surface continuously decreased as the oxygen coverage increased, while a new peak at 12eV appeared at oxygen signals greater than $0.3\mu\text{V}/\mu\text{A}$. The 60eV nickel peak initially decreased in intensity without changing its shape as oxygen coverage increased.

However, above $0.3\mu\text{V}/\mu\text{A}$ oxygen signal, new derivative maxima at 49 and 57 eV increased in intensity as the oxygen coverage increased. At oxygen saturation, these new maxima dominated and the entire peak shifted about 3eV lower in energy. The origin of the 12eV peak and shifts of the 60eV peak will be discussed later.

4) Work function changes. To demonstrate that variations in the emission of secondary electrons reflected variations in the work function due to adsorbed oxygen, changes of the work function were measured by the retarding potential method and are compared to the secondary emission coefficient, oxygen coverage, and temperature in Table 5 and, with the secondary emission coefficients in Figure 25. The data are numbered in order of increasing oxygen exposure in Figure 25. It can be seen that changes in δ do reflect changes in the work function but that the relation was not linear. When the work function increased, δ decreased and vice versa. Data points in Figure 25 labelled 16-18 were taken at 147°K and will be described shortly.

In addition to δ , changes in the true secondary electron peak height are expected to correlate with work

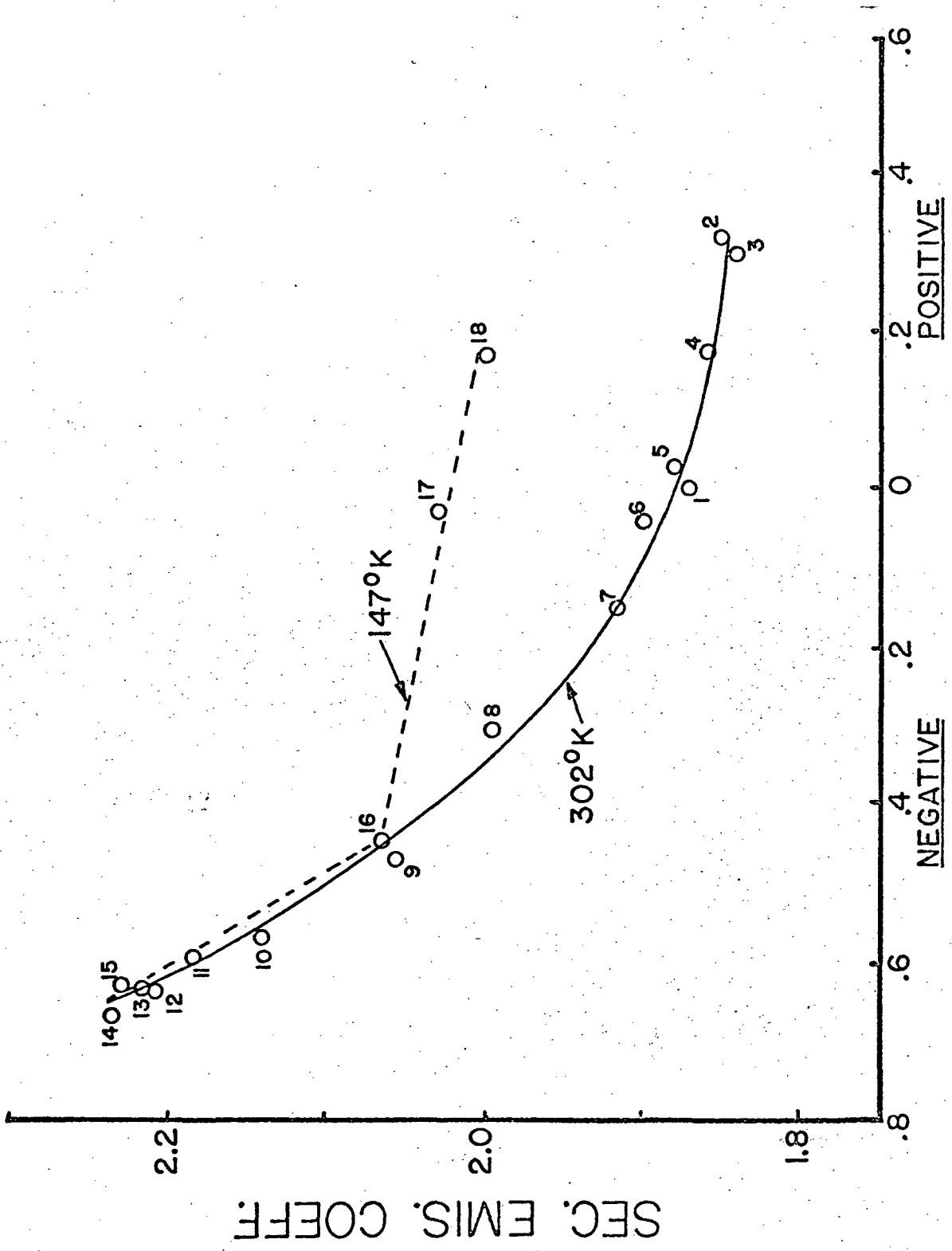
TABLE 5

Work function changes versus secondary emission coefficient, oxygen coverage, and temperature on (100) nickel.

$\Delta\phi$ (volts) ^a	δ	θ_0 ($\mu\text{V}/\mu\text{A}$)	T ($^{\circ}\text{K}$)
0.0	1.92	0.075	302
+0.32	1.90	0.15	302
+0.30	1.89	0.18	302
+0.18	1.91	0.21	302
+0.02	1.93	0.25	302
-0.05	1.95	0.29	302
-0.16	1.97	0.34	302
-0.31	2.05	0.44	302
-0.48	2.11	0.57	302
-0.58	2.19	0.68	302
-0.60	2.24	0.78	302
-0.64	2.26	0.84	302
-0.64	2.27	0.86	302
-0.67	2.29	0.87	302
-0.64	2.28	0.88	302
-0.45	2.12	0.88	147
+0.04	2.08	0.89	147
+0.17	2.05	0.93	147

a Positive indicates an increased work function; negative indicates a decreased work function.

Figure 25 Secondary electron emission coefficient versus changes of the work function for oxygen on (100) nickel. (Positive denotes increased work function; negative denotes decreased work function.)



WORK FUNC. CHANGE (VOLTS)

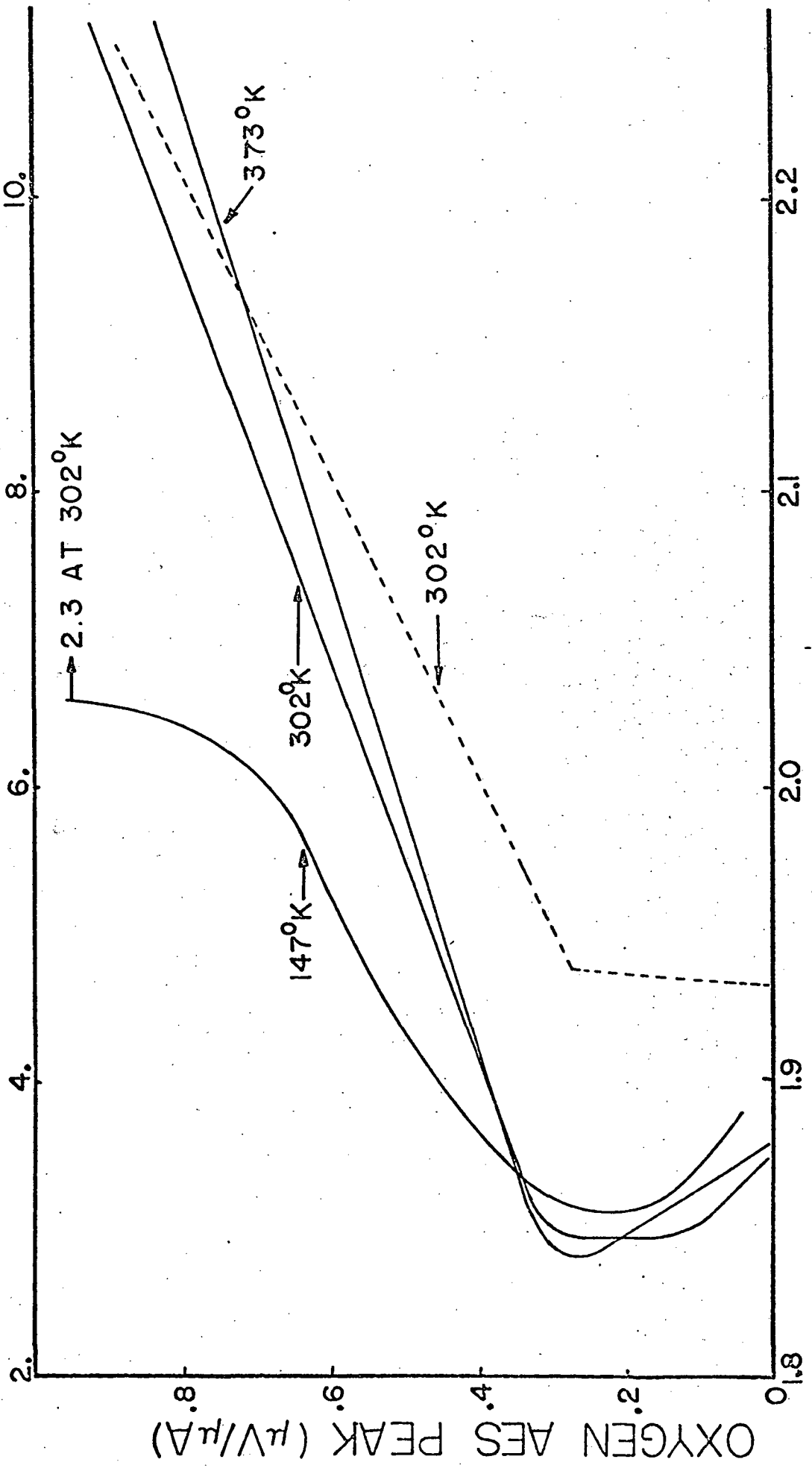
function changes. Variations of δ and the true secondary peak height are used to indicate changes in the work function versus oxygen coverage as shown in Figure 26. During the initial rapid adsorption of oxygen, the changes in δ indicated that the work function increased. By comparison with Figure 25, the maximum increase was 0.3 volts. Changes in the true secondary peak indicated that the work function initially decreased slightly; the increased true secondary peak height is believed to result from interference with the 8eV peak which decrease in height as oxygen coverage increased.

The position of the maximum positive derivative and the width between the derivative maxima of the true secondary peak may also be used to characterize the work function variations. The true secondary peak maximum shifted to higher energies and the peak broadened as the work function increased, and vice versa as the work function decreased.

With increased oxygen coverage beyond $0.3\mu\text{V}/\mu\text{A}$, both δ and the true secondary peak height increased, indicating a reduction in the work function to a value below that of the clean nickel surface. By comparison with Figure 25, the maximum negative work function change

Figure 26 The secondary emission coefficient (solid lines) and the true secondary electrons peak height (dotted line) versus oxygen coverage on (100) nickel.

TRUE SEC. PK. HT. ($mV/\mu A$ - DOTTED LN.)



SEC. EMIS. COEFF. (SOLID LN.)

was 0.6 volts. The behavior of δ with oxygen coverage was similar for temperatures above 302°K except that the work function increased slightly more at low coverage and decreased slightly more at higher coverages. At 147°K, the initial behavior of δ was similar, but the work function did not decrease at saturation to a value as low as at 302°K. However, upon warming the sample to room temperature in residual vacuum, δ did increase to a value consistent with previous 302°K data. To demonstrate that δ truly reflected changes of the work function in this case, a surface saturated with oxygen at 302°K was cooled to 147°K and exposed to oxygen. As shown in Figure 25 (data points 16-18), the retarding potential measurement indicated that the decrease in δ was associated with an increase in the work function to above the clean surface value. However, the δ - work function relationship was not the same as previously observed at 302°K. The reasons for this will be discussed later.

To further investigate the variation of δ (and therefore the work function) with temperature, a surface was saturated at 147°K and warmed to higher temperatures as rapidly as possible. Changes in δ and the oxygen AES

peak height were monitored. The oxygen peak height decreased by about $.03\mu\text{V}/\mu\text{A}$ upon warming from 147°K to 373°K . The peak then increased about $.03\mu\text{V}/\mu\text{A}$ upon recooling to 147°K and exposing the surface to oxygen, thus indicating a reversibly adsorbed oxygen species. However, δ was a more sensitive measure of changes on the surface. Upon warming from 147°K to 192°K , a rapid decrease followed by an exponential time decay for δ was observed. After δ stabilized, warming to 221°K , 245°K , and 373°K produced similar results. Near 147°K , the magnitude of the rapid decrease and of the exponential decrease of δ were both about 0.05. Near 300°K , the magnitude of the rapid decrease of δ was about 0.005 and the exponential decrease was about 0.03.

This behavior indicates that a weakly reversibly bound species is adsorbed on the oxygen rich surface with a total coverage of about $.04\text{ML}$ (absorption effects are negligible in this case). The decrease of surface coverage and increase of δ as the temperature increased indicated desorption of this species. The fact that this occurred over such a large range of temperature indicated a range of adsorption energies for the species. The adsorption energy range may be calculated from the

measured time constants for the increase of δ (Table 6) since the mean stay time, τ , for an adsorbed species may be written:

$$\tau = \tau_0 e^{E_a/RT} \quad (6)$$

where τ_0 is the desorption attempt frequency, E_a is the adsorption energy, and T is absolute temperature. Assuming $\tau_0 = 10^{-13} \text{ sec}^{-1}$, the adsorption energy is found to range from 12 to 25 kcal/mole (Table 6).

5) Oxygen coverage beyond saturation. Under normal operating conditions, the concentration of oxygen on nickel did not increase beyond the saturation value of about $0.87 \mu\text{V}/\mu\text{A}$. However, if the substrate was exposed to oxygen for long times at 147°K , or at 302°K with a high partial pressure of oxygen, then further uptake was observed. This is shown in Table 7, where after 2180L at 147°K with 1.6×10^{-7} torr oxygen, the oxygen concentration increased to $0.98 \mu\text{V}/\mu\text{A}$. After 2.5×10^6 L at 302°K with 1×10^{-4} torr oxygen, the oxygen concentration increased to $1.05 \mu\text{V}/\mu\text{A}$. At 302°K , δ was decreased when oxygen was in the system indicating that the work function increased at an oxygen pressure of 10^{-4} torr. Data from a control test at 302°K with

TABLE 6

Adsorption energies calculated from changes of the secondary emission coefficient at various temperatures.

τ (sec)	T ($^{\circ}$ K)	E_a (kcal/mole)
120	170	11.7
155	221	15.3
390	245	17.5
110	373	25.6

TABLE 7

Conditions for which oxygen coverage increased beyond the saturation value.

Condition	Exposure $\times 10^6$ (torr-sec)	Time (sec)	Oxygen Pk. Ht. ($\mu\text{V}/\mu\text{A}$)
$T = 147^\circ\text{K}$ $P_{\text{O}_2} = 1.6 \times 10^{-7}$ torr	96.	6.0×10^2	0.88
	548.	3.4×10^3	0.93
	1650.	1.03×10^4	0.97
	2180.	1.36×10^4	0.98
$T = 302^\circ\text{K}$ $P_{\text{O}_2} = 1.6 \times 10^{-7}$ torr	120.	7.5×10^2	0.81
	5760.	3.6×10^4	0.89
$T = 302^\circ\text{K}$ $P_{\text{O}_2} = 1 \times 10^{-4}$ torr	2.25 (1×10^{-6} torr)	2.25	0.88
	7.4×10^4	7.4×10^2	0.90
	9.8×10^5	9.8×10^3	0.94
	2.5×10^6	2.5×10^4	1.05

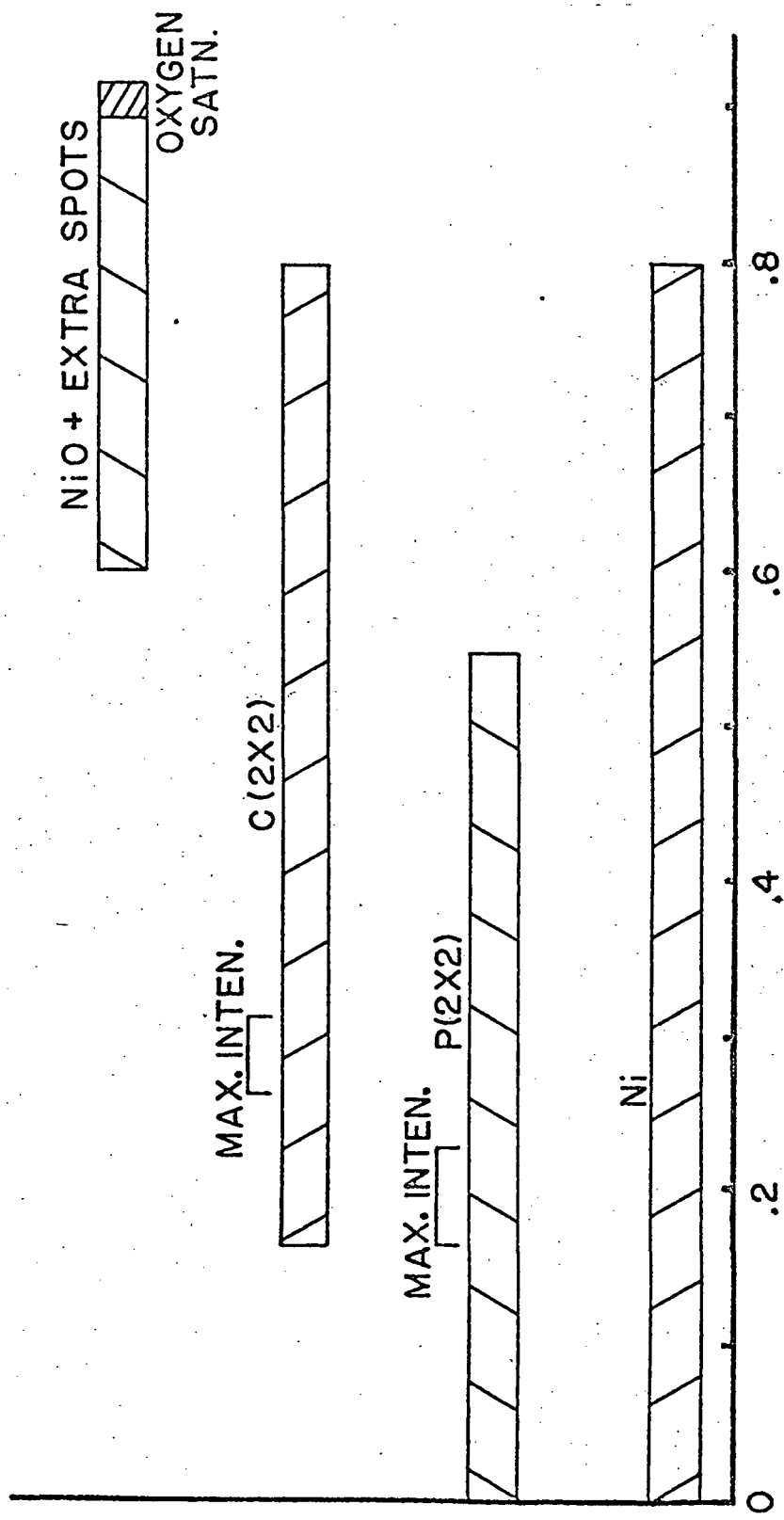
1.6×10^{-7} torr oxygen are also shown in Table 7 and indicate that the saturation concentration was not exceeded.

A discussion of the magnitude of the effect of inelastic scattering on the measured oxygen signal at these higher coverages will be delayed until the discussion section. We will anticipate the conclusion that absorption effects are very significant in this case. Because of this fact plus experimental difficulties in working at high oxygen pressures, this additional oxygen uptake was not studied in detail.

6) Low-energy electron diffraction. The LEED patterns observed in previous studies of oxygen on (100) nickel, shown in Table 1, were largely confirmed in this study (see especially references 55 and 56). At room temperature and low exposures, streaks were observed through the $h + \frac{1}{2}k + \frac{1}{2}$ positions and were parallel to the [10] and [01] reciprocal lattice directions but did not pass through the integral order spots. They indicate a one-dimensional disorder at low coverages. With increasing exposure, the streaks sharpened into spots forming a $p(2 \times 2)$ structure. The maximum intensity of

a diffraction pattern was very crudely estimated by judging intensities from consecutive photographs taken under nearly identical conditions and correlated with AES. The ranges of detectible and maximum intensities versus oxygen coverage at room temperature for the $p(2 \times 2)$ structure was judged by the $(\frac{1}{2}0)$ spots (Figure 27). The same information for other patterns is also shown in Figure 27. For the $p(2 \times 2)$, the maximum intensity was observed in the coverage range of 0.16 to 0.22 $\mu\text{V}/\mu\text{A}$ (which will be shown to be 0.23 to 0.32 ML) and, surprisingly, the $(\frac{1}{2}0)$ spots were observed up to 0.55 $\mu\text{V}/\mu\text{A}$, although the intensities are very low at this coverage. Beyond 0.16 $\mu\text{V}/\mu\text{A}$ coverage, the $(\frac{1}{2}\frac{1}{2})$ and corresponding spots increased in intensity, marking the onset of the $c(2 \times 2)$ surface structure. This occurred without streaking or diffuseness, contrary to the $p(2 \times 2)$ case. The $(\frac{1}{2}\frac{1}{2})$ spot reached maximum intensity between 0.27 to 0.31 $\mu\text{V}/\mu\text{A}$ (0.39 and 0.45 ML), but a $(\frac{1}{2}\frac{1}{2})$ spot was distinguishable up to 0.8 $\mu\text{V}/\mu\text{A}$ coverage. At a coverage of 0.6 $\mu\text{V}/\mu\text{A}$ the background intensity had increased and a very diffuse NiO pattern was observed, the intensity of which increased until saturation. The oxide (100) plane was parallel to the

Figure 27 Ranges and maximum intensities of LEED patterns versus oxygen coverage on (100) nickel.

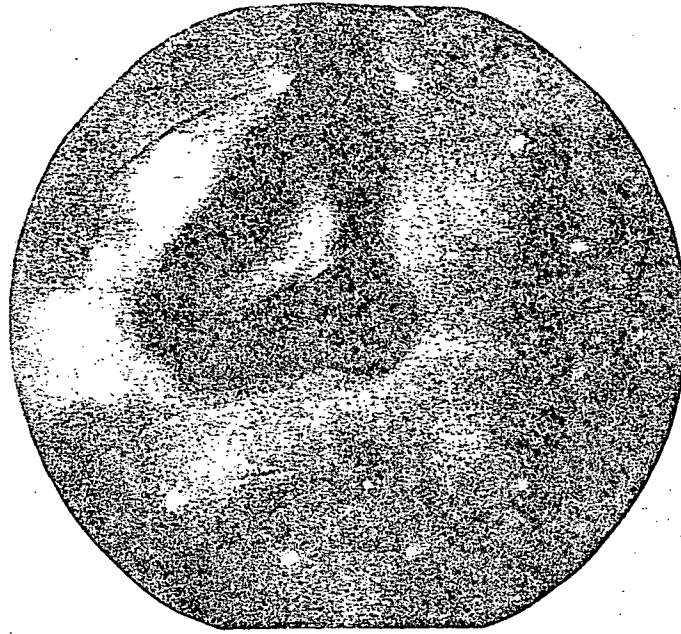


OXYGEN AES PEAK ($\mu\text{V}/\mu\text{A}$)

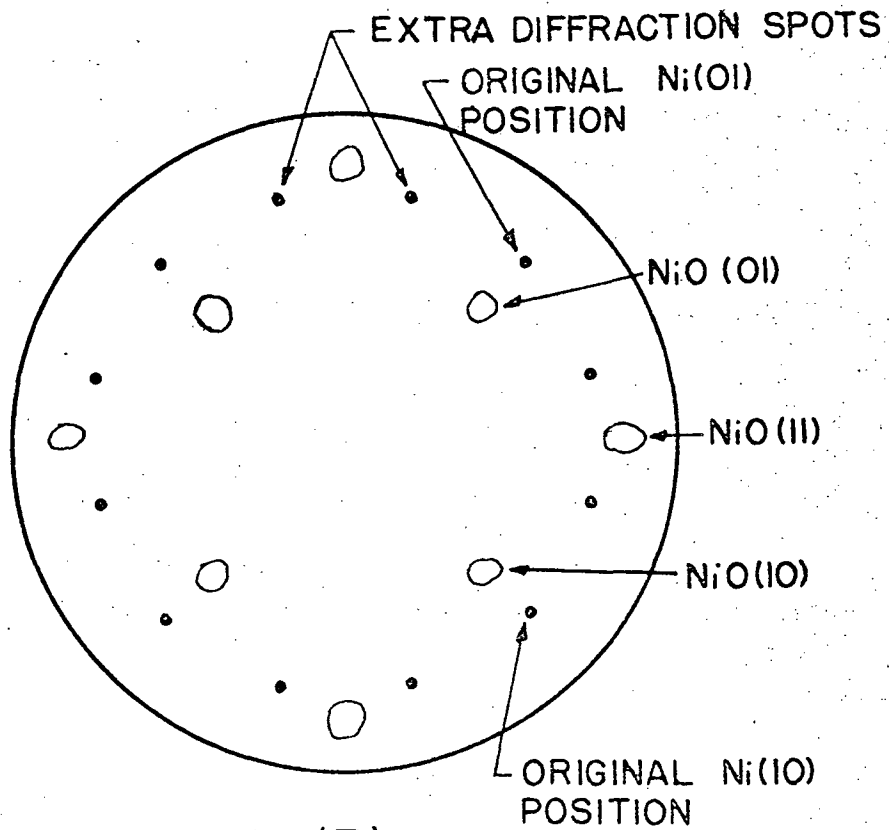
(100) nickel plane and the [011] directions were parallel. The identification of the pattern as NiO was based on both symmetry and approximate correlation between the calculated lattice parameter and the parameter reported for NiO. The calculated lattice parameter varied about $\pm 10\%$ about the expected value, presumably because of uncertainty in the measured diffraction spot separations caused by the diffuseness of the spots. It is therefore uncertain whether a "pseudo-oxide" with NiO symmetry but with a 5% smaller lattice parameter, as reported by May and Germer⁷⁴ for (110) nickel, existed on (100) nickel.

In addition to the previously reported LEED sequence described above, unreported diffraction spots were observed to develop along with the NiO spots. These are shown in Figure 28 and were two additional sets of diffraction spots, each consisting of four spots, observed at a radius equivalent to the original nickel (10) spot; one set was rotated 30° while the second set was rotated 60° about the reciprocal lattice normal. These spots were independent of the point on the surface sampled by the LEED beam and were reproducible. Attempts to account for them by multiple diffraction have been

Figure 28 LEED pattern showing diffuse NiO plus unexplained diffraction spots. (a) Photograph of LEED patterns. (b) Schematic identifying diffraction spots. ($\theta_0 = 0.87\mu\text{V}/\mu\text{A}; 86\text{V}$)



(A)



(B)

unsuccessful and they do not behave as facet beams. Their origin is uncertain, but will be discussed later.

Comparing oxygen coverages versus exposure (Figure 21) and oxygen coverage versus LEED patterns (Figure 27) at 302°K, one sees that the p(2 x 2) structure maximized at about 8L while the c(2 x 2) structure maximized at about 20 to 30 L. Comparing the low energy secondary electron spectrum shown in Figure 24 with Figure 27, one sees that the 8eV and 60eV peaks decreased in amplitude during the formation of the p(2 x 2) and c(2 x 2) structures. During formation of NiO, the 12eV peak appeared and increased in intensity while the 60eV peak changed shape and shifted downward. The sticking coefficient (Figure 22) reached a minimum shortly after the p(2 x 2) structure maximized, then increased during formation of the c(2 x 2) structure and NiO. Similarly, the work function (Figures 25 and 26) increased during formation of the p(2 x 2) structure and remained high, but began to decrease at about the same time the diffracted intensity from the c(2 x 2) structure maximized. It decreased below the clean surface value during NiO formation.

The LEED patterns from samples exposed at elevated temperatures were similar to those observed at

302°K, except that the patterns were sharper for all structures (i.e. $p(2 \times 2)$, $c(2 \times 2)$, and NiO) and the $(0\frac{1}{2})$ spots were not observed to such high coverages. The new diffraction spots equivalent to nickel (10) were reduced in intensity at elevated temperatures; the NiO spots were still very diffuse. The fact that higher temperatures cause sharper LEED patterns has been reported previously (Table 1) as has the fact that heating an oxygen covered surface sometimes causes sharper LEED patterns.

The LEED patterns observed at 147°K were similar to the 302°K results in that the $p(2 \times 2)$, $c(2 \times 2)$, and NiO (with the nickel-equivalent spots) sequence was observed. However, all of these patterns were weak at 147°K and the NiO pattern was almost undetectable. The NiO pattern was very apparent though, after the substrate was warmed to room temperature in residual vacuum.

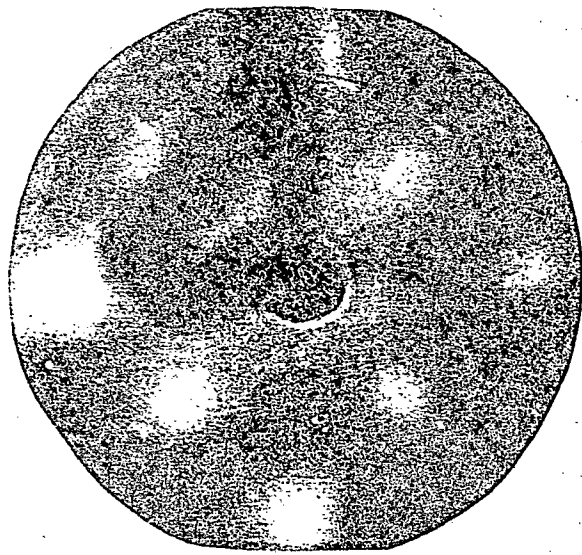
Carbon accumulation on the surface during the reaction (Figure 23) was not observed to affect the LEED patterns. However, the patterns were affected when the initial carbon coverage was as high as .55ML.

In this case, the initial $h + \frac{1}{2}k + \frac{1}{2}$ streaking was followed by a $p(2 \times 2)$ structure in which the $(\frac{1}{2}0)$ and $(0\frac{1}{2})$ spots were missing. This is one of the patterns reported by Onchi and Farnsworth⁵⁴ and by Armstrong¹¹³ for CO adsorbed on (100) nickel. With increasing oxygen coverage, a NiO pattern with the nickel-equivalent spots was observed and at saturation completely displaced the CO pattern.

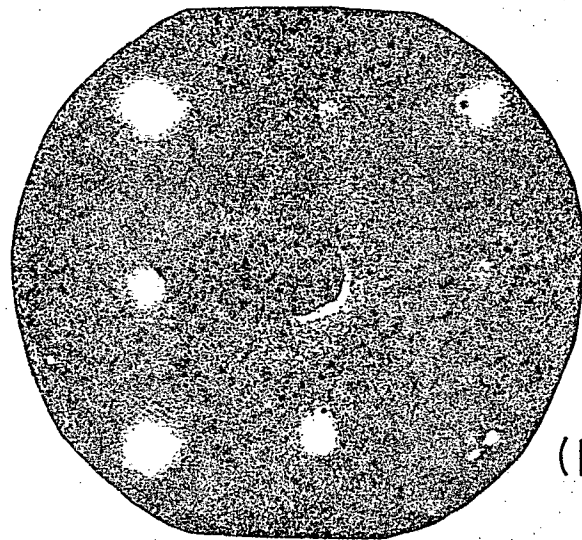
LEED was used to determine whether ion bombardment would cause surface structure degradation in the reverse order as gas exposure. Ion bombardment causes removal of surface oxygen and the LEED patterns shown in Figure 29 indicate that patterns from NiO, $c(2 \times 2)$, and $p(2 \times 2)$ structures are observed with decreasing oxygen coverage, i.e. the sequence observed for increasing oxygen coverage is observed in reverse order for decreasing oxygen coverage.

7) Electron induced desorption. AES was used to study EID, but none could be detected by this method for the substrate at 302°K or higher for oxygen coverages at or below saturation. EID was only observed with the substrate at 147°K and oxygen coverage near the saturation value. The AES oxygen signal decreased due to EID, but

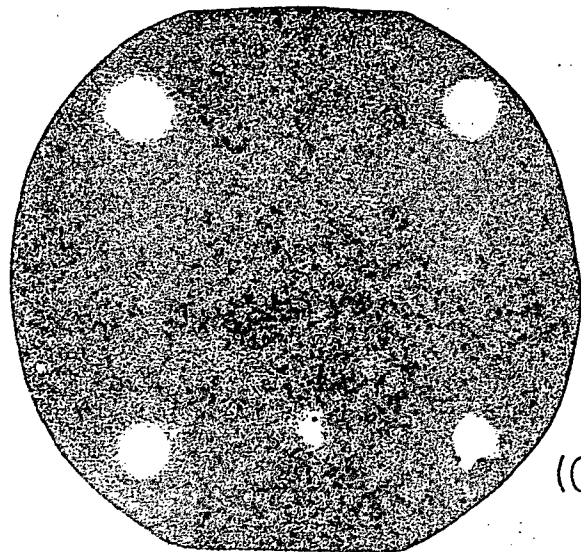
Figure 29 LEED patterns showing that the sequence (a) NiO ($\theta = 0.87\mu\text{V}/\mu\text{A}$; 86V), (b) $c(2 \times 2)$ ($\theta = 0.30\mu\text{V}/\mu\text{A}$; 68V), and (c) $p(2 \times 2)$ ($\theta = 0.15\mu\text{V}/\mu\text{A}$; 74V) structures are observed with decreasing surface coverage.



(A)



(B)



(C)

since the signal level was only slightly above the noise level, the measurement was not very accurate. The secondary emission coefficient, δ , increased exponentially with electron bombardment time, and was thus a more sensitive measure of EID. The total cross-section calculated from variation of δ was $5. \times 10^{-19} \text{ cm}^2$. EID apparently occurred from the loosely bound species previously shown to exist at 147°K.

B. Oxygen on Clean (111) Nickel Surfaces

The study of oxygen reacting with (111) nickel surface is not as complete as that for the (100) surface due to inadvertent destruction of the crystal. The results do allow considerable insight into the reaction, however.

1) Clean (111) surfaces. No reversible segregation of carbon between the bulk and the surface was observed for the (111) oriented samples, but large quantities of sulfur segregated to the surface. Self oxidation of CO on the (111) surface was not demonstrated, but on the basis of data for CO on (111) nickel by Edmonds and Pitkethley⁴, self oxidation probably occurred. Small peaks caused by carbon and oxygen were observed on

the "clean" surface; the average values are shown in Table 3. If the carbon and/or oxygen peaks were judged to be too high before a run, the sample was heated to 773°K in 30 seconds, held at temperature for one minute, then cooled again to the reaction temperature. This treatment generally produced an acceptably clean surface. The Auger electron peaks from this surface were identical to those observed from the (100) surface and listed in Table 4. The strong peak at 8eV was not observed, but a very weak peak at 12eV was observed on the clean surface. The LEED pattern from the clean surface was that which was expected from termination of the bulk lattice as shown schematically in Figure 4a.

2) Inelastically scattered electrons. Upon exposing the clean (111) surface to gas phase oxygen, the oxygen AES peaks near 500eV increased until a saturation value was reached. The saturation spectrum from 0 to 1000 V was identical to (100) nickel shown in Figure 19. The average nickel and oxygen AES peak heights are shown in Table 3. The magnitude of the oxygen 507eV peak is shown in Figures 30 and 31 for short and long exposures, respectively. Although the reaction occurred faster than on the (100) surface, the same sequence of rapid adsorption,

Figure 30 Oxygen coverage versus short exposures for
(111) nickel. \diamond - 147°K; \square - 302°K; ∇ - 366°K;
 \triangle - 423°K.

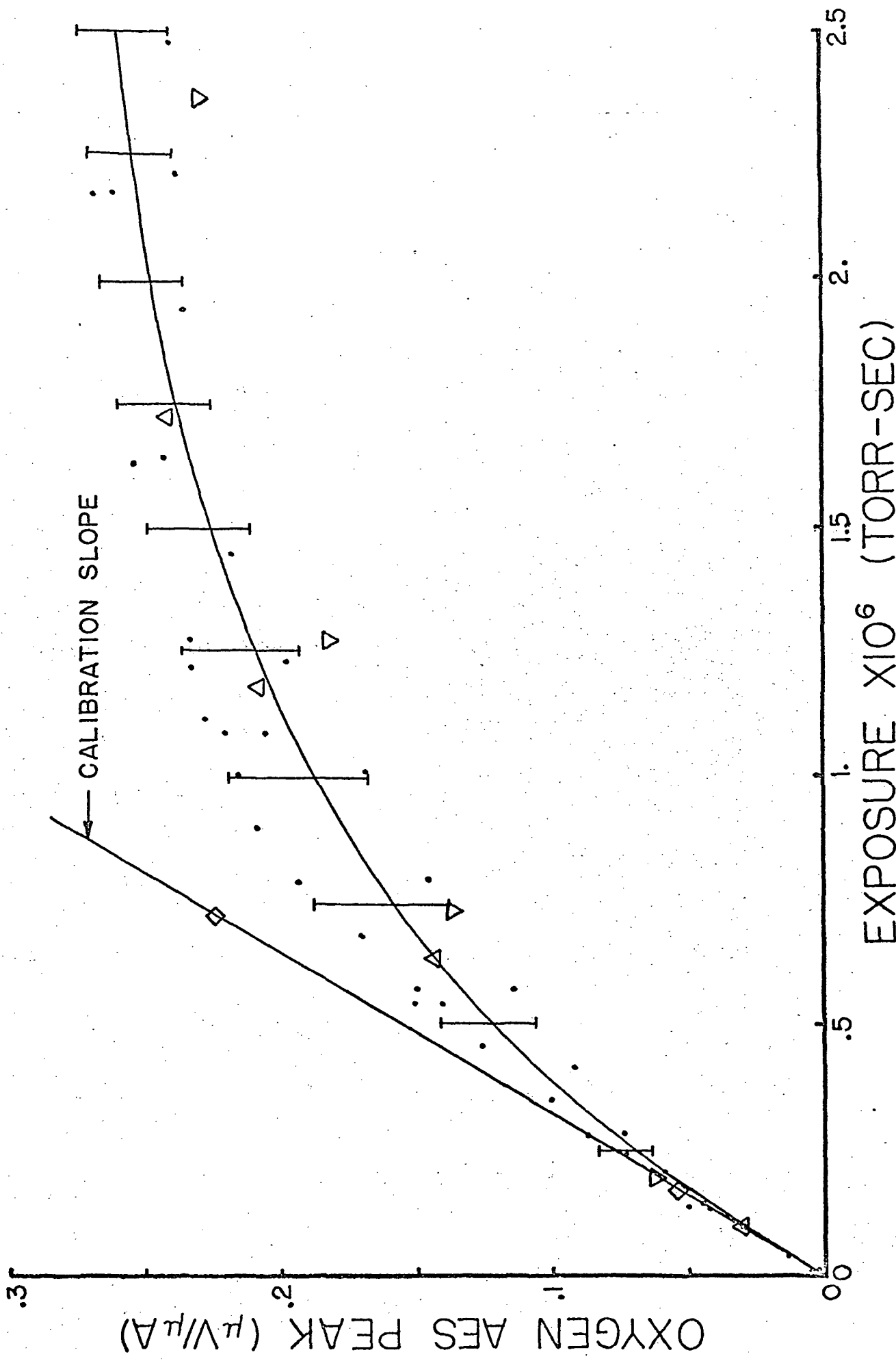
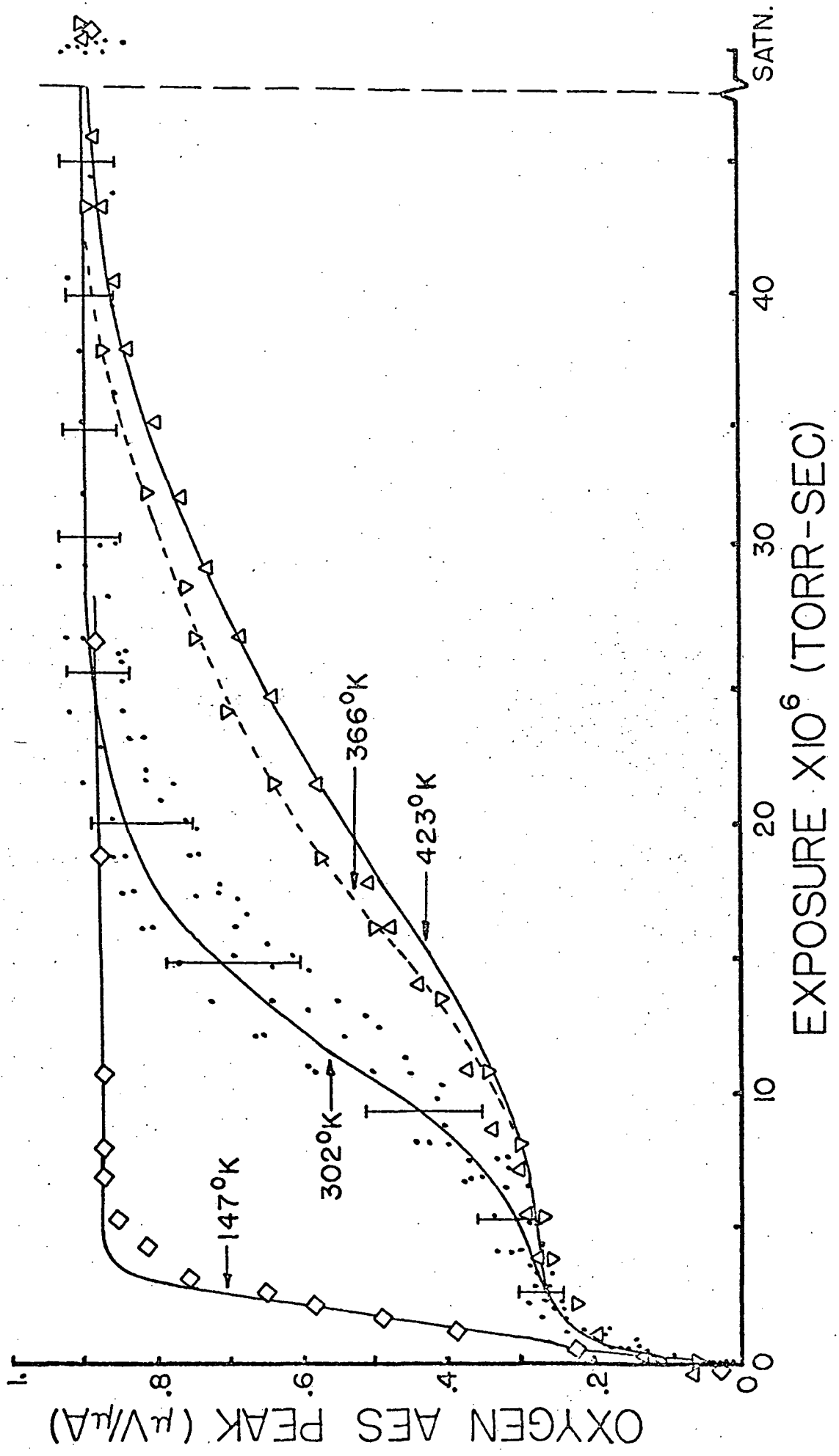


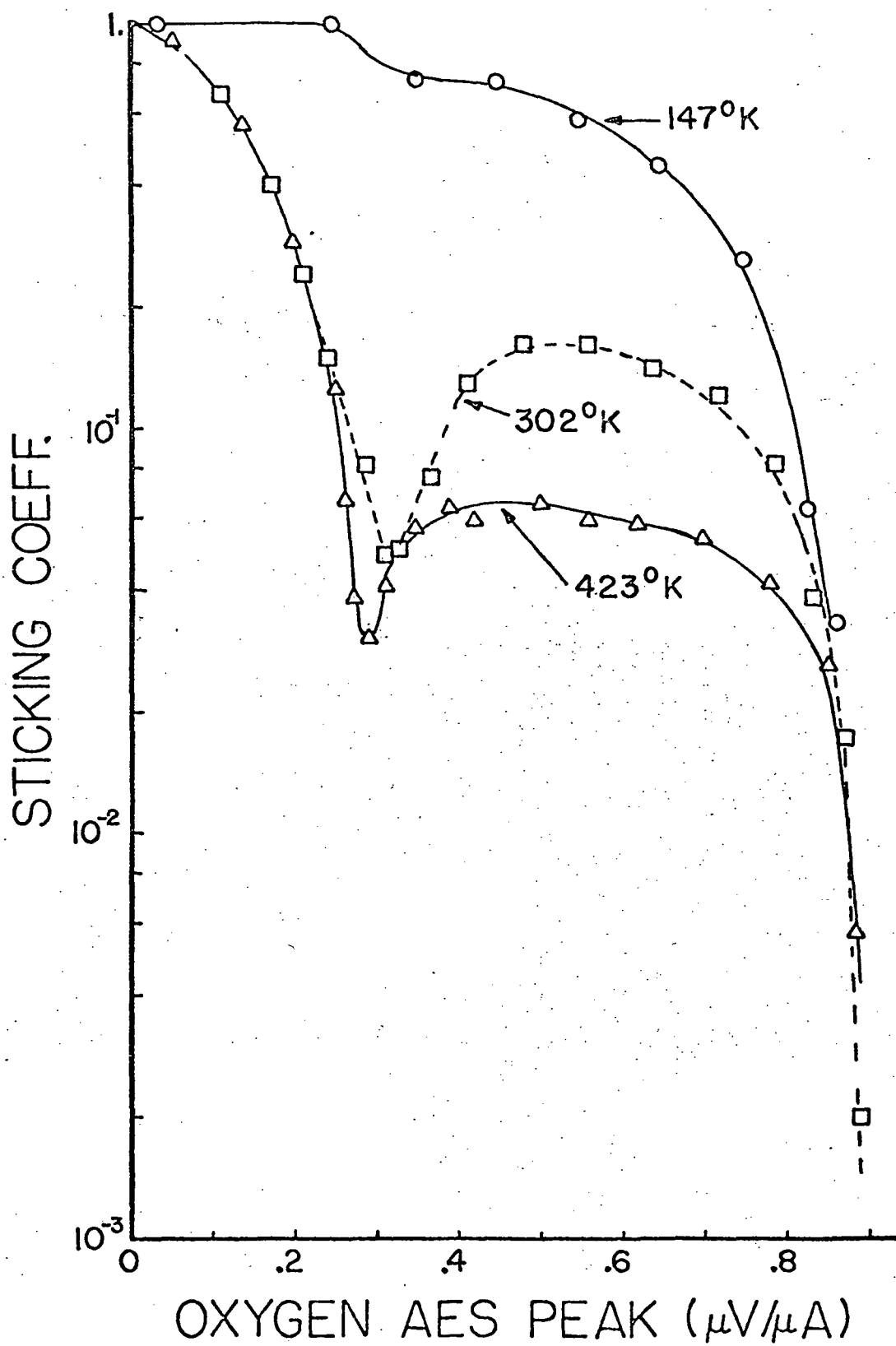
Figure 31 Oxygen coverage versus long exposure for
(111) nickel. \diamond - 147°K; \square - 302°K; ∇ - 366°K
 \triangle - 423°K.



slow adsorption, fast adsorption, and saturation was observed. The effects of temperature were also similar; raising the temperature decreased the reaction rate while lowering the temperature had the opposite effect. The saturation oxygen value was not measurably increased by exposures to 1×10^{-6} torr oxygen for twelve hours. The data have been corrected by a factor equal to the sum of the 60, 103, and 843 eV clean nickel peak heights divided by the sum of the average peak heights.

The amount by which the true oxygen surface coverage differs from the measured oxygen AES signal due to absorption effects will be discussed later. As for the (100) surface, some results will be anticipated. Absorption effects for oxygen on (111) nickel are negligible for coverages of less than $.3\mu\text{V}/\mu\text{A}$, and at saturation the true surface coverage differs from the measured coverage by less than 15%. The sticking coefficient can therefore be calculated and is shown in Figure 32. It is generally higher than for the (100) surface, but the shape versus oxygen coverage is similar. Initially, s was high but decreased to a minimum of .04 at $0.3\mu\text{V}/\mu\text{A}$ (0.34ML), then increased to a broad maximum of 0.1, and finally decreased to less than 10^{-3} at $0.89\mu\text{V}/\mu\text{A}$.

Figure 32 Oxygen sticking coefficient versus oxygen coverage on (111) nickel.



Increasing the temperature decreased δ and vice versa.

3) Low energy secondary electron spectrum.

The electron spectrum from 0 to 80eV for a clean surface was similar to that for (100) nickel, except that the strong peak at 8eV was not observed from the (111) surface. Instead a very weak peak at 12eV was observed as shown in Figure 33. As oxygen coverage increased this peak disappeared, but at still higher coverages a peak appeared at essentially the same energy (see Figure 33) and grew until saturation was reached. The 60eV nickel peak behaved as for the (100) surface in that it decreased in magnitude and new derivative maxima were formed which shifted the peak to a lower energy at oxygen saturation.

The true secondary peak first decreased then increased in magnitude with increasing oxygen coverage. This is shown both in Figure 33 and 34. The width between derivative maxima increased as the height decreased and vice versa. Similar behavior is exhibited by the secondary emission coefficient (Figure 34). The behavior of both δ and the true secondary peak indicated that the work function initially increased, then at $0.28\mu\text{V}/\mu\text{A}$ it began to decrease and at saturation had

Figure 33 Changes in secondary electron peaks between 0 and 70 eV as a function of oxygen coverage on (100) nickel (2 VPP modulation voltages; oxygen coverage in $\mu\text{V}/\mu\text{A}$).

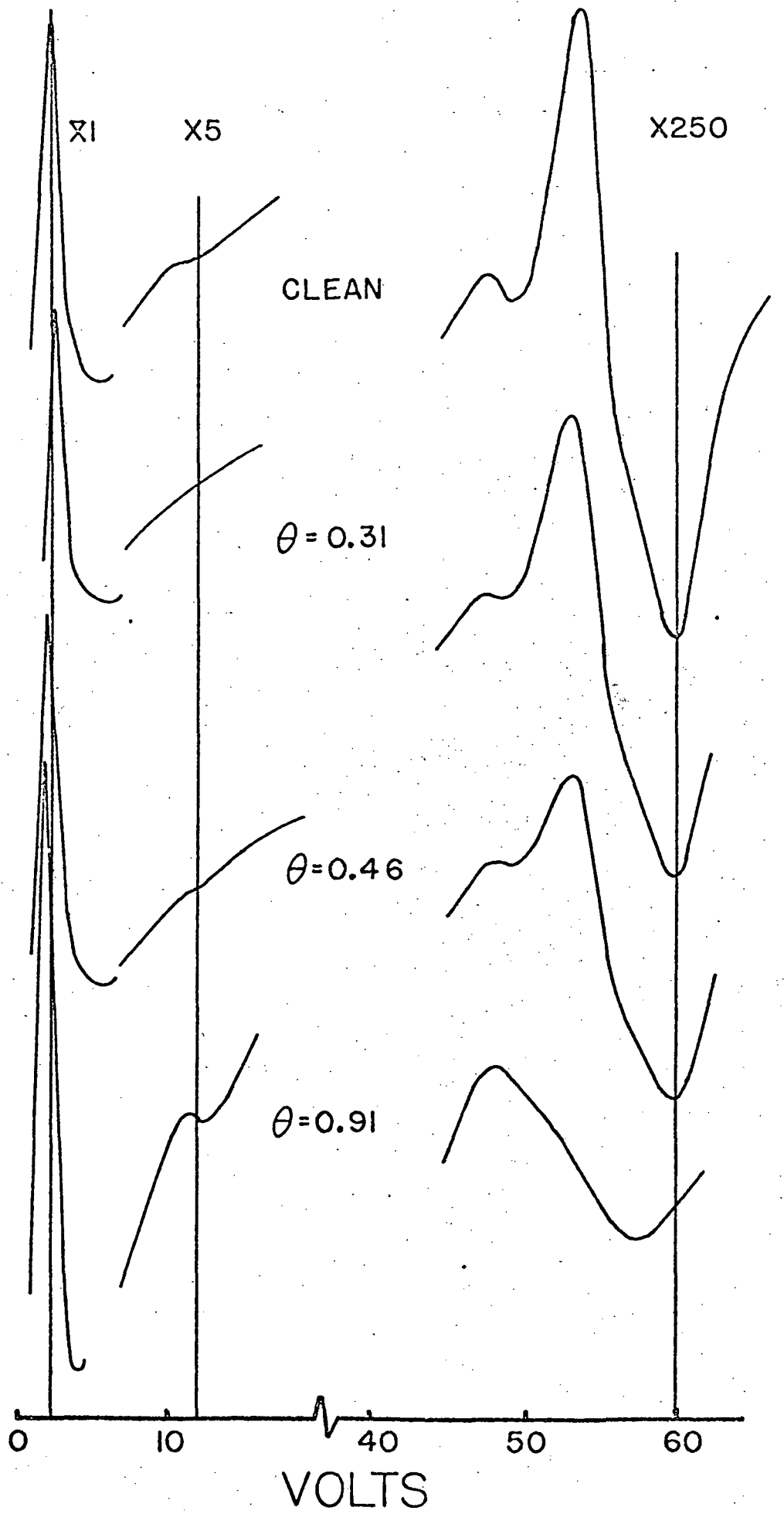
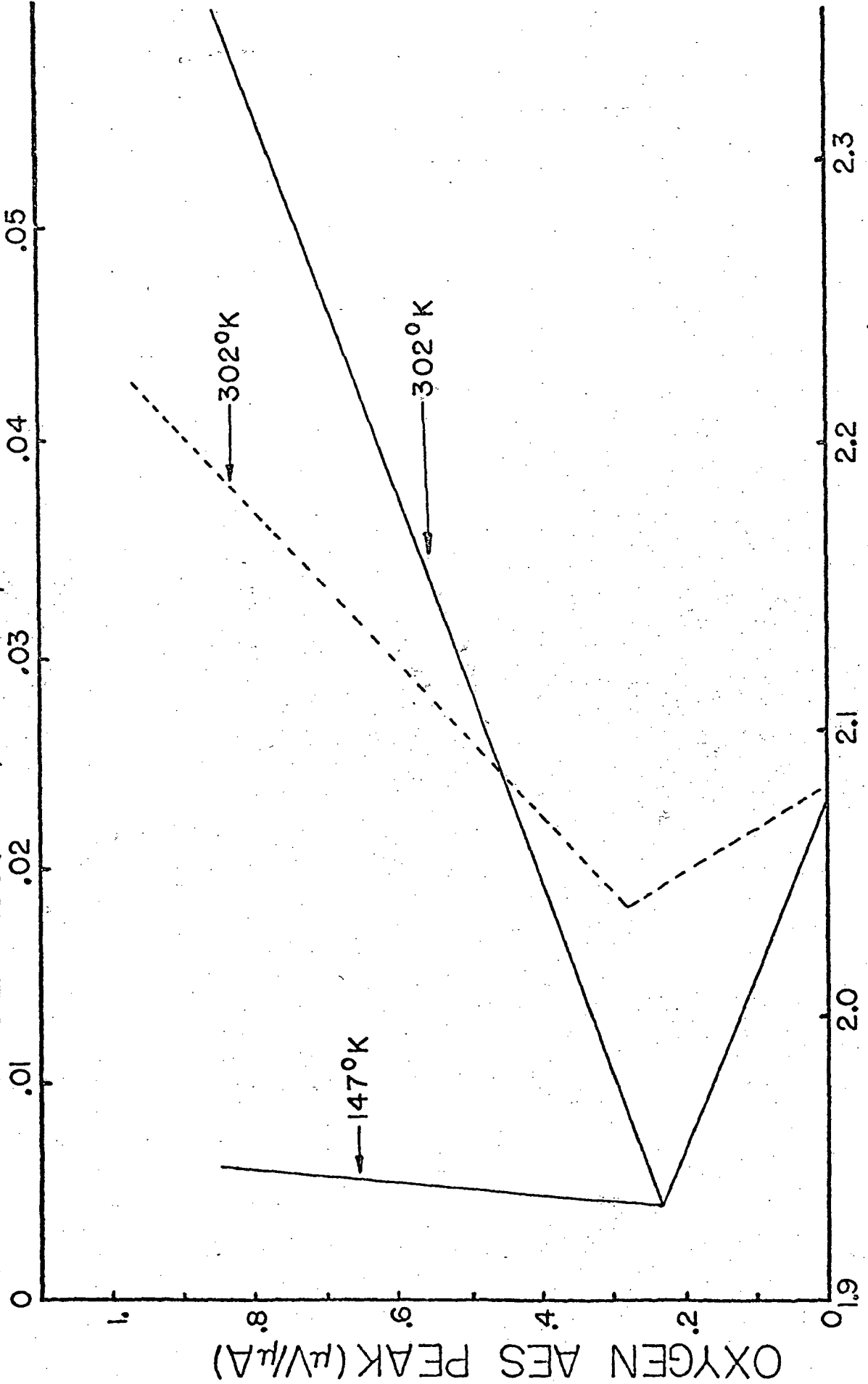


Figure 34 Secondary emission coefficient (solid lines) and true secondary electrons peak height (dotted line) versus oxygen coverage on (111) nickel.

TRUE SEC. PK. HT. (V/μ A-DOTTED LN)



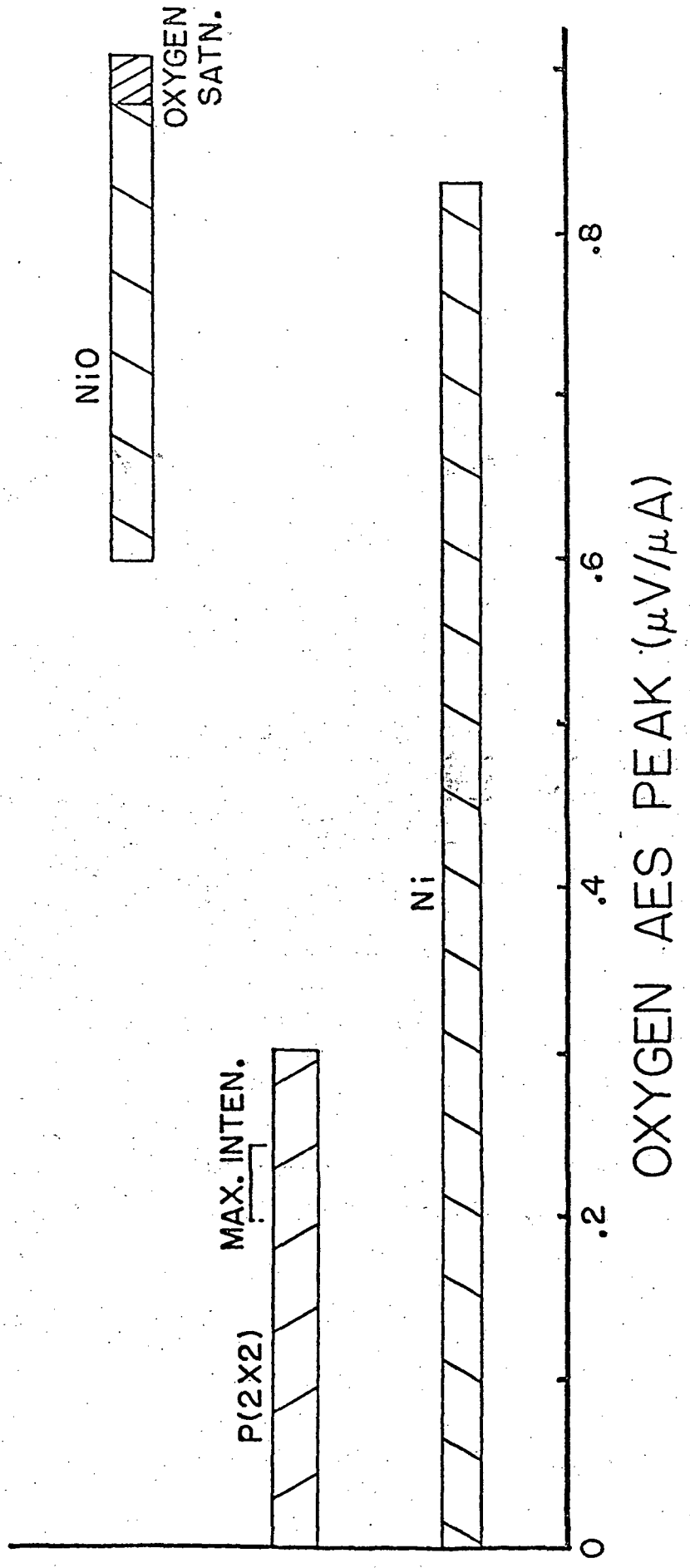
OXYGEN AES PEAK ($\mu V/\mu A$)

SEC. EMIS. COEFF. (SOLID LN)

decreased to below the value for the clean surface. At 147°K, measurement of δ indicated that the work function remained high, probably as a result of a loosely bound oxygen species as for the (100) surface.

4) Low-energy electron diffraction. The sequence of LEED patterns observed for the (111) surface with increasing oxygen coverage was patterns caused by nickel, nickel plus p(2 x 2), nickel, nickel plus NiO, and NiO. LEED studies at coverages below 0.19 μ V/ μ A (0.24ML) were incomplete; therefore it was not determined if the p(2 x 2) spots were initially streaked or diffuse as in the case of the (100) surface. Such an effect is not reported in the literature. The lower limit on the maximum intensity range for the p(2 x 2) structure is also uncertain, but the upper limit of 0.24 μ V/ μ A (0.3ML) was established (Figure 35). Above 0.3 μ V/ μ A, the p(2 x 2) pattern was no longer distinguishable. The nickel pattern was visible until 0.83 μ V/ μ A and above 0.59 μ V/ μ A, a very diffuse NiO pattern on a high intensity background was visible. The (1 $\bar{1}$ 1) NiO plane was parallel to the (111) nickel plane with parallel [110] directions as reported by Park and Farnsworth⁶⁹. The ($\sqrt{3}$ x $\sqrt{3}$)R30° structure reported by MacRae⁵⁵ was not observed. LEED patterns

Figure 35 Ranges and maximum intensities of LEED patterns versus oxygen coverage on (111) nickel.



at temperatures other than 302°K were not obtained.

Comparing oxygen coverage versus exposure (Figure 31) and oxygen coverage versus LEED patterns (Figure 35), one sees that the $p(2 \times 2)$ structure maximized at an exposure of about 1L while NiO was observed above 15L. Comparing the sticking coefficient (Figure 32) with the LEED patterns, one sees that the $p(2 \times 2)$ structure was observed when the sticking coefficient was high, but the sticking coefficient minimum was not associated with a LEED pattern. The sticking coefficient was at the broad maximum when NiO was first detectable with LEED. Comparing LEED patterns with Figure 33 one sees that the true secondary, initial 12eV, and the 60eV peaks all decreased during formation of the $p(2 \times 2)$ structure. The true secondary and second 12eV peak increased while the 60eV peak changed shape and shifted down in energy during formation of NiO.

5) Electron induced desorption. Only the AES technique was used to study EID on the (111) surface with no desorption being detected at 302°K.

C. Oxygen on Nickel (111) Pre-Contaminated with Sulfur

1) Surface preparation. To prepare a sulfur contaminated surface, the substrate was initially ion

bombarded, annealed, and checked for extraneous AES peaks as previously described. Sulfur induced structures were developed by heating the sample to 1023-1073°K during which mass spectrometry indicated that sulfur was desorbed from the surface. Sulfur coverage was evidenced by a large sulfur peak at 150eV and a smaller peak at 139eV as shown in Table 4. Structure on the 150eV peak as reported by Dalmai-Imelik, et.al.¹¹⁴, could be observed. Average peak heights are shown in Table 3.

Two sulfur structures, as determined by LEED, were observed, depending on the initial condition of the system. These structures, shown in Figures 36 and 37, have been observed previously by Perdereau and Oudar¹¹⁵ and by Edmonds, et.al.¹¹⁶ The latter authors identified them as coincidence structures having symmetries $(5\sqrt{3} \times 2)$ and $(8\sqrt{3} \times 2)$. Using radioactive tracer techniques, Perdereau and Oudar reported that 7.5×10^{14} atom/cm² and 8.1×10^{14} atom/cm² of sulfur were present for these structures (compared to 1.9×10^{15} atoms/cm² for clean (111) nickel). Perdereau¹¹⁷ has calibrated AES by the adsorption of radioactive sulfur on nickel, and by his data, these concentrations of sulfur should result in ratios of 150eV sulfur to 60eV

Figuer 36 LEED pattern due to sulfur in a $(5\sqrt{3} \times 2)$
structure on (111) nickel. (74V)

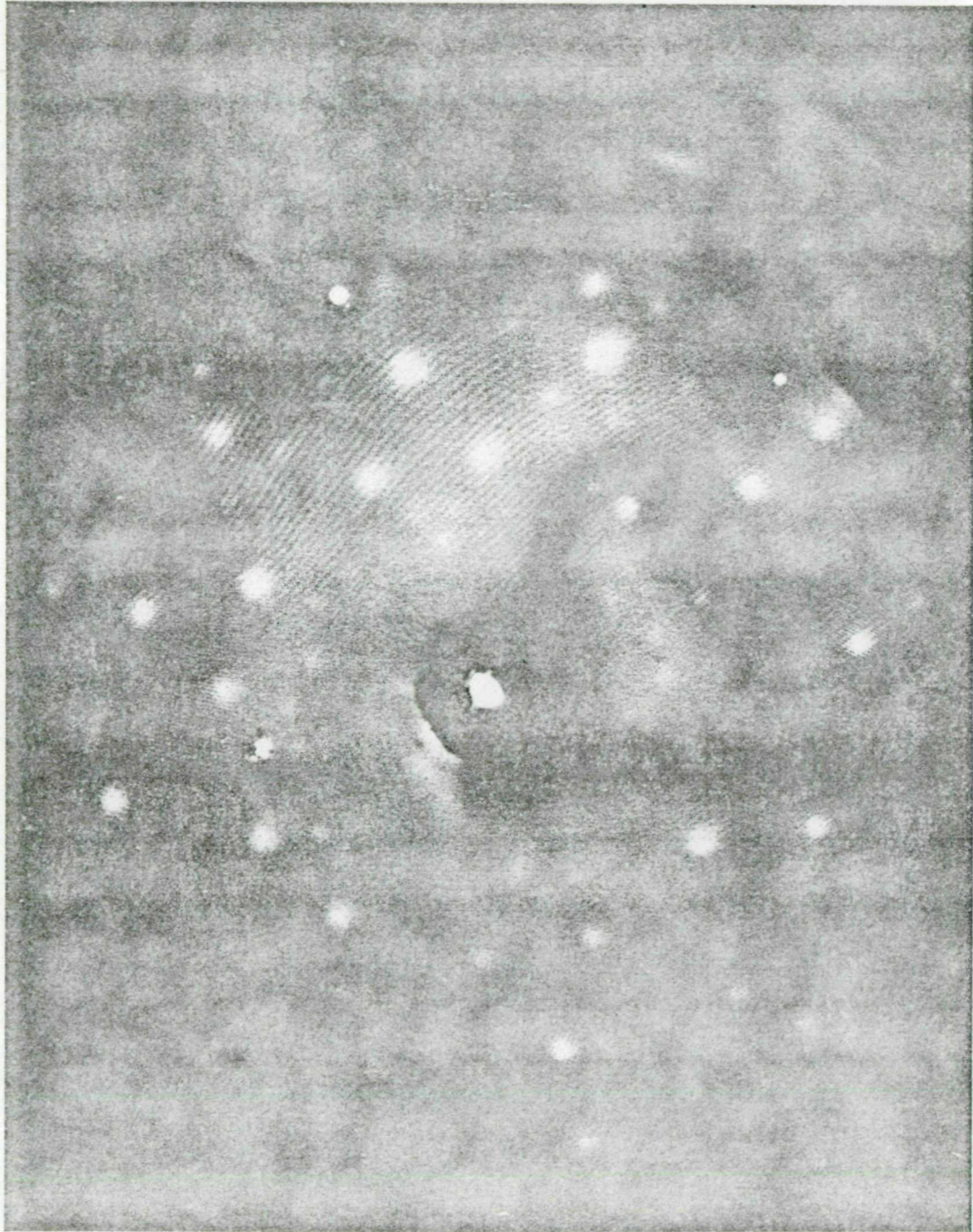
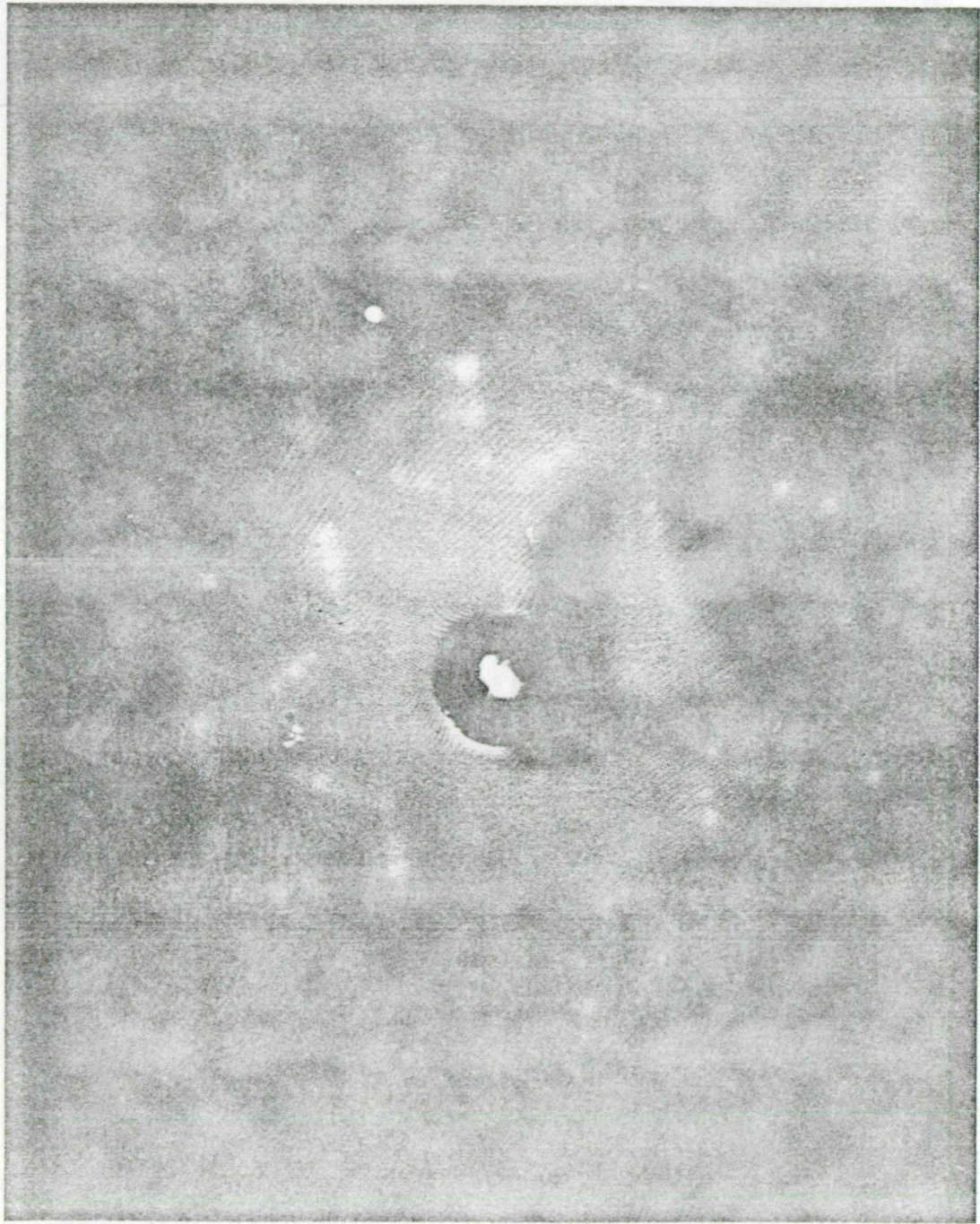


Figure 37 LEED pattern due to sulfur in a $(8\sqrt{3} \times 2)$
structure on (111) nickel. (78V)



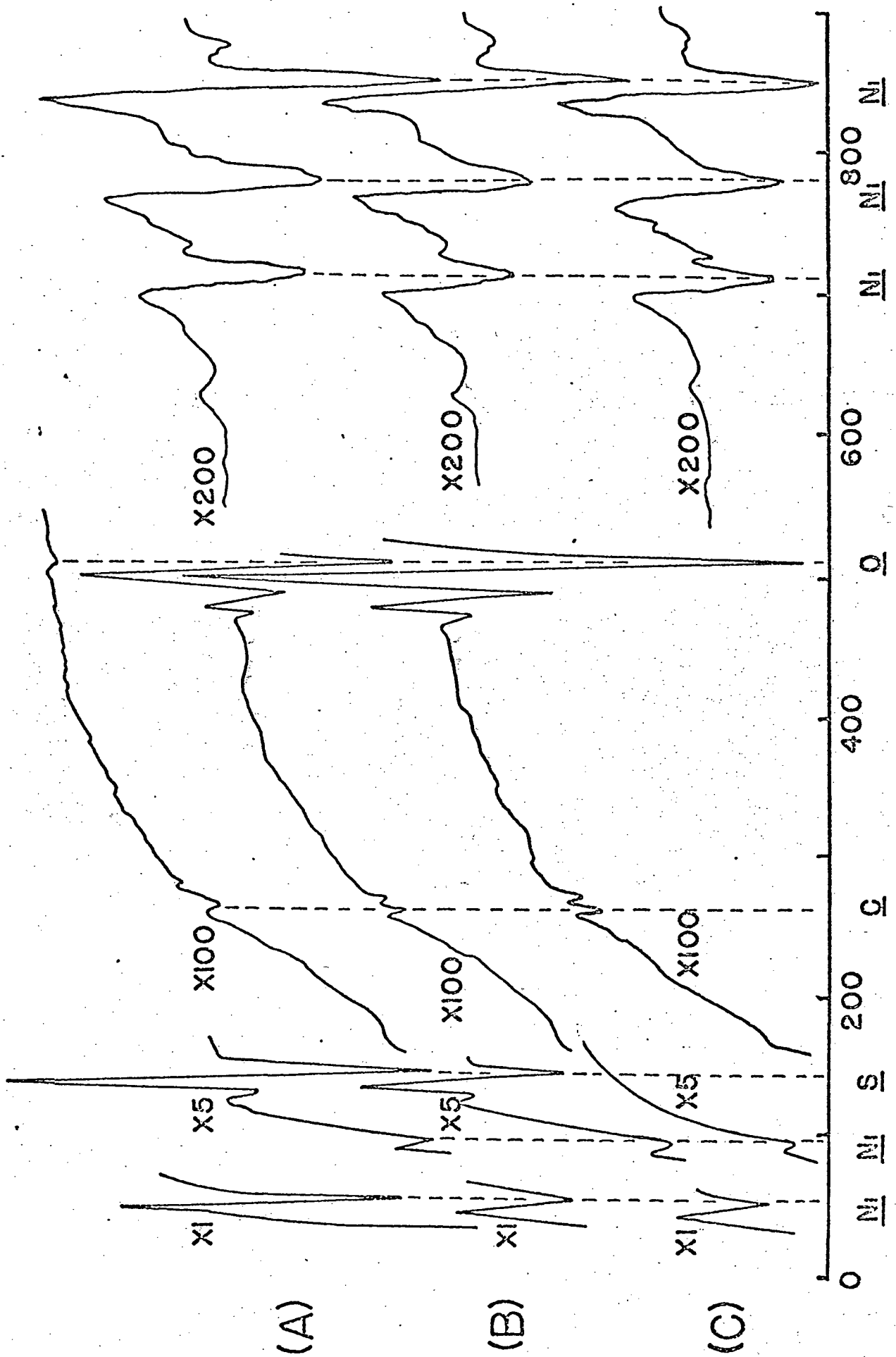
nickel peaks of 0.275 and 0.29 for the $(5\sqrt{3} \times 2)$ and $(8\sqrt{3} \times 2)$ structures, respectively. In the present case average respective ratios of 0.27 and 0.28 are observed and therefore the above values of absolute sulfur concentrations are adopted.

In the present experiments, the $(5\sqrt{3} \times 2)$ structure was most often observed. The $(8\sqrt{3} \times 2)$ structure was observed only on those occasions when the system had been opened to the atmosphere, reevacuated and baked, and the sulfur structure developed by short heating times. In retrospect, this was unfortunate, as the $(8\sqrt{3} \times 2)$ structure appeared to be more nearly perfect (uniformly sharp LEED spots) and gave more reproducible results in the kinetics studies.

For both structures the AES spectra in the range 0-1000V showed only large peaks for sulfur and nickel and small peaks caused by carbon and oxygen as shown in Figure 38.

2) Kinetic studies. Upon exposing sulfur-rich surfaces to oxygen, AES indicated the sulfur coverage decreased while the oxygen coverage increased. AES traces obtained in one such experiment are shown in Figure 38 for the initial surface, the partially reacted

Figure 38 AES spectra from 0 to 1000 V showing (a) sulfur saturated surface, (b) oxygen/sulfur reaction 50% complete, and (c) reaction nearly to completion.



(A)

(B)

(C)

surface, and the completely reacted surface. The results of these AES measurements can be summarized in plots of the relative surface coverage of sulfur and oxygen as a function of oxygen exposure. These plots are shown in Figures 39 and 40 for the two surface structures studied. In these plots, $\theta_s = I/I_{sat}$, where I is the peak-to-peak height of the sulfur AES peak at any instant and I_{sat} is the height of the peak observed for the sulfur saturated surface. θ_0 is defined similarly. Data presented represent experiments run at different oxygen pressures and experiments in which the oxygen pressure was changed during the run, both of which indicated that for any given value of θ_s , the reaction rate was directly proportional to the oxygen pressure; that is, the extent of the reaction, $(1 - \theta_s)$, was a function of oxygen exposure.

The oxygen coverage at the conclusion of the reaction, based on the ratio of AES peak heights for oxygen and nickel, was the same as that observed for the saturation of oxygen on the clean surface of the same (111) oriented crystal. In addition, the 60eV AES peak was observed to broaden and shift to a lower energy indicating that oxygen occupied the surface as NiO.

Figure 39. Relative coverages of oxygen and sulfur with sulfur in the $(5\sqrt{3} \times 2)$ structure.

- - No. 1 (302°K);
- ▲ - No. 2 (305°K);
- - No. 3 (303°K);
- - No. 4 (373°K);
- ▽ - No. 5 (233°K).

The variation of oxygen coverage is shown only for No. 2.

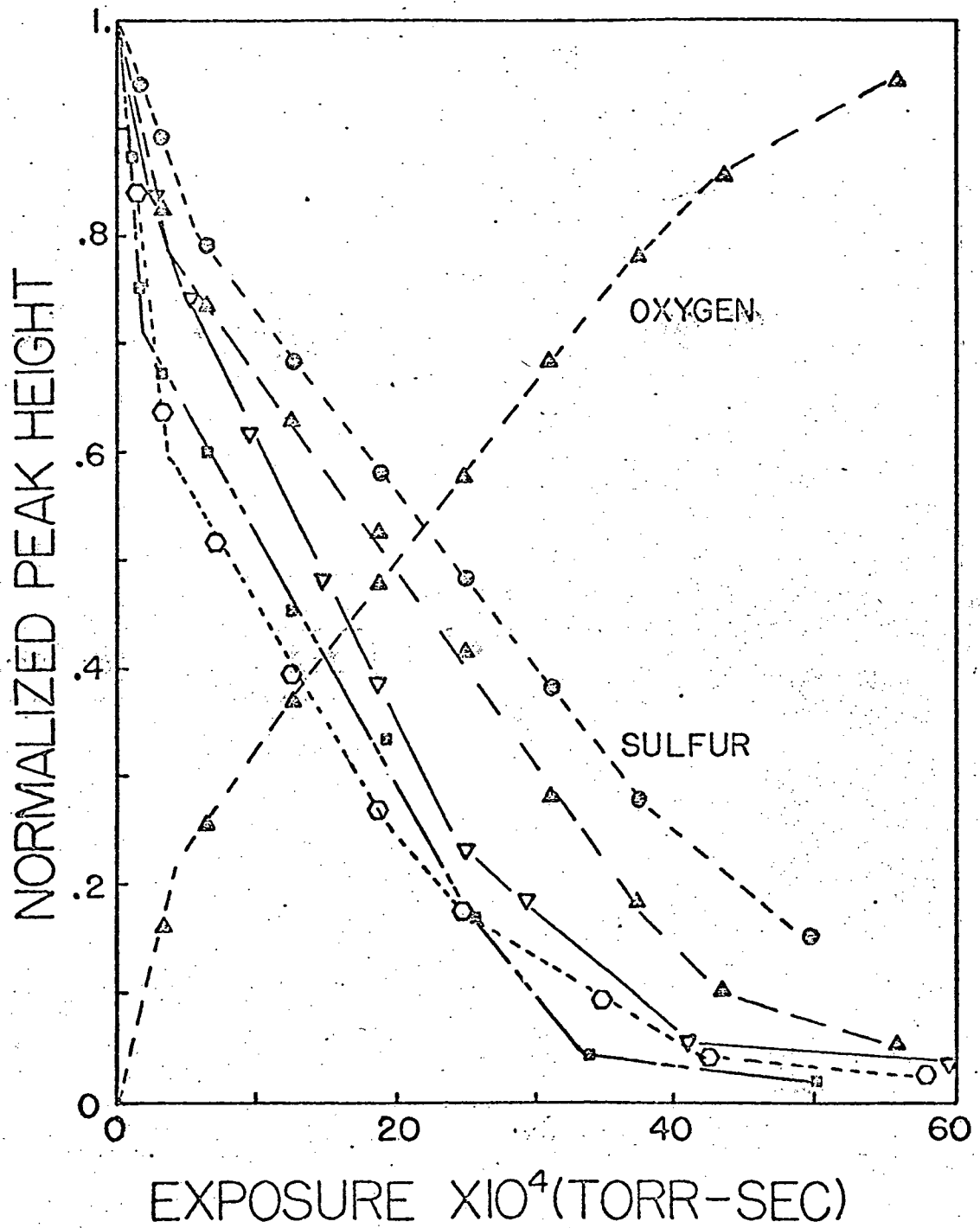
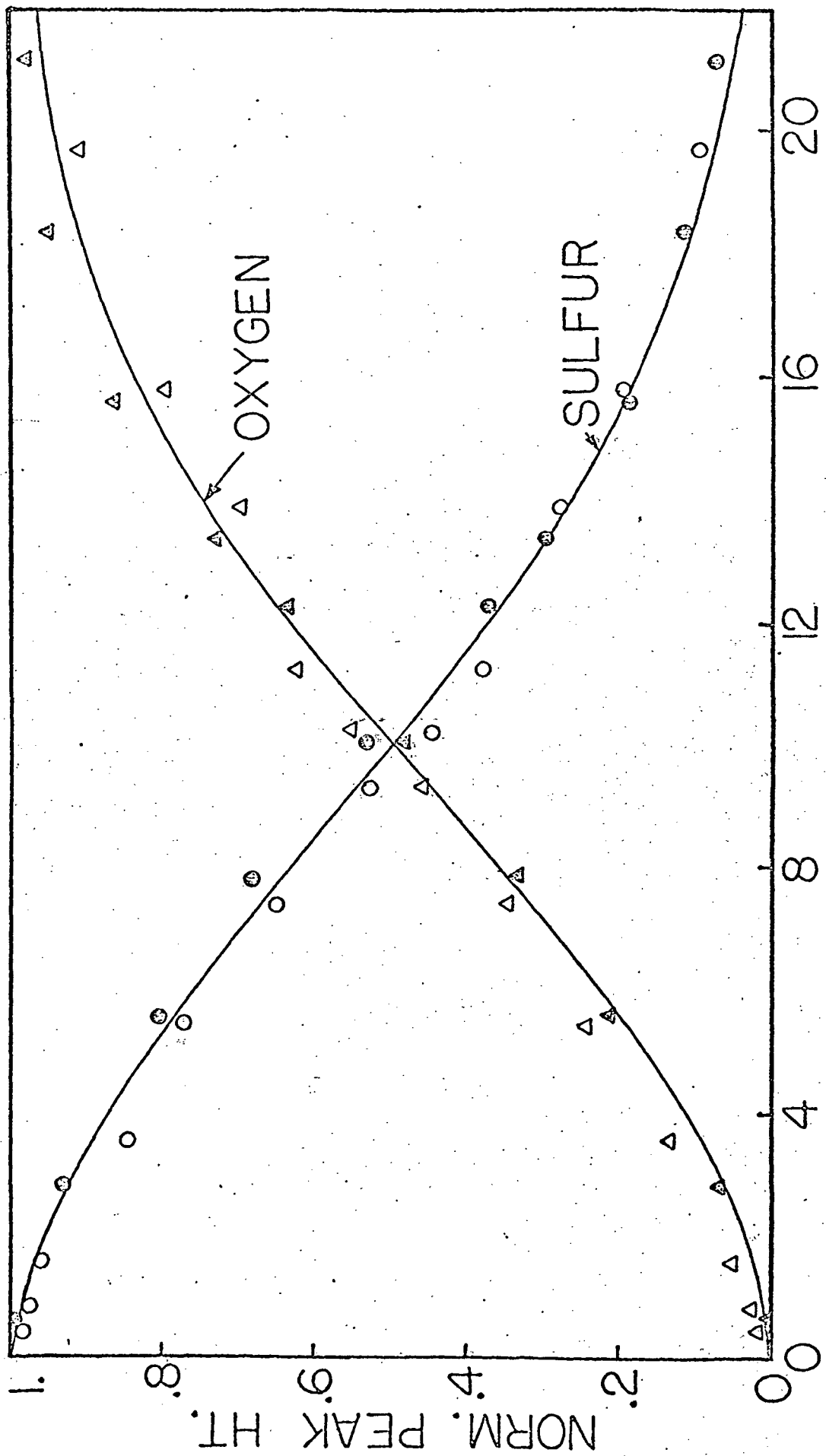


Figure 40 Relative coverage of oxygen and sulfur with sulfur in the $(8\sqrt{3} \times 2)$ structure. (302°K; 2 runs)

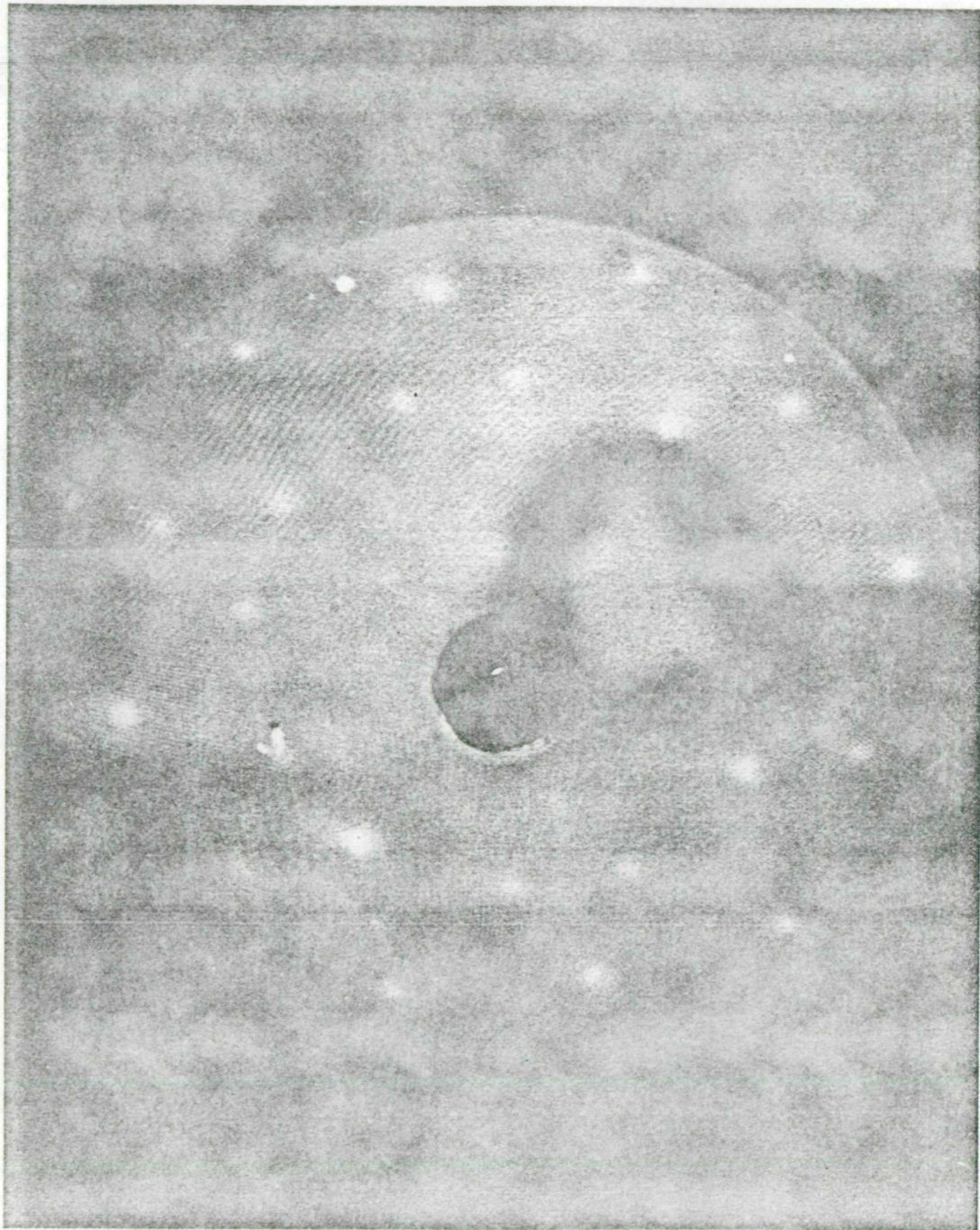


EXPOSURE $\times 10^4$ (TORR-SEC)

LEED patterns observed during the reaction, such as the one shown in Figure 41, indicated a progressive increase in the background intensity with the sulfur diffraction spots remaining sharp. The original pattern could be distinguished from background until the reaction was approximately 75% complete. At the conclusion of the reaction, no LEED pattern could be observed at any voltage. This is in contrast to the results observed for oxygen adsorption on the clean surface, in which a LEED pattern typical of NiO (111) is observed at the same oxygen coverage.

In order to determine the gas-phase reaction products, the sample was rotated to face the mass spectrometer during some of the reaction sequences. Peaks were observed at 48 and 64 AMU, in the ratio of 0.78/1. Bonzel¹⁰⁰, in his study of this same reaction on Cu(110), also observed mass spectrometer peaks at 48 and 64 AMU in a ratio of 0.61/1, and showed by direct calibration with gaseous SO₂ that the peak at 48 AMU was due to cracking of the parent SO₂ molecule in the mass spectrometer. It appears likely that the 48 AMU peak observed here has the same origin, and we conclude that the sole

Figure 41 LEED pattern from $(5\sqrt{3} \times 2)$ sulfur structure and increased background intensity due to oxygen; reaction is 60% complete. (74V)



gaseous reaction product is SO_2 . While the observed mass spectrometer peaks were large enough to permit identification of the reaction product, they were too small (due to slow rate of reaction at the low temperatures used in this study) to be used to characterize the reaction rate.

It was observed that the rate of reaction could be affected by the presence of hot filaments or electron beams operating in the system during the reaction process. Reproducible results could be obtained only by turning off all filaments and electron beams except that of the mass spectrometer during the reaction. (The mass spectrometer had a low temperature filament and time on was minimized.) The nature of these effects suggest that they involve the generation of atomic oxygen which then reacts rapidly with the adsorbed sulfur.

PART VI
DISCUSSION

A. Oxygen on Clean Nickel

Before proceeding with a detailed discussion of the experimental results, we will briefly summarize them and indicate how they will be analyzed in later discussion. Based on the experimental data, the interaction of oxygen with clean nickel surfaces exhibits three well-defined reaction regions. The first region is the reaction taking place before the minimum in the sticking coefficient and is associated with chemisorption of oxygen, i.e. chemisorbed surface structures are formed with periodicities related to that of the underlying nickel substrate. The sticking coefficient rapidly decreases in this region while the work function increases. We shall see that this region can be analyzed in terms of adsorbed oxygen blocking adsorption sites and preventing further chemisorption of oxygen. We shall see that inelastic scattering of Auger electrons is not important during this reaction region.

The second reaction region is associated with the formation of nickel oxide. During NiO formation,

the work function decreases to below the clean surface value, the sticking coefficient increases to a broad plateau and then decreases to a low value, changes of the low energy secondary electron peaks occur, and a diffuse oxide LEED pattern is observed. We shall see that the kinetics of NiO formation may be analyzed in terms of nucleation and growth of oxide islands on the surface. Island perimeter sites will be shown to be the active sites for the growth process. We shall also see that absorption of oxygen Auger electrons by overlying material occurs in this reaction region and the observed oxygen signal must be corrected for this effect. An explanation for the saturation coverage of NiO will be developed based on an argument concerning the physical processes occurring during island growth.

The third reaction region is associated with thickening of the oxide beyond the normal saturation value. This ability to thicken has been associated with an adsorbed oxygen species which increases the work function of the substrate. An explanation for this will be discussed in terms of present low-temperature oxidation theories.

1) Calibration of the AES signal. To analyze the kinetics of the interaction of oxygen with a clean nickel surface, knowledge of the amount of oxygen which has accumulated on the surface is very important. At low coverages where absorption effects are negligible, a calibration between AES peak height and the amount of oxygen on the surface has been established by assuming that the initial sticking coefficient was unity. This value for the initial sticking coefficient is based upon data from the literature^{91,92}. The calibration has been shown consistent with the expected 0.25ML concentration of oxygen for the p(2 x 2) structure observed on both the (100) and (111) surfaces.

The measured calibration constant should be independent of the oxygen concentration on the surface but we have already predicted that at coverages near saturation the oxygen will be distributed over a distance normal to the surface. In this case absorption effects are expected, i.e. some oxygen Auger electrons will be inelastically scattered by overlying material causing the measured oxygen AES signal to indicate a surface coverage which is less than the true surface coverage.

By considering the geometry of the emission of

Auger electrons, if the oxygen is distributed only one layer deep, absorption should have a negligible effect on the observed AES signal. This is supported by several studies which have shown that the AES peak height increases linearly with surface concentration for coverages up to one monolayer¹. In the present study, chemisorbed oxygen structures cover the surface in the first reaction region, but are only one layer deep and absorption effects should not influence the data. In the second reaction region, LEED patterns, changes in AES peaks, and work function changes all indicate that nickel oxide is formed. We shall see that the kinetics of NiO formation may be described by growth of oxide islands which are 1.8 layers thick. Since escape distances are on the order of four layers of material for Auger electrons, absorption effects should be appreciable for the second reaction region and must be considered.

We have previously discussed the reported studies of absorption of Auger electrons. Gallon³¹ has reported one such study in which he developed a finite layer model to describe absorption effects. By considering the probabilities of the scattering of a primary electron and the creation of a back-scattered Auger electron which

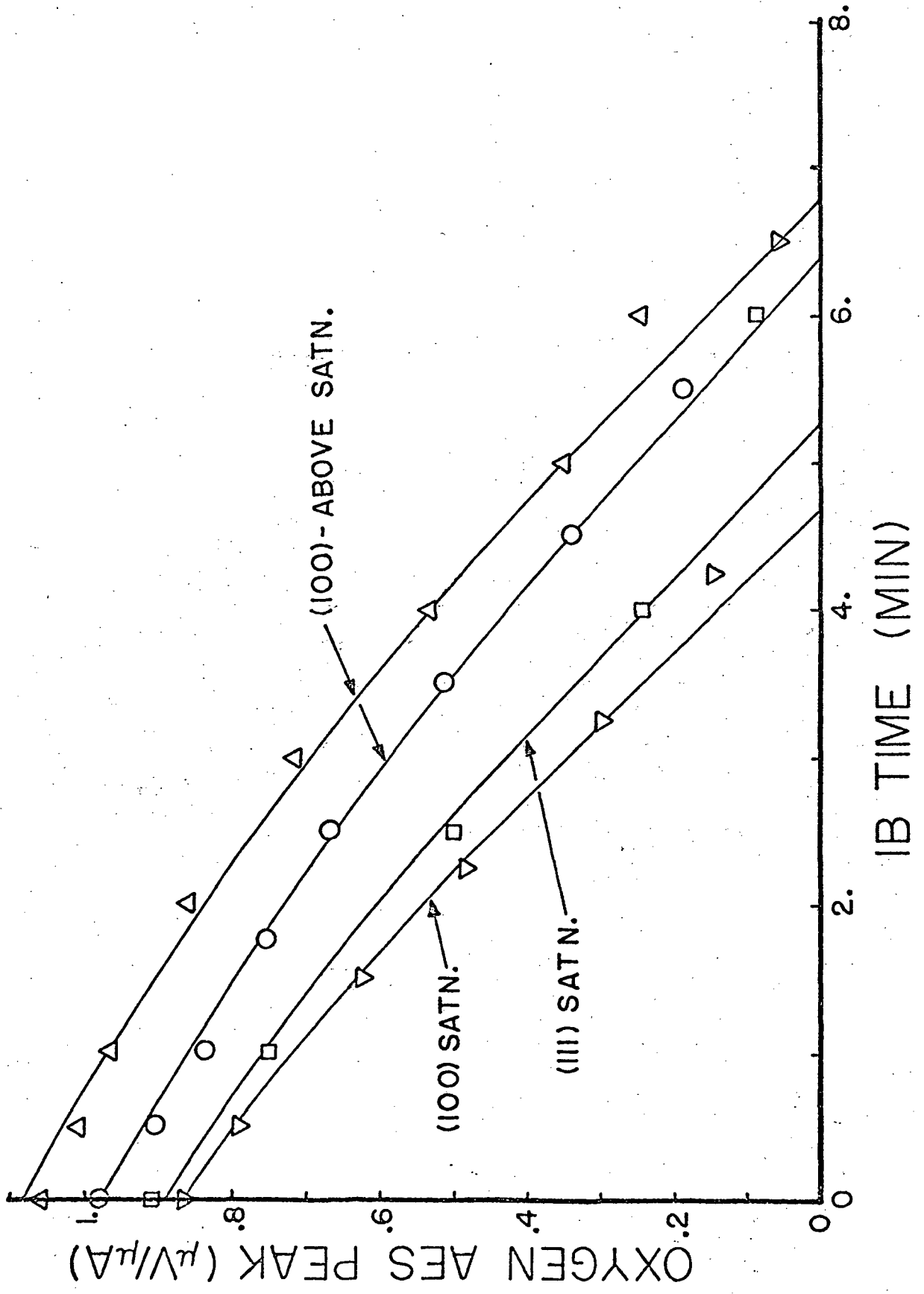
has a finite probability of being inelastically scattered by overlying material, Gallon concluded that the intensity of the AES signal from n layers of material, I_n , is given by

$$I_n = I_{\infty} \left[1 - \left(1 - I_1/I_{\infty} \right)^n \right] \quad (6)$$

where I_{∞} is the magnitude of the signal from the bulk material and I_1 is the signal from a single layer of the material. Attempts to measure I_{∞} directly for oxygen in NiO were unsuccessful. However, we can approximate the value of I_{∞} by curve fitting experimental data.

The oxygen coverage was decreased by intermittent IB on (100) and (111) surfaces with saturation oxygen coverages and on (100) surfaces with coverages above saturation. Assuming the rate of oxygen removal was linear with time, any curvature in the AES signal versus IB time is caused by absorption of Auger electrons. Experimental data is compared to calculated curves (equation (6)) in Figure 42 where I_{∞} was selected to be $2.2 \mu\text{V}/\mu\text{A}$ and I_1 was calculated from the calibration constant and the theoretical densities of one layer of (100) and (111) oriented NiO; as is obvious, the agreement between experimental and calculated data is good except

Figure 42 Oxygen AES peak height versus IB time for (100) and (111) surfaces. (Solid lines are calculated curves, filled circles are data points. Time scale for data from (111) surface multiplied by 0.5.)



at low oxygen coverages where readsorption of CO_x gases maintained a residual oxygen coverage. Equation (6) can thus be used with these values of I_1 and I_{∞} to calculate the material thickness corresponding to any observed signal, I_n . On this basis, the saturation oxide coverage is 1.8 layers on the (111) surface and 2.0 layers on the (100) surface. The percentage error resulting from absorption of Auger electrons is given by;

$$E = \frac{I_T - I_n}{I_n} \times 100 \quad (7)$$

where I_T is the calculated signal corrected for absorption effects and I_n is the observed signal. The error at saturation oxygen coverage is found to be 13% and 14% for the (111) and (100) surfaces. The error in the observed signals for coverages above saturation on the (100) surface is calculated to be 17% for the lower coverage and 24% for the higher coverage.

To determine if the calculated I_{∞} is reasonable, consider the signal observed for a thick layer of NiO. For a layer of NiO of thickness x with a mean free path for oxygen Auger electrons of μ , the observed signal is:

$$I = I_1 \mu (1 - e^{-x/\mu}) \quad (8)$$

or,

$$I_{\infty} = I_1 \mu \quad (9)$$

For $I_{\infty} = 2.2 \mu\text{V}/\mu\text{A}$, $\mu = 9.5\text{\AA}$ for 507eV electrons in NiO.

This mean-free-path can be compared with other data in the literature.

Palmberg and Rhodin⁶ report mean-free-path lengths for Auger electrons in silver of 4\AA and 8\AA for electron energies of 72 and 362 eV; Jacobi and Holzl¹¹⁸ report a path length of 7.5\AA for 262eV electrons in carbon foil; Baker and McNatt¹¹⁹ report path lengths of 2.5\AA and 4\AA for 76 and 186 eV electrons in yttrium; and Baer, et.al.¹²⁰, report a path length of 22\AA for 1200eV electrons in gold. The mean-free-path is not a sensitive function of the absorbing material as demonstrated by the data for Auger electrons in silver⁶ versus carbon¹¹⁸. (The electron density of silver is six times that of carbon.) This observation is consistent with work on the mechanism of inelastic scattering of low energy electrons in solids^{121,122}. The mean-free-path is dependent upon the electron energy however, and Jones, et.al.¹²² report that it varies as $E^{\frac{1}{2}}$ for electrons in silver with an energy greater than 120eV. Assuming the mean-free-path is independent of the absorbing

material and applying an $E^{1/2}$ correction to determine the path length of 507eV electrons the average value from the literature data is $10. \pm 4. \overset{\circ}{\text{A}}$ in good agreement with observed $9.5\overset{\circ}{\text{A}}$.

Restating the conclusion drawn from the present discussion of the effects of absorption on the measured heights of the oxygen AES peak, there are no errors due to absorption effects on the oxygen AES signal with chemisorbed structures on the surface. For NiO on the surface, absorption of Auger electrons decreases the observed AES peak height by about 14% from the true peak height. This effect must be accounted for in deriving the kinetics of the growth of oxide islands on the surface. Beyond the saturation coverage of NiO, the error in the measured oxygen AES peak caused by absorption effects rapidly becomes larger.

2) Kinetics of the formation of chemisorbed surface structures. The initial reaction region of oxygen with clean nickel surfaces has been associated with the formation of chemisorbed oxygen surface structures. Confining our attention to the initial region at exposures less than 3L, it is seen that the adsorption rate is essentially independent of temperature, the extent of

the reaction is directly related to exposure, and the sticking coefficient decreases with increasing coverage. LEED shows that the $p(2 \times 2)$ structure forms and disappears on the (111) face and only the nickel pattern is observed at 0.34ML where the sticking coefficient is very low. On the (100) face, the minimum in s coincides with the maximum in the diffracted intensity for the $p(2 \times 2)$ structure. Since the AES signals indicate that there are about 0.25ML of oxygen atoms or 0.125ML of oxygen molecules on the surface when the $p(2 \times 2)$ patterns are observed, and since it is difficult to rationalize such diffraction patterns if it is assumed that oxygen occupies the adsorption site as O_2 molecules we conclude that the oxygen is dissociatively adsorbed. This conclusion is at odds with Horgan and King's postulate^{91,92} of non-dissociative chemisorption in this region, but we have already observed that other data in the literature dispute the basis (low heat of adsorption) for their conclusion.

There are at least three types of analysis which could reasonably be applied to the region up to 0.34ML on the (111) and 0.25ML on the (100) surfaces. Since the sticking coefficient decreases monotonically

with increasing oxygen coverage, precursor adsorption and island formation, as reported for oxygen on tungsten⁸¹, is discounted. Since periodic surface structures are formed by the adsorbed oxygen, atomic mobility for at least a few atom distances is required at these temperatures, therefore a second possibility is dissociative Langmuirian adsorption into a mobile state. For this case the sticking coefficient would be $(1 - \theta)^2$ where θ is the relative coverage and is unity at 0.34ML on the (111) and 0.25ML on the (100) surfaces. Then

$$(1 - \theta) = \frac{N_0(1 - \theta_i)}{2it(1 - \theta_i) + N_0} \quad (10)$$

where θ_i is the initial relative oxygen coverage, i is the impingement rate of molecular oxygen, t is time, and N_0 is the number of surface sites filled when θ is unity. By comparing expression (10) with the data, it is easily determined that it does not describe the observed adsorption behavior. The third possible analysis is Langmuirian adsorption but with the condition for non-dissociative adsorption. In this case, the sticking coefficient is $(1 - \theta)$, and

$$(1 - \theta) = (1 - \theta_i) \text{EXP} \left(-\frac{2i}{N_0} t \right). \quad (11)$$

This expression fits the data very well as shown by the

solid lines in Figures 20 and 30 for the (100) and (111) surfaces. The apparently conflicting observations that oxygen is dissociatively adsorbed but follows non-dissociative adsorption kinetics can be reconciled by observing that the oxygen atoms are mobile and do not cover every possible surface site, so the probability that two adjacent and energetically favorable adsorption sites are empty is approximately $(1 - \theta)$.

The coverage of oxygen increases rapidly at 147°K and it is difficult to distinguish the initial from the second adsorption region. An increased adsorption rate at low temperatures is not unexpected since the mean stay time of a loosely bound (e.g. physisorbed) state increases as the temperature decreases. At low temperatures, a molecule may physisorb on sites already covered with oxygen but diffuse over the surface to and be captured by unoccupied sites, thereby increasing the sticking coefficient and adsorption rate.

The minimum sticking coefficient is observed to correspond to the oxygen coverage reached during the initial exponential region for the (111) surface. This corresponds to about 6.3×10^{14} atoms/cm² of oxygen. However, on the (100) surface, the oxygen coverage

continues to increase beyond that described by Langmuirian adsorption, but the sticking coefficient continues to decrease as the coverage increases. Intensification of the $(\frac{1}{2}\frac{1}{2})$ LEED spots during this period indicates further adsorption into a $c(2 \times 2)$ structure, but the diffracted intensity from this structure reached a maximum at a coverage below 0.5ML and the diffracted intensity had decreased at an oxygen coverage corresponding to 0.5ML. This plus observation of $(\frac{1}{2}0)$ spots to high coverages indicate the $c(2 \times 2)$ structure does not fully develop and cover the surface. Due to large data scatter, no attempt will be made to fit a theoretical expression to adsorption into the chemisorbed structure beyond 0.25ML on the (100) surface.

The oxygen coverage at which the sticking coefficient minimized on the (100) surface was a function of temperature. At 373 to 423°K, the minimum occurred at 6.4×10^{14} atoms/cm² while at 302°K, it occurred at 5.1×10^{14} atoms/cm². Possible explanations for this will be discussed later.

The region prior to a minimum sticking coefficient is therefore a result of dissociative chemisorption of oxygen onto clean nickel. The conclusion that the initial

adsorption region represents chemisorption is based on the fact that the periodicities of the surface structures are related to that of nickel and not of nickel oxide. Chemisorption causes small increases in the work function and small decreases in the nickel AES peak heights. There were no measurable energy shifts of the 60eV nickel peak during chemisorption.

3) Kinetics of the formation of NiO up to saturation coverages. The second region of oxygen adsorption on nickel (beyond the minimum sticking coefficient) is characterized by an increase in s followed by a decrease to a very slow rate of adsorption, a decrease of the work function, and a temperature sensitivity of the reaction rate. A new phase is formed in this region as demonstrated by the observation of NiO LEED patterns. A reaction rate which increases (i.e. s increases) with increasing oxygen coverage excludes the possibility of a Langmuirian type adsorption in this region and can best be interpreted in terms of a "clustering" of the NiO on the surface with the reaction rate being related to the growth kinetics of individual clusters. This is analogous to autocatalytic processes in catalysis work and to growth of metal crystals from the vapor.

Considering the clustering of NiO on the surface, in the present case the reaction rate is not first order in either the fraction of the sample surface covered by islands (the rate slows near completion) or the original surface covered with chemisorbed oxygen (it is initially slow). We shall see that the kinetics can be described if it is assumed that the reaction rate is first order in the perimeter length of the growing oxide islands.

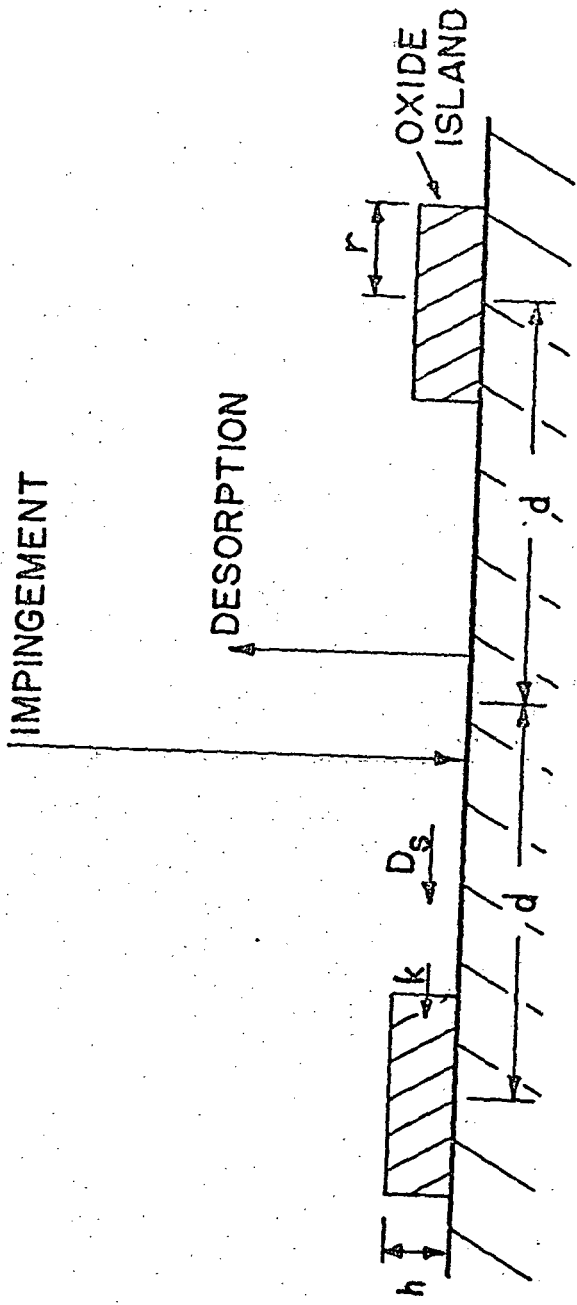
An initially increasing reaction rate has been reported by other authors^{82,83} for oxygen interacting with metal surfaces. Bloomer¹²³ first attributed this effect to oxide island nucleation and growth. Orr⁸³ has analyzed the initial reaction rate for oxygen on the surface of vapor deposited magnesium films using the concept of an active zone for oxygen capture along the perimeter of a growing island of MgO. Oxygen in the active zone can contribute to island growth if adsorption and transport by surface diffusion occurs, or if direct impingement from the vapor onto the perimeter sites occurs. To accomplish an expression for the reaction kinetics, Orr made several assumptions; the six most important assumptions were: (1) Physically adsorbed molecular oxygen existed on the surface with

a mean stay time, τ_p , and an accommodation coefficient into the physisorbed state of unity. (2) Surface diffusion and dissociation of the physisorbed oxygen occurred on the surface; however, the probability of dissociation was small except at a perimeter site.

(3) The oxide islands were circular disks of radius r , height h , and a mean distance between neighboring islands of $2d$, as shown in Figure 43. (4) Smooth atomic planes existed between the oxide islands. (5) The islands all nucleated at the same time and nucleation was complete in an infinitesimally short time beyond time zero. (6) The mean stay time and surface diffusion coefficient of physisorbed oxygen was the same on metal and on MgO.

Orr developed expressions for reaction rates limited by impingement of oxygen onto the surface, limited by oxygen transport by surface diffusion, or limited by capture of oxygen at island perimeter sites. However, the expressions Orr derived were for the sticking coefficient of oxygen during the region of increasing reaction rate. He did not treat the subsequent decrease in reaction rate caused by impingement of growing islands. We will use the same model and essentially the same assumptions in

Figure 43 Schematic of oxide island growth on the surface of a metal.



a simpler derivation of expressions suitable for application to the present data, and will extend the treatment to consider island impingement. This is accomplished in Appendix I.

Recounting briefly this derivation, the theoretical description of nucleation and growth for the three-dimensional case, developed by Johnson and Mehl¹²⁴ and by Avrami¹²⁵, was used to account for island impingement (growth stops at perimeter sites where two oxide islands have grown together). Since we assume that the mean stay time and surface diffusion coefficient of physisorbed oxygen is the same for surfaces covered by chemisorbed oxygen and NiO, reaction rates limited by the oxygen impingement rate would be constant throughout the reaction. This was not observed and this case was not developed in detail. Kinetic expressions for growth rates limited by surface diffusion and by capture of oxygen at island perimeter sites were developed with the results being:

$$(1 - \Theta) = \text{EXP} (-K_i N_0 P^2 t^2) \quad (12)$$

where θ is the fraction of the surface covered by NiO, N_0 is the number of nucleated islands per cm^2 , P is the oxygen pressure, t is time, and K_i is a constant. K_i is

given by:

$$K_i^{\frac{1}{2}} = \frac{2A}{n} (2mkT_g)^{\frac{1}{2}} [2B_i \text{EXP}(E_i/RT) + h] \quad (13)$$

where for rates limited by surface diffusion:

$$B_i = 2 \left(\frac{Z \alpha^2 \nu_1}{\nu_2} \right)^{\frac{1}{2}} ; \quad E_i = \frac{1}{2}(E_a + E_d) \quad (14)$$

and for rates limited by oxygen capture:

$$B_2 = \frac{A^{\frac{1}{2}} \nu_1}{\nu_2} ; \quad E_2 = E_a - E_c \quad (15)$$

In these equations, A is the area per surface site for oxygen, n is the height in layers of the oxide islands, T_g is the temperature of the oxygen gas, and h is the absolute height of the oxide islands. For B_i , z is the reciprocal of the number of nearest adsorption sites, α is the jump distance on the surface, and ν_1 and ν_2 are the vibration frequencies parallel and normal to the surface. For E_i , E_a is the heat of physisorption, E_d is the activation energy for surface diffusion, and E_c is the activation energy for island capture of oxygen.

Equation (12) is the basic equation for describing the kinetics of NiO island growth, but before we can apply it to the experimental data we must consider two other problems in the analysis. First, how does absorption

error in the measured oxygen AES signal affect the analysis, and second, what happens to oxygen in the chemisorbed structure when NiO grows across the surface? To answer these questions, we must anticipate some conclusions from a discussion of the physical processes occurring during oxide island growth which result in a saturation oxygen coverage on the (111) surface of 1.8 layers of NiO. We shall conclude that saturation on the (111) surface occurs when approximately one layer of nickel atoms has been displaced to form NiO and this is why saturation occurs at 1.8 layers. As a result of this model, the average height of individual oxide islands is always 1.8 layers at all times during island growth. Therefore, the error due to absorption of oxygen Auger electrons is a constant factor decreasing the signal contributed from oxygen in NiO to the total observed oxygen AES signal (NiO plus chemisorbed oxygen). On the basis of this model, chemisorbed oxygen is incorporated into oxide as the islands grow laterally across the surface but a chemisorbed structure is maintained in interislands areas as evidenced by continued observation of LEED patterns during oxide growth. To clarify the above arguments, consider that a nickel surface covered with chemisorbed oxygen is

being converted to a nickel surface covered with NiO; let the reaction be θ complete. That is, a fraction θ of the surface is covered with NiO which is 1.8 layers thick, while a fraction $(1 - \theta)$ of the surface is covered with chemisorbed oxygen. Let the oxygen AES signal per unit area from a surface covered only with chemisorbed oxygen be I_c and from a surface covered only with NiO be $I_{1.8}$. Then for a reaction θ complete, the observed oxygen signal would be:

$$I_{\text{obs}} = (1 - \theta) I_c + \theta I_{1.8} \quad (16)$$

But substituting for θ from equation (12), we get

$$I_{\text{obs}} = I_{1.8} - (I_{1.8} - I_c) \text{EXP}(-K_i N_o P^2 t^2) \quad (17)$$

which is an equation like (12) but now related to the experimentally observed oxygen AES data. The experimentally observed data could in turn be corrected for absorption effects as discussed earlier to give the true coverage of NiO on the surface.

Equation (17) is the equation expected to describe the oxygen AES peak height during growth of NiO islands and we proceed to compare it with the experimental data. Values of $K_i N_o$ can be determined by curve fitting and

are shown in Table 8. The curves (shown in Figure 31) fit very well except that at 147°K the reaction does not go to completion as rapidly as predicted. The treatment we have used for island impingement is not rigorously correct for "soft impingement", i.e. impingement of concentration gradients. For small active zones, the treatment is sufficient but at low temperatures where the active zones are wider, the treatment begins to break down.

The energy E_i in the constant K_i (equation (13)) may also be calculated from the experimental data (Figure 31). Recall that the (111) planes of nickel and NiO were parallel, therefore 2.7\AA will be taken as the average jump distance on both nickel and its oxide, A is $0.86\alpha^2$, and the oxide is assumed to be 1.8 layers thick. We assume that $v_1 = v_2$, therefore B_i can be calculated. E_i can be determined by solving the transcendental equation

$$\frac{(K_i N_0)_{T_1}}{(K_i N_0)_{T_2}} = \frac{[2B_i \text{EXP}(E_i/RT_1) + h]^2}{[2B_i \text{EXP}(E_i/RT_2) + h]^2} \quad (18)$$

where N_0 , the number of nuclei, is assumed to be independent of temperature. The value determined was $1.4 \pm \begin{smallmatrix} .9 \\ .6 \end{smallmatrix}$ kcal/mole for the (111) surface.

Using the determined value of E_i and calculating

TABLE 8

Values of the island growth parameter.

	T(°K)	$K_i N_O$ (torr ⁻² -sec ⁻²)
Oxygen on clean (111) Ni	147	3.9×10^{11}
	302	8.7×10^9
	366	2.5×10^9
	423	2.0×10^9
Oxygen on clean (100) Ni	147	
	302	3.0×10^8
	373	1.2×10^8
	423	8.6×10^7
Oxygen on IB (100) Ni	302	6.0×10^9
Oxygen on Ni (111) pre-contaminated with sulfur	302	7.0×10^5

B_i , the nuclei density, N_o , (equal to the island density) on the (111) surface can be calculated to be $1 \times 10^{11} \text{ cm}^{-2}$ and is nearly the same for both the diffusion limited and capture limited cases.

The same considerations about the reaction kinetics should hold for the (100) surface of nickel, but we have already seen that the situation is more complex. Data at 373°K and 423°K indicate the rate of adsorption into the chemisorbed structure decreases rapidly until, at a coverage of $6 \times 10^{14} \text{ atoms/cm}^2$, NiO is nucleated. Because the rate of adsorption into the chemisorbed structure is so slow at these elevated temperatures that any increase in oxygen coverage by this process after nucleation should be negligible, the reaction can be described by island nucleation and growth. However, at 302°K the coverage may increase considerably after nucleation due to adsorption into the chemisorbed structure; therefore island nucleation and growth can only be expected to describe the reaction above a coverage of $0.3 \mu\text{V}/\mu\text{A}$. A value of the constant KN_o at 302°K can still be obtained by curve fitting in the region above $0.3 \mu\text{V}/\mu\text{A}$ as shown in Figure 21 and Table 8. Taking the average jump distance as 2.3\AA , A to be α^2 , and the oxide to be 1.8 layers thick, E_i was

determined to be $1.5 \pm \begin{matrix} .2 \\ .3 \end{matrix}$ kcal/mole for the (100) face. Data taken at 147°K were not included in calculating E_i since it was difficult to decide when nucleation occurred at this temperature and coverage increases in the chemisorbed structure were uncertain. Using the determined value of E_i , the density of nuclei is calculated to be $6 \times 10^9 \text{ cm}^{-2}$ and is nearly the same for diffusion and capture limited cases. Using these two values a theoretical curve for 147°K can be calculated and, as shown in Figure 21, the fit is good.

Since values of E_i have been determined, we would like to discuss the question of rate control by surface diffusion versus rate control by capture of oxygen at perimeter sites. It is very difficult to distinguish between the two cases; the pre-exponential terms are nearly the same leaving only E_i as a basis for distinguishing between them.

There is no basis for estimating the activation energy for capture, E_c , but we can estimate the heat of physisorption, E_a , and the activation energy for surface diffusion, E_d . Therefore, consider the case of rate control by surface diffusion.

From equation (14), if surface diffusion is

rate controlling, $E_i = \frac{1}{2}(E_a - E_d)$. DeBoer¹²⁶ estimates that for a close packed plane of atom, $E_d/E_a = 0.33$. This ratio of E_d to E_a is reasonably consistent with experimental data for tungsten adatoms on tungsten surfaces¹²⁷ ($E_a = 145$ kcal/mole, $E_d = 66$ kcal/mole; $E_d/E_a = 0.45$), for oxygen physisorbed on porous glass¹²⁸ ($E_a = 3$ kcal/mole, $E_d = 1.8$ kcal/mole; $E_d/E_a = 0.6$), and for oxygen physisorbed on tungsten covered with chemisorbed oxygen¹²⁹ ($E_a = 2.8$ kcal/mole, $E_d = 0.9$ kcal/mole; $E_d/E_a = 0.32$). Taking the average of the above ratios of E_d to E_a ($E_d = 0.42 E_a$) and substituting into the expression for E_i , then $E_a = 3.45 E_i$ and since $E_i \approx 1.5$ kcal/mole, $E_a = 5.0$ kcal/mole. Hayward and Trapnell¹³⁰ have estimated the range of E_a for physisorbed oxygen to have a lower bound of 1.6 kcal/mole and an upper bound of 5.0 kcal/mole. Thus the calculated E_a lies in the predicted range of E_a and we conclude that surface diffusion of physisorbed oxygen could limit the rate of formation of NiO.

Consider next the case of reaction rates limited by capture of oxygen by perimeter sites. From equation (15), $E_i = E_a - E_c$. We will consider three values of E_a within the range predicted by Hayward and Trapnell and will calculate E_c using $E_i = 1.5$ kcal/mole and calculate E_d using

$E_d = 0.42 E_a$ (see above). For $E_a = 1.6$ kcal/mole, $E_c = 0.1$ kcal/mole and $E_d = 0.67$ kcal/mole; for $E_a = 3.0$ kcal/mole, $E_c = 1.5$ kcal/mole and $E_d = 1.3$ kcal/mole; for $E_a = 5$ kcal/mole, $E_c = 3.5$ kcal/mole, and $E_d = 2.1$ kcal/mole. Since the pre-exponential terms for the cases of surface diffusion limited and oxygen capture limited kinetics are nearly the same, if oxygen capture were rate controlling, E_c should be much greater than E_d . Since we assume that physisorbed oxygen is the active species, this cannot be the case as shown by the calculated values of E_c and E_d . Even for $E_a = 5$ kcal/mole, the capture process could only be ten times slower than the diffusion process, leading at best to mixed control by both surface diffusion and oxygen capture.

Thus we conclude that the rate of NiO formation is either controlled by surface diffusion or controlled by both surface diffusion and oxygen capture of physisorbed oxygen.

The calculation for oxygen coverage on the (100) surface of nickel was made by assuming that the oxide islands completely covered the surface when the oxygen coverage reached $0.81 \mu\text{V}/\mu\text{A}$. Beyond this coverage, a very slow increase in the AES signal was observed until

the oxygen signal saturated at $0.87 \mu\text{V}/\mu\text{A}$. This phenomenon was not observed for the (111) surface and no attempt to describe the kinetics will be made due to large scatter. However, it seems reasonable that this slow adsorption corresponds to an ultra-thin film oxidation process with the oxide film being sufficiently thin for limited transport to occur without strong electric fields being necessary. Fehlner and Mott¹³¹ have postulated that in general, a metal will rapidly take up a limited amount of oxygen at low temperatures and will reach a saturation value dependent upon the relative magnitudes of the metal and oxide bond strengths and an ill-defined assisting force, suggested to be the image potential of a surface ion. It is suggested that such a mechanism caused the increase from $0.81 \mu\text{V}/\mu\text{A}$ to $0.87 \mu\text{V}/\mu\text{A}$ on the (100) surface. This will be further discussed below.

4) Oxygen adsorption beyond the saturation coverage. An increase of oxygen beyond the saturation coverage for long exposures at 147°K and 6×10^7 torr was associated with an oxygen species adsorbed with an energy of from 12 to 25 kcal/mole. Since the work function was increased by this species, it apparently is ionic or highly polarized. Horgan and King^{91, 92} report

desorption spectra from surfaces saturated at 77°K and warmed slowly towards room temperature. They report that one of the desorption peaks had an adsorption energy of about 13 kcal/mole; the reported desorption spectrum indicates desorption over a rather broad temperature range possibly indicating a distribution of adsorption energies. In addition they report coverages in these states were below 0.05ML which is in excellent agreement with the present data.

The oxygen coverage also increased at 302°K for an oxygen pressure of 10^{-4} torr; δ decreased when oxygen at 10^{-4} torr was present. The population of an adsorption state, at low equilibrium coverage, is equal to $i\tau$, and 10^{-4} torr is the pressure required to achieve a population of about 0.01ML in a state with an adsorption energy of 12.8 kcal/mole. Thus increases in oxygen coverages beyond saturation appear to depend upon a significant population in the adsorption states with energies between 12 and 25 kcal/mole.

To understand the significance of this state, consider the theories of low temperature oxidation¹³¹. Since the activation energy for normal thermally activated diffusion is so high that transport will not occur at

low temperatures, the existence of an adsorbed ionic oxygen species is postulated; this species produces electric fields across the oxide thereby enhancing ionic transport and allowing thickening of the oxide film. It is believed that the adsorbed species observed in this study is the species which assists ionic transport. This is direct experimental evidence supporting a basic concept of all the present theories of low temperature oxidation. Similar adsorbed species with low adsorption energies may also be pertinent to oxide film growth on other metals as Deshpande and Crowell¹³² have reported that molybdenum oxides thicken only if the oxygen pressure is above 10^{-4} torr.

Horgan and King^{91,92} and Klopfer⁸⁵ have reported uptake of several monolayers of oxygen with the sticking coefficient below 10^{-3} . Since they were working with oxygen pressures on the order of 10^{-4} torr, this uptake most probably occurred by the low temperature oxidation process. However, there is evidence that some of this data may have been influenced by phenomena peculiar to evaporated films; this will be discussed later.

The identification of this weakly adsorbed species and its influence on the work function is also pertinent

to the work function studies of oxygen on nickel. Farnsworth and coworkers^{56,69,86} along with others working at low oxygen partial pressures observed that the work function increased for chemisorbed oxygen, then decreased and remained at a value below that of clean nickel as NiO formed. Roberts and co-workers^{78,88} and Delchar and Tompkins⁸⁹, working at higher oxygen pressures, had difficulty seeing the work function decrease below the value for clean nickel. Apparently the weakly adsorbed species maintained a high work function in the latter investigations.

This species may explain another phenomenon observed by Delchar and Tompkins⁸⁹. Upon dose-wise adding oxygen over an evaporated nickel film, they observed a rise followed by a decay in the work function. Although they did not report the progress of the system oxygen pressure, it is expected that the incorporation of the oxygen by the low temperature oxidation process caused pressure decays and allowed a decrease in population of the adsorbed state thereby decreasing the work function. Indeed, Delchar and Tompkins postulated that the effect was caused by incorporation of oxygen, but failed to recognize that the low temperature oxidation process was active.

A third phenomenon which this species obviously explains is the decrease in work function observed when a sample saturated with oxygen at 77°K was warmed towards room temperature^{88,89}.

Observation of this adsorbed polar or ionic species escaped attention in the present investigation for a long time because the experimental system (like most research systems) is not equipped for studies at high oxygen pressures. The present results emphasize the necessity of such a capability if modern surface science research is to be connected with engineering systems.

5) Summary and discussion of the kinetics of the oxygen/nickel reaction. To summarize, the data indicate that oxygen initially chemisorbed on nickel, in a dissociative Langmuirian manner, up to 0.34ML on the (111) and up to 0.25ML on the (100) surfaces. At coverages greater than 6×10^{14} atoms/cm² (0.34ML) on the (111) surface, islands of NiO nucleated and grew until they covered the surface at a coverage of 0.9 μ V/ μ A (1.8 layers of NiO), then the reaction stopped. On the (100) surface, adsorption into the chemisorbed oxygen structure continued beyond 0.25ML until a coverage of about 5×10^{14} atoms/cm²

at 302°K or 6×10^{14} atoms/cm² at 373-423°K was reached. At that time, oxide islands nucleated on the (100) surface and grew until a coverage of 0.81 $\mu\text{V}/\mu\text{A}$ (1.8 layers of NiO) was reached; the reaction rate then slowed considerably but was still appreciable until saturation was obtained at a coverage of 0.87 $\mu\text{V}/\mu\text{A}$ (2 layers of NiO).

Three questions about these processes are obvious:

- (1) What is the nature of the NiO nucleation sites?
- (2) Why does NiO nucleate at coverages of about 5 to 6×10^{14} atoms/cm²?
- (3) Why does island growth cover the surface at 1.8 layers of NiO and what causes a saturation coverage of NiO? There is very little experimental evidence to conclusively answer any of these questions, but some speculation may be desirable.

The density of the nucleation sites observed in this study was 6×10^9 cm⁻² on the (100) and 1×10^{11} cm⁻² on the (111) surfaces. These densities are consistent with that measured by Orr and by others⁸³ on both evaporated films and single crystal surfaces. The number of nuclei was not observed to be a function of pressure in this study and this plus the assumption that N_0 was not a function of temperature is consistent with Orr's work.

The density of the nucleation sites is too

high to correlate with the number of dislocations expected, but it may be consistent with the density of surface steps and/or jogs. This association of nucleation sites and surface defects is consistent with the observation that IB at room temperature increased the rate of NiO formation but did not increase the rate of chemisorption of oxygen (Figures 20 and 21). Since the rate of chemisorption is controlled by the molecular impingement rate and site blockage by previously adsorbed oxygen, surface defects would not be expected to significantly influence the kinetics. However, if an increase in the surface defect density increased the number of nucleation sites, the rate of oxide formation would be increased. The data shown in Figure 21 for oxygen adsorption on a (100) surface after IB was fitted to equation (17) and $K_i N_o$ was determined to be 6×10^9 (Table 8). The nuclei density was found to be $9 \times 10^{10} \text{ cm}^{-2}$, i.e. 15 times higher than that observed for annealed (100) surfaces. Thus the postulate that nucleation sites are connected with surface defects is supported.

A plausible physical reason for associating nucleation sites and surface defects is that the calculated partial pressure of oxygen in equilibrium with nickel is

about 10^{-70} torr at 300°K, indicating that the critical cluster size for nucleation of nickel oxide is very small. On this basis, it is expected that any site which is energetically favorable for formation of NiO would quickly produce clusters greater than the critical size and a rapidly decreasing nucleation rate would be observed.

The second question to be discussed is why NiO nucleates at a coverage of between 5 to 6×10^{14} atoms/cm². One plausible reason for requiring a surface concentration of oxygen before nucleating NiO is thermodynamic considerations. Since chemisorption precedes oxide formation, it is generally assumed that the free energy of chemisorption is more negative than that of oxide formation. This is supported by data for sulfur adsorbed on several metals including nickel¹³³. Additionally, many studies indicate that the heat of chemisorption decreases as the coverage increases^{127,133}, therefore a cross-over of the free energies of chemisorption and oxide formation might be expected. This argument is exactly analogous to arguments concerning phase transitions for three dimensional phases, and phase diagrams relating the surface concentration and the temperature to surface phases might be expected. The existence of such phase diagrams has been amply demonstrated for chemisorbed gas

structures^{44,134} as well as for chemisorbed and reconstructed sulfur structures on metals^{134,135}.

The fact that reducing the surface concentration of oxygen by IB caused the observation in the reverse order of diffraction patterns from NiO, $c(2 \times 2)$, and $p(2 \times 2)$ structures is strong evidence that the transition between chemisorbed oxygen and NiO is governed by thermodynamic rather than kinetic considerations. If NiO was thermodynamically stable compared to the chemisorbed oxygen structures, only a NiO and a nickel pattern would be expected with decreasing oxygen coverage. Since the $p(2 \times 2)$ and $c(2 \times 2)$ structures were observed, oxygen had to leave the NiO structure to form the more energetically favorable chemisorbed structure.

Since the free energy of chemisorption relative to that of oxide formation would be expected to be a function of temperature, the variation with temperature of the coverage for nucleation on (100) nickel is reasonable.

Dissolution of oxygen may complicate the argument concerning when nucleation occurs. Lawless and Mitchell¹³⁶ have investigated the interaction of oxygen with copper single crystals at elevated temperatures using LEED and HEED techniques. They have concluded that oxide was

nucleated on the surface with a chemisorbed structure between these nuclei and have suggested that an induction period prior to nucleation was associated with increasing the concentration of oxygen in solution in the near-surface region of the copper. However, Hansen¹³⁷ reports that only about 0.1 atomic percent of oxygen is soluble in nickel below 873°K. Since atomic transport should not be extensive in the present study and since no information on the width and oxygen concentration profile of the oxide/metal interface is available, the importance of dissolution to the present study is discounted.

Thus, it appears that the transition from growth of chemisorbed oxygen structures to growth of NiO is best explained by thermodynamic arguments.

The third question to be discussed is why island growth covers the surface at 1.8 layers of NiO and what causes a saturation coverage of NiO. We have already argued that oxygen on the surface is incorporated into NiO. Therefore some process of formation of and/or property of NiO must be responsible for the observations that island growth covers the surface at 1.8 layers of NiO and that a saturation coverage is reached at 1.8 to 2 layers of NiO. The atomic density of nickel in NiO

(NaCl type lattice, $a_0 = 4.195\text{\AA}$) is less than the density in nickel (fcc lattice, $a_0 = 3.524\text{\AA}$) and this suggests a plausible explanation for 1.8 layers of NiO covering the nickel when island growth stops. Upon oxidation, the surface layer of nickel is disrupted by the advancing island perimeter. To accommodate the nickel density change, the growing perimeter may either create steps on the surface or displace some nickel atoms to adatom sites. It is envisioned that nickel adatoms would then move across the surface to either a surface step in the area covered by chemisorbed oxygen or to a second layer of NiO growing on top of the original NiO layer. Since it is energetically unfavorable to create surface steps, it seems likely that the second process of moving nickel atoms to adatom sites would be favored. On the basis of this model, one might expect that one monolayer of nickel atoms would be displaced to form 1.4 layers of NiO before islands covered the surface. In reality, 1.25 monolayers of nickel were displaced to form 1.8 layers of NiO before islands covered the surface. This difference is not considered significant since defect sites on the surface and in the path of growing oxide islands might allow disruption of more than one monolayer

of nickel atoms.

The above model provides a plausible explanation for 1.8 layers of NiO when islands cover the surface; this is the saturation oxygen coverage on the (111) surface. Saturation at this coverage is reasonable since further reaction would call for movement of nickel and/or oxygen through at least one layer of NiO and in the absence of electric field, this cannot occur on the (111) surface. However, on the (100) surface, further reaction beyond 1.8 layers does occur until a saturation oxygen coverage amounting to 2 layers of NiO is reached. How and why this occurs on the (100) but not the (111) surface will be discussed.

Since the reaction past island growth on (100) nickel occurred even when the work function was low, the mass transport process does not appear to be ionic transport assisted by electric fields created by adsorbed oxygen (as is the case for further reaction beyond saturation coverages). Fehlner and Mott¹³¹ have suggested that in the absence of field creating species, a reaction might occur by atomic motion of individual nickel and oxygen atoms on the surface when the activation energy for movement is sufficiently reduced by the image force

acting on an ion close to the surface of a solid. We adopt this model as the best explanation for the continued growth of NiO on (100) nickel after the surface is covered by oxide islands. When the NiO reaches a thickness of 2 layers on the (100) surface, the image force is no longer sufficient to assist atomic movement and no further reaction occurs in the absence of a field-creating oxygen species.

Apparently one layer of NiO on the (111) surface is sufficient to eliminate atomic movement due to image forces and therefore the saturation coverage corresponds to the coverage caused by island growth. Three reasons for the difference between (111) and (100) surfaces will be discussed. First, the NiO layers are spaced more widely on the (111) surface (2.42\AA) than on the (100) surface (2.1\AA) and the image force would be smaller for the (111) surface. Second, a nickel atom in one layer of oriented NiO on a (111) surface has three oxygen nearest neighbors at a distance of 2.1\AA , six nickel nearest neighbors at a distance of 2.97\AA , and approximately six nickel nearest neighbors in the nickel lattice. A nickel atom in one layer of oriented NiO on a (100) surface has four oxygen nearest neighbors

at 2.1\AA , four nickel nearest neighbors at 2.97\AA , and approximately four nickel nearest neighbors in the nickel lattice. Thus more bonds must be broken for further reaction on a (111) surface than on a (100) surface. Third, since (111) oriented NiO has alternating layers of nickel and oxygen ions, the transported species must move through a layer of the other species for further reaction on a (111) face. This is not true for (100) oriented NiO. All three of these arguments suggest that after a surface is covered by oxide islands, further reaction to form NiO is easier on (100) surfaces than (111) surfaces in agreement with experimental results.

6) Effect of carbon contamination. To discuss the effects which carbon had on the reaction of oxygen with nickel, it is convenient to consider the effects on formation of chemisorbed oxygen structures and on formation of NiO separately. Consider first the effects on the formation of chemisorbed oxygen structures.

In the results section, we reported that flash data for an oxygen coverage of $0.2 \mu\text{V}/\mu\text{A}$ indicated that the carbon which accumulated on the surface during reaction of oxygen with nickel was in the form of CO. In addition,

LEED and AES data from the surface with 0.55ML of carbon (as opposed to CO) indicate that such carbon reacts quickly with oxygen to form CO. Thus it appears that carbon present during formation of chemisorbed structures was in the form of CO. It seems reasonable that CO molecules on the surface could act in the same manner as O atoms by blocking sites for further oxygen chemisorption and entering into normally observed oxygen surface structures. In this case, there should be little influence on the reaction kinetics in the chemisorbed oxygen region.

Consider next the effects on formation of NiO. The data for oxygen reacting with a (100) surface with 0.55ML of carbon indicate that the oxygen coverage versus exposure was the same as for a clean surface during formation of NiO. In addition, the maximum carbon coverage on a clean (100) surface (Figure 23) coincided with nucleation of NiO and during island growth the carbon coverage decreased reaching a low value when NiO completely covered the surface. Thus it appears that CO does not strongly adsorb on NiO and further, that NiO displaces CO adsorbed on a relatively clean surface.

Thus, the effects of carbon contamination on the present study of oxygen reacting with nickel are not

considered to be significant.

7) Comparison with previous studies. The reaction sequence between oxygen and nickel in the present study may be compared with previous studies of the interaction. While Horgan and King^{91,92} observed similar behavior of sticking coefficient versus coverage and postulated that the increase was due to penetration of the oxygen into the nickel lattice, the present study indicates it is a result of NiO formation. They also report that a film left standing in vacuum for 50 minutes with an oxygen coverage greater than that necessary for a minimum sticking coefficient would exhibit an increased sticking coefficient during subsequent oxygen exposure. Klopfer⁸⁵ has not observed this phenomena nor has present data indicated its occurrences. It is suggested that the effect is an artifact which results from defect enhanced transport in evaporated films. This suggestion is supported by the fact that Farnsworth and Maddin⁶⁶ report variations of LEED intensities with time in residual vacuum when using evaporated films; other investigators, using single crystals, report the LEED intensities to be a function only of exposure⁵⁵.

LEED data for the present study are generally

consistent with previous data. The calibration established for AES signals support previous author's suggestions that the $p(2 \times 2)$ structure is associated with 0.25ML of oxygen, but the previous association of the $c(2 \times 2)$ structure with 0.5ML has been shown to be incorrect. The observation of $(0\frac{1}{2})$ LEED spots, even when the $c(2 \times 2)$ structure was at maximum intensity has also been reported by Farnsworth and Tuul⁴⁸ for a well annealed crystal.

The diffraction patterns observed from nickel oxide were very diffuse. On the basis of the calculated oxide island density, the average island diameter is from 300 to 1300 Å. Since the coherence limit for diffraction of low-energy electrons is on the order of 10^2 to 10^3 Å, coherence broadening is expected to produce a diffuse pattern; this provides direct evidence for the existence of oxide islands on the surface. The existence of sharper LEED patterns for exposures at higher temperatures, as previously reported^{55,56,69}, was observed in the present study. On the basis that warming the substrate from 147°K to 302°K considerably improved the NiO LEED pattern, this effect is attributed to a temperature effect on the degree of order of the surface phases.

A major inconsistency in LEED data between the present and previous studies is the observation of additional diffraction spots located at a radius equivalent to the original nickel spots and generally associated with the formation of NiO. Three possible explanations for these extra spots will be discussed. (1) The spots may indicate a reorganization of the nickel underlying the NiO to three equivalent domains of (100) nickel with one domain oriented as the original and the other two rotated, one 30° and the other 60° , with respect to the original lattice. (2) Another possibility is reorientation of the (100) lattice to a (111) lattice with two equivalent positions 30° apart. No rational explanation for either of these two possibilities can be advanced, especially since only one orientation of NiO was observed with an epitaxial relationship to the original nickel orientation. (3) The spots may also result from a surface structure caused by oxygen adsorbed on top of the oxide. Simmons, et.al.¹³⁸, have reported a diffraction pattern with a close-packed symmetry on the (111) and possibly the (100) surfaces of copper, which they attribute to chemisorbed oxygen ions. The oxygen separation they observed was 3.14Å. To explain the extra spots observed in the present

study on the same basis, a spacing of 2.5\AA , which was fortuitously equal to the nickel spacings, would have to be assumed. This does not seem likely, and, in addition, the spots disappear if the oxygen coverage increases further. This suggests that the scattering centers lie under the NiO, but a reasonable explanation for their occurrence cannot be advanced.

Fehlner and Mott¹³¹, among others, have discussed the low temperature oxidation of metals which they define to be oxidation at temperatures near room temperature. They postulate that oxygen interacts with a clean metal surface in two rapid steps followed by a slow reaction. The first step is chemisorption of oxygen and the second step is formation of an amorphous oxide by a place exchange mechanism. Beyond this rapid region, a slow thickening of the oxide results from field-assisted ionic transport. The present study deals with the initial interaction of oxygen with nickel and confirms that chemisorbed oxygen precedes oxide formation. However, based on data for oxygen on magnesium^{82,83}, this may not be true for every metal. A crystalline oxide replaced chemisorbed oxygen in this study. The rate of oxide formation was usually limited by the number of sites at which oxygen could

dissociate, but a place exchange mechanism, as proposed by Fehlner and Mott, was observed to operate on the (100) surface for a short time. It is interesting to note that oxide formed on a surface contaminated with sulfur was amorphous, and since most oxidation studies start with a "dirty" surface, Fehlner and Mott's postulate that the thin oxide film is amorphous may have some validity.

Chemisorption and oxide formation up to a saturation coverage was rapid in the present study and was followed by a slow oxidation process if an ionic oxygen species was present. This confirms Fehlner and Mott's postulate of such a sequence. The observation of an ionic species which allowed the thickening of NiO beyond saturation has special significance to future studies of the low temperature oxidation process. We did not attempt to test the various theories of ultra-thin film formation.

The interaction of oxygen with surfaces has been studied for many metals at higher temperatures and relatively low oxygen pressures (on the order of 10^{-3} to 1 torr)¹³⁹. Under these conditions, an induction period during which nothing is observed microscopically

is followed by the nucleation and growth of oxide islands to a size visible with an optical or electron microscope. Subsequent growth of these islands is lateral until the surface is covered. While these studies generally start with a surface covered with a room temperature oxide film, the temperatures used are high enough to cause dissolution of the oxygen. If the impingement rate of oxygen is sufficiently low and dissolution does occur, an induction period would be expected before nucleation of the oxide occurred. This sequence is similar to the present study but two other facts concerning previous work must be considered. First a "dirty" surface would be expected to contribute to the induction period, and second the nuclei and oxide formed in the present case would not be visible with an optical microscope. Thus we cannot immediately conclude that the two phenomena are equivalent.

8) Auger electron peak changes. The proposed model of the reaction is supported by the AES peak changes in the 0-80eV region. Chemisorption reduced the intensity of the nickel peaks but their shape and energy were unchanged. With oxide formation, the intensity of the nickel peaks decreased further, a new peak appeared at 12eV, and the 60eV peak changed shape and shifted to a

lower energy. The origin of the 12eV peak associated with NiO is assigned to a $L_{1V}^{O,NiO} V^{NiO}$ transition (Table 4) where the O superscript denotes an oxygen level and the NiO superscript denotes the oxide valence level. Using the band structure and oxygen L_{1V} energy reported for NiO by Wertheim and Huffner¹⁴⁰ and using the correction for Auger emission from an ionized atom as discussed by Chang¹, this transition causes ejection of a 12eV electron, assuming the valence band energy corresponds to that of the maximum density of states. This maximum density lies near the original nickel valence level and a secondary maxima due to the previous oxygen $L_{2,3}$ level lies at a tighter binding energy. There should be another smaller peak which corresponds to the secondary maximum with a calculated energy of 6eV. Some evidence of this peak was observed, but the true secondary peak prevented positive identification.

The shape change and shift of the 60eV peak was essentially a discrete process in that new derivative maxima developed at a lower energy, while the former derivative maxima decreased. Since the shift was not continuous, the concept of a patchy surface consisting of NiO islands on a surface covered by a chemisorbed

structure is supported. The peak energy shift can also be explained by the band structures differences for NiO and nickel. According to Baer, et.al.¹⁴¹, the maximum density of states for clean nickel occurs at about 1eV below the Fermi energy, therefore the $M_{2,3}VV$ transition for clean nickel has a calculated energy of 60eV. When NiO forms, the valence band broadens and the maximum density of states shifts to a tighter binding energy, therefore the $M_{2,3}^{Ni}V^{NiO}$ has a calculated energy of 58eV which gives a peak shift close to the 3eV experimentally observed. No shift was observed during the formation of chemisorbed oxygen structures.

These data on electronic structure changes are in excellent agreement with photoelectron data for oxygen on nickel recently reported by Eastman and Cashion¹⁴². They report that chemisorbed oxygen on nickel is associated with an increased work function and that enhanced electron emission occurs at about 5.5eV from the Fermi level. Chemisorbed oxygen did not change the position of the nickel valence level. With continued exposure, the work function decreased and electron emission probabilities changed significantly in the energy range 2.5 to 11 eV from the Fermi level. The present data complement

Eastman and Cashion's study in proving that these long exposure changes result from NiO formation.

9) Work function changes. The qualitative and quantitative changes of work function with increasing oxygen coverage measured in the present study agree well with previous work^{55,56,78,88,89}. The data for work function changes versus changes in the secondary emission coefficient (Figure 25) indicate that a correlation between the two exists. Data for the true secondary peak height versus oxygen coverage indicates that variations of the peak height may also be used to indicate changes of the work function when interference between peaks can be avoided.

When the nickel surface is converted to NiO the relation between δ and changes of the work function is different (as demonstrated by 147°K data in Figure 25). We have previously pointed out that changes in the inelastic scattering path lengths of the primary and secondary electrons, changes in the Fermi energy, and changes in the work function are the factors which most strongly affect emission of true secondary electrons. We have also pointed out that for low energy electrons, the mean-free-path is relatively insensitive to the material, therefore

the first two parameters should be approximately constant in the present case. Thus we attribute the difference in the relation between δ and changes of the work function for a nickel surface covered with chemisorbed oxygen and for a surface covered with NiO to changes in the Fermi energy.

Thus, the present secondary electron techniques may be used to indicate qualitative changes of the work function but care must be taken to verify that changes in other factors, such as the Fermi energy, do not lead to erroneous conclusions.

10). Clean nickel surfaces. In assigning Auger transitions to the peaks observed in the electron spectrum for nickel (shown in Table 4), we have followed Coad and Riviere^{43,143}. Coad¹⁴³ has recently challenged some of these assignments, but the original assignments will be maintained, since his postulate of split peaks due to electron spin orientations has not been proven. While the transitions causing the Auger electron peaks are not certain, these peaks are generally reported by most investigators. However, the peaks at 8eV and 12eV for the (100) and (111) surfaces, respectively, have been reported by only a few authors. Palmberg and Rhodin⁶

report, without comment, a 6.5eV peak for nickel, a 7eV peak for Cu, and a 12eV peak for Au. Scheibner and Tharp¹⁷ report a 13eV peak for Cu and assign its origin to an interband transition. Seah³² has investigated these low energy peaks and concludes that they are due to a surface-related excited state. It seems likely that the low energy peaks observed in this study have the same origin.

The other aspect of clean nickel surfaces to be discussed is the reversible segregation of carbon to the (100) surface. This was not observed for the (111) face and previous observations of reversible segregation were on a (100) crystal^{42,44} and polycrystalline nickel⁴³. This suggests that the reversible segregation may occur only on the (100) surface, but there are no a priori reasons to support this conclusion. It seems more likely that the observation is fortuitous and that the concentration of carbon in solution in any given sample would control whether surface carbon, which accumulated due to bulk segregation or adsorption of CO and CO₂, would go into solution upon heating and then reappear on the surface during cooling.

Ellis¹⁴⁴ has studied the temperature dependent

reversible segregation of sulfur, carbon, oxygen, and chlorine on thorium. For thorium, the surface segregation of these elements was determined by

$$\frac{X_s}{X_B} = \text{EXP}(\Delta G / RT) \quad (19)$$

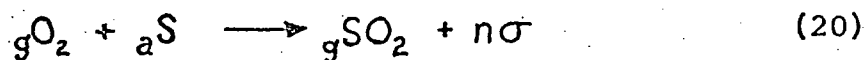
where X_s and X_B were the concentrations on the surface and in the bulk and ΔG was the free energy difference between a surface and a bulk site for the elements. Equation (19) did not describe the segregation versus temperature in the present case (Figure 15) presumably because the carbon segregation was kinetics limited; no serious attempt was made to approach equilibrium.

B. Oxygen/Sulfur Surface Reactions

Before discussing the oxygen/sulfur reaction in detail, we will indicate how the reaction kinetics will be analyzed. The data from surfaces pre-contaminated with sulfur demonstrate that oxygen reacted with adsorbed sulfur and removed it from the surface as SO_2 . We shall see that NiO is formed in areas where sulfur has been removed. We shall also see that the kinetics of removal of sulfur in the $(8\sqrt{3} \times 2)$ surface structure may be described by the island growth model which also describes

NiO formation on nickel surfaces covered by chemisorbed oxygen.

The mass spectrometric studies indicated that the only gas-phase reaction product was SO_2 . The AES studies indicated that as sulfur was removed from the surface, oxygen accumulated, and, moreover, that at all times in all experiments the sum $\theta_0 + \theta_S = 1$. We are thus dealing with the two consecutive reactions:



where g represents a component in the gas phase, a an adsorbed species and σ an adsorption site for oxygen.

Since $\theta_0 + \theta_S$ was always unity, reaction (20) is slow compared to reaction (21). This observation is in agreement with the data for oxygen adsorption on the clean surface, for which the observed rate was always much greater than the rate observed for reaction (20).

Since changes in the relative coverages of oxygen and sulfur are a function of exposure rather than time, the rate dependence of the reaction is first order with respect to the exposure parameter (Figures 39 and 40). However, the rate is not first order with respect to $a\text{S}$, i.e. with θ_S . First order dependence would yield an

exponential decrease in θ_s with exposure. The data for the $(5\sqrt{3} \times 2)$ structure do show a monotonically decreasing reaction rate, but the rate of decrease is much slower than exponential and a great deal of scatter is observed from run to run. Because of this scatter we will not attempt analysis of this case.

The results for the $(8\sqrt{3} \times 2)$ structure are much more regular, and warrant further attention. We have already seen that the reaction rate is first order with respect to the exposure parameter even though there is an oxygen signal from the surface when the reaction is only partially completed (Figure 38). We shall see that this oxygen is in the form of NiO and since isolated "molecules" of NiO cannot exist on the surface, an island morphology of oxygen and sulfur is suggested. In addition, the increase in reaction rate with increasing coverage is exactly analogous to the reaction of oxygen with nickel covered by chemisorbed oxygen. We can therefore use the same concept of oxide nucleation and growth, to describe the sulfur/oxygen reaction (see Appendix I). The oxide nucleates at selected sites on the sulfur-rich surface and grows as islands to cover the surface with the sulfur being converted to SO_2 and displaced as the

oxide spreads. This process may be classified as a Langmuir-Hinshelwood type surface reaction, since both species are adsorbed and must be adjacent for the reaction to proceed.

Considering the process which is rate controlling for the reaction, since the reaction rate increases with time, the reaction is not limited by the impingement rate of oxygen. The other two possibilities are surface diffusion limited or capture limited kinetics. The data are described very well by equation (13), as shown by the solid lines in Figure 40, where the constant $K_i N_o$ is selected as $7 \times 10^5 \text{ torr}^{-2} \text{ sec}^{-2}$ (Table 8). If the average value of E_i for oxygen on clean nickel (1.45 kcal/mole) is assumed to apply to the present reaction, and because B_i is about the same for either the diffusion or capture limited case, the island density is calculated to be about $2 \times 10^7 \text{ cm}^{-2}$.

Since the oxygen concentration on the (111) surface after the sulfur is displaced is the same as the saturation coverage on clean (111) surfaces, the oxygen signal is expected to be affected by absorption effects as previously discussed. However, in using equation (13) to analyze the oxygen/sulfur data, we only

assume that the fractional surface coverages (as opposed to the absolute surface coverages) of oxygen and sulfur are directly proportional to the AES signals, and absorption of Auger electron should not invalidate this assumption.

The island density for oxygen on sulfur-rich surfaces is much lower than for oxide on the clean nickel surface, but it is still a realistic value. It is not certain why the two should be so different. We have associated nucleation sites with surface defect sites, therefore the density of surface defects which are energetically favorable for nucleation of NiO must be significantly reduced by the presence of sulfur.

The above assumption that E_i is the same for oxygen reacting with a surface covered with either sulfur or chemisorbed oxygen should be correct if the reaction is limited by the surface diffusion of physisorbed oxygen. If oxygen capture was important, it is still a reasonable assumption since the capture step is presumed to be the dissociation of oxygen and the incorporation into nickel oxide.

For the oxygen/sulfur reaction, the adsorbed oxygen did not produce a NiO pattern for reasons which

are unknown. That NiO was formed is established by the 60eV AES peak which at saturation was broadened and shifted to a lower energy, just as for the initially clean surface where NiO formation was established.

Since no oxide pattern was observed, direct support for island formation is not available, but indirect support is provided by the sulfur LEED patterns. These patterns were observed until the reaction was 75% complete; the LEED spots were very sharp until they were no longer visible. As discussed by Estrup and Anderson¹⁴⁵, while this behavior does not prove the existence of islands, it is consistent with their formation.

The observation that electron beams and hot filaments in combination with gas phase oxygen increased the rate of this surface reaction is easily understood in terms of our analysis. We have assumed that oxygen is only dissociated at the island perimeter sites, i.e. that dissociation is activated on the NiO and sulfur rich regions and therefore the reaction only proceeds at the perimeter. Electron beams and hot filaments would produce gas phase atomic oxygen which would eliminate the requirement for a perimeter site and general attack of the surface could proceed. The same reasoning would

apply to the reaction of oxygen with clean nickel surfaces, but the reaction was so fast in this case that the effect was negligible.

2) ($5\sqrt{3} \times 2$) structure. In contrast to the ($8\sqrt{3} \times 2$) structure, data for the ($5\sqrt{3} \times 2$) structure cannot be analyzed. Presumably this is a result of non-reproducibility of the starting surface. An imperfect surface is suggested by variations across the surface in perfection of the LEED patterns. The observation that sulfur desorbs from the surface at high temperatures may be significant to the ability to produce a consistently high, uniform sulfur concentration on nickel simply by heating for long times in vacuum.

3) Comparison with Bonzel's study. Finally, we wish to compare our results to those for the surface reaction between oxygen and sulfur on the (110) face of copper. Bonzel¹⁰⁰ adsorbed sulfur from the gas phase and observed the subsequent reaction with oxygen at temperatures in the range of 883°K to 1103°K. Not surprisingly, his results appear different, but similarities also exist.

One similarity is that both studies conclude that free sites are required in order to dissociate O_2

and thus form SO_2 . A major difference is that in the present study, immobile NiO existed on the surface previously occupied by sulfur, while this did not occur in the study by Bonzel because of the different temperature region used in his study. The number of free sites was limited in the present study by the presence of NiO and the number was small compared to the copper study. Thus, rate control in the copper study was associated with a step subsequent to O_2 dissociation (see Bonzel), while diffusion to or capture by sites where dissociation of O_2 occurred was rate controlling in the present study.

C. Future Effort

Auger electron spectroscopy is a very powerful technique as has been demonstrated by this and other studies; its principal disadvantage is the problem of establishing a calibration, especially when the material is distributed over a distance normal to the surface. It would be very advantageous to know more about the inelastic scattering of electrons in solids and to develop a more quantitative knowledge of the AES signal contributed from material a finite distance away from the surface. One interesting technique which may be used in the latter

case is atomic layer sectioning accomplished with ion bombardment.

With regard to the model developed to describe the reaction, it would be of interest to check the general applicability. Magnesium might be an interesting material to study with LEED and AES since it apparently does not exhibit a chemisorbed oxygen structure. Study of the relation to ultra-thin film oxidation would seem profitable.

We have applied the island growth model to describe the surface reaction between oxygen and sulfur, and some of the implications of this to catalytic reactions might be studied. It would also be interesting to see whether such a model could be used to describe the reaction between oxygen and carbon on a nickel surface. The reversible segregation with temperature of carbon in nickel suggests a good way to repeatedly dose the surface with a known quantity of carbon. Further characterization of carbon and CO on nickel could be carried out during this study since the literature is rather confusing in this area.

Finally, the effects of heating the substrate during the oxygen interaction and heating with oxygen

on the surface would be interesting phenomena to study. Besides observing the kinetics at temperatures higher than the present study, the dissolution and diffusion of oxygen could be studied. The effects of dissolution on oxide nucleation and the solubility limits for oxygen in the near surface region would be of interest. Of course, this would cause a depth distribution of oxygen which creates problems with AES as discussed previously.

PART VII

SUMMARY

The reaction of clean and sulfur pre-contaminated nickel surfaces with oxygen has been studied by LEED, AES, and EID. A secondary electron technique has been compared to the retarding potential method for measuring changes in the work function. The secondary electron technique was shown to characterize work function changes. A clean nickel surface was produced by ion bombardment sometimes used in conjunction with an oxygen surface chemical reaction. The secondary electron spectra from a clean nickel surface was reported, including some peaks from a low energy surface-related excited state. A calibration between the oxygen AES peak and the oxygen coverage was established by assuming the initial sticking coefficient was unity. A correction for inelastic scattering of oxygen Auger electrons was obtained from experimental data.

A. Oxygen on Clean Nickel

The reaction of oxygen with clean nickel surfaces has been found to proceed by the initial formation of chemisorbed oxygen structures followed by nucleation and growth of oxide islands. For the (111) surface, the

rate of chemisorption monotonically decreased until a coverage of 0.34ML was reached. The $p(2 \times 2)$ surface structure occurred at 0.25ML coverage, and the work function increased due to chemisorption. At 0.34ML, NiO was nucleated and the sticking coefficient, calculated from the rate of change of oxygen coverage, increased to a plateau with increasing oxygen coverage, then decreased to a low value at a saturation coverage of 1.8 layers of NiO. The work function, decreased with increasing coverage and a very diffuse NiO pattern was observed with parallel (111) planes and $[1\bar{1}0]$ directions for nickel and nickel oxide. The diffuseness of the NiO pattern was attributed to coherence broadening which is direct proof of the existence of oxide islands on the surface.

For the (100) surface, the rate of chemisorption decreased rapidly until an oxygen coverage of 0.25ML was reached. The $p(2 \times 2)$ structure exhibited maximum LEED intensity at this coverage. A subsequent slower and decreasing rate of adsorption into the chemisorbed structure was accompanied by intensification of the $c(2 \times 2)$ pattern, but NiO nucleated at a coverage between 0.3ML (302°K) and 0.4ML (373-423°K), dependent upon the

temperature. Following nucleation, the sticking coefficient increased to a plateau then decreased to a low value at a saturation oxygen coverage of 2.0 layers of NiO. The work function increased with formation of the chemisorbed structures, but decreased when NiO grew on the surface. A diffuse NiO pattern was again observed, but in this case the (100) planes and [011] directions of nickel and nickel oxide were parallel. The appearance of two new sets of diffraction spots, which were equivalent to but which were rotated with respect to the original nickel spots, was associated with NiO growth but could not be explained.

Chemisorbed oxygen was dissociatively adsorbed on nickel and the adsorption kinetics for the (111) face were Langmuirian (i.e. decreased exponentially with exposure). This was also true for the (100) surface up to 0.25ML coverage but between 0.25ML and the coverage for oxide nucleation, the kinetics were not described.

A model developed by Orr⁸³ to describe the initial growth of oxide islands was extended and shown to describe the observed oxide growth kinetics very well. The model assumes the perimeter sites of oxide islands are active growth sites and that the reaction is limited

by either impingement of oxygen, surface diffusion of physisorbed molecular oxygen, or capture at the island perimeter of physisorbed oxygen. The reaction rates in the present case were limited by surface diffusion or by both surface diffusion and oxygen capture. The reaction rate increased with decreasing temperature and the negative activation energy was determined to be 1.4 kcal/mole for the (111) and 1.5 kcal/mole for the (100) surfaces of nickel. The density of oxide islands was calculated to be $1 \times 10^{11} \text{ cm}^{-2}$ for the (111) and $6 \times 10^9 \text{ cm}^{-2}$ for the (100) surfaces.

The oxygen coverage on (100) nickel was observed to increase slowly beyond the saturation coverage at 147°K and 6×10^{-7} torr or at 302°K and 10^{-4} torr of oxygen. An oxygen species was observed under these conditions which had an adsorption energy distributed over the range of 12 to 25 kcal/mole and which increased the work function. It was concluded that this oxygen species assisted ionic transport allowing increased oxygen coverages. The total EID cross-section for 1500eV electrons of this low energy adsorption state was determined to be $5 \times 10^{-19} \text{ cm}^2$.

Broadening and energy shifts of the 60eV nickel Auger electron peak and the appearance of a new Auger

electron peak at 12eV were associated with NiO formation and were interpreted in terms of the differences in the band structures of nickel and nickel oxide.

B. Oxygen on (111) Nickel Pre-Contaminated with Sulfur

The following conclusions may be drawn from the data on the surface reaction between oxygen and sulfur on a (111) nickel surface.

The $(5\sqrt{3} \times 2)$ and $(8\sqrt{3} \times 2)$ coincidence structures previously reported^{115,116} to result from adsorption of sulfur on Ni (111) can also result from segregation of sulfur from the bulk to the surface during heating in ultra-high vacuum.

The sulfur in these structures will react with gas phase oxygen at temperatures near room temperature. The result is an exposure-dependent decrease in sulfur, and a concomitant increase in nickel oxide on the surface. Gas phase mass spectrometry indicates that the reaction product is SO_2 .

The kinetics of the oxygen reaction with sulfur in the $(8\sqrt{3} \times 2)$ structure can be analyzed in terms of rate control by the production of atomic oxygen at the perimeter sites of growing oxygen-rich regions.

The surface represented by a $(5\sqrt{3} \times 2)$ LEED structure was not entirely reproducible.

Accelerations of the reaction rates were observed when the AES primary electron beam, the ion gauge, and/or the mass spectrometer were used with gas phase oxygen present.

PART VIII

LITERATURE CITED

1. C. C. Chang, *Surface Sci.*, 25, 53 (1971).
2. E. A. Bauer, *Techniques of Metals Research*, Vol. II, Pt. 2, R. F. Bunshad, Ed. (Interscience Publishers, N. Y., 1969), p. 559.
3. P. A. Redhead, J. P. Hobson, and E. V. Kornelsen, *The Physical Basis of Ultra-High Vacuum*, (Chapman and Hall, London, 1968).
4. T. Edmonds and R. C. Pitkethley, *Surface Sci.*, 15, 137 (1969).
5. O. Hachenberg and W. Brauer, *Adv. Electronics Electron Phys.*, 11, 413 (1959).
6. P. W. Palmberg and T. N. Rhodin, *J. Appl. Phys.*, 39, 2425 (1968).
7. C. J. Davisson and L. H. Germer, *Proc. Natl. Acad. Sci.*, 14, 317 (1928).
8. H. E. Farnsworth, *Phys. Rev.*, 40, 684 (1932).
9. H. E. Farnsworth, *Adv. Catalysis*, 15, 31 (1964).
10. L. H. Germer and C. D. Hartman, *Rev. Sci. Instrum.*, 31, 784 (1960).
11. J. J. Lander, J. Morrison, and F. Unterwald, *Rev. Sci. Instrum.*, 33, 782 (1962).
12. J. W. May, *Adv. Catalysis*, 21, 151 (1970).
13. J. J. Lander, *Prog. Solid State Chemistry*, 2, 26 (1965).
14. G. A. Somorjai and H. H. Farrell, *Adv. Chemical Physics*, 20, 215 (1971).
15. E. A. Wood, *J. Appl. Phys.*, 35, 1306 (1964).

16. R. E. Weber and W. T. Peria, *J. Appl. Phys.*, 38, 4355 (1967).
17. E. J. Scheibner and L. N. Tharp, *Surface Sci.*, 8, 247 (1967).
18. P. W. Palmberg, *J. Appl. Phys.*, 38, 2137 (1967).
19. O. Klemperer and J. P. G. Shepard, *Advan. Phys.*, 12, 355 (1963).
20. H. Raether, *Surface Sci.*, 8, 233 (1967).
21. W. M. Mularie and T. W. Rusch, *Surface Sci.*, 19, 469 (1970).
22. L. H. Jenkins and M. F. Chang, *Surface Sci.*, 26, 151 (1971).
23. H. E. Bishop and J. C. Riviere, *Appl. Phys. Lett.*, 16, 21 (1970).
24. E. H. S. Burhop, The Auger Effect and Other Radiationless Transitions, (Cambridge U. Press, N. Y., 1952).
25. I. Bergstrom and C. Nordling, Alpha, Beta, and Gamma Ray Spectroscopy, (North Holland, London, 1965), Vol. 2, p. 1523.
26. J. A. Bearden and A. F. Burr, *Rev. Mod. Phys.*, 39, 135 (1967).
27. G. J. Dooley and T. W. Haas, *J. Metals*, 22, 17 (1970).
28. T. W. Haas, J. T. Grant and G. J. Dooley, *J. Appl. Phys.*, 43, 1853 (1972).
29. J. J. Lander, *Phys. Rev.*, 91, 1382 (1953).
30. L. A. Harris, *J. Appl. Phys.*, 39, 1419 (1968); *ibid.*, 39, 1428 (1968).
31. T. E. Gallon, *Surface Sci.*, 17, 486 (1969).
32. M. P. Seah, *Surface Sci.*, 17, 132 (1969).

33. G. F. Amelio, *J. Vac. Sci. Tech.*, 7, 593 (1970).
34. I. M. Bronshtein and S. S. Denisov, *Sov. Phys. Solid State*, 7, 316 (1965).
35. H. Bruining, Physics and Applications of Secondary Electron Emission, (McGraw-Hill, N. Y., 1954), Chap. 5.
36. T. E. Madey and J. T. Yates, *J. Vac. Sci. Tech.*, 8, 525 (1971).
37. P. A. Redhead, *Can. J. Phys.*, 42, 886 (1964).
38. D. Menzel and R. Gomer, *J. Chem. Phys.*, 41, 3311 (1964); *ibid.*, 41, 3329 (1964).
39. P. A. Redhead, *J. Vac. Sci. Tech.*, 7, 182 (1970).
40. E. N. Sickafus, *Surface Sci.*, 19, 181 (1970).
41. R. Riwan, *Surface Sci.*, 27, 267 (1971).
42. J. M. Blakely, J. S. Kim, and H. C. Potter, *J. Appl. Phys.*, 41, 2693 (1970).
43. J. P. Coad and J. C. Riviere, *Surface Sci.*, 25, 609 (1971).
44. J. C. Tracy, *J. Chem. Phys.*, 56, 2736 (1972).
45. J. A. Dillon, *Trans. Nat. Symp. Vac. Tech.*, 8, 113 (1961).
46. R. W. Roberts, *Brit. J. Appl. Phys.*, 14, 537 (1963).
47. H. E. Farnsworth, T. H. George, and R. M. Burger, *J. Appl. Phys.*, 26, 252 (1959).
48. H. E. Farnsworth and J. Tuul, *J. Phys. Chem. Solids*, 9, 48 (1958).
49. R. O. Rantanen, A. L. Moen, and E. E. Donaldson, *J. Vac. Sci. Tech.*, 7, 18 (1970).

50. J. M. Rojo and L. Bru, Microscopie Electronique 1970, P. Favard, Ed. (Societe Francaise de Microscopie Electronique, Paris, 1970), Vol. II, p. 235.
51. L. H. Germer and A. U. MacRae, J. Appl. Phys., 33, 2923 (1962).
52. H. E. Farnsworth, Adv. Catalysis, 15, 31 (1964).
53. K. Klier, A. C. Zettlemoyer, and H. Leidheiser, J. Chem. Phys., 52, 589 (1970).
54. M. Onchi and H. E. Farnsworth, Surface Sci., 11, 203 (1968).
55. A. U. MacRae, Surface Sci., 1, 319 (1964).
56. H. E. Farnsworth and H. H. Maddin, J. Appl. Phys., 32, 1933 (1961).
57. L. H. Germer and C. D. Hartman, J. Appl. Phys., 31, 2085 (1960).
58. R. E. Schlier and H. E. Farnsworth, Adv. Catalysis, 9, 434 (1957).
59. H. E. Farnsworth, Appl. Phys. Lett., 2, 199 (1963).
60. R. L. Park and H. E. Farnsworth, J. Chem. Phys., 43, 2351 (1965).
61. H. E. Farnsworth and H. H. Madden, Adv. Chemistry, 33, 114 (1961).
62. L. H. Germer, Adv. Catalysis, 13, 191 (1962).
63. L. H. Germer, R. Stern, and A. U. MacRae, Metal Surfaces, (American Society for Metals, Metals Park, Ohio, 1963), p. 287.
64. E. A. Bauer, Adsorption et Croissance Cristalline, (Centre National de la Recherche Scientifique, Paris, 1965), p. 19.
65. A. U. MacRae, Science, 139, 379 (1963).

66. H. E. Farnsworth and H. H. Madden, Structure and Properties of Thin Films, C. A. Neugebauer, J. B. Newkirk, and D. A. Vermilyea, Ed. (Wiley, N. Y., 1959), p. 517.
67. H. H. Madden and H. E. Farnsworth, Bull. Amer. Phys. Soc., 5, 349 (1960).
68. H. E. Farnsworth, J. Phys. Chem., 74, 2912 (1970).
69. R. L. Park and H. E. Farnsworth, Appl. Phys. Lett., 3, 167 (1963).
70. G. E. Becker and H. D. Hagstrum, Surface Sci., 30, 505 (1972).
71. A. U. MacRae, Appl. Phys. Lett., 2, 88 (1963).
72. L. H. Germer, E. J. Scheibner, and C. D. Hartman, Phil. Mag., 5, 222 (1960).
73. L. H. Germer and C. D. Hartman, J. Phys. Chem. Solids, 14, 75 (1960).
74. J. W. May and L. H. Germer, Surface Sci., 11, 443 (1968).
75. L. H. Germer, Surface Sci., 5, 147 (1966).
76. J. W. May and C. E. Carroll, Surface Sci., 29, 85 (1972).
77. H. D. Hagstrum and G. E. Becker, J. Chem. Phys., 54, 1015 (1971).
78. M. W. Roberts, Recent Prog. Surface Sci., 3, 1 (1970).
79. E. A. Bauer, Surface Sci., 5, 152 (1962).
80. R. T. Lewis and R. Gomer, Surface Sci., 26, 197 (1971).
81. J. C. Tracy and J. M. Blakely, Surface Sci., 15, 257 (1969).

82. T. N. Rhodin, W. H. Orr, and D. Walton, Processus de Nucleation dans les Reactions des Gaz sur les Metaux et Problemes Connexes, (Centre National de la Recherche Scientifique, Paris, 1965), p. 67.
83. W. H. Orr, Thesis, Cornell University, Ithaca, New York, (1962).
84. J. R. Young, J. Appl. Phys., 31, 921 (1970).
85. A. Klopfer, Berichte der Bunsen-Gesellschaft, 75, 1070 (1971).
86. R. L. Park and H. E. Farnsworth, Surface Sci., 3, 287 (1965).
87. J. S. Anderson and D. F. Kl emperer, Proc. Roy. Soc., A258, 350 (1960).
88. M. W. Roberts and B. R. Wells, Trans. Faraday Soc., 62, 1608 (1966).
89. T. A. Delchar and F. C. Tompkins, Proc. Roy. Soc., 300, 141 (1967).
90. D. Brennan, D. O. Hayward, and B. M. W. Trapnell, Proc. Roy. Soc., A256, 81 (1960).
91. A. M. Horgan and D. A. King, The Structure and Chemistry of Solid Surfaces, G. A. Somorjai, Ed. (Wiley, N. Y., 1969), p. 57-1.
92. A. M. Horgan and D. A. King, Surface Sci., 23, 259 (1970).
93. D. Brennan and M. J. Graham, Disc. Faraday Soc., 41, 95 (1966).
94. S. Cerny, Disc. Faraday Soc., 41, 111 (1966).
95. K. D. Rendulic, Applications of Field Ion Microscopy in Physical Metallurgy and Corrosion, (Georgia Institute of Technology Foundation, Atlanta, Ga., 1969), p. 413.

96. G. Ehrlich, Metal Surfaces, (American Society for Metals, Metals Park, Ohio, 1963), p. 221.
97. R. Gomer, *J. Chem. Phys.*, 21, 293 (1953).
98. G. K. L. Cranstoun, Structure et Proprietes des Surfaces des Solids, (Centre National de la Recherche Scientifique, Paris, 1970).
99. J. J. Lander, *Surface Sci.*, 1, 125 (1964).
100. H. P. Bonzel, *Surface Sci.*, 27, 387 (1971).
101. A. J. B. Robertson, Catalysis of Gas Reactions by Metals, (Springer-Verlag, N. Y., 1970), p. 33.
102. P. H. Holloway and J. B. Hudson, *Rev. Sci. Instrum.*, 43, 1045 (1972).
103. J. B. Hudson, *Rev. Sci. Instrum.*, in press.
104. T. W. Haas, J. T. Grant, and G. J. Dooley, *J. Vac. Sci. Tech.*, 7, 43 (1970).
105. T. A. Flair and P. D. Ownby, *J. Vac. Sci. Tech.*, 8, 661 (1971).
106. S. Dushman and J. M. Lafferty, Scientific Foundations of Vacuum Techniques, (Wiley, N. Y., 1962), p. 322.
107. P. H. Holloway and J. B. Hudson, *Rev. Sci. Instrum.*, 43, 828 (1972).
108. P. W. Palmberg, *Appl. Phys. Lett.*, 13, 183 (1968).
109. N. J. Taylor, *Rev. Sci. Instrum.*, 40, 792 (1969).
110. Instruction Manual, Precision Lock-In Amplifier, Model HR-8, (Princeton Applied Research Corp., Princeton, N. J., 1969).
111. J. C. Rieviere, Solid State Surface Science, Vol. 1, M. Green, Ed. (Marcel Dekker, N. Y., 1969), p. 197.
112. J. M. Martinez-Duart, private communications.

113. R. A. Armstrong, The Structure and Chemistry of Solid Surfaces, G. A. Somorjai, Ed. (Wiley, N. Y., 1969), p. 52-1.
114. G. Dalmai-Imelik, J. C. Bertolini, and J. Rousseau, Surface Sci., 27, 379 (1971).
115. M. Perdereau and J. Oudar, Surface Sci., 20, 80 (1970).
-
116. T. Edmonds, J. J. McCarroll, and R. C. Pitkethley, J. Vac. Sci. Tech., 8, 53 (1971).
117. M. Perdereau, Surface Sci., 24, 239 (1971).
118. K. Jacobi and J. Holzl, Surface Sci., 26, 54 (1970).
119. J. M. Baker and J. L. McNatt, J. Vac. Sci. Tech., 9, 792 (1972).
120. Y. Baer, P. H. Heden, J. Hedman, M. Klasson and C. Nordling, Solid State Commun., 8, 1479 (1970).
121. C. B. Duke and C. W. Tucker, Surface Sci., 15, 231 (1969).
122. E. R. Jones, J. T. McKinney, and M. B. Webb, Phys. Rev., 151, 476 (1966).
123. R. N. Blommer, Brit. J. Appl. Phys., 8, 321 (1957).
124. W. A. Johnson and R. F. Mehl, Trans. Am. Inst. Mining Met. Engrs., 135, 416 (1939).
125. M. Avrami, J. Chem. Phys., 7, 1103 (1939); 8, 212 (1940); 9, 177 (1941).
126. J. H. DeBoer, The Dynamical Character of Adsorption, (Oxford U. Press, London, 1953).
127. G. Ehrlich, Surface Phenomena of Metals, (Society of Chemical Industry, London, 1968), p. 13.
128. R. M. Barrer, Brit. J. Appl. Phys. Suppl., 3, 49 (1954).

129. R. Gomer and J. K. Hulm, *J. Chem. Phys.*, 27, 1363 (1957).
130. D. O. Hayward and B. M. W. Trapnell, Chemisorption, (Buttersworth, Washington, 1964).
131. F. P. Fehlner and N. F. Mott, *Oxidation of Metals*, 2, 59 (1970).
132. S. M. Deshpande and A. D. Crowell, *J. Vac. Sci. Tech.*, 9, 97 (1972).
133. J. Benard, *Catalysis Reviews*, 3, 93 (1969).
134. J. Oudar, *J. Vac. Sci. Tech.*, 9, 657 (1972).
135. J. L. Domange, *J. Vac. Sci. Tech.*, 9, 682 (1972).
136. G. W. Simmons and K. R. Lawless, *Trans. Amer. Crystallog. Asso.*, 4, 72 (1968).
137. M. Hansen, Constitution of Binary Alloys, 2nd Edition, (McGraw-Hill, N. Y., 1958), p. 1024.
138. G. W. Simmons, D. F. Mitchell, and K. R. Lawless, *Surface Sci.*, 8, 130 (1967).
139. K. R. Lawless, Energetics in Metallurgical Phenomena, Vol. I, W. M. Mueller, Ed. (Gordon and Breach, N. Y., 1965).
140. G. K. Wertheim and S. Huffner, *Phys. Rev. Lett.*, 28, 1028 (1972).
141. Y. Baer, P. F. Heden, J. Hedman, M. Klasson, C. Nordling, and K. Siegbahn, *Physica Scripta*, 1, 55 (1970).
142. D. E. Eastman and J. K. Cashion, *Phys. Rev. Lett.*, 27, 1520 (1971).
143. J. P. Coad, *Surface Sci.*, 30, 687 (1972).
144. W. P. Ellis, *J. Vac. Sci. Tech.*, 9, 1027 (1972).
145. P. J. Estrup and J. Anderson, *Surface Sci.*, 8, 101 (1967).

PART IX

APPENDIX I

Kinetics of the Growth of Oxide Islands

We shall consider the lateral growth of circular oxide islands and investigate the three cases of growth rates limited by oxygen impingement from the gas phase (transport and capture being rapid), by surface diffusion of oxygen, and by capture of the oxygen at perimeter sites.

To accomplish an expression for the growth kinetics, we make the following five assumptions:

- (1) Physically adsorbed oxygen exists on the surface with a mean stay time τ_p , a surface diffusion coefficient D_s , and an accommodation coefficient into the physisorbed state of unity.
- (2) The probability of dissociation of oxygen is small except at a perimeter site.
- (3) The oxide islands are circular.
- (4) The mean stay time and diffusion coefficient are the same for surfaces covered with chemisorbed oxygen and covered with NiO.
- (5) All oxide islands are nucleated in a time short compared to the total time of oxide formation.

We shall consider the effects of impingement

of oxide islands on the growth kinetics, and to account for this the theoretical description of three-dimensional nucleation and growth, developed by Johnson and Mehl^{1A} and Avrami^{2A}, will be paraphrased for the present two-dimensional case.

The area of a single circular island, a_η , which nucleated at time η and has grown until time t is given by

$$a_\eta = \pi u^2 (t - \eta)^2 \quad (1A)$$

in which $u = dr/dt$ is the linear radial growth rate of the island. In order to relate the areas of the individual islands to the overall extent of transformation, one makes use of the concept of an "extended area" of transformation; this is the extent to which the transformation would have occurred in time t if one neglects such processes as growth stoppage due to island impingement and neglects inclusion in the nucleation rate of grains nucleated in already transformed regions of the surface. For this case, the extended degree of transformation, θ_{ex} , is

$$\theta_{ex} = \int_0^t a_\eta i \, d\eta = \int_0^t \pi u^2 (t - \eta)^2 i \, d\eta \quad (2A)$$

where i is the nucleation rate. It can be shown rigorously^{1A, 2A}

that the actual extent of transformation, θ , is related to θ_{ex} by

$$\Theta = 1 - e^{-\Theta_{ex}} \quad (3A)$$

or, by rearranging and taking the log of both sides and substituting for θ_{ex} from equation (2A), we have

$$\ln(1 - \Theta) = - \int_0^t \pi u^2 (t - \eta)^2 i d\eta \quad (4A)$$

In order to integrate expression (4A), we require expressions for u and i . Consider first the linear radial growth rate. Since we have assumed that r_p and D_s are the same for both NiO and nickel surfaces covered by chemisorbed oxygen, rates limited by oxygen impingement from the gas-phase onto the surface would be constant until the surface was covered by NiO. (This is true since surface transport to and capture by the perimeter sites would be rapid compared to the rate at which oxygen reaches the surface.) Since a constant reaction rate was not observed, this limiting case will not be considered further.

Considering next the case of oxide growth limited by surface diffusion of physisorbed oxygen, we

proceed as follows. For an impingement rate for oxygen molecules of \dot{I} with dimensions $\text{cm}^{-2}\text{sec}^{-1}$, the impingement rate per surface site is $\dot{I}A$, where A is the area per surface site. The average distance, R , traveled by an oxygen molecule on the surface during a mean stay time, τ_p , as given by the random walk process^{3A}, is

$$R = (4D_s \tau_p)^{1/2} \quad (5A)$$

where D_s is the surface diffusion coefficient. Since surface motion is assumed random, one fourth of the molecules within a distance R in either direction from the island perimeter will reach that perimeter. On this basis, the number of molecules reaching a perimeter site per second by surface diffusion is $4\dot{I}A^{1/2}(D_s \tau_p)^{1/2}$.

Since we are considering the case of growth limited by transport of oxygen to the perimeter sites, direct impingement from the vapor on a perimeter site will increase the growth rate. The impingement rate per unit site around the island perimeter is given by $\dot{I}A^{1/2}h$, where h is the island height. Then the rate of change of the island radius, when growth is limited by the rate of surface diffusion, is given by:

$$u_D = \frac{8A\dot{I}}{n} (D_s \tau_p)^{1/2} + \frac{2Ah\dot{I}}{n} \quad (6A)$$

where a factor of 2 accounts for dissociation of oxygen at the perimeter, the perimeter advances a distance $A^{1/2}/n$ for each oxygen atom, and n is the number of oxide layers in an island.

~~Consider last the case where growth is limited~~
by capture of oxygen at perimeter sites into the oxide island; k is defined to be the rate constant describing this incorporation of oxygen. The concentration of oxygen adjacent to the perimeter will be assumed to be the equilibrium concentration of oxygen, which is \dot{i}_p . Then the rate of incorporation is $\dot{i}_p k A$, or considering capture from both sides of the interface, dissociation of oxygen, and direct impingement from the vapor, dr/dt can be written:

$$u_c = \frac{4A^{3/2}}{n} \dot{i}_p k T_p + \frac{2Ah\dot{i}}{n} \quad (7A)$$

(It is not certain that a direct impingement term should be included in this expression; this could only be ascertained by knowledge of the physical process limiting incorporation. However the term does not significantly alter the values calculated below and therefore remains.)

Since \dot{i} may be written $(2\pi mkT_g)^{-1/2} P$ where T_g is the gas

temperature, expressions (6A) and (7A) may be written:

$$u_D = \frac{K_1^{1/2}}{\pi^{1/2}} P \quad (8A)$$

and

$$u_C = \frac{K_2^{1/2}}{\pi^{1/2}} P \quad (9A)$$

where

$$K_1^{1/2} = \frac{2A}{n} (2mkT_g)^{-1/2} (4(D_s T_p)^{1/2} + h) \quad (10A)$$

and

$$K_2^{1/2} = \frac{2A}{n} (2mkT_g)^{-1/2} (2A^{1/2} kT_p + h) \quad (11A)$$

The above are equivalent to expressions which may be derived from the formulation by Orr^{4A}. Essentially the same assumptions are employed; a major exception is that for the diffusion controlled case the present derivation does not assume an equilibrium concentration of oxygen on the surface.

We will proceed using expressions (8A) and (9A) for u , and consider next the nucleation frequency. We have assumed that oxide nucleates in a time short compared to the time of the experiment. To express this mathematically, assume that the nucleation rate

decreased rapidly with time. If at $t = 0$, N_0 sites exist, if the nucleation probability per unit time per unit site is ν , and if after a time η , N nucleation sites remain, then the nucleation rate, $i = dN/dt$, is given by:

$$i = N_0 \nu e^{-\nu \eta} \quad (12A)$$

From expressions (8A) and (9A), the linear radial growth rate for both the diffusion and capture limited processes can be written as $K_i \pi^{1/2} P^{-1/2}$, and by substituting this expression plus (12A) into (4A) and integrating by parts:

$$\ln(1-\Theta) = 2 K_i N_0 P^2 \nu^{-2} \left(e^{-\nu t} - 1 + \nu t - \frac{\nu^2 t^2}{2} \right) \quad (13A)$$

If ν is large, i.e. the nucleation occurs in a time short compared to the time required for appreciable reaction, then the terms $e^{-\nu t}$, 1, and νt can be neglected compared to $(\nu^2 t^2)/2$, and

$$(1-\Theta) = \text{EXP}(-K_i N_0 P^2 t^2) \quad (14A)$$

where K_i is K_1 for the diffusion limited and K_2 for the capture limited cases.

Expressions (10A) and (11A) for the constant K_i can be reduced further because the factors D_s^{3A} , τ_p^{3A} , and k^{4A} can be written

$$D_s = Z \alpha^2 \nu_1 \text{EXP}(-E_d/RT) \quad (15A)$$

$$\tau_p = \frac{1}{\nu_2} \text{EXP}(E_a/RT) \quad (16A)$$

$$k = \nu_1 \text{EXP}(-E_c/RT) \quad (17A)$$

where ν_1 and ν_2 are the vibration frequencies parallel and normal to the surface, α is a mean jump distance, and z is the reciprocal of the number of nearest adsorption sites. Then the constant K_i can be written:

$$K_i^{1/2} = \frac{2A}{n} (2 m k T_g)^{-1/2} [2 B_i \text{EXP}(E_i/RT) + h] \quad (18A)$$

where

$$B_1 = 2 \left(\frac{Z \alpha^2 \nu_1}{\nu_2} \right)^{1/2} ; E = \frac{1}{2} (E_a - E_d) \quad (19A)$$

and

$$B_2 = \frac{A^{1/2} \nu_1}{\nu_2} ; E_2 = E_a - E_c \quad (20A)$$

Thus, expressions (14A), (18A), (19A), and (20A) describe the kinetics of the growth of oxide islands for growth rates limited by surface diffusion of oxygen or capture of oxygen at perimeter sites.

- 1A. W. A. Johnson and R. F. Mehl, *Trans. Am. Inst. Mining Met. Engrs.*, 135, 416 (1939).
- 2A. M. Avrami, *J. Chem. Phys.*, 7, 1103 (1939); 8, 212 (1940); 9, 177 (1941).
- 3A. J. W. Christian, *The Theory of Transformation in Metals and Alloys*, (Pergamon Press, N. Y., 1965).
-
- 4A. W. H. Orr, Thesis, Cornell University, Ithaca, New York (1962).

APPENDIX C

The Adsorption and Decomposition of CO on Pt(111)

by

J. M. Martinez and J. B. Hudson

The Adsorption and Decomposition of CO on Pt (111)

by

J. M. Martinez* and J. B. Hudson

Materials Division

Rensselaer Polytechnic Institute

Troy, New York 12181

*Address after September 1972

Departamento de Física

Universidad Autónoma de Madrid

Madrid-34, Spain

Abstract

A cylindrical mirror electron energy analyzer has been used to study the adsorption and decomposition of CO on an initially clean Pt (111) surface. The observed rate of adsorption and fractional surface coverage as a function of CO exposure are identical to those observed previously in this laboratory by flash filament adsorption technique. This result provides an absolute calibration of the Auger spectrometry system for carbon and oxygen. Beam-induced decomposition of CO was observed at high incident fluxes. The surface oxygen coverage decreased exponentially to zero during electron bombardment, while surface carbon decreased and then levelled off at a finite value. CO adsorption studies on this carbon contaminated surface showed decreasing CO adsorption rate and decreasing saturation coverage with increasing carbon contamination. The adsorption rate approached zero at high carbon concentration.

Introduction

The importance of platinum as a catalyst for many reactions has led to an increasing number of studies of the adsorptive properties of well-characterized platinum surfaces. In many of these studies it appears that surface impurities have pronounced effects on this adsorptive behavior, and in several cases it appears clear that adsorbed carbon is the responsible species. Catalytic studies of the hydrogenation of CO (1), decomposition of methane (2) ammonia (3) and formic acid (4), oxidation of CO (5) and dehydrogenation of ethane (6) have all indicated poisoning by impurities. Low energy electron diffraction studies of CO adsorption on Pt(100) (7) and on Pt(100) and Pt(111) (8) have shown spurious surface structures which have been explained by Palmberg (9) as arising from surface carbon contamination, either present initially or formed by electron-beam-induced decomposition of CO.

We have studied the adsorption of CO on Pt(111) and the decomposition of this adsorbed CO to yield surface carbon, using Auger Electron Spectroscopy (AES) to measure surface carbon and oxygen concentrations. Comparison of the CO adsorption behavior with results of a previous study of the same process by the flash filament adsorption technique (10) provide an absolute calibration of the AES peak heights. The mechanism of the decomposition process is inferred from measurements of the decomposition kinetics.

Experimental System

The experimental system is very similar to the one described by Palmberg et al (11). The all stainless steel vacuum system is pumped by a combination of ion and sublimation pumps to an ultimate pressure of 5×10^{-10} torr. The electron energy analyzer is a homemade cylindrical mirror type with a coaxial electron gun. The sweep voltage is obtained from a programmable operational power supply and modulated by the 0 to 10 V peak to peak sinusoidal reference signal from a PAR HR-8 lock-in amplifier at a frequency of 7.5kHz. The derivative with respect to the energy of the electron energy distribution is recorded by synchronously detecting the multiplier output with the lock-in amplifier.

Surface Preparation

The sample studied was a high purity platinum ribbon of approximate dimensions 6 x 0.5 x 0.05 centimeters. After being heated to about 1300°C in ultrahigh vacuum for 1 or 2 days it was examined by x-ray diffraction and determined to be a single crystal with a (111) plane parallel to the ribbon surface. AES measurements made on this surface indicated heavy carbon contamination. Attempts to remove this contamination by heating failed, as the carbon segregated reversibly between the bulk and surface of the sample in the temperature range between 800 and 1200 °C. The cleaning of the sample, as determined by AES, was eventually accomplished

by heating the sample to a temperature of about 1200°C in an atmosphere of 10^{-6} torr of oxygen for periods of time which varied from a few minutes to several hours depending on the degree of carbon contamination, followed by flashing in ultrahigh vacuum until the oxygen was removed from the surface. These observations are in agreement with previous studies which indicated that high temperature treatment alone was insufficient to remove carbon from platinum (9, 12-14). Following this cleaning, no segregation of carbon from the bulk was observed even after extended periods at high temperature, apparently because most of the carbon had been removed from the bulk. The Auger spectrum of the cleaned Pt(111) surface was in good agreement with those reported in the literature (9, 13, 15).

CO Adsorption on Clean Pt(111)

Recently, Baldwin & Hudson (10) have measured the adsorption of CO on a platinum surface prepared from the same starting material by the same treatment as just described. They found, using the flash filament desorption technique, that over the pressure range from 5×10^{-9} to 2×10^{-8} torr CO was adsorbed by first order kinetics up to a saturation coverage of about 7×10^{14} molec/cm². Since the number of platinum atoms per cm² on the (111) surface is 1.5×10^{15} they concluded that at saturation one CO molecule occupied two platinum sites on the surface.

4

In the present work, we have observed CO adsorption on the cleaned platinum at a CO pressure of about 5×10^{-9} torr at room temperature, recording the heights of the C (270eV) and O (510eV) Auger peaks as a function of CO exposure, that is, the product of gas phase CO pressure and exposure time. Measurements were made at a primary electron energy of 1570eV, using a modulation amplitude of 5 volts peak to peak. This was the largest modulation voltage that could be used without causing interference between the 270eV carbon peak and the nearby 250eV peak of platinum. Measurements were made intermittently during the adsorption run, at a primary electron current of $7\mu\text{a}/\text{mm}^2$, the lowest value consistent with adequate sensitivity, in order to avoid beam effects. The criteria for success of this procedure were that the original clean-surface Auger spectrum could be restored after the adsorption run by flashing the surface briefly to 650°C , and that the carbon and oxygen AES peaks were always in the same ratio.

The results of these measurements are shown in Figure 1. Here the results of Baldwin and Hudson (10) are plotted as a solid line, showing adlayer coverage as a function of CO exposure. The observed AES peaks for carbon and oxygen, normalized to the same saturation coverage value, are plotted as solid circles and triangles respectively. The agreement between the two techniques is very good, the scatter of the oxygen peaks being larger due to their smaller magnitude and to the higher noise of our equipment in that energy range.

This result, therefore, provides an absolute calibration of the Auger spectrometry system for carbon and oxygen. The straight line in Figure 2 has been drawn assuming a sticking coefficient equal to one. It can be seen that the sticking coefficient for CO on Pt(111) is close to unity and fairly constant at low coverages.

CO Adsorption on Carbon - Contaminated Pt(111)

We have observed that heating our platinum sample in a CO atmosphere for short periods of time does not produce measureable carbon contamination, but that, as previously observed by Palmberg (9), surface carbon can be formed by cracking of adsorbed CO by the electron beam of the Auger apparatus. In particular, we have found that cracking of CO by the 1570eV, $7\mu\text{A}/\text{mm}^2$ electron beam at about 10^{-8} torr of CO allows the deposition of precise amounts of carbon in a region the size of the electron beam cross section, as checked by moving the sample across the beam.

We have used this technique to prepare surfaces with varying amounts of carbon contamination, and then studied CO adsorption on these surfaces. The measurement technique was the same as explained earlier for the clean surface case, except that after development of the contamination layer, the surface was heated to 1000°C in about two seconds and held for 5 minutes to remove all CO before each adsorption run. The results of these measurements are also shown in Figure 1.

Curves labelled 2_c and 2_o , for instance, represent the carbon and oxygen Auger peaks respectively for the same run. The degree of carbon contamination can be inferred from the intersection of curves 2_c and 5_c with the vertical axis. It can be seen that the quantity of CO adsorbed and the initial sticking coefficient decrease with increasing carbon contamination. The shape of the CO coverage versus exposure curve is similar to that observed for the clean surface, but with the vertical axis proportionally shrunk. That is, the adsorption process proceeds as though the only effect of the carbon contamination was to reduce the surface area available for CO adsorption. For high carbon contamination there is no CO adsorption at all (curves 5_c and 5_o) indicating that the carbon covered surface does not adsorb CO in any appreciable amount under our experimental conditions.

The magnitude of the C (270eV) Auger peak observed for the completely contaminated surface is roughly 4.6 times that observed for the non-contaminated but CO-saturated surface. This figure is very close to the ratio of the carbon atom density in the c-face of the graphite structure ($3.8 \times 10^{15} \text{cm}^{-2}$) to the carbon atom density for the saturated CO layer ($7.5 \times 10^{14} \text{cm}^{-2}$), suggesting that the contaminant is present as a close-packed carbon monolayer on the surface.

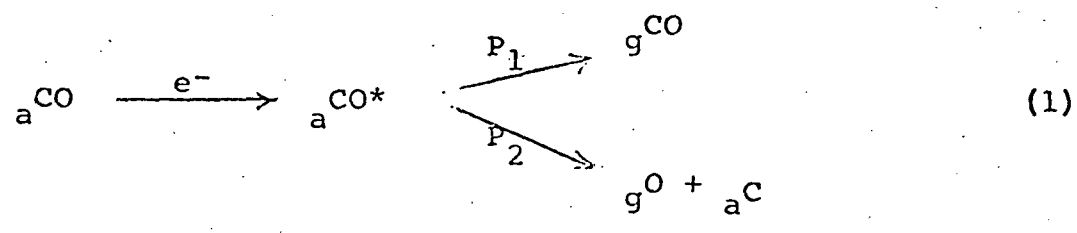
Electron-Beam-Induced Decomposition

For the study of the electron-beam-induced contamination

process, the cleaned platinum surface was saturated with CO at a partial pressure of about 5×10^{-9} torr. The electron beam was then turned on and the oxygen and carbon Auger peaks were monitored as a function of time. In this case the incident beam current was increased to $11 \mu\text{A}/\text{mm}^2$, to enhance the decomposition or desorption processes, but the modulation signal was maintained at 5V peak to peak to avoid interference with the platinum Auger transition to 250eV.

Figure 2 shows the variation with time of the normalized oxygen and carbon Auger peaks. The oxygen peak decreases exponentially to zero but the carbon peak decreases more slowly, and eventually levels off at a constant value of about 1/3 its original amount, thus giving rise to the observed carbon contamination.

This behavior can be explained in terms of a variation of a mechanism of the electron induced desorption processes developed by Redhead (16), in which the rate-determining process is the excitation of an adsorbed CO molecule by an incident electron. In the present case, the adsorbed species may then decay by one of two paths, one yielding a gas phase CO molecule or ion, the other yielding a gas-phase oxygen atom or ion and an adsorbed carbon atom. Schematically,



in which the subscripts a and g indicate adsorbed and gaseous species respectively, the * indicates an activated or ionized species, and P_1 and P_2 are the reaction probabilities of the two paths.

If such a mechanism is operative, then the rate of change of the CO population, σ_{CO} (molecules/cm²), which occurs by both path 1 and path 2, should be given by

$$\frac{d\sigma_{CO}}{dt} = -k(P_1 + P_2)\sigma_{CO} \quad (2)$$

in which k is the product of the cross-section for the excitation of adsorbed CO, Q, and the bombarding electron current density, J. The rate of change of the adsorbed contaminant carbon population, σ_c (atom/cm²), which occurs by path 2 only, should be given by

$$\frac{d\sigma_c}{dt} = kP_2\sigma_{CO} \quad (3)$$

Integrating the above equations, taking into account the boundary conditions

$$\sigma_{CO}(t=0) = \sigma_i = 7.5 \times 10^{14} \text{ molecules/cm}^{-2}$$

$$\sigma_{CO}(t=\infty) = 0, \quad \sigma_c(t=0) = 0$$

one gets

$$\sigma_{CO}(t) = \sigma_i e^{-t/\tau} \quad (4)$$

$$\sigma_c(t) = r\sigma_i(1 - e^{-t/\tau}) \quad (5)$$

where $\tau = (P_1 + P_2)e/JQ$, with e being the electronic charge and $r = P_2/(P_1 + P_2)$.

These concentrations can be related to the observed

oxygen and carbon Auger peak heights, I_o and I_c , (normalized) using the relations

$$\frac{I_o(t)}{I_o(0)} = \frac{\sigma_{co}(t)}{\sigma_{co}(0)} = e^{-t/\tau} \quad (6)$$

for oxygen, and

$$\frac{I_c(t)}{I_c(0)} = \frac{(\sigma_{co} + \sigma_c)(t)}{\sigma_{co}(0)} = (1-r)e^{-t/\tau} + r \quad (7)$$

for carbon.

The solid lines on Figure 4 represent the fit of Equations (6) and (7) to the oxygen and carbon Auger peak heights respectively, using $Q = 2 \times 10^{-19} \text{ cm}^2$ and $r = 0.3$. It can be seen that the agreement is very good.

General Discussion

The results presented in the foregoing sections have a number of interesting implications to the study of adsorption in general and to the question of carbon contamination of surfaces in particular.

It is seen, first, that AES provides a reliable means of studying the kinetics of the adsorption process, provided that adequate care is taken to insure freedom from effects associated with electron-beam-induced desorption or decomposition, and provided that an absolute calibration of the sensitivity of the Auger spectrometer can be made, as was done in the present case by comparison with the earlier flash filament results.

Insofar as the question of carbon contamination is concerned, we have confirmed the beam-induced decomposition of adsorbed CO noted by Palmberg (9), and shown in addition that the decomposition process involves both desorption and decomposition. This process is one which warrants further study, as our present study provides no information on the state of the products desorbed. Further mass spectrometric studies of the electron-induced desorption process will be required to resolve this question. Some work along these lines has been previously reported by Baldwin and Hudson (17), and by Huber and Rettinghaus (18), but comparison with the present study is difficult, as both of these studies involved the coadsorption of H₂ and CO, and very significant interaction effects between the two gases were noted.

Acknowledgement

This research was supported in part by the National Aeronautics and Space Administration, under Grant No. NGL33-018-066 and in part by the Office of Naval Research, under contract No. N00014-67-A-0117-0016.

References

1. E. F. G. Herington and E. K. Rideal, *Trans. Faraday Soc.*, 40, 505 (1944).
2. P. LeGoff, *J. Chim. Phys.*, 53, 380 (1956).
3. A. J. B. Robertson and E. M. A. Willhoft, *Trans. Faraday Soc.*, 63, 476 (1967).
4. E. M. A. Willhoft and A. J. B. Robertson, *J. Catalysis*, 9, 358 (1967).
5. I. Langmuir, *J. Amer. Chem. Soc.*, 40, 1361 (1918).
6. D. J. Fabian and A. J. B. Robertson, *Proc. R. Soc.*, A237, 1 (1956).
7. C. W. Tucker, *Surface Sci.*, 2, 516 (1964).
8. A. E. Morgan and G. A. Somorjai, *J. Chem. Phys.*, 51, 3309 (1969).
9. P. W. Palmberg, in: *The Structure and Chemistry of Solid Surfaces*, ed. G. A. Somorjai (J. W. Wiley, New York 1969), p. 29-1.
10. V. H. Baldwin and J. B. Hudson - article submitted to *Surface Science*.
11. P. W. Palmberg, G. K. Bohn and J. C. Tracy, *Appl. Phys. Letters*, 15, 254 (1969).
12. R. M. Lambert, W. H. Weinberg, C. M. Comrie and J. W. Linnett, *Surface Sci.*, 27, 653 (1971).
13. H. P. Bonzel and R. Ku, *J. Vac. Sci. Technol.*, 9, 663 (1972).
14. B. Lang, R. W. Joyner and G. A. Somorjai, *Surface Sci.*, 30, 454 (1972).
15. T. W. Haas, J. T. Grant and G. J. Dooley, *Phys. Rev.*, B1, 1449 (1970).
16. P. A. Redhead, J. P. Hobson and E. V. Kornelsen, *The Physical Basis of Ultra-high Vacuum*, Chapman and Hall, London 1968.
17. V. H. Baldwin and J. B. Hudson, *J. Vac. Sci. Technol.*, 8, 49 (1971).
18. W. K. Huber and G. Rettinghaus, *J. Vac. Sci. Technol.*, 7, 289 (1970).

Figure Captions

Fig. 1 Adsorption of CO on a Pt(111) surface at $P_{CO} = 5 \times 10^{-9}$ torr, $T = 300^\circ\text{K}$. Curve 1 refers to the clean surface. Curves 2 to 5 refer to the carbon contaminated surface.

Fig. 2 Electron-impact desorption and decomposition of CO on Pt(111). $E_p = 1570\text{eV}$, $i_p = 11\mu\text{A}$ on 1mm^2 .

